STATES IN ^{96}TC POPULATED IN THE (α,n) REACTION

by

© HENRYK ANDRZEJ MACH, B.Sc.

A Thesis
Submitted to the School of Graduate Studies
in Partial Fulfillment of the Requirements
for the Degree
Doctor of Philosophy

McMaster University
April 1981

DOCTOR OF PHILOSOPHY (1981)
(Physics)

McMASTER UNIVERSITY
Hamilton, Ontario

TITLE:	States in ^{96}Tc populated in the (α,n) reaction
AUTHOR:	Henryk Andrzej Mach, B.Sc. (McMaster University)
SUPERVISOR:	Professor M.W. Johns
NUMBER OF PAGES:	xiv, 217

ABSTRACT

The levels of odd-odd ^{96}Tc were investigated using the ^{93}Nb(α,n)^{96}Tc reaction at alpha beam energies of 14 and 18 MeV. The experiments involved singles, gamma-gamma coincidences, neutron-gamma coincidences, excitation functions, gamma-ray angular distributions, measurements of the gamma-ray linear polarization coefficients and electron internal conversion coefficients. At 14 MeV a rich level structure was established involving low-lying states of low and medium spins and of both parities. The position of the positive parity sextet of levels resulting from the coupling of an odd $g_{9/2}$ proton to an odd $d_{5/2}$ neutron was clarified to be: 7^+ ground state, 34.4 keV (4^+), 35.6 keV ((2)$^+$), 36.4 keV (3^+), 45.3 keV (5^+) and 49.3 keV (6^+). The measurements performed with 18 MeV beam revealed an extensive high-spin positive parity level structure extending in excitation energy up to ∿ 3 MeV and populating levels of spin up to 13. Spin and parity assignments are given with a high degree of confidence to most of the 105 energy levels. These states are connected by 251 gamma-ray ~~tran-~~ sitions. Attempts have been made to relate this level structure to those of other nuclei in the mass 100 region.

A new method of spin assignment using the maxima of the excitation functions following the (α,n) reaction has been proposed. A theoretical justification for this apparently empirical method is developed using the Hauser-Feshbach formalism. This theory also gives

a strong theoretical basis for a method of spin assignment based on the ratio of gamma-ray intensities obtained at two beam energies.

Theoretical estimates of attenuation coefficients for angular distributions following (Heavy Ion,xn) reaction are provided. These involved modifying existing methods to make them applicable to nuclei with high spin ground states.

ACKNOWLEDGEMENTS

I wish to express thanks to all those people who have contributed either directly or indirectly to the work contained in this thesis. My highest appreciation is for those, who provided encouragement in those critical moments of depression, when the problems seemed to overwhelm me. In particular, I would like to thank Professor Martin Johns for his friendship and understanding as well as for his guidance and thorough supervision of my thesis work; my parents, whose personal example of sacrifice and determination I have taken as my own model in life; my sister Maria, for her help and support; Miss Gail Akoon-Chang; whose friendship and encouragement I shall always treasure.

I would also like to express my appreciation to friends and colleagues in the McMaster Tandem Accelerator Laboratory who taught me the experimental techniques, assisted in the measurements and involved me in fruitful discussion. I am very grateful to: Drs. Jim Waddington and Richard Tomlinson, the members of my supervisory committee, for their valuable advice over the years; to Kay Marshall-Thompson, John Thompson and Bill Stott for their generous help in the experiments and for the interest they always showed in my research; to Tasneem Khan and Nasib Singhal for their assistance in the experimental work; to Drs. John Cameron, John Kuehner and Aadu Pilt for the vigorous and fruitful discussions; to John McKay, Phil Ashbaugh, Hector Blanchard and other members of the technical staff for the tender care they have

given the experimental facilities which made my experiments successful; and finally to my fellow graduate students whose help was always available.

This thesis would never have reached its final format without the help of Miss Gail Akoon-Chang, Mrs. Jane Forde and Miss Suzanna den Bleker, who helped me type the manuscript, and Miss Maria Krystalski, who assisted with the drawings.

This work has been supported by research grants from the Natural Sciences and Engineering Research Council of Canada.

TABLE OF CONTENTS

TABLE OF CONTENTS (continued)

TABLE OF CONTENTS (continued)

LIST OF TABLES

LIST OF ILLUSTRATIONS

LIST OF ILLUSTRATIONS (continued)

LIST OF ILLUSTRATIONS (continued)

LIST OF ILLUSTRATIONS (continued)

CHAPTER 1

INTRODUCTION

Gamma-ray spectroscopy has provided a powerful tool for the investigation of nuclear structure. In particular, the refinements in techniques that have occured in the last decade have made it possible to study the very complex family of odd-odd nuclei. Gamma-ray spectroscopy involves a group of techniques and a variety of experimental arrangements. Results from these experiments reveal the characteristics of gamma-ray transitions, which in turn indirectly provide information on the nuclear levels involved in the reaction.

Gamma-ray spectroscopy benefits from the development of accelerators capable of providing a large variety of charged particles with a wide range of energies. By choosing a particular combination of beam particles and target material one can produce nuclear species not present in nature. Moreover, by properly selecting the beam energy one can accentuate the desired reaction and minimize others.

The development of high resolution gamma-ray detectors and electron spectrometers, used with fast solid-state electronic circuits, make it possible to study even the complex spectra formed by heavy-ion induced reactions. The analysis of the rich gamma-ray and electron spectra resulting from these reactions requires sophisticated methods of statistical analysis (in particular, peak-fitting programs) and the availability of large computers, which can handle elaborate and lengthy calculations. Thus from the perspective of the experimental methods and tools available, the stage is set for the investigation of the odd-odd nuclei.

The subject of this thesis is the structure of the odd-odd nucleus, ^{96}Tc. This nucleus has 43 protons and 53 neutrons. If one assumes that ^{88}Sr has a semiclosed shell structure, then ^{96}Tc possesses three neutrons in the $d_{5/2}$ shell "outside" the spherical core and five protons of which two are in the $p_{1/2}$ shell and three in the $g_{9/2}$ shell. The shell model predicts that the coupling of a $d_{5/2}$ neutron and a $g_{9/2}$ proton will result in the formation of a configuration of six positive parity levels ranging in spin from 2^+ to 7^+. In ^{96}Tc, these form the ground state configuration. Since ^{96}Tc is far from the region of closed-shell nuclei, one could expect to find nuclear levels related to the collective motion of nucleons.

The work described in this thesis is mainly experimental in character. Seventeen experiments were performed to search for the effects (mentioned above) in the nuclear structure of ^{96}Tc via the ^{93}Nb(α,n)^{96}Tc reaction. In addition eight experiments involving ^{95}Mo(^{3}He,d)^{96}Tc , ^{95}Mo(α,t)^{96}Tc and ^{92}Zr(^{7}Li,3n)^{96}Tc reactions were performed and partially analysed to support or complement the results of the alpha induced reaction. These additional results are not quoted in this thesis, since in the course of this work the fully analysed (^{3}He,d) results were published by Emigh et al. (1979), while results from the (^{7}Li,3n) reaction confirm the (α,n) data.

The (α,n) experiments have led to the identification of the low-lying energy sextet mentioned above. The configurations responsible for the remaining energy levels remain a subject of speculation. Neither the collective nor shell models have proven very successful in accounting for these levels.

In the course of our work on ^{96}Tc a new nuclear model: the Interacting Boson Model (IBM) was developed by Arima and Iachello (1976) and successfully tested on the even-even nuclei in a large range of nuclear species. Recently this model was extended to the odd-A nuclei in the form of the Interacting Boson Fermion Model (IBFM) and was successfully applied to the Pd nuclei by Casten and Smith (1979) and to the Rb region by Kaup et al. (1980). It remains to be seen if this, so far, most promising nuclear model can explain the nuclear structure in the odd-odd ^{96}Tc.

The prime aim of this thesis was neither to search for a complete theoretical model nor to elaborate on existing ones, but to contribute through refined techniques high quality experimental information on the levels of ^{96}Tc. Such data may be used as tests of nuclear models yet to be proposed, which can handle odd-odd nuclei satisfactorily.

This investigation necessitated the development of a number of sophisticated computer programs. Some of these represent essential improvements to the existing codes but most of them are new. These programs include: a) the peak fitting programs for electron internal conversion spectra (ANABEL) and for gamma-ray spectra (HELENA); b) the theoretical estimates of the cross-sections associated with the (α,nγ) and (α,2nγ) reaction channels using Hauser-Feshbach formalism (GlGl); c) estimates of attenuation coefficients (NELLY); and d) programs for fitting experimental data to model estimates in angular distributions (FATIMA) and linear polarization measurements (MABEL). Some of these programs will be discussed in this thesis.

CHAPTER 2

THE THEORETICAL BASIS FOR THE TECHNIQUES USED IN THIS STUDY

2.1 Introduction

The following chapter outlines the basic principles and theory on which the experimental methods and techniques used in the present work are founded. Since a detailed description of these methods is given in standard books on nuclear spectroscopy (Hamilton (1975)) most of the sections in this chapter are treated rather briefly. However, sections 2.2 and 2.4 are given more attention since they include calculations some of which are original to this thesis.

There is a single and important factor common to all these techniques which are used to obtain and analyse the experimental data. Despite the fact that the final results reveal the properties of nuclear levels, these results are obtained in a process of analysis, which is independent of any particular nuclear structure. These techniques are based on the conservation of energy and the total angular momentum, on the applicability of statistical descriptions to large ensembles of nuclei, and on well understood phenomena such as electromagnetic radiation and internal conversion.

2.2 Excitation Functions

2.2.1 Theoretical Calculations

This section includes theoretical estimates of the excitation functions for the ^{93}Nb(α,nγ)^{96}Tc and ^{93}Nb(α,2nγ)^{95}Tc reactions, and a discussion of their significance for the data analysis. The notation used in the theoretical expressions is essentially that of Jägare (1967).

The cross-section for a particular exit channel depends strongly on beam energy.

The $^{93}Nb(\alpha,n)^{96}Tc$ and $^{93}Nb(\alpha,2n)^{95}Tc$ reactions in the alpha energy range from 14 to 30 MeV proceed predominantly through the compound nuclear mechanism (Matsuo et al. (1965)). According to the theory of compound nuclear formation, the cross-section for the formation of a compound nucleus of ^{97}Tc with spin J_c by an alpha beam is given by:

$$\sigma_c(J_c,E_\alpha) = \frac{\pi\hbar^2}{2m_\alpha E_\alpha} \cdot \frac{2J_c+1}{2J_t+1} \sum_{\ell=|J_c-J_t|}^{J_c+J_t} T_{\alpha\ell}(E_\alpha) \qquad [2 - 1]$$

where m_α and E_α are the mass and energy of the alpha particle measured in the Center of Mass System, J_t is the spin of the target nucleus, and $T_{\alpha\ell}$ is the transmission coefficient for an alpha particle with orbital angular momentum ℓ (see Fig. 2.1).

The compound nucleus of ^{97}Tc will decay to ^{96}Tc by neutron decay. Assuming no competition from the charged particle exit channels, one obtains the cross-section for the population of all states in ^{96}Tc of spin J_1, formed by the neutron decay channel, as follows:

$$\sigma_1(J_1,E_\alpha) = \sum_{J_c} \sigma_c(J_c,E_\alpha) \cdot G(J_c,J_1,E_1) \qquad [2 - 2]$$

where the summation is over all those values of J_c, whose partial cross-sections contribute to the population of the J_1 states. E_1 ($= E_\alpha + Q_1$) is the maximum excitation energy of the residual nucleus where Q_1 is the Q-value for the (α,n) reaction channel. Q_1 is intrinsically negative. $G(J_c,J_1,E_1)$ is the fraction (branching ratio) of the total possible modes of neutron

Figure 2.1

Schematic description of alpha particle capture by ^{93}Nb and the decay of two neutrons from the compound nucleus ^{97}Tc. The diagram also illustrates the relationship between the particle energies and the Q-values involved.

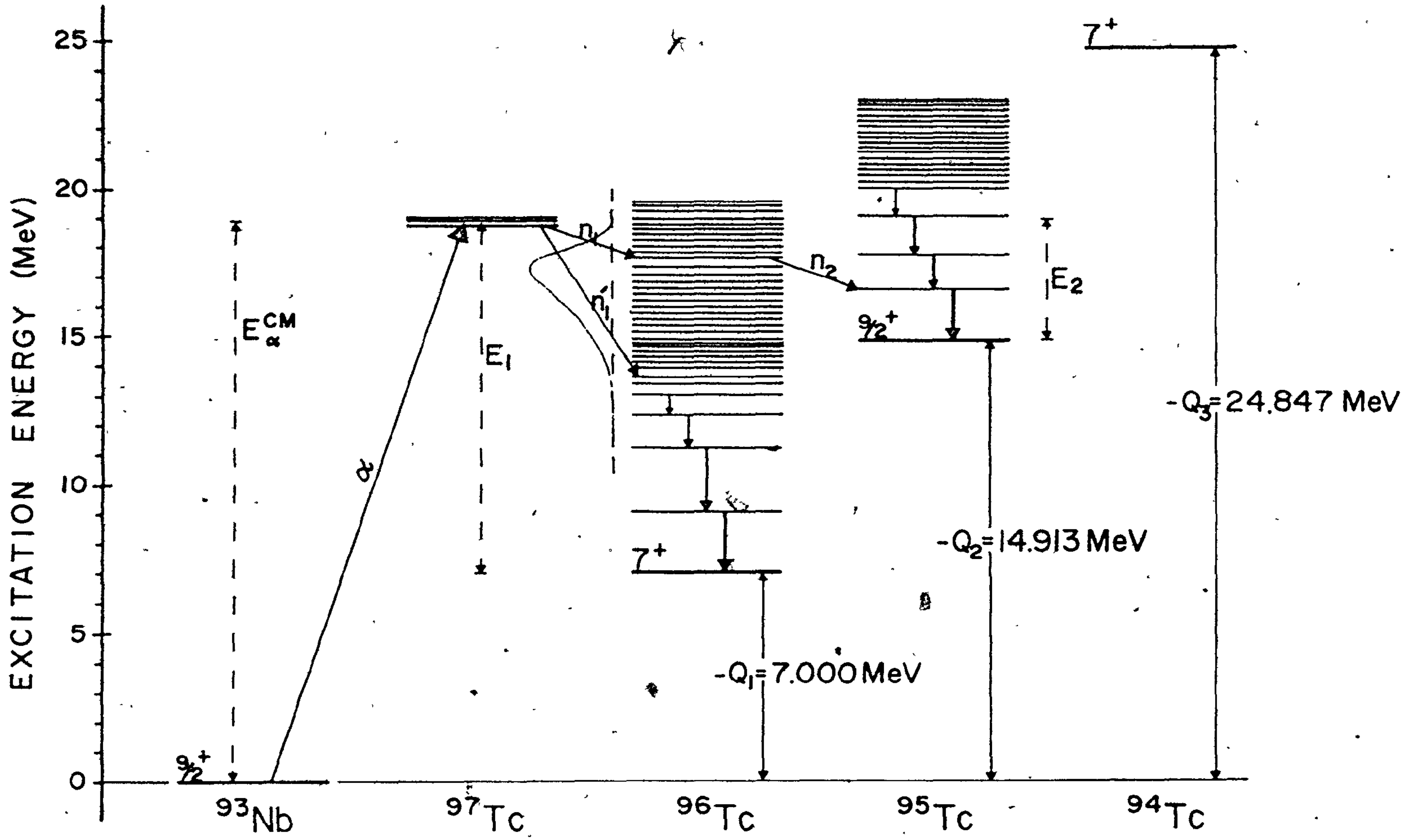
EXCITATION ENERGY (MeV)
0
5
10
15
20
25
^{93}Nb
^{97}Tc
^{96}Tc
^{95}Tc
^{94}Tc
$9/2^+$
E_α^{CM}
α
E_1
n_1
n_1'
n_2
7^+
$9/2^+$
E_2
7^+
$-Q_1 = 7.000$ MeV
$-Q_2 = 14.913$ MeV
$-Q_3 = 24.847$ MeV

emission from a compound nucleus of spin J_c that result in ^{96}Tc states of spin J_1. $G(J_c,J_1,E_1)$ is given by:

$$G(J_c,J_1,E_1) = \left[\rho(J_1,\eta) \sum_{s=|J_1-1/2|}^{J_1+1/2} \sum_{\ell=|J_c-s|}^{J_c+s} f_{1\ell}(E_1) \right] \cdot \left[\sum_{\ell=0}^{\infty} f_{1\ell}(E_1) \sum_{s=|J_c-\ell|}^{J_c+\ell} \sum_{J=|s-1/2|}^{s+1/2} \rho(J,\eta) \right]^{-1} \qquad [2-3]$$

In this expression, $\rho(J,\eta)$ is the spin level density defined by the equation:

$$\rho(J,\eta) = \frac{2J+1}{2\eta^2} \exp\left(- \frac{J(J+1)}{2\eta^2} \right) \qquad [2-4]$$

where η is the spin cut-off parameter. The function $f_{1\ell}(E_1)$ is defined by the integral

$$f_{1\ell}(E_1) = \int_0^{E_1} \omega_1(E_1-\varepsilon) \cdot T'_{n\ell}(\varepsilon)\, d\varepsilon \qquad [2-5]$$

It is formed as the product of the level density at the ^{96}Tc excitation energy corresponding to the emission of a neutron of energy ε and the transmission coefficient for a neutron of that energy with angular momentum ℓ. The integral is over all possible neutron energies. The function $\omega_1(E)$ is estimated through the equation

$$\omega_1(E) = C_1 \exp (4aE)^{1/2} \qquad [2-6]$$

where C_1 and a are constants for any given nucleus. The choice of C_1 can be quite arbitrary since it appears in both the numerator and denominator of equation [2-3].

In the numerator of [2-3] the summations are over all values of ℓ and s which lead to a state in ^{96}Tc of spin J_1. In the denominator, the summation is over all possible modes of decay from states of spin J_c in ^{97}Tc to states in ^{96}Tc.

The calculation of the excitation functions of ^{96}Tc, in the 13 to 24 MeV alpha energy range requires one to obtain the difference between the (α,n) and (α,2n) reaction cross-sections. It is tacitly assumed that any other reaction channels are unimportant. The (α,2n) reaction is a three-step process in which the first step is the production of the compound nucleus, the second is neutron emission to form ^{96}Tc and the third is the decay of ^{96}Tc to ^{95}Tc by neutron emission. As soon as the alpha beam energy crosses the (α,2n) threshold energy, ^{95}Tc formation begins to compete with gamma-ray emission from ^{96}Tc. This threshold is given by $E_\alpha = -Q_2$ where Q_2 is the Q-value for the (α,2n) reaction. However, a particular spin channel in ^{95}Tc is only open when E_α is greater than the sum of the threshold energy and the Yrast energy in ^{95}Tc for that spin. Thus the maximum energy, $E_2(J_2)$ available for a channel of spin J_2 in ^{95}Tc is given by

$$E_2(J_2) = E_\alpha + Q_2 - \delta(J_2) \qquad [2 - 7]$$

where $\delta(J_2)$ is the excitation energy in ^{95}Tc corresponding to the J_2 Yrast level. Based on the data of Marshall et al. (1978), the function $\delta(J_2)$ can be empirically expressed as

$$\left.\begin{aligned} \delta(J_2) &= 0 && \text{for} \quad J_2 < 9/2 \\ &= 0.4\ (J_2 - 9/2) && \text{for} \quad J_2 \geq 9/2 \end{aligned}\right\} \qquad [2 - 8]$$

where δ is expressed in MeV.

The cross-section for the $(\alpha,2n)$ reaction can be estimated theoretically in a fashion similar to that worked out above for the (α,n) process. $\sigma_2(J_2,E_\alpha)$ is given by:

$$\sigma_2(J_2,E_\alpha) = \sum_{J_1} \sigma_1(J_1,E_\alpha) \cdot P(J_1,J_2,E_\alpha) \qquad [2-9]$$

where the summation is over the spins of all states in ^{96}Tc which populate levels of spin J_2 in ^{95}Tc. The statistical factor $P(J_1,J_2,E_\alpha)$ is given by:

$$P(J_1,J_2,E_\alpha) = H(J_1,J_2,E_\alpha) \;/\; P_0 \qquad [2-10]$$

where

$$P_0 = \int_0^{E_1} \sum_{\ell=0}^{\infty} (2\ell+1)\; T'_{n\ell}(\varepsilon) \cdot \omega_1(E_1-\varepsilon)\; d\varepsilon \qquad [2-11]$$

P_0, the normalizing factor, represents the total cross-section for the (α,n) channel. The $H(J_1,J_2,E_\alpha)$ function is the contribution to the $(\alpha,2n)$ channel of spin J_2 coming from the (α,n) channel of spin J_1 and is defined as:

$$H(J_1,J_2,E_\alpha) = \int_0^{E_2} \sum_{\ell=0}^{\infty} T'_{n\ell}(\varepsilon) \cdot \omega_1(E_1-\varepsilon) \cdot G(J_1,J_2,E_2-\varepsilon)\; d\varepsilon \qquad [2-12]$$

In this expression the $G(J_1,J_2,E)$ function is determined according to the equations [2-3] to [2-6], except that the $T'_{n\ell}$ coefficients are replaced by $T''_{n\ell}$ - the transmission coefficients for emission of a neutron by ^{96}Tc, and the level densities ω_2 are those of ^{95}Tc and are characterized by a constant C_2. As in the case of the (α,n) channel, the C_1 and C_2 coefficients play no role in the σ_2 cross-sections since they appear in both the numerator and denominator of the expression for $\sigma_2(J_2,E_\alpha)$.

The excitation functions of spin J_1, $\sigma_1'(J_1,E_\alpha)$, observed in ^{96}Tc are defined as a difference between the cross-section for a particular spin channel in ^{96}Tc and that fraction of the cross-section, which feeds the states in ^{95}Tc by decay of a second neutron. Therefore the excitation functions are calculated in the following manner:

$$\begin{aligned}\sigma_1'(J_1,E_\alpha) &= \sigma_1(J_1,E_\alpha) - \sum_{J_2} \sigma_1(J_1,E_\alpha) \cdot P(J_1,J_2,E_\alpha) \\ &= \sigma_1(J_1,E_\alpha) \{ 1 - \sum_{J_2} P(J_1,J_2,E_\alpha) \}\end{aligned} \qquad [2 - 13]$$

where the summation is over all possible spin channels in ^{95}Tc accessible through the decay of a second neutron.

The calculations were done using a computer program GIGI. The $T_{\alpha\ell}$ transmission coefficients were those of Huizenga and Igo (1961), while the $T_{n\ell}$ transmission coefficients were taken from tables of Moldauer (1961); the a and C_2 parameters for level densities in odd-A nucleus of ^{95}Tc were estimated from table 17-2 of Preston (1963), and were taken as $a=6.2$ MeV^{-1} and $C_2=0.075$ MeV^{-1}. The value of C_1 for the odd-odd nucleus of ^{96}Tc is simply $C_1=2C_2$. The spin cut-off parameter η was asumed to be constant and identical for all nuclei involved, and the value of $\eta=4$ was used in the calculations. The Q-values for the (α,n) and $(\alpha,2n)$ reactions were taken from tables of Gove and Wapstra (1972) as $Q_1=-7.000$ MeV and $Q_2=-14.913$ MeV.

The results of these calculations are shown in Fig. 2.2 which presents σ_1' as a function of J_1 (solid curve) and σ_2 as a function of J_2 (dashed curve) for a series of values of E_α in the laboratory reference

Figure 2.2

Theoretical estimates of the $\sigma_1'(J_i,E_\alpha)$ and $\sigma_2(J_2,E_\alpha)$, as a function of J for selected choices of alpha energy. The solid and dotted curves present (α,n) and (α,2n) cross-sections respectively. The rapid decrease in the (α,n) cross-sections as the beam energy passes the (α,2n) threshold is very striking.

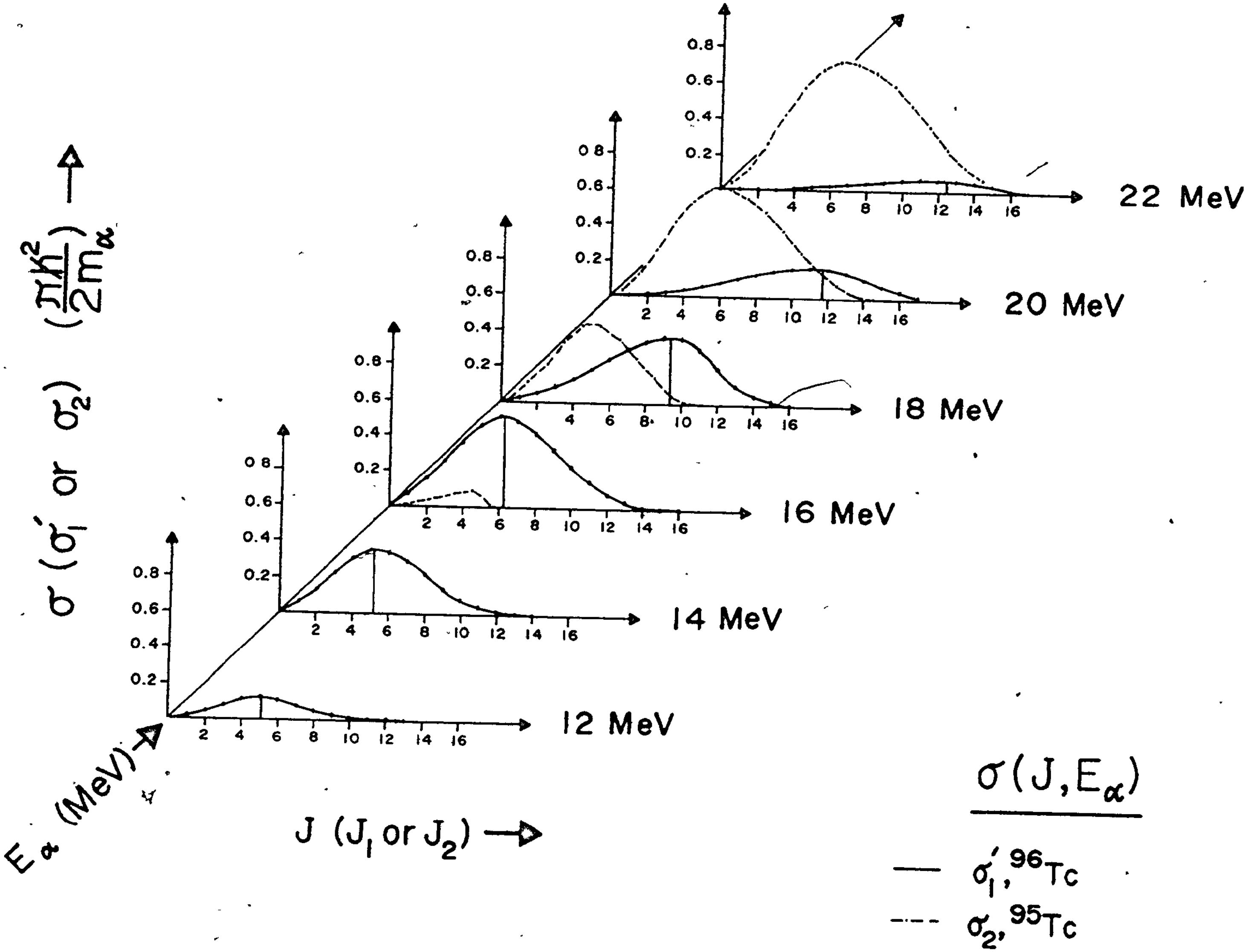
σ (σ_1' or σ_2) $\left(\frac{\pi\hbar^2}{2m_\alpha}\right)$
E_α (MeV)
J (J_1 or J_2)
0.2
0.4
0.6
0.8
2
4
6
8
10
12
14
16
12 MeV
14 MeV
16 MeV
18 MeV
20 MeV
22 MeV
$\sigma(J, E_\alpha)$
σ_1', ^{96}Tc
σ_2, ^{95}Tc

system. The maximum in σ_1' shifts steadily to higher spin values as E_α increases. Moreover, this maximum first increases with E_α and then decreases as competition from the (α,2n) reaction increases in importance. Although, over the range of energies shown, the σ_2 cross-section continues to rise, it too will eventually fall as the beam energy crosses the (α,3n) threshold. It is obvious from Fig 2.2, that, as far as ^{96}Tc is concerned, the only reason for increasing the beam energy beyond 14 MeV is to increase the relative population of high spin states.

2.2.2 Application of the Theory to Spin Determination

Fig. 2.3A shows as solid curves the experimental excitation functions for a 2^+ state at 256 keV, a 5^+ state at 177 keV and an 8^+ state at 947 keV in ^{96}Tc, measured through the intensities of deexciting gamma-rays of energy 219, 127 and 371 keV respectively (see chapters 4 and 5 for the experimental details and data analysis). The experimental data of Fig. 2.3 were corrected for the change in the beam energy due to the finite target thickness. In the same figure are shown the excitation functions derived from the model for states of spin 2, 5 and 8, normalized so that the experimental and calculated functions have equal maximum cross-sections. The agreement is quite respectable. It might be argued that the model curves are strictly applicable only to states in the ^{96}Tc formation region, about 8 to 10 MeV above the ground state, while the three experimental curves apply to states populated by a cascade of gamma-rays from the formation states. An attempt to improve the model by assuming an n-fold cascade of dipole transitions between the states in the "formation" region and those in the "experimental" region was carried out for values of n ranging from 2 to 4. This calculation showed that the multiple branching

Figure 2.3

A) A comparison of the experimental and theoretical excitation functions for low, medium and high spin states in ^{96}Tc.

B) The dependence of the position of the maximum in the ^{96}Tc excitation function on the spin of the initial state. The curve through the points with error bars presents the experimental relationship; the curve through open circles the theoretical prediction. The dotted curve shows the relationship between the excitation and spin of the Yrast levels in ^{95}Tc. The relationship of this curve to the situation in ^{96}Tc is discussed in the text.

C) and D) The experimental points present ratios of the photon intensity measured at an alpha energy of 18 MeV to the intensity at 14 MeV for a large number of ^{96}Tc transitions. These points are plotted against the spin value of the state in which the transition originated.

On each figure, the three theoretical curves relating the ratio R(J) to J, correspond to situations where the initial state is fed directly by neutron emission, by a neutron followed by a two-fold or a four-fold gamma-ray cascade, respectively.

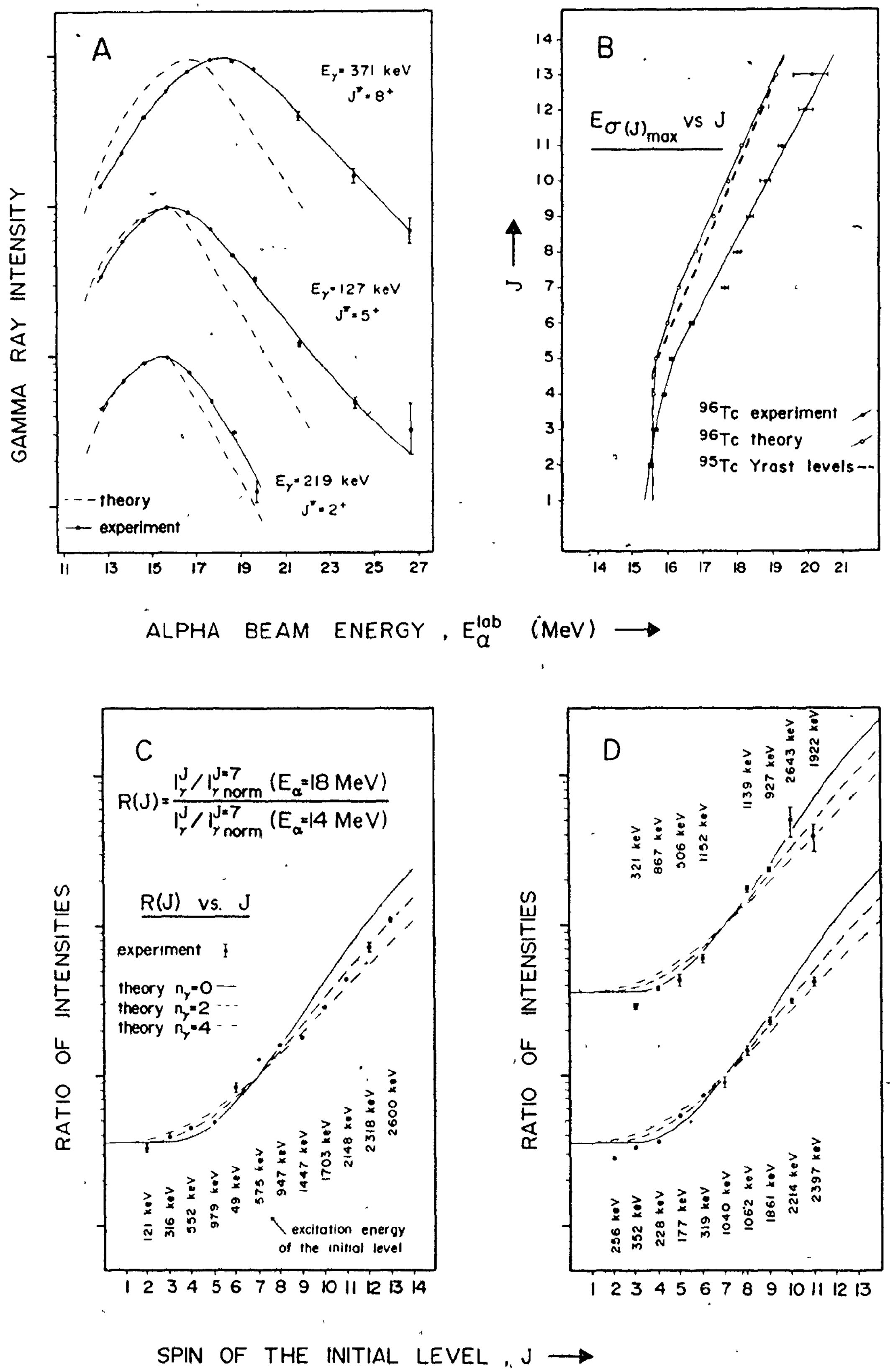
A
E_γ= 371 keV
J^π= 8+
E_γ= 127 keV
J^π= 5+
E_γ= 219 keV
J^π= 2+
--- theory
—•— experiment
GAMMA RAY INTENSITY
11 13 15 17 19 21 23 25 27
B
$E_{\sigma(J)_{max}}$ vs J
J
1 2 3 4 5 6 7 8 9 10 11 12 13 14
14 15 16 17 18 19 20 21
96Tc experiment
96Tc theory
95Tc Yrast levels
ALPHA BEAM ENERGY, E_α^{lab} (MeV)
C
$R(J) = \frac{I_\gamma^J / I_{\gamma\,norm}^{J=7}\ (E_\alpha = 18\ MeV)}{I_\gamma^J / I_{\gamma\,norm}^{J=7}\ (E_\alpha = 14\ MeV)}$
R(J) vs. J
experiment
theory n_γ=0
theory n_γ=2
theory n_γ=4
121 keV
316 keV
552 keV
979 keV
49 keV
575 keV
947 keV
1447 keV
1703 keV
2148 keV
2318 keV
2600 keV
excitation energy of the initial level
RATIO OF INTENSITIES
1 2 3 4 5 6 7 8 9 10 11 12 13 14
D
321 keV
867 keV
506 keV
1152 keV
1139 keV
927 keV
2643 keV
1922 keV
256 keV
352 keV
228 keV
177 keV
319 keV
1040 keV
1062 keV
1861 keV
2214 keV
2397 keV
RATIO OF INTENSITIES
1 2 3 4 5 6 7 8 9 10 11 12 13
SPIN OF THE INITIAL LEVEL, J

involved in this process did not significantly shift the energy corresponding to the maximum cross-section for a given spin ($\Delta E_{\sigma_{max}} \sim 0.2$ keV) but merely broadened the peak in the excitation function.

If one plots the energy of maximum cross-section for a state of given J versus J, ie. $E_{\sigma_1'(J_1)_{max}}$ versus J_1, one obtains curves of the type shown in Fig. 2.3B. The solid curve is drawn through the experimental points obtained from an analysis of the excitation curves determined for actual states in ^{96}Tc (experimental details available in chapter 5). When the allowance is made for the uncertainty in determining $E_{\sigma(J)_{max}}$, the points fit remarkably well on a smooth curve. The open circles curve is obtained from an analysis of the excitation functions derived from equation [2-13]. It shows much the same shape as the experimental curve but predicts that the excitation functions should peak at a lower excitation energy than that actually observed.

The shape of the function defined by equation [2-13] and more particularly the value of E_α corresponding to its maximum value for given J, is a reflection of the Yrast levels in ^{95}Tc. This is a simple consequence of the fact that competition from the (α,2n) reaction grows exponentially as soon as the (α,2n) threshold is passed and reduces the (α,n) cross-section rapidly. That this process is responsible for the sharp maximum in the excitation functions is made evident by the plot of $[\delta(J_2)-Q_2]_{Lab}$ versus J_2 shown as dashed curve in Fig. 2.3B . The values of $\delta(J_2)$ are given by equation [2-8] and the energies are adjusted for the transition from the Center of Mass to the laboratory system. This curve is simply a plot of the energy at which neutron emission to the Yrast level of spin J_2 in ^{95}Tc becomes energetically possible. Its resemblance to the curve derived from equation [2-13] is very striking.

Finally, the curves of Fig. 2.3C and 2.3D present the ratios of the production cross-section at a beam energy of 18 MeV to that at 14 MeV for states with spin values in the zero to fourteen range. These ratios have been normalized to unity for J=7. The solid curve of Fig. 2.3C and 2.3D is derived from the expression for $\sigma_1'(J_1, E_\alpha)$ given in equation [2-13] . The ratios predicted by this equation are quite insensitive to the values of a and η chosen for the calculation. However, they are, strictly speaking, only valid for states in ^{96}Tc at an excitation corresponding to the formation of ^{96}Tc, perhaps 5 to 10 MeV above the states for which experimental ratios can be determined. Whereas the energy at which $\sigma_1'(J_1, E_\alpha)$ peaks for a given spin value is quite insensitive to the cascade process which connects the formation states to the observed ones, the cascade process has a significant effect on the ratios of the cross-sections at 18 and 14 MeV. The dotted curve of these two figures present the ratios expected for the cases where the formation and observed states are connected either by two-step or four-step cascades of dipole transitions between states of spin J and states of J-1, J and J+1 with equal probability. The cross-section ratios derived assuming unequal probability for ΔJ=-1, or 0 or +1 transitions are not significantly different.

On the same figures are placed the experimentally determined cross-section ratios for a wide range of ^{96}Tc transitions. The fit between the experimental points and the curves for the two-step process is very good. Some comment on the experimental points is given in the next paragraph.

Because all the experimental intensities at both 14 and 18 MeV were measured relative to the intense 525 keV ($7^+ \rightarrow 6^+$) transition, the experimental cross-section ratio for the 525 keV transition is by definition unity, and one would therefore expect to be able to superpose the cross-section ratios derived from the experimental intensities of Table 5.1 directly on Figures 2.3C and 2.3D. Unfortunately, the 7^+ 575.0 keV level in which the 525 keV transition originates cannot be considered a perfect choice for normalization to a statistical theory, since instead of having balanced feeding from states of spin 6, 7 and 8, it is fed mainly from 8^+ and 9^+ levels. As a consequence, it behaves more like a "statistical 8" state than a "statistical 7" state as far as its excitation function is concerned. Ideally, one would like to use the average cross-section ratio for a large number of J=7 states for comparison with predictions of a statistical theory. In practise, there are available only two J=7 states suitable for obtaining such an average; the 575 keV state and another one at 1040.8 keV. The average cross-section ratio for these two is 0.8 rather than unity. Consequently, the experimental ratios derived from Table 5.1 have all been increased by factor of 1.25 to make comparison with the predictions of the statistical model more appropriate. The experimental points shown on Fig. 2.3C and 2.3D are all "scaled up" experimental ratios.

In general the model predictions reflect the pattern of experimental results quite well. The most significant deviation is that of Fig. 2.3B and it can be attributed to several factors. For practical reasons the density of states in ^{96}Tc was not described by a discrete distribution of levels but was approximated by a continuous one.

This approximation would not affect the overall rate of second neutron emission, but could cause a slight redistribution of strength in ^{96}Tc. The inclusion of gamma-ray competition to the neutron decay could increase the cross-section σ_1' on the expense of σ_2, thus shifting the maxima of σ_1' toward higher beam energies. Also in the energy range under consideration the compound nuclear mechanism is only responsible for 80 - 90% of all the (α,n) reaction channel. The remaining part could be attributed to the pre-compound neutron emission, following an alpha capture (Miller, 1973). In the pre-compound nuclear reaction the emitted neutron has rather large kinetic energy, which could make the emission of a second neutron impossible. This mechanism again would strengthen the σ_1' channel over σ_2, with the consequence of shifting the excitation function maximum toward higher beam energies. The pre-compound nuclear mechanism is revealed by tailing on the high energy side of the excitation function and by the reduction in the rate of increase of the (α,2n) excitation function. There may well be other mechanisms contributing to the overall effect.

The theoretical curve of Fig. 2.3B is a mirror reflection of the Yrast states in ^{95}Tc. This is a simple consequence of the fact that the competition from the (α,2n) reaction gains strength exponentially, as soon as its spin channel is energetically accessible. The linearity of both the theoretical and experimental curves of Fig. 2.3B for $J_1>4$ reflect the linearity of the Yrast curve in ^{95}Tc; the fact that $E_{\sigma(J)_{max}}$ is almost independent of J for $J\leq4$ is consequence of the relatively high spin of the ground state ($J=9/2^+$) in ^{95}Tc.

In the same way, the spin of 7^+ for the ground state in ^{96}Tc tends to separate the excitation functions into those associated with $J<7$ and those associated with $J>7$. The lack of high intensity cascades connecting levels with spin from 7 to 0 means that the low spin states will reach their maximum excitations at a slightly lower beam energy than predicted. In a similar way the excitation functions for the states of spin 7, 8 and 9 will reach their maxima at slightly higher energies than predicted. This result has been commented on in the discussion of the normalization procedure for Fig. 2.3C and D and is obvious in Fig. 2.3B. There may of course be other factors contributing to the effect.

Since the total intensity of the reaction tends to be channelled through a few low-lying states, one would expect that the excitation functions for the transitions deexciting low-lying states are likely to be predominantly populated by transitions from states of higher spin. As a consequence their excitation functions lose some of their own characteristics and acquire higher excitation maxima character of states with higher spin. An inspection of Table 5.2 does not reveal clear cut evidence for this expectation, since low-lying and high-lying states of the same spin appear to have the same maximum excitation energy. The chief exception is the 575.0 keV level of spin 7^+ for which at least 68% of the feed is from states of spin 8 and 9. A similar but smaller effect is found for states of spin 8.

Both the maxima of the excitation functions and the ratio of intensities at two alpha beam energies may be used to estimate the spins of levels in ^{96}Tc. The theoretical model supports the empirical observation that both $E_{\sigma(J)_{\max}}$ and the ratio R(J) increase in a regular fashion with the spin of the initial level involved. This conclusion is valid, irregardless of the parameters and approximations used in the model. In the model discussed above there are no free and adjustable parameters. To apply these methods to spin assignment, all that one needs to do is to construct empirical curves based on levels whose spins are known. These curves can then be used as means of assigning spins to other levels.

As far as this author has been able to determine, the use of the maxima in the excitation function as a means of making spin assignments has not been used by other workers. While the intensity-ratio method was developed independently in this work, a search of the literature shows that a very similar version of the method was used by Malcolm Macphail (1973), who did his work in this laboratory. Macphail used the ratio of gamma-ray intensities obtained at two alpha beam energies following the ^{141}Pr(α,n) ^{144}Pm reaction. He used the quantity of beam charge collected in the Faraday cup to normalize his photon intensities and constructed an experimental curve for the ratio of photon intensities as a function of initial spin. It is evident that, for at least the ^{141}Pr (α,n) ^{144}Pm and ^{93}Nb (α,n) ^{96}Tc reactions, these methods work. Furthermore, this thesis shows that they have a sound theoretical base in the statistical model.

2.3 Coincidence Method

The well-established gamma-gamma and neutron-gamma coincidence techniques are based on the fact that the sequence of neutrons and gamma-rays emitted from a compound nucleus as it loses its excitation energy proceeds so rapidly that the events may be regarded as having occurred simultaneously as far as coincidence circuits with time resolution in the nanosecond range are concerned. Because of this fact, such a circuit can select from the very large number of unrelated gamma-rays (or neutrons) emitted by a target those gamma-rays which originated in a common compound nucleus. The coincidence spectra thus provide direct evidence of the generic relationships that exist among the gamma-rays emitted from the source and enable one to establish level structures with great confidence. Without this technique, it would be almost hopeless to establish the level scheme for a nucleus as complex as ^{96}Tc.

If a nuclear state has a mean life which is long compared to the time resolution of the coincidence circuit, there will be very few coincidences between gamma-rays feeding and deexciting this state. Thus the absence of coincidences involving a transition can often be used as a diagnostic test for an isomeric state and the coincidence technique modified to determine the half-life of the state.

2.4 Estimates of Attenuation Coefficients

This section deals with the determination of attenuation coefficients, which describe the spatial alignment of nuclei produced in a nuclear reaction. The knowledge of these parameters is important in the interpretation of angular distributions and to a lesser extent of linear polarization measurements.

Because in-beam experiments involve interactions between incoming particles and randomly arranged target nuclei, one is led to a statistically averaged description of the alignment of the ensemble of nuclei under study. The proper quantum mechanical treatment of the ensemble of states formed by incoherent superpositions of pure quantum states of individual nuclei necessitates the density matrix formalism. The density matrix completely describes the state of the ensemble. The matrix is Hermitian in character, and therefore it can be diagonalized by a unitary transformation. The diagonal representation can be then chosen in such way, that the diagonal elements of the density matrix represent the probability of occupation of a pure state by a member of the ensemble.

In the heavy-ion induced reactions, the target nuclei receive from the incident particles a large amount of angular momentum, whose vector is always directed within the plane whose normal is the beam axes. If the target nuclei have intrinsic angular momentum randomly distributed in space, then the vectors of the total angular momenta of the compound nuclei will be spatially confined to a narrow band centered in the plane whose normal is the beam direction. The subsequent decay of the compound nucleus by a neutron plus gamma-ray cascade does not significantly alter this strong alignment.

The population parameters $\rho_J(m)$ describe the population of state $|J,m\rangle$ characterized by spin J and its projection m onto the z-axis. Following the heavy-ion reaction the population parameters for states of +m and -m are equal and can be approximated by the distribution:

$$\rho_J(m) = C \cdot \exp(-m^2 | 2\sigma^2) \qquad [2 - 14]$$

In this expression σ is the width of the Gaussian and the constant C can be obtained from the normalization condition:

$$\sum_m \rho_J(m) = 1 \qquad [2 - 15]$$

If the oriented compound nuclear system is axially symmetric with respect to the beam direction, then the attenuation coefficients $\alpha_\lambda(J)$ completely represent the oriented ensemble. The relationship between the population parameters and the $\alpha_\lambda(J)$ coefficients is given by:

$$\alpha_\lambda(J) = (2J+1)^{\frac{1}{2}} \sum_{m=-J}^{J} (-1)^{J+m} \langle J,-m,J,m|\lambda,0\rangle \rho_J(m) \qquad [2-16]$$

where the term in brackets is a Clebsch-Gordan vector-addition coefficient.

The attenuation coefficients depend only on conservation of angular momentum and statistical assumptions, and therefore it is possible to estimate them using compound nuclear reaction formalism. Instead of using the quite elaborate calculation technique of section 2.2 the simpler model described below was found to be satisfactory.

The attenuation coefficients have been estimated using a modification of the method used by Shibata et al. (1975) for states excited by the ^{93}Nb $(\alpha,2n)$ ^{95}Tc reaction. The work of these authors was in turn an extension of the work by Ejiri et al. (1972) on the alignment of levels in the ground state band of nuclei produced through $(\alpha,2n)$ reactions on target of zero spin. The method which is discussed below is illustrated in Fig. 2.4. The actual calculations employed a computer program entitled NELLY.

The normalized population parameters for the compound nucleus, $P(J_c)$, and the associated attenuation coefficients $B_\lambda(J_c)$ were calculated for levels of spin J_c in ^{97}Tc. This nucleus is formed by the transfer of ℓ units of orbital angular momentum to a randomly oriented

Figure 2.4

Attenuation coefficients in the compound nucleus ^{97}Tc, the relative population of states in ^{97}Tc, a schematic of the deexcitation process and various estimates of attenuation coefficients for states of ^{96}Tc as a function of spin. This figure serves to guide the reader through the discussion in the text.

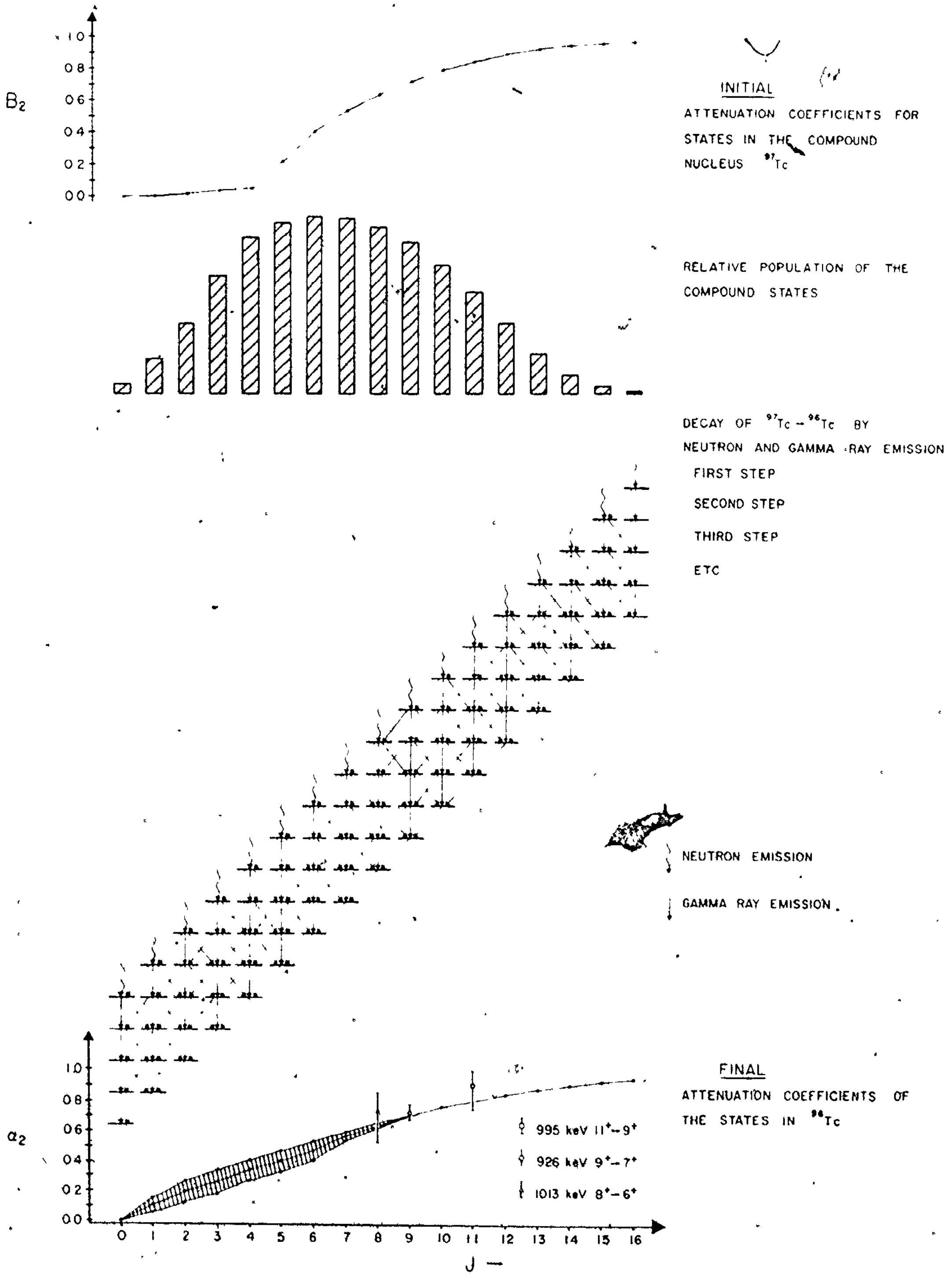
B2
1.0
0.8
0.6
0.4
0.2
0.0
INITIAL
ATTENUATION COEFFICIENTS FOR STATES IN THE COMPOUND NUCLEUS 97Tc
RELATIVE POPULATION OF THE COMPOUND STATES
DECAY OF 97Tc → 96Tc BY NEUTRON AND GAMMA RAY EMISSION
FIRST STEP
SECOND STEP
THIRD STEP
ETC
NEUTRON EMISSION
GAMMA RAY EMISSION
FINAL
ATTENUATION COEFFICIENTS OF THE STATES IN 96Tc
α2
995 keV 11+→9+
926 keV 9+→7+
1013 keV 8+→6+
0
1
2
3
4
5
6
7
8
9
10
11
12
13
14
15
16
J →

^{93}Nb target nucleus of spin J_t by means of the incoming α particle. $P(J_c)$ is given by:

$$P(J_c) = \left[\sum_{\ell=|J_c-J_t|}^{J_c+J_t} p_\ell(J_c) \right] / \left[\sum_{J'=0}^{\ell_{max}+J_t} \sum_{\ell=|J'-J_t|}^{J'+J_t} p_\ell(J') \right] \qquad [2 - 17]$$

where the $p_\ell(J)$ functions used in the above equation are defined as:

$$p_\ell(J) = [\ (2J + 1)\ /\ (2J_t + 1)\ ] \cdot T_{\alpha\ell}(E_\alpha) \qquad [2 - 18]$$

$T_{\alpha\ell}$ is the transmission coefficient for α capture with a transfer of ℓ units of angular momentum, E_α is the particle energy and ℓ_{max} is the maximum ℓ transfer that can occur at the beam energy used. The transmission coefficients required in the calculation have been taken from the tables of Huizenga and Igo (1961).

The alignment parameters $B_\lambda(J_c)$ which define the average orientation of the spin vector J_c of the compound nucleus with respect to the beam axis are given by:

$$B_\lambda(J_c) = [\ \sum_\ell p_\ell(J_c) \cdot U_\lambda(\ell \xrightarrow{J_t} J_c)\ ]\ /\ [\ \sum_\ell p_\ell(J_c)\ ] \qquad [2 - 19]$$

for λ=2, 4, 6, etc.

In this expression:

$$U_\lambda(J_1 \xrightarrow{J} J_2) = (2J_1+1)^{1/2}(2J_2+1)^{1/2}\ W(J_1,\lambda,J,J_2;J_1,J_2) \qquad [2 - 20]$$

The values of $B_2(J_c)$ and $P(J_c)$ derived from the calculation are shown as a function of J_c in the curve and histogram at the top of Fig. 2.4. Although the values of J_c are half-integral, the $P(J_c)$ and $B_2(J_c)$ values are plotted vs J_c-1/2 for convenience of presentation. These coefficients form the starting point for calculating the attenuation which occurs as the compound nucleus deexcites by the emission of one neutron and many gamma-rays to the observed levels of ^{96}Tc.

The attenuation coefficients before and after the emission of a single particle or gamma-ray are related by the expression:

$$\alpha_\lambda^f(J_f) = \alpha_\lambda^i(J_i) \cdot U_\lambda(J_i \xrightarrow{j} J_f) \qquad [2-21]$$

where i and f are the initial and final states of spin J_i and J_f and j is the angular momentum carried away in the transition.

For the case of neutron emission, however, it is more convenient to use a slightly different expression which takes into account the preponderance of $\Delta j=\frac{1}{2}$ neutrons in the decay process. In neutron emission, a given final state is fed by the initial states of spin $J_f \pm \frac{1}{2}$ for s-wave and by the initial states of spin $J_f \pm \frac{1}{2}$, $J_f \pm 3/2$ for p-wave neutrons. By ignoring spin changes of $\frac{1}{2}$ and treating neutron emission as if no change of spin results, the following approximate expression which takes account of both s and p wave neutrons may be used;

$$\alpha_\lambda^{fn}(J_c) = \alpha_\lambda^i(J_i)\Big|_{J_i=J_f}[(1-R)U_\lambda^o + R\,U_\lambda^1] \qquad [2-22]$$

where R is the fractional $\Delta j=3/2$ intensity ($\sim$0.4 for ^{96}Tc) and

$$U_\lambda^o = U_\lambda(J_f \xrightarrow{j=0} J_f) \qquad [2-23]$$

$$U_\lambda^1 = \frac{1}{3}\cdot[U_\lambda(J_f+1 \xrightarrow{j=1} J_f) + U_\lambda(J_f \xrightarrow{j=1} J_f) + U_\lambda(J_f-1 \xrightarrow{j=1} J_f)]$$

In general, a given state may be fed by both neutron and gamma-ray processes, each with its own fractional intensity. Since any one nucleus can decay by only one path, the average attenuation coefficient for any given level can be formed by computing the weighted average of the attenuation associated with all possible feeding processes. Thus

$$\alpha_\lambda^{f}(J_f) = [I_n \alpha_\lambda^{fn}(J_f) + \sum_k I_k \, \alpha_\lambda^{i}(J_k) \cdot U_\lambda(J_k \xrightarrow{j_k} J_f)]/I_f \qquad [2-24]$$

where $I_f = I_n + \sum_k I_k$ is the total intensity of all branches feeding level f. The neutron intensity in equation [2-24] will be the value of $P(J_c)$ appropriate to the spin of the state being fed; the photon intensities, from any given spin value will be assumed to be equally divided between all possible decay modes ($\Delta J = +1$, 0, and -1 for states of moderate spin, $\Delta J = -1$, 0 for states immediately above the Yrast band and $\Delta J = -1$ for Yrast states).

With these assumptions, the calculation proceeds in a straightforward manner, commencing with the decay of the state of the compound nucleus J_{max} with the maximum spin. In the first step, this state may decay to any one of a group of states with the same spin, all experiencing the same attenuation. In the second stage, the calculation considers both the group of states of spin $J_{max}-1$ which are fed by the neutron and photons from states of J_{max} and the group of second generation states of spin J_{max}. The attenuation coefficients are calculated for each group. In the third stage, groups of states of $J_{max}-2$, $J_{max}-1$ and J_{max} are considered and so on. After an N-fold cascade, the spin J_{max} states reach the Yrast level and must transfer all their intensity to $J_{max}-1$ levels. The process thus builds up more and more side feeding as it continues to states of lower and lower excitation, maintaining the high degree of alignment characteristic of the compound nucleus in the observed states. The results are essentially independent of the value N chosen (the value of α_2 obtained for calculations with N=4 and N=7 at E_α=18 MeV differed by less than 3%).

The values of α_2 resulting from these calculations for a beam of energy of 18 MeV are represented in Fig. 2.4. The upper curve results from the model if one assumes that the side feeding is continued down to zero spin. Since this is clearly not so, the attenuation was also calculated on the assumption that 66% of the intensity following the Yrast path to states of J=7, 8, 9 is trapped by the 7^+ ground state, and that similar trapping occurs for the low-lying 3^+ and 4^+ states. This trapping reduces the degree of side feeding and the consequent alignment of all states with J less than 9. The lower curve in the α_2 vs. J plot of Fig. 2.4 present the result of this calculation. The true state of affairs lies somewhere between these limits and the mean value curve which bisects the cross-hatched region is as good an estimate as any. This estimate was used in the analysis of the 18 MeV data.

Whereas the α_ν values predicted in the manner discussed above worked well for the 18 MeV experimental data, the attenuation coefficients for the low-spin states excited by a 14 MeV beam were found to be much smaller than the lowest limits predicted by a model which postulated that much of the intensity was provided by transitions cascading from states of higher spin. After unsuccessful attempts to adjust the model to enable it to predict the extremely low anisotropies observed for transitions from low-spin states, an alternative and simpler mechanism was considered. This mechanism assumes that the low-spin states are fed by a simple chain of transitions involving a single neutron following by no more than one gamma-ray cascading from states in ^{97}Tc. With this mechanism, the attenuation coefficients for the low-spin states in ^{96}Tc should be about the same as those for states of equivalent spin in the compound nucleus. Thus one can regard the B_2 values of Fig. 2.4 as representing the lower limits for the attenuation coefficients whose upper limits are shown in the α_2 vs J plot.

The statistical model outlined above has already been published (Mach et al. 1980). It should be noted that Fig. 2.4 of this thesis does not agree with Fig. 7 of that paper. The published B_2 and α_2 values are incorrect because the transmission coefficients from Huizenga and Igo's table were incorrectly fed into the computer program NELLY. The correct B_2 and α_2 values resulting from the calculation are to be found in Fig. 2.4.

Since there is a one to one correspondence between σ and α_2 and α_4 values, it was possible to deduce the σ values corresponding to the theoretical estimates of attenuation coefficients. The basic relationship between those parameters is defined by equations [2-14] and [2-16]. In general, the σ parameters are more often used in the literature than attenuation coefficients.

The values of σ used in the data analysis are presented in Table 5.4. The σ values of Table 5.4 were based on the incorrect B_2 and α_2 values of Fig. 7. Since the values of σ derived from the correct values of B_2 and α_2 differ by only 4 to 6% from these values, and since the uncertainty in all σ values is relatively large, it was not considered worthwhile to repeat all the calculations.

The statistical method used in estimating the attenuation coefficients is closely related to that used for computing excitation functions. Thus it is not surprising that the attenuation of the angular distribution of gamma-ray can serve as a rough indicator of the spin of the initial state involved.

2.5 Angular Distributions

Angular distributions, gamma-ray linear polarizations and internal conversion coefficients are phenomena from which important nuclear structure parameters may be extracted by comparing the experimental data to theoretical predictions. It is thus important that these predictions are independent of nuclear theory.

An angular distribution pattern depends strongly on the population parameters $p_J(m)$ of the initial state, the spins of the states involved in the transition and the degree to which multipole mixing (defined by δ) occurs in the transition. The model describing the distribution pattern can be parametrized into statistical, electromagnetic interaction and nuclear structure terms.

The population parameters (the statistical term) can be estimated theoretically (see section 2.4) or approximated by a Gaussian distribution of width σ where σ can be treated as a free and adjustable parameter. The electromagnetic interaction term can be calculated exactly, while the nuclear structure term, δ, is treated in the model as a free parameter.

The observed probability of gamma-ray emission depends on the angle θ between the direction of the emitted radiation and the direction of the beam, and is described as: [2 - 25]

$$W(\theta) = A_0[1 + \sum_\nu A_\nu P_\nu(\cos\theta)] \quad \nu = 2, 4, \ldots$$

where P_ν is a Legendre polynomial and A_0 is the gamma-ray intensity. All the information included in the experimental angular distribution pattern is contained in the A_ν coefficients. Those experimental coefficients can be now tested against those predicted by a theoretical model for all possible $J_i \rightarrow J_f$ spin combinations, all possible choices of the δ mixing ratio, and for a range of population parameters. The theoretical A_ν coefficients are given by (see Hamilton (1975) for more details):

$$\begin{aligned} A_\nu &= \alpha_\nu \cdot (F_\nu^1 + 2\delta F_\nu^2 + \delta^2 F_\nu^3)/(1 + \delta^2) \\ &= \alpha_\nu \cdot f_\nu(J_i, J_f, \delta) \end{aligned} \qquad [2 - 26]$$

where:

$$\begin{aligned} F_\nu^1 &= F_\nu(J_i, L, L, J_f) \\ F_\nu^2 &= F_\nu(J_i, L, L+1, J_f) \\ F_\nu^3 &= F_\nu(J_i, L+1, L+1, J_f) \end{aligned} \qquad [2 - 27]$$

In general ν is restricted to the values 2 and 4. F_ν is readily calculable (Yamazaki, 1967), depending as it does on Clebsch-Gordan coefficients, the spins of the levels involved and the multipole order of the transition between them. The α_ν cofficients are the attenuation coefficients already discussed in section 2.4.

Since the strong alignment of the compound nuclei produced in the alpha induced reactions persists through the cascades of the residual nucleus, the emitted gamma-rays are characterized by strongly anisotropic distributions (except for the case of low-spin states) and as such can lead to definite information as to the nature of the spin change involved in the transition.

2.6 Linear Polarization of Gamma-Rays

The gamma-ray radiation from aligned nuclei can exhibit linear polarization. The linear polarization angular distribution depends on the spins and parities of the involved nuclear levels and the degree of multipole mixing in the transition. If the angle between the polarization vector and the plane of the reaction is ψ, then the angular distribution of a polarized radiation is given by:

$$W(\theta,\psi) = \sum_\nu (A_\nu P_\nu(\cos\theta) \pm \cos 2\psi \cdot A'_\nu P_\nu^{(2)}(\cos\theta)) \qquad [2-28]$$

where $P_\nu^{(2)}$ is the unnormalized associated Legendre function, the plus and minus signs refer to magnetic and electric multipole transitions respectively, while A'_ν is given by:

$$A'_\nu = \alpha_\nu \cdot (-K^1_\nu F^1_\nu + 2\delta K^2_\nu F^2_\nu + \delta^2 K^3_\nu F^3_\nu)/(1+\delta^2) \qquad [2-29]$$

$$= \alpha_\nu \cdot f'_\nu(J_i,J_f,\delta)$$

where

$$K^1_\nu = K_\nu(L,L)$$
$$K^2_\nu = K_\nu(L,L+1) \qquad [2-30]$$
$$K^3_\nu = K_\nu(L+1,L+1)$$

The coefficients A_ν, α_ν and the F_ν functions have already been discussed in section 2.5, while function K_ν is defined and tabulated by Fagg and Hanna (1959). One should note that if the state of polarization cannot be observed (i.e. integration over ψ takes place) the equation [2 - 28] is reduced to equation [2 - 25].

The function P(θ) is generally used to describe the state of gamma-ray polarization and is defined as:

$$P(\theta) = \frac{W(\theta,\psi=0^{o}) - W(\theta,\psi=90^{o})}{W(\theta,\psi=0^{o}) + W(\theta,\psi=90^{o})} \qquad [2 - 31]$$

After substituting equation [2 - 28] into [2 - 31] it becomes clear that for a transition from J_i to J_f, the sign of P(θ) is opposite for magnetic and electric radiation of the same polarity.

2.7 Internal Conversion Process

In the internal conversion process, the energy of a transition between two nuclear levels is transferred completely to a K, L or M atomic electron with the consequent ejection of that electron with energy equal to the transition energy less the binding energy of the shell. The ratio of the probability of ejection of an electron to the probability of gamma-ray transition is called the internal conversion coefficient. Because the purely nuclear factors in the electron and gamma-ray processes are the same, the ratio does not depend on nuclear structure factors but only on the multipole nature and the energy of the emitted gamma-ray. Thus the measurement of an internal conversion coefficients can distinguish between E1 and M1 radiation in the same way as a linear polarization measurement can do. Because the conversion coefficients for E1, M1 and E2 transitions differ quite markedly, even rather imprecise internal conversion measurements can distinguish between those types of transitions.

Multipole information is obtained from the measured internal conversion coefficients by comparing them to the theoretical values found in the very extensive tabulation of Hager and Seltzer (1968). The theoretical values are believed to be reliable to ∿ 3%.

CHAPTER 3

NUCLEAR MODELS

3.1 Introduction

Over the last thirty years, a vast amount of experimental data on nuclear structure has become available and also a large number of nuclear models have been proposed to interpret the experimental observations. A structure as complex as a nucleus must be described as a dynamical many-body system. In a quantum mechanical sense a complete description of a nuclear system is enclosed in the total wave function. However, neither the analytical description of many-body interactions, nor the full understanding of the experimentally observed two nucleon interaction is available at the moment, thus a Hamiltonian, which provides a proper description of nuclear system, cannot be established. It is doubtful if such a Hamiltonian could be solved exactly, even if it were possible to establish it. Consequently, efforts to improve our understanding of nuclear structure must depend on developing "nuclear models", in which the prominent characteristics of nuclei are incorporated. Furthermore, in the framework of those models the experimental results must be explained in simple terms.

Since no one model is capable of describing the total structure, a rather large number of simple models have been developed. Each of these is capable of reproducing the observed nuclear properties for one or more classes of nuclei in a relatively satisfatory manner. These models originally fall into two distinct categories, the shell model and the collective model, and attempts to synthesize them have led to a number of "unified models" of increasing sophistication.

The region around mass 100[1], which is of prime interest for this thésis, is one in which nearly all of those models seem to be partially applicable. However, none of these provide a good description of the observed nuclear properties, and we are still awaiting the development of one suitable for this mass range. Such a model would be an extension of the existing models and as such would provide an important step toward a further understanding of nuclear structure.

There is no space in this thesis for a detailed description of these models. Thus, the following chapter limits itself to a statement concerning features of those models which have some relevance to ^{96}Tc.

3.2 Simple Nuclear Models

The simple nuclear models include the shell model and the collective model and constitute a first approach to an interpretation of nuclear structure. The ideas were taken from the atomic physics, where the concepts of shell and collective motions were already well established.

The shell model describes the nucleons in their individual single nucleon degrees of freedom, while the collective models introduce collective coordinates to describe the overall state of the nucleus. Thus the shell model attempts to describe the microscopic structure of the nucleus, while the collective model focusses on its macroscopic features and ignores the behaviour of the individual particles. Whereas the collective model involves only a few degrees of freedom to achieve its goal, the shell model involves numerous degrees of freedom (depending on the approximations applied).

3.2.1 Shell Models

The shell model was derived about 30 years ago (Mayer and Jensen, 1955) to account for systematic changes that occurred in nuclear stability, ground state spin, ground state quadrupole moments, excitation energies of the first excited states and other nuclear properties as a function of mass number.

According to the model nucleons move independently in a central potential field, in which the orbital angular momentum, ℓ, of each nucleus is a constant of motion. Each nucleon is also characterized by its intrinsic angular momentum s. The model requires a strong $\ell.s$ coupling in order to reproduce the experimental data. The total angular momentum j of a nucleon ($\vec{j} = \vec{\ell} + \vec{s}$) is also a constant of motion in the central potential field. Protons and neutrons independently fill the energy shells, which are 2j+1 degenerate, starting with the shell of lowest potential energy.

The name "shell model" needs some clarification. Originally it referred to the model discussed above. After many modifications the name came to be used in a different sense by many workers. In this text it is assumed that the name "shell model" implies one, which describes microscopically the nuclear system through the individual degrees of freedom of the nucleons and includes nucleon-nucleon interactions.

When another nucleon is added to the system it experiences interactions both with the nucleons in the already filled (closed) shells and with nucleons outside these shells. The interaction with those in the closed shells create the central (or distorted) potential. On the other hand, the interaction with nucleons from still unfilled shells (so called valence nucleons) must be treated separately. The latter type of interaction is called the residual interaction.

As long as the residual interaction can be treated as a perturbation term to the shell model Hamiltonian, the formalism of the simple shell model can be retained. However, if the mutual interactions affects the shape of the core (polarization effect) then it must be treated in the framework of the Nilsson model, which will be discussed in section 3.3.1.

In the extreme single-particle model, which is an extension of the simple shell model, only valence particles are considered. This model is based on the experimentally verified phenomena, that two nucleons in the same shell substantially lower their potential energy by coupling their individual angular momenta j to zero. To break down this so-called "coupled pair" requires ∿ 1 MeV of energy. Furthermore, the paired nucleons in the already filled shells produce a spherical and mostly inactive inert core with total J=0.

Thus the characteristic of the nucleus is primarily determined by the odd neutron and/or odd proton left over after pairing has occurred.

In the odd-odd nuclear system the ground state configuration is determined by the coupling of an odd proton to an odd neutron. If the odd proton is characterized by the total angular momentum j_p, while the odd neutron has j_n, then the resulting multiplet of states may have any spin value in the range

$$|j_n - j_p| \le J \le j_n + j_p \qquad [3 - 1]$$

Since the residual interaction between these particles removes the degeneracy of the multiplet states, one of those levels becomes the ground state of the nucleus. The remaining members of the multiplet form the ground state configuration.

Useful empirical formulae for estimating the ground state spin of an odd-odd nucleus are given by the Nordheim rules (Nordheim, 1950):

the strong rule:

$$J = |j_n - j_p| \qquad \text{for } j_n = l_n \pm 1/2,\ j_p = l_p \mp 1/2$$

the weak rule: [3 - 2]

$$|j_n - j_p| \le J \le j_n + j_p \qquad \text{for } j_n = l_n \pm 1/2,\ j_p = l_p \pm 1/2$$

The strong rule makes a definite prediction, while the weak rule merely specifies a range of spins. One should note, that small configuration mixing or small perturbations can break the strong rule and reverse the order within the multiplet.

In summary the shell-model is credited with correct predictions (for most cases) of the ground state spins, rough estimates of magnetic and electric quadrupole moments and with limited success in predicting the spins of the low-lying levels.

3.2.2 Collective Motion of Nucleons

The properties of nuclear matter as revealed by a large number of nuclei, indicate that nucleons do not entirely move independently as in the shell model picture, but more coherently with well defined phases. Such motion implies a correlation of nucleons. The nuclei exhibiting such collective motion are characterized by rotational or vibrational type of spectra. The following two sections describe the vibrational and rotational models in their simplest form. While these models fail to account for the actual nuclear properties with any precision, the ideas embodied in them have been incorporated in the more refined unified models to be discussed in section 3.3.

3.2.3 Vibrational Model

Nuclear matter is characterized by a short range nuclear force, constant nuclear density inside the nucleus and a molecular-type dependence of nucleon binding energy on mass number. This characteristic suggests a similarity between a liquid drop and a nucleus.

The theory of Bohr and Mottelson (1953) describes the nucleus as an incompressible liquid drop oscillating about an equilibrium value. The surface of the nucleus can be conveniently expressed in terms of spherical harmonics Y_λ^μ as follows (Preston, 1963).

$$R = R_0[1 + \sum_{\lambda=0}^{\infty} \sum_{\mu=-\lambda}^{\lambda} \alpha_{\lambda\mu} Y_\lambda{}^\mu(\theta,\phi)] \qquad [3 - 3]$$

where R_0 is the radius of the undeformed sphere, θ and ϕ are polar angles with respect to arbitrary axes and $\alpha_{\lambda\mu}$ are time dependent variables describing the nuclear oscillation.

The mode of vibrational oscillation (called phonon) is characterized (in the irrotational motion) by the order of the vibrational mode λ, the angular momentum quantum number λ, the parity $(-1)^{\lambda}$ and the energy of vibration $\hbar\omega_{\lambda}$. The collective states of a vibrational nucleus have excitation energy E_{vib} given by:

$$E_{vib} = \sum_{\lambda} n_{\lambda} \hbar\omega_{\lambda} \qquad [3 - 4]$$

where the integer n_{λ} describes the number of phonons of order λ contributing to the excited state.

From general considerations one can deduce that for $\lambda = 0$ or 1 $\hbar\omega_{\lambda} = 0$, and also that the first excited state in the vibrational even-even nuclei should be 2^{+}, while the group of degenerate states at twice that energy, should include levels of $J^{\pi} = 3^{-}, 0^{+}, 2^{+}$ and 4^{+}.

3.2.4 Rotational Model

The rotational motion of the nucleons can be described as a pair of "tidal waves" moving around the nuclear core. Such a motion is caused by a partial break-down of the shell structure for a number of nucleons in the valence shells. Such a configuration of nucleons has a large quadrupole moment (which is a good indicator of the degree of departure from spherical shape) and can be treated by analogy with a rigid rotor.

The characteristic energy of the rotational system is:

$$E_{rot} = \frac{\hbar^{2}}{2I_{0}} J(J + 1) \qquad [3 - 5]$$

where I_0 is the moment of inertia of a rigid rotor and J is the spin of the nuclear level. For a nucleus, whose shape is symmetric with respect to reflection about its center, the spin J is restricted to even values. In such cases a typical rotational series of levels with spins 2^+, 4^+, 6^+ etc. and excitation energies proportional to J(J + 1) can be observed. In general, nuclei may exhibit rotational and vibrational modes of motion, as well as particle excitations.

3.3 Unified Models

Since nuclei exhibit both single particle and collective behaviour, models which unify the previously described approaches are needed. In general unified models use the Bohr-Mottelson (1953) approach, in which particle degrees of freedom are treated independently from those of the collective motion. Thus the total Hamiltonian is given by:

$$H = H_{collective} + H_{s.p.} + V_{int} \qquad [3 - 6]$$

where V_{int} is the coupling term between the single particle and the collective motions.

The two types of unified models are based on substantially different methods of solving the total Hamiltonian. In the geometric approach, which is a direct extension of the simple models already described, the particle and collective coordinates are defined in the real three-dimensional space, while the interaction terms are deduced from the intuitive judgement of the three-dimensional deformation of the nuclear sphere.

In the second approach the models are formulated and solved using second quantization formalism and group theories. In those models the collective pairs of nucleons are approximated by bosons, while the single particle character is retained for the odd valence nucleon.

The unified models can explain the nuclear structure for a large class of nuclei. However, they incorporate into the theory a large number of adjustable parameters.

3.3.1 The Geometric Approach

A basic difficulty with the early unified models was that of choosing a suitable interaction between the individual degrees of freedom of the particle and those of the core (which are related to the collective motion). The potential acting on the valence particles must depend on the details of the nuclear surface, which can be described by the collective variables of equation [3 - 3]. Since the surface oscillations are slow by comparison to the fast moving particles, the theory treats the outer nucleons as moving in the slowly changing potential field due to the core.

This coupling potential is small for spherical nuclei (weak coupling limit) but it may be very strong (strong coupling limit) in the mass region where nuclei exhibit large departure from the spherical shape (so-called "deformed region"). This potential introduces a perturbation, which breaks down the degeneracy of the vibrational states for odd-A nuclei and causes mixing of states with the same spin and parity.

The simple shell model of section 3.2 cannot represent single particle motion in the framework of the coupling scheme described above and is replaced by a more general shell model based on the deformed potential (Nilsson, 1955). This model needs some further explanation.

The Hamiltonian of the Nilsson model includes an axially symmetric oscillator and a spin-orbit coupling potential. This single-particle Hamiltonian depends on the deformation parameter δ and reduces to the simple shell model when $\delta = 0$. The parameter δ describes the extent of the deformation and to the first approximation represents the ratio of the difference between the major and minor axes of the ellipsoid to its mean diameter.

The total angular momentum j of the valence particle is no longer conserved. However, its projection on the symmetry axis, Ω, is still a good quantum number. Whereas the simple shell model state contains (2j+1) degenerate orbitals, the Nilsson model removes this degeneracy by creating j + 1/2 orbitals with two particles in each corresponding to the projection $+\Omega$ and $-\Omega$ with respect to the symmetry axis. The separation of the j + 1/2 orbitals depends on the deformation parameter δ. As in the simple shell model, the nucleons fill independently Nilsson model states, starting with the state of lowest potential energy. The model predicts correctly the sequence of single-particle orbits, although the predicted excitation energies do not correspond exactly to those observed experimentally.

Despite the fact that many variants of the unified model have been developed, the simplicity of the Nilsson model in which the nuclear wave functions can be expressed as a linear combination of simple and readily calculable wave functions, continues to make it very popular.

The combining of the single-particle motion to that of the core introduces new phenomena. Some of these are related to the Coriolis coupling potential, which describes the coupling of the single-particle and the rotational motion of the core. This potential may distort the rotational band pattern for high j orbitals, or for bands built on a $\Omega = 1/2$ projection. It also may cause mixing of close-lying bands which differ in the rotational quantum number K by one unit. For further details, the reader is referred to any number of standard text books, of which Preston (1962) is one.

As in the shell model, the odd neutron and odd proton in an odd-odd nucleus are coupled. Rules analogous to those provided by Nordheim for non-deformed nuclei, have been proposed by Gallagher and Moszkowski (1958).

3.3.2 Boson Approximation

Recently, much attention has been given to the Interacting Boson Approximation (IBA) model of Arima and Iachello (1975). In their model the collective excitations of the even-even nuclei are described by the mutual interaction of s and d bosons, possessing no intrinsic spin, characterized by angular momentum 0 and 2 respectively. The total number of bosons is N ($N = n_s + n_d$), which is roughly equal to half of the total number of nucleons or holes in the last unfilled shells. Consequently each series of collective excitations is terminated by some maximum angular momentum This property has no equivalent in the geometric models. Thus the IBA model is only capable of describing the low-excitation region, unless an extension is made to include also in the interaction the bosons equivalent to the last closed shell.

The microscopic foundation of this model is based on the pairing property of the nucleon-nucleon interaction. Nucleons in the same shell tend to form strongly bound pairs, gaining a large amount of potential energy by coupling their individual angular momenta to zero. The pairing interaction is still attractive but of smaller strength for the J = 2 particle coupling. Since the most active nucleons belong to the last unfilled shells, which, let's say, contain 2N nucleons (both neutrons and protons) one may attempt to describe the system in terms of N nucleon-pairs with angular momenta J = 0 or J = 2.

The Hamiltonian can then be formulated in terms of s and d bosons pairs and the multiple Fermion treatment of the shell model carried over to describe the intrinsic boson structure.

The IBA model is credited with providing a unified description of the vibrational, rotational and transitional nuclei using only six linearly independent parameters. Besides predicting the excitation energies of the ground state bands it also estimates the excitation energies of the so-called "side bands" in a natural manner thus avoiding the ad-hoc treatment of the "side-bands" inherent in the geometric model. An extensive review of the features of the IBA model has been given by Scholten (1980).

The IBA model is still not fully developed. Efforts are still being made to understand the origin of the empirical parameters, their relation to the boson structure, and their microscopic description in terms of a many-Fermion model.

The Interacting Boson Approximation describes the positive parity states in the even-even nuclei satisfactorily. This model has been extended in the Interacting Boson-Fermion Approximation (IBFA) of Arima and Iachello (1976) in order to describe the behaviour of odd-A nuclei. In this extension, an additional Fermion is coupled to the bosons of the even-even nuclear core. The required coupling potential introduces a large number of parameters depending on the number of shells the odd particle can occupy.

It was found that only two terms dominate the interaction (Arima and Iachello, 1976): The Fermion-boson quadrupole interaction (related to the particle-core coupling of the geometrical models) and the exchange force, which originates in the identity between the odd-particle and the particles of the coupled pairs approximated by bosons.

In the strong-coupling limit the IBFA can reproduce the results of the Nilsson model, and also describe naturally the location of the side-bands (a direct consequence of the IBA connection). In the weak-coupling limit the model is capable of describing particle-vibration oscillations.

The IBFA model has already had some impressive successes in dealing with odd-A nuclei over an extensive mass range (Scholten (1980), Casten and Smith (1979), Kaup et al (1978) and others). However, the nature of the Fermion-boson interaction is not well understood, nor do the approximations applied in the calculations find a full explanation.

It is pertinent to ask if the IBFA model can be extended to odd-odd nuclei. In commenting, one should note that the theory already requires lengthy calculations, and that the complexity of the model and the amount of calculation would be greatly increased were it to be extended to these much more complex nuclei. Thus the difficulties are very formidable, and it is unlikely that it will be attempted in the immediate future.

3.4 Gamma-Ray Transitions

Nuclear levels are characterized by excitation energy, spin and parity and these properties define the gross features of the structure of the nucleus under question. Any successful nuclear model must be able to predict these properties. A more sensitive test of the model is provided by its ability to predict correctly the probabilities of transitions between nuclear states. This section discusses the theoretical framework for such tests.

Transitions between nuclear levels can proceed by gamma-ray or internal conversion processes. Both of those are electromagnetic in nature and are described by identical matrix elements. Although only gamma-ray transitions will be considered, the results are applicable to the internal conversion as well.

A gamma-ray transition of multipolarity λ and energy $\hbar\omega$, between initial and final states of spin and parity J_i, π_i and J_f, π_f respectively must satisfy the following general conditions:

$$|J_i - J_f| \leq \lambda \leq J_i + J_f \qquad [3 - 7]$$

and

$$\pi_i \pi_f = (-1)^{\lambda+\eta} \qquad [3-8]$$

where $\eta = 0$ for electric and $\eta = 1$ for magnetic radiation. The probability of a gamma-ray transition between the states is given by:

$$T(R,\lambda,J_i \rightarrow J_f) = \frac{8\pi(\lambda+1)}{\lambda[(2\lambda+1)!!]^2} \frac{1}{\hbar} \left(\frac{\omega}{c}\right)^{2\lambda+1} \cdot B(R,\lambda,J_i \rightarrow J_f) \qquad [3-9]$$

where R symbolizes its magnetic (M) or electric (E) character and where $B(R,\lambda,J_i \rightarrow J_f)$ is the reduced transition probability. The reduced transition probability depends on the wave functions of the involved states and the transition operator $O^R_{\lambda\mu}$ of order λ in the following way:

$$B(R,\lambda,J_i \rightarrow J_f) = \frac{1}{2J_i+1} \sum_{m_i,m_f,\mu} |\langle J_f m_f | O^R_{\lambda\mu} | J_i m_i \rangle|^2 \qquad [3-10]$$

where the summation is over all μ components of the transition operator and the magnetic substates of the initial and final states. The reduced transition probability $B(R,\lambda,J_i \rightarrow J_f)$, which can be determined experimentally, is independent of gamma-ray energy and calculated in terms of nuclear wave functions. Therefore it can be used as a test of the wave functions generated by the theoretical models.

Crude theoretical predictions of electromagnetic transition rates are provided by the Weisskopf (1951) formulae which are based on a very primitive single particle model. These formulae state that:

$$\left.\begin{array}{l} T(E,\lambda)/T(M,\lambda) \sim 10^2 \\ T(R,\lambda)/T(R,\lambda+1) \sim 10^6 \end{array}\right\} \qquad [3-11]$$

These estimates order electric and magnetic transitions of increasing multipole order in a scale of decreasing probability in the manner shown: E1 , M1, E2, M2, E3, M3, E4. The dotted and solid lines indicated transitions which connect states of the opposite and same parity respectively. Since no nuclear states have mixed parity, this means that the transitions between states when equation [3 - 7] would allow E1, M2 and E3 components, the E1 component will be completely dominant. The only exception to the rule that the transition of lowest permitted multipole order will dominate is for M1 + E2 admixtures. In this case, collective motions can increase the E2 matrix element so that the E2 component may be many times larger than the M1 component. The presence of large E2 component in M1 + E2 mixtures is a strong indication that collective motions are responsible for the nuclear structure.

CHAPTER 4

EXPERIMENTAL DETAILS

4.1 Introduction

This chapter describes the apparatus and the methods employed in the experiments, with emphasis on the techniques applied in data analysis. The limitations in these techniques affect the quality of the results, and therefore will also be included in the discussion.

4.2 Beam Production System

Alpha beams are provided by the McMaster Tandem Van de Graaff Accelerator. Negative helium ions produced in the duoplasmotron source are extracted and focused before being accelerated by the positive high voltage at the terminal. Upon reaching the terminal, the ions pass through a thin foil which strips the electrons from them. The resultant positive particles are repelled from the terminal, undergoing a second stage of acceleration. These are then analysed by a system consisting of object slits, a large analysing magnet and a second pair of slits which serves to stabilize the energy of the beam. This device ensures that monoenergetic alpha particles enter the switching magnet which directs the beam into one of the experimental areas. Two such areas were used: a 33° line guiding the beam to the "orange" type beta-ray spectrometer, and a 0° line leading to an arrangement suitable for angular distribution experiments.

4.3 Experimental Set-up

Monoisotopic ^{93}Nb was obtained from Oak Ridge National Laboratories in Tennessee, and was used to prepare thin self-supporting targets by cold rolling small globules of the metal to the desired thickness. Targets produced in this way varied from 0.9 mg/cm^2 for electron measurements to 1.5 - 3.5 mg/cm^2 for gamma-ray measurements.

The alpha beam energy ranged from 13 to 27 MeV for the excitation function measurements, while the rest of the experiments were performed at 14 or 18 MeV.

The electron conversion coefficient measurements and gamma-ray polarization measurements, were carried out on the 33° line. The rest of the measurements were performed on the 0° line. In the neutron-gamma and the first gamma-gamma experiments, a metallic chamber was used. In the remaining measurements performed on the 0° line, the mettalic chamber was replaced by a lucite one suitable for the detection of low energy gamma rays. Since many of the transitions of interest in ^{96}Tc are in the 40 to 100 keV region, care was taken to minimize the interference created by X-rays coming from the beam stopping and shielding materials. A series of tests revealed that a combination of lead as shielding and tantalum at the slits and in the beam stopper provided the cleanest spectra.

4.4 Analysis of Gamma-Ray Spectra

4.4.1 Detection of Gamma-Ray Radiation

A gamma-ray interacts with matter through three main processes; the photoelectric effect in which the incident radiation is absorbed by an electron bound in an atomic system with the consequent ejection of the electron, the Compton effect in which the incident radiation experiences an inelastic collision with a free electron and loses part of its energy, or pair production in which high energy radiation converts itself into a position-electron pair in the electric field of the nucleus. In large volume detectors the likelihood of multiple interactions is high, thus causing the probability of full energy absorption to be enhanced over the value expected from a single interaction.

In the process of detection, a high voltage is applied between two sides of a pure germanium (intrinsic Ge detector) or a lithium drifted germanium Ge(Li) crystal . The incoming radiation deposits in the crystal part or all of its energy. This energy is related to the total number of ion pairs produced. The electric field created by the high voltage attracts these ions to metallic plates which collect the total charge and develop an electric pulse whose height is proportional to the energy deposited in the crystal. This pulse is amplified by a Preamplifier and a Linear Amplifier, reshaped, passed through a Linear Gate and Stretcher and finally converted from a continuous pulse to a number by an analog to digital converter (ADC) before it is stored in the memory of a computer. The resulting spectrum is a histogram, which displays the number of events stored in each of the digital channels against the channel number. The channel number is proportional to the energy of the gamma ray.

A beam of monoenergetic gamma-rays produces a complex spectrum, which in most cases consists of an intense full energy peak (all the energy of the radiation being absorbed by the detector) and an extensive low energy Compton tail (marked by a broad Compton Edge) stretching down to zero energy. If the radiation is not monoenergetic, a superposition of such structures takes place. The final spectrum appears as many peaks placed on top of a smoothly varying background. These peaks closely approximate a Gaussian shape, with some skewing on the low energy side.

The exact peak shape depends on many factors including detector characteristics, the count rate and the set up of the electronics. The peak shape changes smoothly with energy but cannot be expressed by any simple analytical function.

There are two main parameters characterizing a detector: efficiency and resolution. The absolute peak efficiency indicates the fraction of monoenergetic gamma-rays passing through the volume of a crystal which are stored in the full energy peak. The resolution is defined by the Full-Width-at-Half-Maximum(FWHM) parameter, and indicates how broad the peak is. Both of these parameters depend strongly on gamma-ray energy.

4.4.2 Fitting of the Gamma-Ray Spectrum

An ideal analysis would require a decomposition of a spectrum into a sequence of individual response functions for monoenergetic gamma-rays using Fourier Transforms or similar techniques. Due to the complexity of this approach, it is customary to follow a simpler procedure. The full energy peak position and intensity can be successfully correlated with gamma-ray energy and intensity. Thus one needs only to extract peak parameters to obtain full information on gamma-rays in a spectrum.

In data analysis a portion of a spectrum, called a "window", which includes a given peak plus some slowly varying background on both sides of it, is considered.

In the Shape Independent Analysis used in a computer program SOFT, this locally linear background is estimated by a χ^2- fitting of a linear function to the background points, and then the background contribution is subtracted from all the channels of the window, leaving only the peak behind. The peak position and intensity are then defined by the equations:

$$\text{Peak Position} = \frac{\Sigma_i\, y_i x_i}{\Sigma_i\, y_i} \quad ; \qquad \text{Peak Intensity} = \Sigma_i\, y_i \; , \qquad [4 - 1]$$

where x_i and y_i are the i-th channel and its associated residual intensity. The summation is over all window channels which make a significant contribution to the peak.

This simple procedure fails in cases of unresolved or partially resolved peaks. For such cases a more complex Peak Fitting Technique is required. The technique is embodied in the basic program JAGSPOT which was developed at the Chalk River Laboratories (Graham et al., 1972) and modified for use with the McMaster computer by Brian Cook (Cook et al., 1972). A simpler and more flexible program HELENA was developed from JAGSPOT by the present author and used in spectra analysis. The following discussion describes the main principles and limitations of the Peak Fitting method used.

The number of events stored in channel x is adequately represented by the empirical function:

$$I(x) = [a + bx] + \sum_{j=1}^{N} \gamma_j \int_{-\infty}^{A_j} e^{\varepsilon(z - A_j)}\, e^{-\delta(x - z)^2}\, dz \qquad [4 - 2]$$

The two terms in this expression represent the contribution from a linear background and from N skewed Gaussian peaks respectively. Two parameters γ_j and A_j are related to the intensity and position of j-th peak, while the parameters δ and ε define the width and the degree of low energy tailing for each of the peaks in a window.

The χ^2- fitting of a window with all parameters free is meaningful only for strong single peaks. For weak or unresolved peaks, constraints on the parameters are required. In the spectra reported in this work, $1/\delta$ and $1/\varepsilon$ are slowly varying linear functions of energy (channel number). These functions were established through the free fitting of strong single peaks well spanned over the spectrum and were then used to assign δ and ε for weak or complex peaks.

Over the range of one "window" (up to 110 channels), it was feasible to treat both δ and ε as fixed, using values determined for the mid point of the window. Since each of these parameters varied by about 4% across the largest windows used, and the area of a peak was given by

$$\text{Area} = \frac{\gamma}{\varepsilon} \left(\frac{\pi}{\delta} \right)^{1/2} \qquad [4 - 3]$$

The effect of this approximation is to introduce errors in peak area of up to 3%, an error normally small compared to other fitting errors.

The problem of fitting of composite peaks is also compounded by the nonlinearity of the background. This problem is most severe for weak peaks located on a Compton Edge. In such cases, neither the peak positions nor the intensities are as secure as the calculated statistical errors would predict; indeed, the true intensities may differ by ~30% from the measured values.

The fact that a continuous function is being fitted to a discrete set of points also creates problems, as the ensuing discussion will show. Although the ability to resolve two close-lying peaks in a spectrum depends directly on the detector's resolution, other factors do play an important role. These factors include the relative intensities of the peaks, the peak to background ratios, the counting statistics, the broadening which occurs at high counting rates and how closely the analytic function used to describe a single peak resembles the experimental distribution. Adjustments in the electronics can alter both the width of the peak and the degree of low-energy tailing present. It was found more profitable to keep the tailing at a minimum and accept the slightly poorer resolution which resulted from this adjustment.

Since in most experiments it was necessary to cover a 1500 keV spectral range with 4096 channels, the dispersion was roughly 3 channels/keV. On the other hand, the FWHM value for typical detectors ranged from 1 keV at 100 keV to 2.4 keV at 1 MeV. Thus the number of channels available to represent a peak varied from ~5 to ~15 over the stated energy range. The number of experimental points in a peak in the low-energy region was marginally sufficient for a proper statistical analysis, and in many cases (especially for intense peaks) the χ^2_{norm} exceeded 2, with a consequent increase in the uncertainty of the energy and area determination.

The χ^2- peak fitting program does not preserve the area of a peak and tends to give undue weight to points far off the smooth curve. As a consequence, for peaks with relatively poor statistics, the areas derived from a program can be quite erroneous and, in general are less reliable than those obtained from SOFT for the cases where SOFT could be applied.

The 511 keV annihilation peak is present in all gamma-ray spectra, interfering with the important 506 and 516 keV lines. The absence of this peak from electron spectra indicates that no gamma-ray of significant strength overlapped with it. Since the fitting programs made no provision for the treatment of a broad 511 peak adjacent to much narrower gamma-ray peaks, it became necessary to subtract the former peak from the spectrum before the peak-fitting analysis was undertaken. A Gaussian fit was made to a series of points defining the annihilation peak and its contribution subtracted from the total spectrum, as indicated in Fig. 4.3.

The neutron peaks around 700 keV could not be dealt with in this way because their position is a function of the direction of the detector relative to the beam axis, and in the individual spectra the statistics were too poor to define their shapes clearly.

4.5 Gamma-Ray Energies and Intensities

This section deals with methods used to establish the gamma-ray energies and intensities required to determine a level structure. Results for the high spin states populated by the (α,n) reaction with 18 MeV alpha particles have been already published (Mach et al., 1980). The energy calibration method used in this paper proved inadequate for a study of the dense structure of low-lying low-spin states in ^{96}Tc and a more complex method was therefore developed. Both are described in section 4.5.1. The procedures used for intensity determinations were common to both sets of experiments.

4.5.1 The Determination of Gamma-Ray Energies

In the published work referred to above, the relationship between channel number and energy was established using radioactive sources alone and then this function was used to calibrate the in-beam spectrum recorded under precisely the same conditions with no radioactive sources present. This procedure resulted in systematic errors of the order of 0.15 keV.

For the 14 MeV results which are reported in this thesis, a three stage process was followed, as described below. A high resolution (11%) intrinsic germanium detector was placed 20 cm from the target at an angle of 56^0 to the beam axis and used to record in sequence a pure in-beam spectrum and an in-beam spectrum contaminated by gamma-rays from a number of standard sources such as ^{241}Am, ^{137}Cs, ^{59}Co and ^{60}Co (see Fig. 4.1 A and 4.2 A). Both spectra were recorded with a counting rate of ∿2000 cps, and both required 4096 channels to cover the range for gamma-ray energy from 30 to 1200 keV. The contaminated spectrum, which included peaks from the radioactive standards as well as peaks of well-established energies from the ^{96}Mo decay and Pb - X ray lines, was then analysed to determine the peak positions of the standards and to establish by χ^2- fitting the function relating energy to peak positions. This function was then used to establish the energies of some fifty of the strongest lines in ^{96}Tc; lines which served as secondary standards in the analysis of the remaining ^{96}Tc peaks in the pure in-beam

Figure 4.1

Construction details for the chambers and geometrical arrangements used in the gamma-ray experiments.

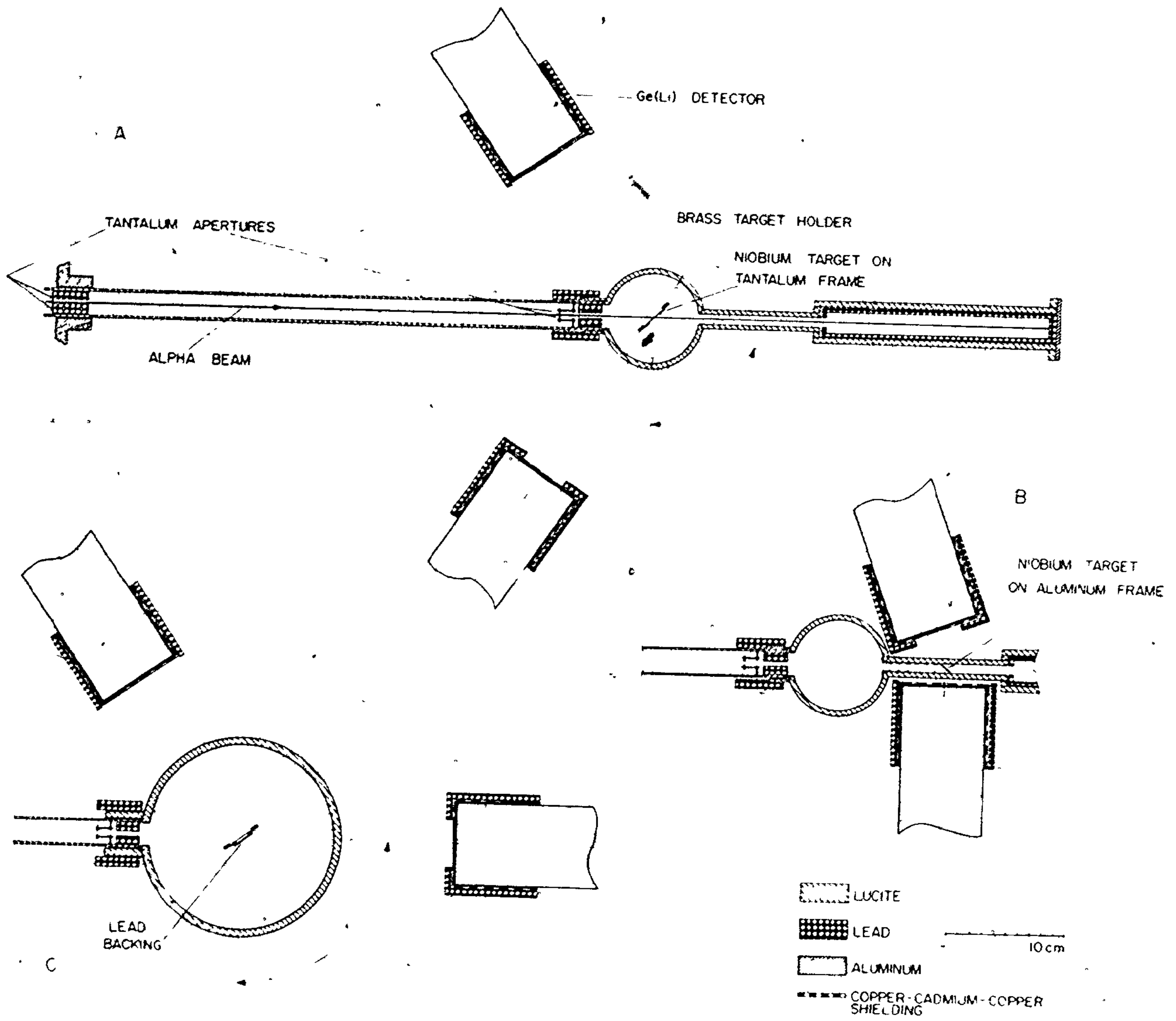
A
Ge(Li) DETECTOR
BRASS TARGET HOLDER
TANTALUM APERTURES
NIOBIUM TARGET ON TANTALUM FRAME
ALPHA BEAM
B
NIOBIUM TARGET ON ALUMINUM FRAME
C
LEAD BACKING
LUCITE
LEAD
ALUMINUM
COPPER-CADMIUM-COPPER SHIELDING
10 cm

Figure 4.2

Block diagram for the electronic circuits used (A) in the singles and (B) in the gamma-gamma coincidence experiments.

(A)

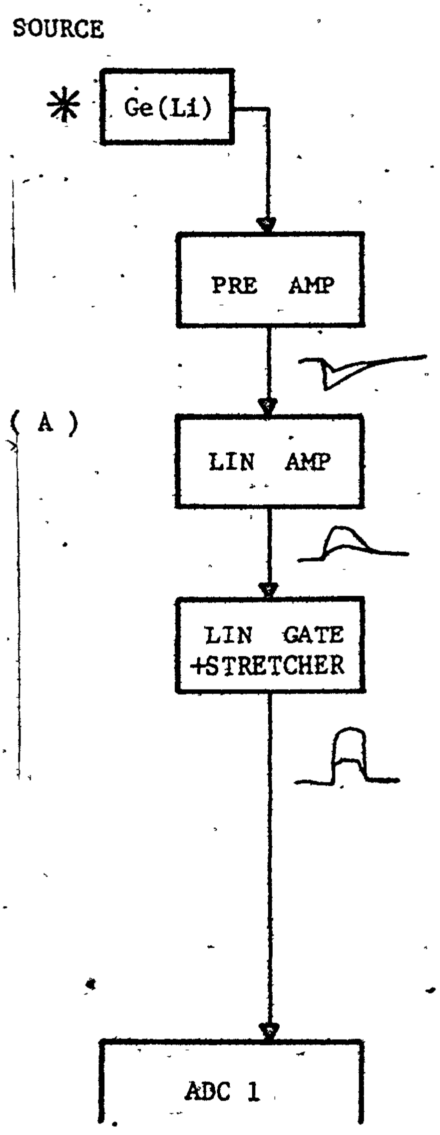
SOURCE
Ge(Li)
PRE AMP
LIN AMP
LIN GATE +STRETCHER
ADC 1

(B)

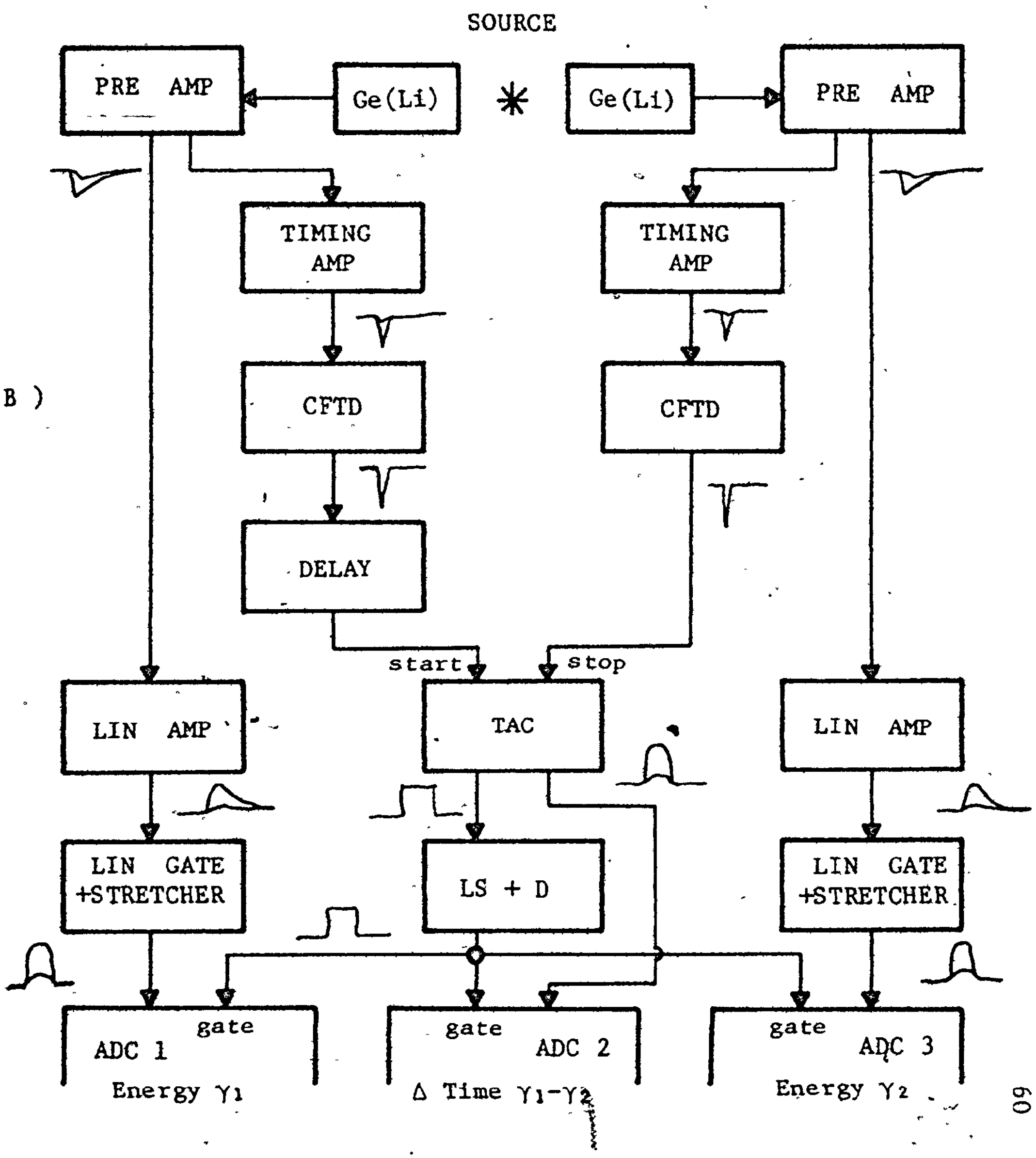
SOURCE
Ge(Li)
Ge(Li)
PRE AMP
PRE AMP
TIMING AMP
TIMING AMP
CFTD
CFTD
DELAY
start
stop
TAC
LIN AMP
LIN AMP
LIN GATE +STRETCHER
LS + D
LIN GATE +STRETCHER
gate
ADC 1
Energy γ1
gate
ADC 2
Δ Time γ1-γ2
gate
ADC 3
Energy γ2

spectrum (presented in Fig. 4.3).

These secondary standards were also used in the analysis of the gamma-gamma coincidence spectra. In the gated spectra of events in coincidence with a single gamma-ray, most of the peaks are single, therefore it was possible to determine both peak positions and intensities using SOFT.

The coincidence spectra are characterized by a very good peak to background ratio, therefore it was possible to obtain reliable energy determination for peaks with as few as 100 counts. To improve the quality of results a weighted average of energies was obtained for transitions which appeared in a number of gated spectra. The coincidence measurements were particularly helpful in gaining information concerning gamma-rays masked by strong peaks in "singles" spectra.

Since gamma-rays of energy greater than 1200 keV are in general only weakly excited at 14 MeV, data recorded at 16 MeV in the determination of excitation functions was drawn upon to improve the precision. The 1460.81 keV gamma-ray from the decay of ^{40}K provided a useful built-in standard for this region.

The low energy region up to 200 keV was also studied with an 18 MeV alpha beam using small high resolution Si(Li) and Ge(Li) detectors. The in-beam calibration peaks for these spectra were obtained for ^{59}Co and ^{241}Am sources. The results of all these energy measurements are summarized in Table 5.1.

4.5.2 Intensity Measurements

The weakest transitions which could be recorded in these experiments had an intensity of 0.5% of the strongest gamma-rays present in

Figure 4.3

The gamma-ray spectrum of ^{96}Tc obtained with a high resolution 11% intrinsic Ge detector placed at 56° to a 14 MeV alpha beam. The dotted line shows the position of the 511 keV annihilation peak before it was subtracted from the spectrum. Transitions identified as belonging to ^{96}Tc are labelled.

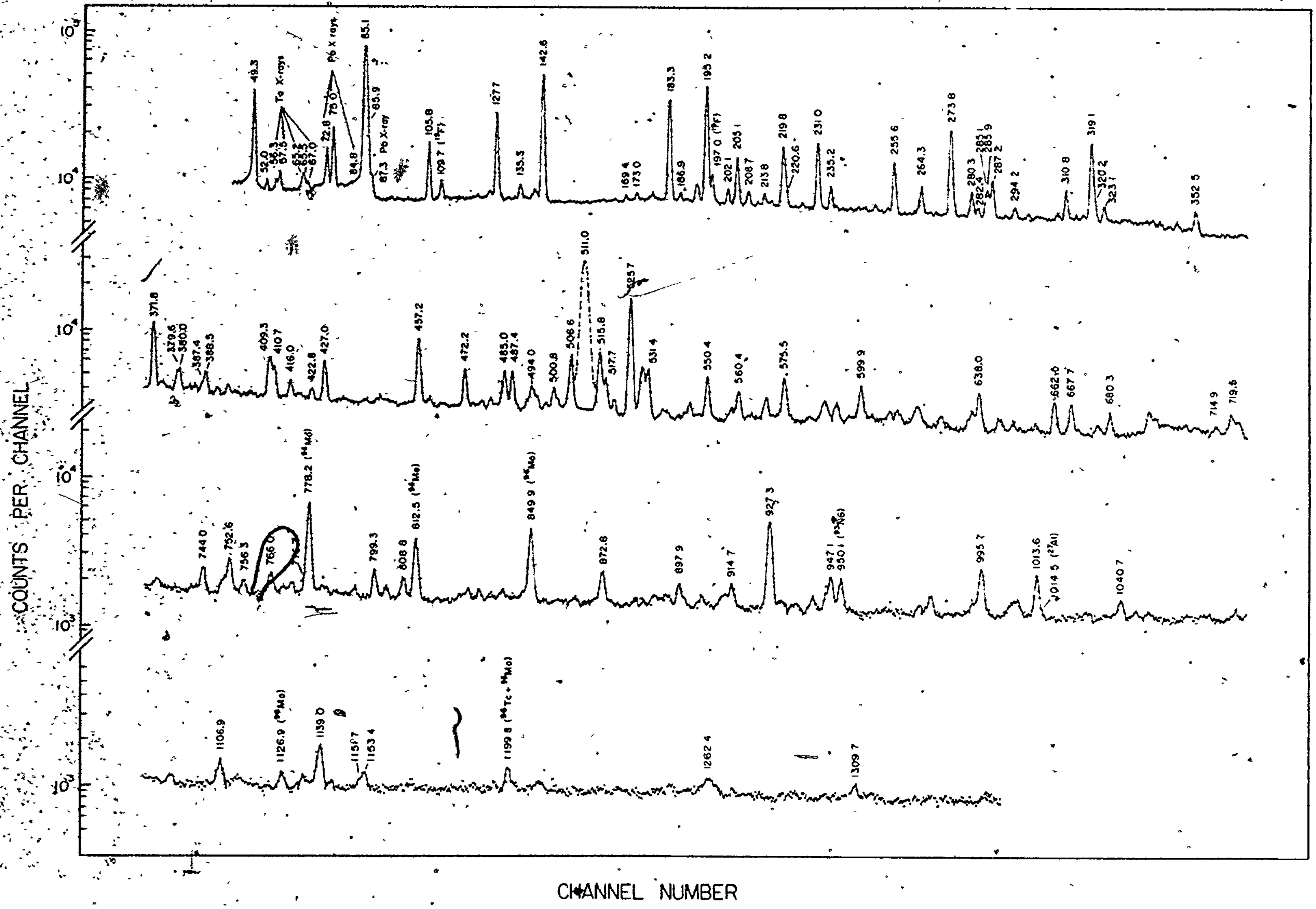
COUNTS PER CHANNEL
CHANNEL NUMBER
10^5
10^4
10^4
10^3
10^3
49.3
52.0
56.3
57.5
Te X-rays
65.2
65.5
67.0
72.8
75.0
Pb X rays
84.8
85.1
85.9
87.3 Pb X-ray
105.8
109.7 (^{19}F)
127.7
135.3
142.6
169.4
173.0
183.3
186.9
195.2
197.0 (^{19}F)
202.1
205.1
208.7
213.8
219.8
220.6
231.0
235.2
255.6
264.3
273.8
280.3
282.4
285.1
285.9
287.2
294.2
310.8
319.1
320.2
323.1
352.5
371.8
379.6
380.0
387.4
388.5
409.3
410.7
416.0
422.8
427.0
457.2
472.2
485.0
487.4
494.0
500.8
506.6
511.0
515.8
517.7
525.7
531.4
550.4
560.4
575.5
599.9
638.0
662.6
667.7
680.3
714.9
719.6
744.0
752.6
756.3
766.0
778.2 (^{94}Mo)
799.3
808.8
812.5 (^{94}Mo)
849.9 (^{94}Mo)
872.8
897.9
914.7
927.3
947.1
950.1 (^{93}Nb)
995.7
1013.6
1014.5 (^{27}Al)
1040.7
1106.9
1126.9 (^{94}Mo)
1139.0
1151.7
1153.4
1199.8 (^{94}Tc + ^{94}Mo)
1262.4
1309.7

Figure 4.4

The gamma-ray spectrum of ^{96}Tc recorded at an angle of 56° to the 18 MeV alpha beam with a 14 cc Ge(Li) detector.

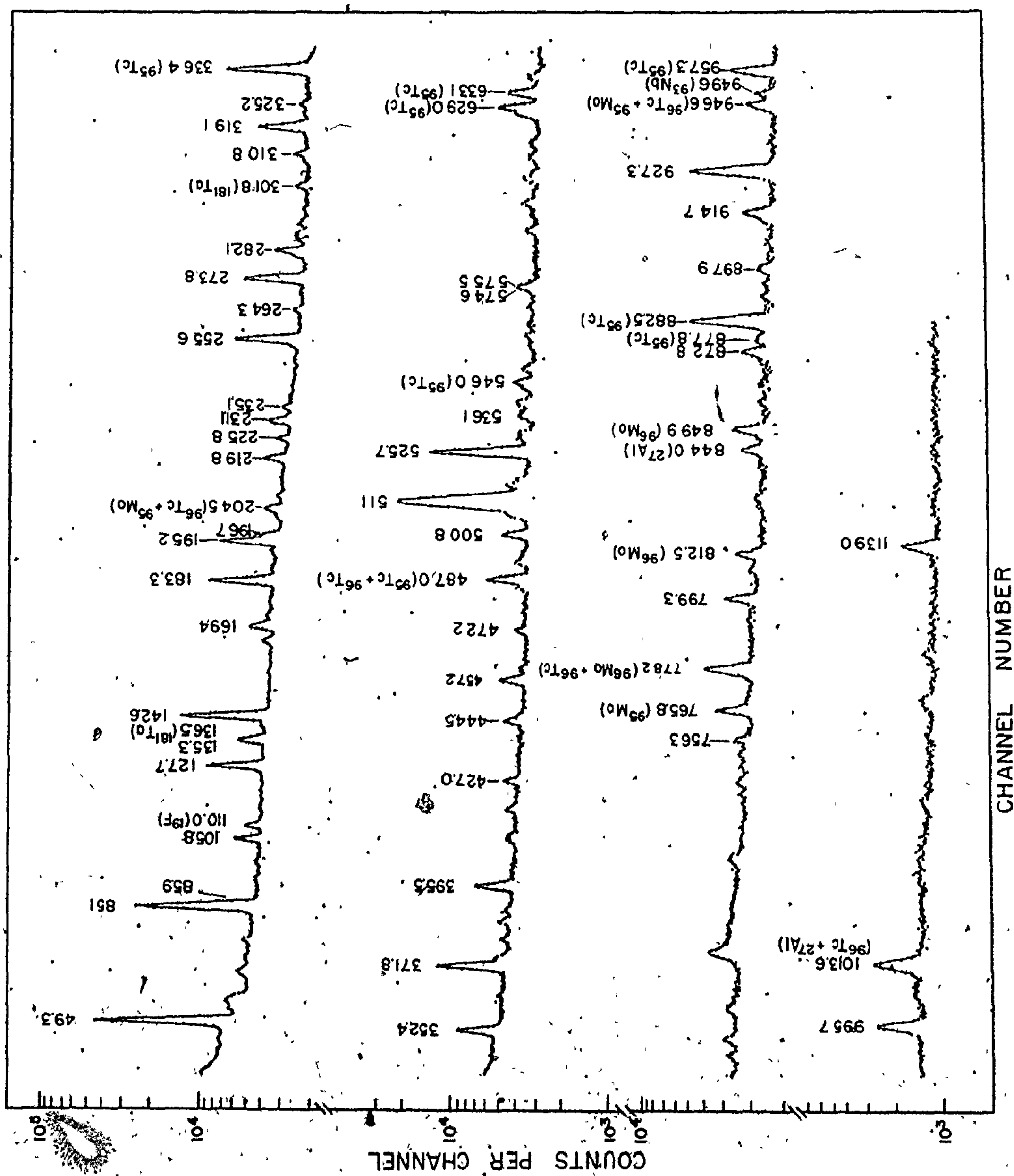
COUNTS PER CHANNEL
10^5
10^4
10^4
10^3
10^4
10^3
CHANNEL NUMBER
49.3
85.1
85.9
105.8
110.0 (^{19}F)
127.7
135.3
136.5 (^{181}Ta)
142.6
169.4
183.3
195.2
196.7
204.5 (^{96}Tc + ^{95}Mo)
219.8
225.8
231.1
235.1
255.6
264.3
273.8
282.1
301.8 (^{181}Ta)
310.8
319.1
325.2
336.4 (^{95}Tc)
352.4
371.8
395.5
427.0
444.5
457.2
472.2
487.0 (^{95}Tc + ^{96}Tc)
500.8
511
525.7
536.1
546.0 (^{95}Tc)
574.6
575.5
629.0 (^{95}Tc)
633.1 (^{95}Tc)
756.3
765.8 (^{95}Mo)
778.2 (^{96}Mo + ^{96}Tc)
799.3
812.5 (^{96}Mo)
844.0 (^{27}Al)
849.9 (^{96}Mo)
872.8
877.8 (^{95}Tc)
882.5 (^{95}Tc)
897.9
914.7
927.3
946.6 (^{96}Tc + ^{95}Mo)
949.6 (^{93}Nb)
957.3 (^{95}Tc)
995.7
1013.6 (^{96}Tc + ^{27}Al)
1139.0

the spectra. It is important that the relative intensities of transitions be known as accurately as possible to provide tests of the decay scheme, to extract useful branching ratios, to establish internal conversion coefficients and to interpret the gamma-gamma coincidence data.

Gamma-ray intensities are spatially anisotropic and strongly dependent on beam energy. The intensities given in Table 5.1 are quoted for beam energies of 14 and 18 MeV. The transitions with higher intensities at 18 MeV are generally associated with high spin states in ^{96}Tc.

The spatial distribution of gamma radiation from a nuclear reaction is described by the equation:

$$W(\theta) = A_0 \left(1 + A_2 P_2 (\cos\theta) + A_4 P_4 (\cos\theta) + \ldots \right) \quad [4 - 4]$$

where A_0 represents the intensity of the gamma-ray averaged over all directions. Since $P_2(\cos\theta)$ vanishes at $\theta = 56^\circ$ and since the A_4 coefficient is usually small, gamma-ray intensity measurements taken at 56° to the beam axis closely approximate average intensities.

The efficiency response of each detector was determined through the use of radioactive sources in a source-detector geometry as nearly identical as possible to that used in the in-beam experiment. ^{152}Eu and ^{182}Ta, which emit a large number of gamma-rays of known relative intensities were particularly useful for calibration purposes. The efficiency curve so obtained, when plotted on a log-log scale were approximately linear over the range 200 to 1500 keV. In this region, the efficiency curves seemed to be reliable to ∿3%. In the low energy domain where the efficiency was changing more rapidly, the reliability was ~ 7%.

The very rich spectra characteristic of this odd-odd nucleus contained many unresolved doublets. For doublets created by the imposition of decay lines on the reaction lines, it was often possible to sort out the relative intensities of the two components by comparing the beam-on and beam-off spectra. In other cases, the gamma-gamma experiments provided a mechanism for assigning intensities to the unresolved pair. If the intensity of a line in the coincidence spectra differed consistently by more than 30% from the "singles" intensity, the possibility of a doublet was investigated.

Most of the intensities quoted in Table 5.1 were derived from angular distribution experiments (parameter A_0 in eq. 4-4), with uncertainties of 8 to 16%. For the remainder, the intensities were derived by other methods, as indicated in the footnotes. For these the uncertainties are generally much larger.

The quoted intensities are all normalized to 100 for the strong 525 keV transition. Although the 49 and 85 keV gamma-rays are more intense than the 525, they are less suitable for normalization due to the difficulty of determining detector efficiencies in the low energy region.

4.6. Techniques of Gamma-Ray Identification

A number of techniques used to assign a given gamma-ray to the proper nucleus or to associate it with a given level in that nucleus are described in the following section. Some of these provide an indication only, while others can lead to assignments with a high degree of confidence.

4.6.1 Excitation Functions

The yield of a given transition (i.e. the number of gamma-rays recorded per micro-coulomb of beam delivered to the target) is a sensitive function of beam energy and the energy-dependence of such an excitation function can provide a strong indication of the nucleus to which the transition belongs. Since relative yields are adequate to distinguish transitions from different nuclear reactions, the experimental arrangements are relatively simple. It should be pointed out, however, that the shapes of excitation functions obtained with different targets are not strictly comparable since the mean interaction energy of the beam with the target is a function of target thickness and is always somewhat less than the beam energy. The differences which may be very significant for heavy ions like lithium or boron, are relatively unimportant for alpha particles.

Two sets of excitation functions for ^{96}Tc were determined. In the first set, a 37cc Ge(Li) detector was used on the 33° beam line in the geometry of Fig. 4.5B. The beam charge was measured by means of a Faraday cup located 2.5 meters down-stream from the 3.5 mg/cm^2 target and spectra were recorded at beam energies of 13, 15 and 17 MeV. The physical arrangements and the selection of beam energies were chosen to be compatible with those of the measurements recorded from 17 to 27 MeV by Kay Marshall and John Thompson of this laboratory in their study of the ^{93}Nb (α,2n) ^{95}Tc reaction. These results made it possible to distinguish ^{96}Tc transitions from those in ^{95}Tc, ^{95,96}Mo and ^{93}Nb.

Figure 4.5

Schematic of the experimental set-up on the "orange" beam line for (A) the electron internal conversion measurements and (B) gamma-ray experiments.

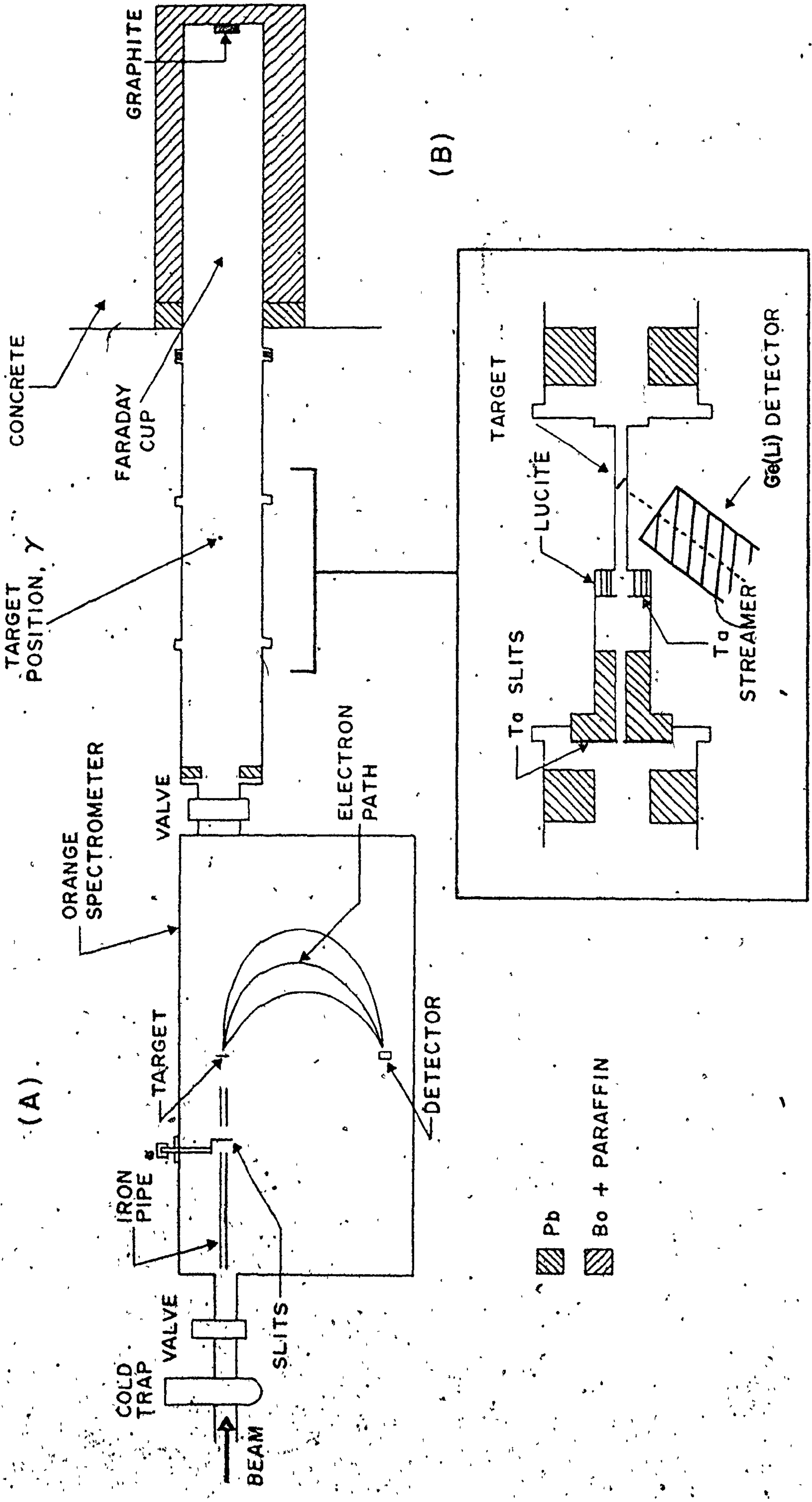
(A)
(B)
BEAM
COLD TRAP
VALVE
SLITS
IRON PIPE
TARGET
ORANGE SPECTROMETER
ELECTRON PATH
DETECTOR
VALVE
TARGET POSITION, γ
FARADAY CUP
CONCRETE
GRAPHITE
Ta SLITS
LUCITE
TARGET
Ta STREAMER
Ge(Li) DETECTOR
Pb
Ba + PARAFFIN

After the analysis of the data was completed, it became clear that additional information could be obtained if the excitation functions were explored with smaller energy increments, (see Fig. 5.1 and 5.2).

The second experiment was carried out on the 0° line using a lucite chamber in the geometry of Fig. 4.1 A. Gamma-ray energies were recorded from 30 to 1700 keV using two Ge(Li) detectors (14 cc and 50 cc) and spectra collected over the alpha beam energy range from 13 to 20 MeV in 1 MeV steps. The target for this sequence was 1.5 mg/cm^2 thick and the beam charge collected by a Faraday cup was used to normalize relative yields.

4.6.2 Neutron-Gamma Coincidences

The neutron-gamma coincidence measurements served to confirm assignments made on the basis of gamma-ray excitation functions and to add some new information. The gamma-ray spectra in coincidence with neutron gates accentuate transitions excited in the (α,2n) reaction over those from the (α,n) reaction and are completely free of ^{95,96}Mo or ^{19}F decay lines. The experiment served to identify a few ^{96}Tc lines, which were masked in the excitation functions.

The neutron-gamma coincidence experiment was carried out at 18 MeV on the 0° line in the arrangement of Fig. 4.6 B. A 37 cc Ge(Li) detector and a large NE 213 plastic scintillator were used for gamma-rays and neutrons respectively. Since the neutron detector is also sensitive to gamma-rays, it was necessary to use a thick lead shielding to reduce the gamma-ray response of the detector to manageable proportions (shown in Fig. 4.6 C). Standard pulse discrimination techniques (see Fig. 4.7)

Figure 4.6

The neutron-gammaray coincidence experiment:

(A) the true and chance gated coincidence spectra.

(B) the geometrical arrangements for the detectors used.

(C) the time separation between the gamma-ray and neutron pulses observed in the NE213 scintillation detector.

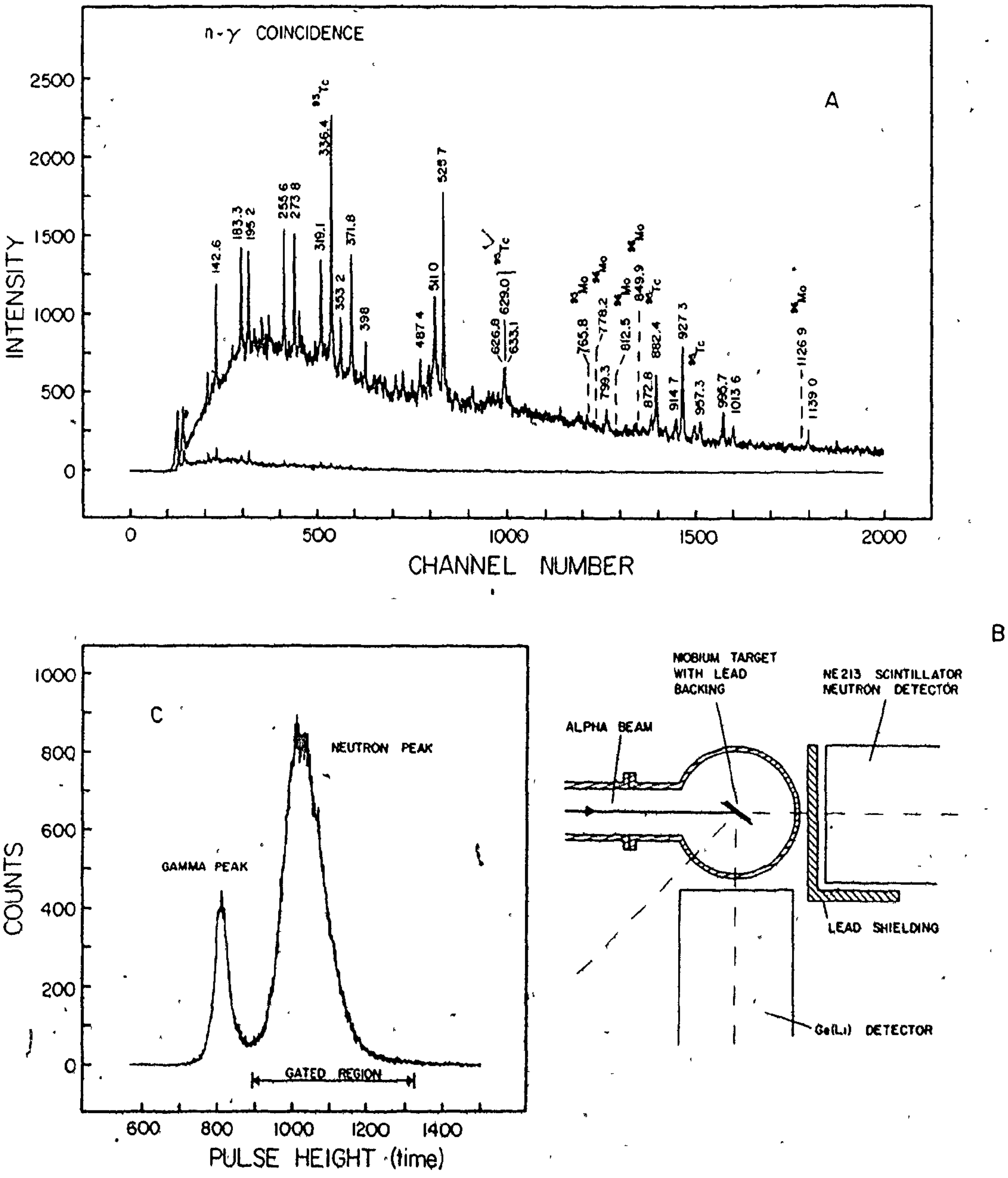
n-γ COINCIDENCE
A
INTENSITY
2500
2000
1500
1000
500
0
142.6
183.3
195.2
255.6
273.8
319.1
93Tc
336.4
353.2
371.8
398
487.4
511.0
525.7
Tc
626.8
629.0
633.1
Mo
765.8
Mo
778.2
799.3
Mo
812.5
Mo
849.9
Tc
872.8
882.4
914.7
927.3
Tc
957.3
995.7
1013.6
Mo
1126.9
1139.0
0
500
1000
1500
2000
CHANNEL NUMBER
C
COUNTS
1000
800
600
400
200
0
GAMMA PEAK
NEUTRON PEAK
GATED REGION
600
800
1000
1200
1400
PULSE HEIGHT (time)
B
NIOBIUM TARGET WITH LEAD BACKING
NE213 SCINTILLATOR NEUTRON DETECTOR
ALPHA BEAM
LEAD SHIELDING
Ge(Li) DETECTOR

Figure 4.7

Block diagram of the electronics circuit used in the neutron-gammaray coincidence experiment.

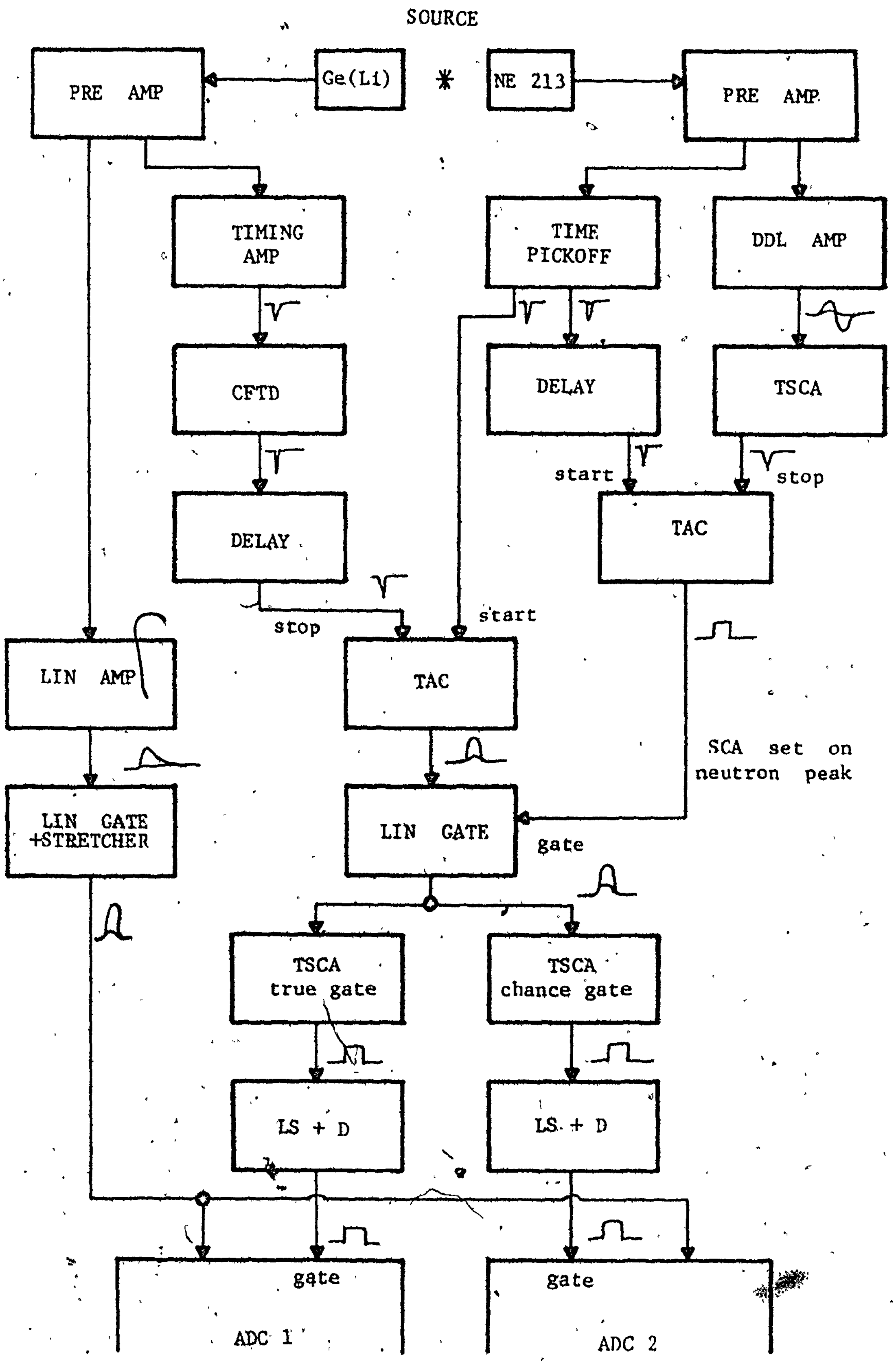
SOURCE
PRE AMP
Ge(Li)
*
NE 213
PRE AMP
TIMING AMP
TIME PICKOFF
DDL AMP
CFTD
DELAY
TSCA
start
stop
DELAY
TAC
stop
start
LIN AMP
TAC
SCA set on neutron peak
LIN GATE +STRETCHER
LIN GATE
gate
TSCA true gate
TSCA chance gate
LS + D
LS + D
gate
ADC 1
gate
ADC 2

were utilized to distinguish between the fast-rising gamma-ray and the slow-rising neutron pulses in the scintillation detector.

Pulses from the two detectors were fed to a standard fast-slow coincidence circuit and coincidence events selected by setting a window on the Gaussian peak in the TAC (Time to Analog Converter) spectrum created by neutron starting pulses and gamma-ray stopping pulses. A window of equal width was set on a flat portion of the TAC background to monitor the chance neutron-gamma coincidence rate. Both the true and chance spectra are presented in Fig. 4.6 A.

4.6.3 Gamma-Gamma Coincidence Measurements

Gamma-gamma coincidence measurements provide a powerful tool for identifying the positions of gamma-ray transitions in the level scheme. Indeed, for a nucleus with as complex structure as ^{96}Tc, the construction of a decay scheme is fundamentally based on this technique, with support from energy measurements and excitation functions.

In all, five gamma-gamma experiments were carried out; an exploratory experiment at 18 MeV using two large Ge(Li) detectors and a metallic chamber, whose walls effectively eliminated coincidences with gamma-rays of energy less than 100 keV, and two sequences of two experiments at 18 and 14 MeV respectively using a lucite chamber in the geometry of Fig. 4.1 B and a variety of detectors. The results reported in this thesis come from the last four experiments.

The important low-energy region was studied in the first experiment of the 18 MeV sequence (similar arrangements characterized the first experiment in the 14 MeV sequence). A high resolution 1cc Ge(Li) and a

10cc intrinsic Ge detector with minimal absorbers present were used to observe 4 x 10^6 coincident pairs of gamma-rays of energy greater than 26 keV.

In the second experiment of the 18 MeV sequence, a medium-size high resolution 10cc intrinsic Ge detector and a large 17% detector of high efficiency were utilized to record 2 x 10^7 coincident pairs in the energy range from 35 to 3000 keV. In the 14 MeV sequence, 9cc and 50cc Ge(Li) detectors were used to cover the 35 - 1500 KeV region and 3 x 10^7 coincidence pairs recorded.

In all these experiments a standard fast-slow coincidence circuit was used, schematically presented in Fig. 4.2 B. The coincidence data was written on magnetic tape in a format which recorded the energies of the start pulse from detector A, the stop pulse from detector B, and the time delay between them as provided by the TAC output pulse. A detailed description of the binary coding system used has been given by Cook (1972) and Smith (1977). The prompt coincidence pairs created an approximately Gaussian peak in the TAC spectrum of width ∿8 ns and ∿12 ns for the 18 MeV and 14 MeV experiments respectively.

During the course of the experiment, a broad window was set over this TAC peak and the total energy spectra of all the prompt "start pulses" from detector A (projection A) and the total spectrum of all prompt "stop pulses" from detector B (projection B) were separately cumulated. Once the experiment was completed, the magnetic tape records could be scanned using any combination of TAC, projection A, and projection B windows desired. To accommodate differential time delays in the recording of pulses from high and low energy transitions, and to avoid discrimination against gamma-rays associated with states of lifetimes in the nanosecond region, the TAC window was generally set at 200 ns. A comparison of scans carried out with 20 and 200 ns TAC windows showed that the chance coincidence rate was negligible.

The spectrum of events in detector B in prompt coincidence with events in the photopeak of a single gamma-ray in detector A was obtained in the following manner. The computer was used to set three windows on projection A for each such spectrum; a narrow window of width just wide enough to include the desired photopeak and two background windows. The total width of the two background windows was made to equal that of the peak window, and was chosen to select events in the Compton background above and below the peak of interest and as close to the peak as possible. In the process of scanning the record, the events in B paired (by the timing restrictions set by the TAC window) with events in the photopeak window were added to the spectrum while those paired with events in the background were subtracted to yield a spectrum of events in detector B in coincidence with the photopeak of a single gamma-ray recorded in detector A.

The areas of the peaks observed in the coincidence spectra were used to obtain coincidence probabilities between the gating transition γ_i and the transitions γ_j observed in coincidence with it. The number of coincidences N_{ij} recorded between the two full energy peaks γ_i and γ_j is related to the coincidence probabilities c_{ij} by the expression:

$$c_{ij} = \frac{N_{ij}}{N\ f\ \varepsilon_i\ \varepsilon_j\ \varepsilon_{ij}\ \omega_{12}\ W(\theta_{ij})} \qquad [4 - 5]$$

where N is the number of ^{96}Tc nuclei produced by the alpha beam during the course of measurements; f is the fraction of the full energy peak of the gating transition that is included in the gate; ε_i, ε_j and ε_{ij} are the detector efficiencies of the two detectors and the coincidence efficiency of the circuit respectively; ω_{12} is the product of the geometric solid angles covered by the detectors; and $W(\theta_{ij})$ is the spatial anisotropy of the involved transitions. In the geometrical configuration of the experimental set-up $W(\theta_{ij})$ is close to unity. The factor f equals unity for isolated gating peaks but takes on smaller values when the gate is set to pick out the component of a partially resolved pair. The coincidence efficiency was found to be unity for all coincident events involving gamma-rays of energy greater than 100 keV.

The expression [4 - 5] can be simplified for the purpose of analysis to the form:

$$c_{ij} = \frac{N_{ij}}{N_0\ f\ \varepsilon_i\ \varepsilon_j} \qquad [4 - 6]$$

where N_0 is a constant that can be determined from a number of strong cascades for which c_{ij} parameters are known. The values of ε_i and ε_j are deduced from the measured efficiency curves of the detectors.

The experimental values of c_{ij} must agree within experimental error with the values derived from the proposed level scheme and the measured photon intensities if the proposed scheme is valid.

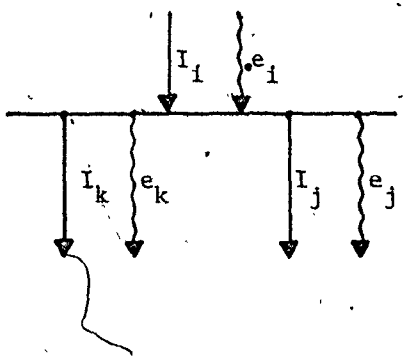

An example will illustrate how c_{ij} coefficients are obtained from the properties of the level structure. Assume that three gamma-rays of intensities I_i, I_j, I_k are related in the manner shown on the diagram. Corresponding to each transition, there is a conversion electron component, e_i, e_j and e_k, whose intensity normally is a small fraction of the photon intensity. Then:

$$c_{ij} = I_i F_j \qquad [4 - 7]$$

where

$$F_j = \frac{I_j}{I_j + I_k + e_j + e_k} \simeq \frac{I_j}{I_j + I_k} \qquad [4 - 8]$$

Even though neither the "experimental" c_{ij} values nor the ones derived from the decay scheme can be determined with a precision of better than ∿20%, the comparison provides an important test.

There are several cases when the experimental c_{ij} values are particularly useful. If one of the coincident gamma-rays is part of an unresolved doublet in the singles spectrum, the coincidence probability provides the only practical means of estimating the photon intensity.

Gamma-gamma coincidence measurements can often be used to determine internal conversion coefficients for transitions, in which the gamma-ray intensity is comparable to the intensity of the conversion electrons. If j is such a transition and all the other transitions decaying from levels a and b (illustrated on the diagram) are symbolically represented by m and h transitions, then

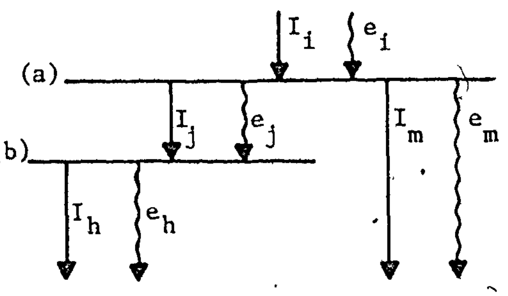

$$c_{ij} = \frac{I_i\, I_j}{I_j + e_j + I_m + e_m} \qquad c_{ih} = \frac{I_i(I_j + e_j)}{I_j + e_j + I_m + e_m} \cdot \frac{I_h}{I_h + e_h}$$

whence

$$\frac{c_{ih}}{c_{ij}} = (1 + \alpha^j)\, \frac{I_h}{I_h + e_h} \qquad [4 - 9]$$

where $\alpha^j = e_j/I_j$ is the total internal conversion coefficient for transition j.

If the h transitions are not strongly converted, the last factor can be approximated as unity and $\alpha^j = (c_{ih}/c_{ij}) - 1$. It should be noted that neither the photon nor electron intensity of transition j is required for this method to work.

From detailed balancing of intensities feeding and deexciting a level it is also possible to deduce conversion coefficients for strongly converted transitions. Consider a level fed by a number of transitions and deexcited by a single, strongly converted transition j. Then:

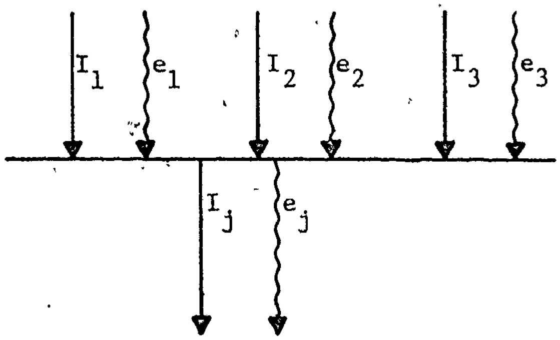

$$I_j + e_j = \sum_{i=1}^{N} (I_i + e_i)$$

and

$$\alpha^j = \frac{\Sigma(I_i + e_i)}{I_j} - 1 \qquad [4 - 10]$$

In general, none of the transitions feeding the intermediate state are strongly converted, which leads to an estimate of the total conversion coefficient of the deexciting transition without measurements of any electron intensities.

4.7 Experimental Methods Leading to Spin and Parity Assignments

The following discussion will focus on methods of establishing changes of spin and parity between states connected by gamma-ray transitions. These methods in general are unable to do more than limit the possibilities; however, in a number of cases they can lead to unique assignments.

4.7.1 Angular Distribution of Gamma-Rays

In this section, the experimental details related to the four angular distribution experiments are described. The focus is on factors affecting the overall precision of the measurements. For convenience, the four experiments will be labelled A, B, C and D.

In experiment A at 18 MeV which accentuated transitions between high spin states the beam was stopped in a 152 mg/cm^2 lead foil behind and in contact with the target (see Fig. 4.1 C). This arrangement permitted measurements to be carried out at seven angles from 0^{o} to 90^{o}. Useful data was obtained in the energy range 150 - 1400 keV; at lower energies, the corrections for gamma-ray absorption in the beam stopper rendered the data useless.

Experiment B was similar to A, except that a beam energy of 14 MeV and a 98mg/cm^2 beam stopper were used. Measurements were taken at 9 angles between 0^{o} and 90^{o}. The use of the thinner lead beam-stopper extended the useful energy range down to 100 keV.

In experiments C and D carried out at 14 MeV, the beam was stopped in a tantalum foil 30cm from the target. This arrangement, shown in Fig. 4.1 A, restricted the measurements to angles greater than 15° with a consequent reduction in the precision of the A_4 coefficients deduced from the data. In D, a 1cc Ge(Li) detector was used to resolve the 85.3 - 86.1 keV doublet sufficiently to provide high quality angular distributions, and to obtain useful distributions for a large number of gamma-rays in the 30 - 350 keV range. Interference from lead X- rays was reduced by using tantalum beam stoppers and copper and cadmium shields.

In the experiments A, B and C, a 14cc Ge(Li) detector was used to yield high resolution and good efficiency over the energy region of interest (100 - 1400 keV). In all four experiments, a second detector of comparable size placed at 125° to the beam direction monitored the count rate, which was then used to normalize the intensities obtained in the movable detector. Usual corrections were made for counting losses, for the finite solid angle subtended by the detector at target, and where applicable, for differential absorption in the lead stopping foil.

Corrections for the lack of centering were made by comparing the intensity of a number of decay lines in the fixed and movable detectors at each angle. In experiment A, the uncertainty in the corrected data was of the order of 2%, small by comparison with the observed anisotropies of the gamma-ray distributions at 18 MeV. In experiment B, spectra were recorded at each angle with the beam both on and off. The centering corrections in this case could be made more precisely, and yielded a combined uncertainty in the results of less than 1%.

In experiment C, technical problems made it necessary to record the decay spectra after the in-beam measurements had been completed, and the reaction chamber returned to atmospheric pressure. The change in pressure caused the chamber to shift its position, so that the centering had to be completely based on decay lines in the in-beam spectra. As a consequence the angular distributions from this experiment lacked the precision of experiment B.

Since no strong ^{96}Tc peaks were available in the low energy spectra of experiment D, and since an attempt to obtain the centering corrections by the use of radioactive sources placed in the target position at atmospheric pressure failed for the reasons described in experiment C, it was necessary to use some of the ^{96}Tc lines whose angular distributions were known from experiments B to obtain the corrections required. It is estimated that centering errors in experiment D were of the order of 1%. In this experiment, reliable angular distributions were obtained for the 49 keV transition and both members of the 85 keV doublet.

4.7.2 Linear Polarization of Gamma-Rays

Linear polarization measurements were carried out using a Compton-scattering polarimeter designed in this laboratory (Khan et al., 1980). Polarization data must be used in conjunction with the angular distribution coefficients.

The high resolution two-crystal polarimeter consists of two hyperpure germanium crystals mounted in a common cryostat. These crystals are identically shaped discs 23 mm in diameter and 6 mm thick, placed side by side 15 mm apart, with their flat surfaces parallel (see Fig. 4.8A). The operation of the polarimeter depends on the fact that the Compton-scattering cross-section is a function of the angle between the electric vector of the gamma-ray and the normal to the scattering plane. If a gamma-ray Compton-scattered in one crystal is fully absorbed in the other, then the sum of energies deposited in both detectors will equal the full energy of the radiation. Since these scattering and absorption events are coincident within the time response of a fast-slow coincidence circuit, such a circuit can serve to separate these events from other events recorded in the detectors. The electronics circuit (shown in Fig. 4.8 C) was arranged and tuned to give equal amplification for both detectors. Under these conditions, the sum of the energies of the coincidence events add up to a single full energy peak regardless of which crystal acted as scatterer or absorber.

The experiment was performed on the 33° line with a 14 MeV alpha beam, in the geometry of Fig. 4.8B. The polarimeter was mounted on a table, which could be rotated about a vertical axis passing through the target position. The polarimeter crystals were located symmetrically with respect to this axis and 10 cm below the target. By rotating the table, it was thus possible to place the flat faces of the polarimeter crystals either normal to or parallel to the reaction plane defined by both the beam axis and the vertical axis through the target. A 37 cc Ge(Li) detector was placed at 56° to the beam direction and recorded the gamma-rays emitted from the target for normalization purposes.

Polarimeter spectra were recorded alternately in each of the

Figure 4.8

The gamma-ray linear polarization measurements:
(A) orientation of the germanium crystals in the perpendicular and parallel positions.
(B) geometrical arrangement of the polarimeter relative to the beam axis.
(C) block diagram of the electronics circuit used with the polarimeter.

(from Khan et al., 1980)

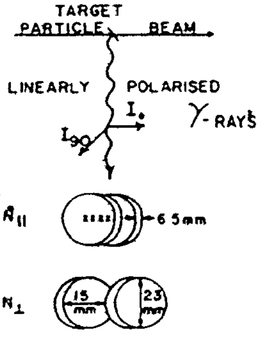
TARGET
PARTICLE
BEAM
LINEARLY
POLARISED
I_0
γ-RAYS
I_{90}
$N_{\parallel}$
6.5mm
$N_{\perp}$
15 mm
23 mm

(a)

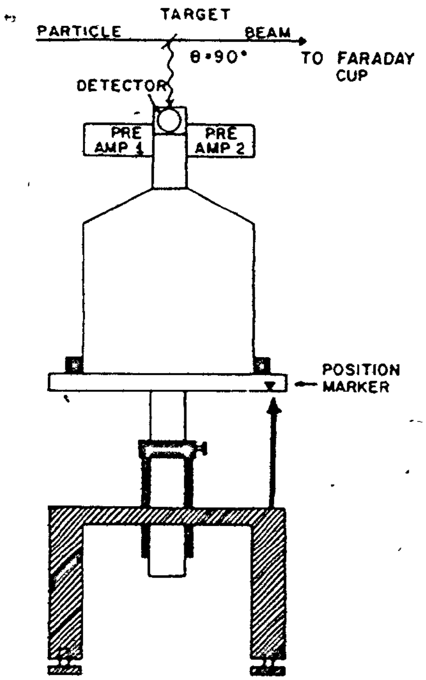
TARGET
PARTICLE
BEAM
θ=90°
TO FARADAY CUP
DETECTOR
PRE AMP 1
PRE AMP 2
POSITION MARKER

(b)

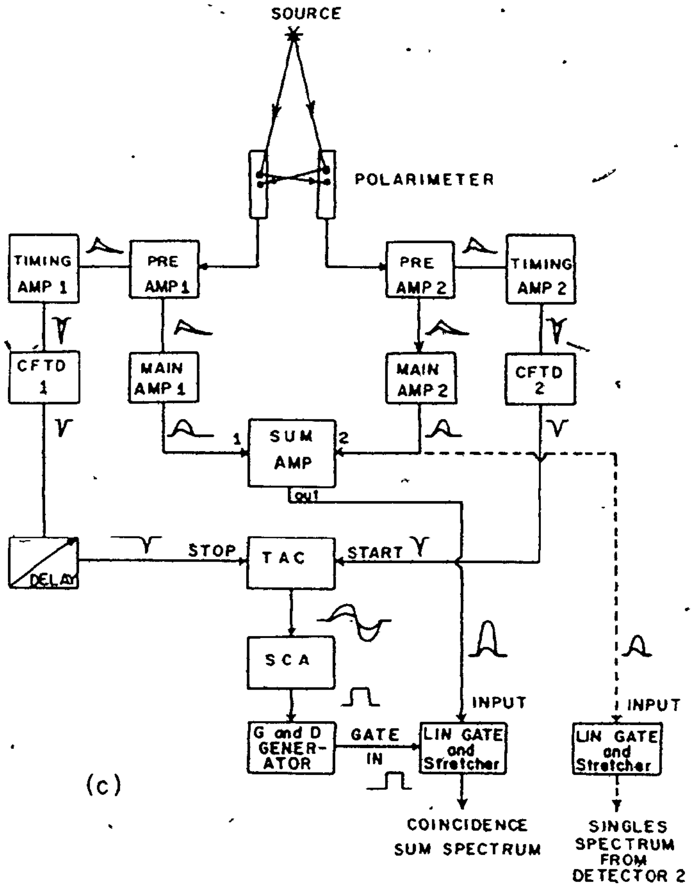
SOURCE
POLARIMETER
TIMING AMP 1
PRE AMP 1
PRE AMP 2
TIMING AMP 2
CFTD 1
MAIN AMP 1
MAIN AMP 2
CFTD 2
SUM AMP
1
2
OUT
DELAY
STOP
TAC
START
SCA
G and D GENERATOR
GATE
IN
INPUT
LIN GATE and Stretcher
INPUT
LIN GATE and Stretcher
COINCIDENCE SUM SPECTRUM
SINGLES SPECTRUM FROM DETECTOR 2

(c)

two orientations, and the spectra in each orientation cumulated throughout the experiment. The spectra extended from 100 to 1200 keV and are shown in Fig. 4.9.

The measured asymmetry of a given photopeak, Δ, is given by:

$$\Delta = (N_p - N_n) / (N_p + N_n) \qquad [4 - 11]$$

where N_p and N_n refer to peak areas recorded in the parallel and normal orientations respectively, and normalized to the same reaction rate by means of the normalization detector.

The polarization, P, is defined by the equation:

$$P = \Delta / S \qquad [4 - 12]$$

where S is the polarization sensitivity of the polarimeter.

The sensitivity function (Fig. 4.10) was obtained experimentally using a number of stretched E2 transitions in the ground state band of ^{164}Er excited in the ^{162}Dy (α,2n) ^{164}Er reaction. For these transitions, the asymmetry was determined as described above and combined with the theoretically deduced polarization coefficient to obtain S. For stretched E2 transitions, the polarization is given by:

$$P = \frac{3A_2 + 1.25A_4}{2 - A_2 + 0.75A_4} \qquad [4 - 13]$$

where A_2 and A_4 are the angular distribution coefficients determined in section 4.7.1.

Figure 4.9

The gamma-ray spectra from the polarimeter obtained in the parallel and perpendicular orientations, using a 14 MeV alpha beam.

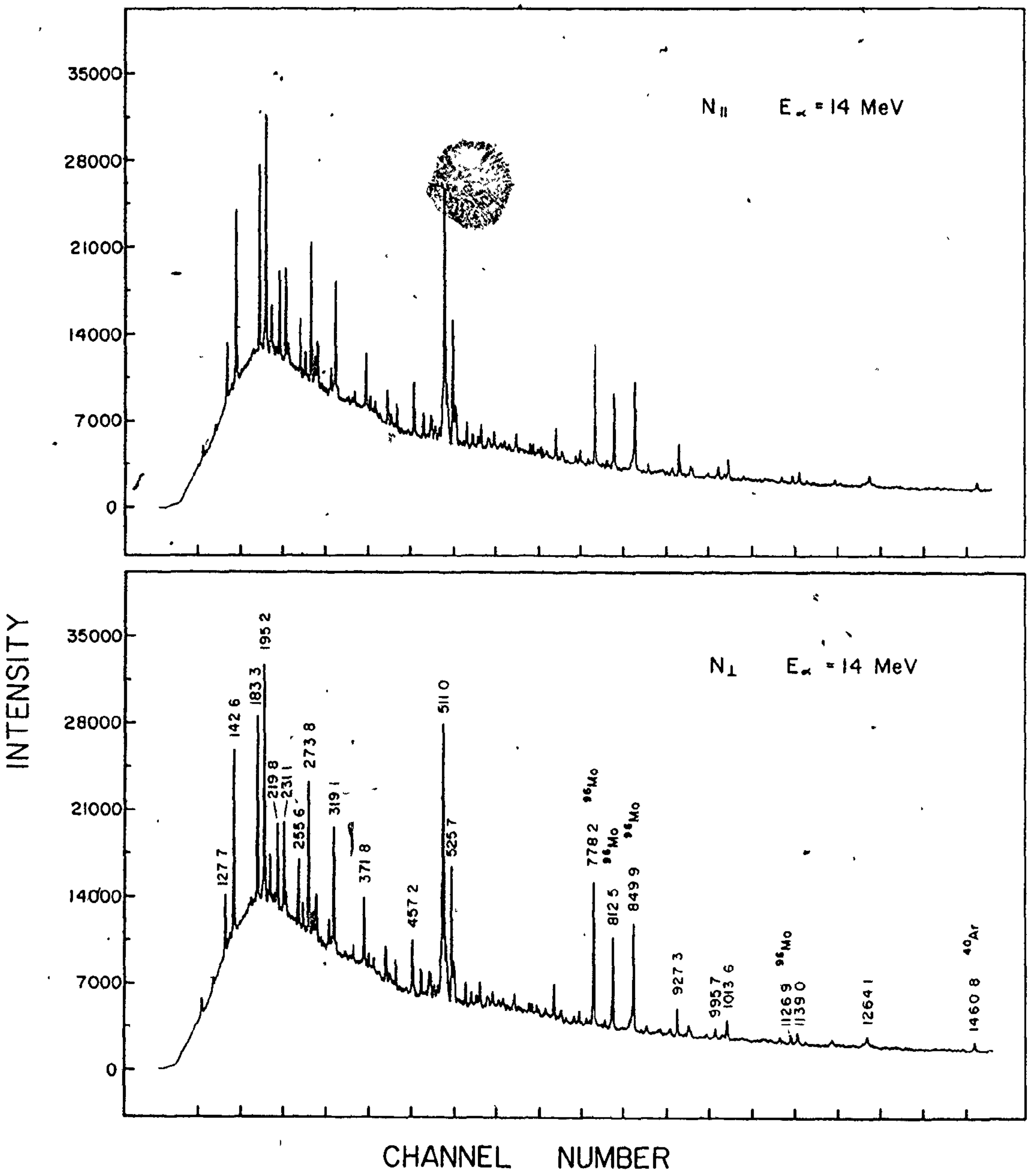
N∥ Eα = 14 MeV
N⊥ Eα = 14 MeV
INTENSITY
CHANNEL NUMBER
35000
28000
21000
14000
7000
0
127 7
142 6
183 3
195 2
219 8
231 1
255 6
273 8
319 1
371 8
457 2
511 0
525 7
96Mo 778 2
96Mo 812 5
96Mo 849 9
927 3
995 7
1013 6
96Mo 1126 9
1139 0
1264 1
40Ar 1460 8

Figure 4.10

The sensitivity curve for the McMaster two crystal polarimeter deduced from the ^{164}Er, ^{149}Tb and ^{157}Tb data (Khan et al. 1980).

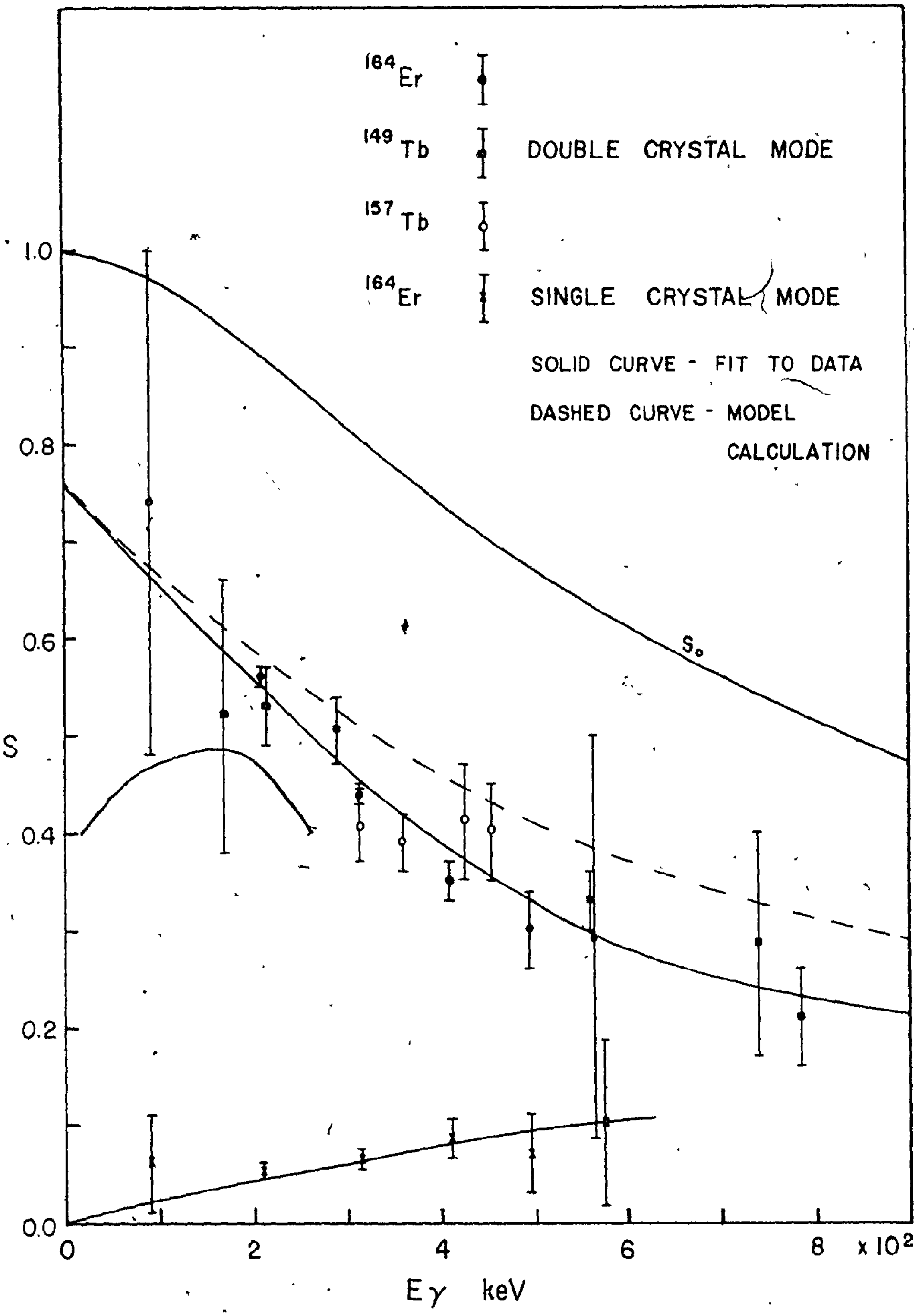
^{164}Er
^{149}Tb
DOUBLE CRYSTAL MODE
^{157}Tb
^{164}Er
SINGLE CRYSTAL MODE
SOLID CURVE - FIT TO DATA
DASHED CURVE - MODEL CALCULATION
S_0
S
1.0
0.8
0.6
0.4
0.2
0.0
0
2
4
6
8
x 10^2
Eγ keV

The efficiency of the polarimeter peaks in the 200 - 300 keV region. It falls off very rapidly below 200 keV partly because the Compton cross-section, upon which its operation depends, is overwhelmed by the photoelectric contribution to the total interaction cross-section as the photon energy decreases, and partly because the energy of the scattered photon is too low to trigger the coincidence circuit with 100% efficiency. For photon energies above 600 keV, both the efficiency and sensitivity decrease because the thin crystals used have a low detection efficiency and because the Compton process becomes less anisotropic with increasing photon energy.

4.7.3 Internal-Conversion Measurements

This section outlines the method used to study the internal conversion electrons emitted by ^{96}Tc. The transition energy, E_γ, may be given to either the photon or to an electron in the i-th shell of the atom. The latter process, internal conversion, leads to a monoenergetic group of electrons of energy $E_\gamma - B_i$ where B_i is the binding energy of the i-th shell. The ratio of the intensity of this electron group e^i to the photon intensity I associated with the same transition defines the internal conversion coefficient:

$$\alpha_i = \frac{e^i}{I} \qquad [4 - 14]$$

Since the value of α_i depends strongly on the transition energy and multipolarity, and the atomic shell from which the electrons came, a determination of α_i can serve as a powerful tool in the assignments of spins and parities to nuclear states. The effort in this work was directed to measuring K-shell conversion coefficients, since the K-shell conversion electrons in general form the strongest group for a given transition. In practice, the less abundant L and M-shell conversion electrons simply made the conversion electron spectra more difficult to analyse, while providing no useful results.

When an electron with charge e moves at right angle to a uniform magnetic field B, it is deflected into a circular path whose radius ρ is related to the field and the electron momentum p through the equation:

$$B\rho = p/e \qquad [4\text{-}15]$$

For any magnetic spectrometer in which the source and detector positions are fixed, the value of ρ remains constant and B or $B\rho$ becomes a useful measure of electron momentum. In such instruments, the momentum spectrum can be scanned by changing the magnetic field in a step wise fashion and recording the number of electrons at each momentum setting.

The "orange" Beta-ray spectrometer used in this laboratory was patterned after the one constructed by Geiger (1965) at Chalk River. It consists of seven 1/r sector type spectrometers of the Kofoed-Hansen (1950) design spaced symmetrically around a vertical axis (see Fig. 4.11). A Rawson probe placed in one of the gaps measures the magnetic field and provides a means of stabilizing the field to 5 parts in 10^5. Electrons from the target are focussed by each of the six remaining gaps on to a common scintillation detector. The detector is a cylinder 10 mm in diameter and 5 mm in height made of NE 102 located on the axis of the

Figure 4.11

The general design of the six gap "orange" type beta-ray spectrometer (from Geiger, 1965).

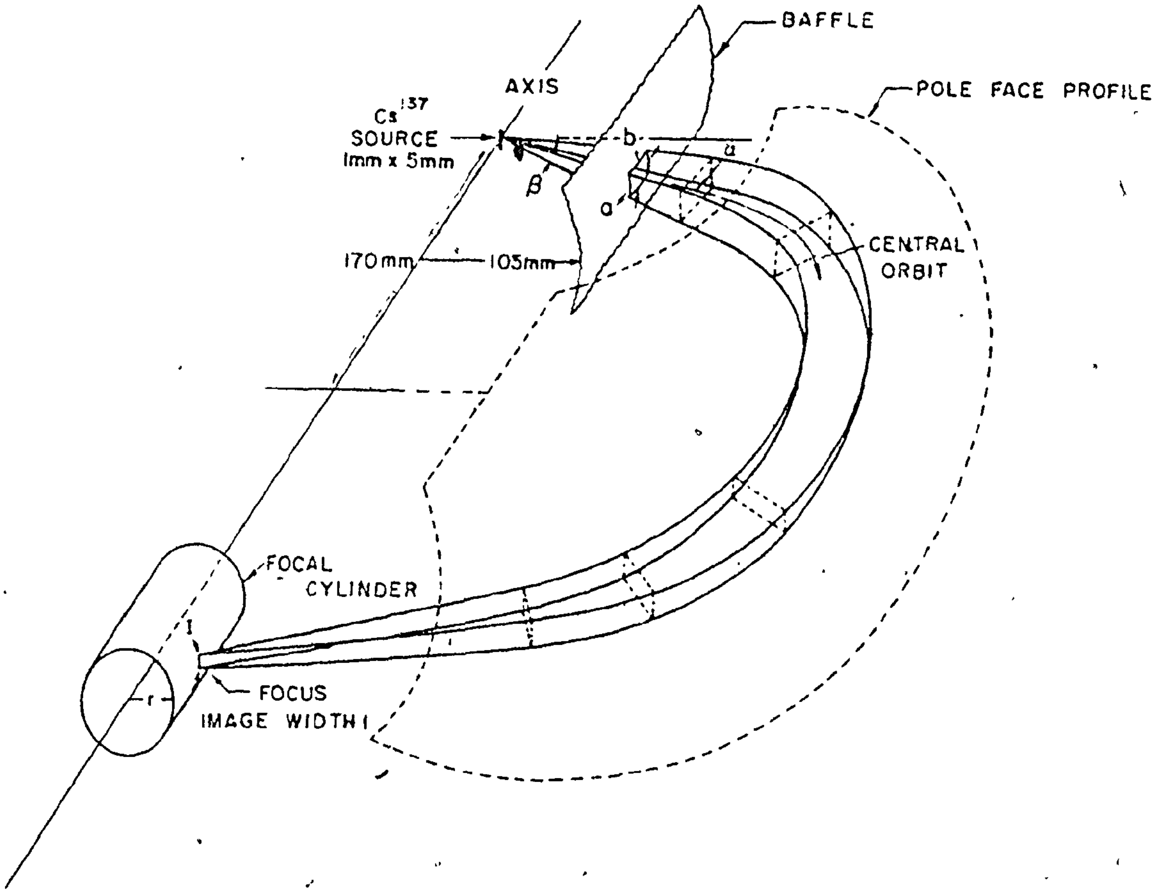
BAFFLE
AXIS
POLE FACE PROFILE
Cs^{137}
SOURCE
1mm x 5mm
b
α
β
a
170mm
105mm
CENTRAL
ORBIT
FOCAL
CYLINDER
I
r
FOCUS
IMAGE WIDTH I

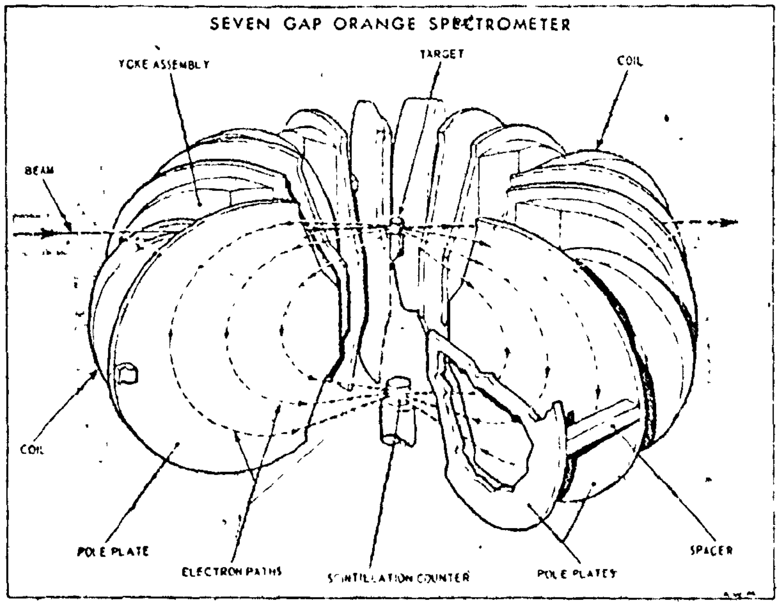
SEVEN GAP ORANGE SPECTROMETER
YOKE ASSEMBLY
TARGET
COIL
BEAM
COIL
POLE PLATE
ELECTRON PATHS
SCINTILLATION COUNTER
POLE PLATES
SPACER

Figure 4.12

The target-detector geometry and the electron and gamma-ray shielding used with the "orange" beta-ray spectrometer (from Khoo, 1972).

ORANGE SPECTROMETER

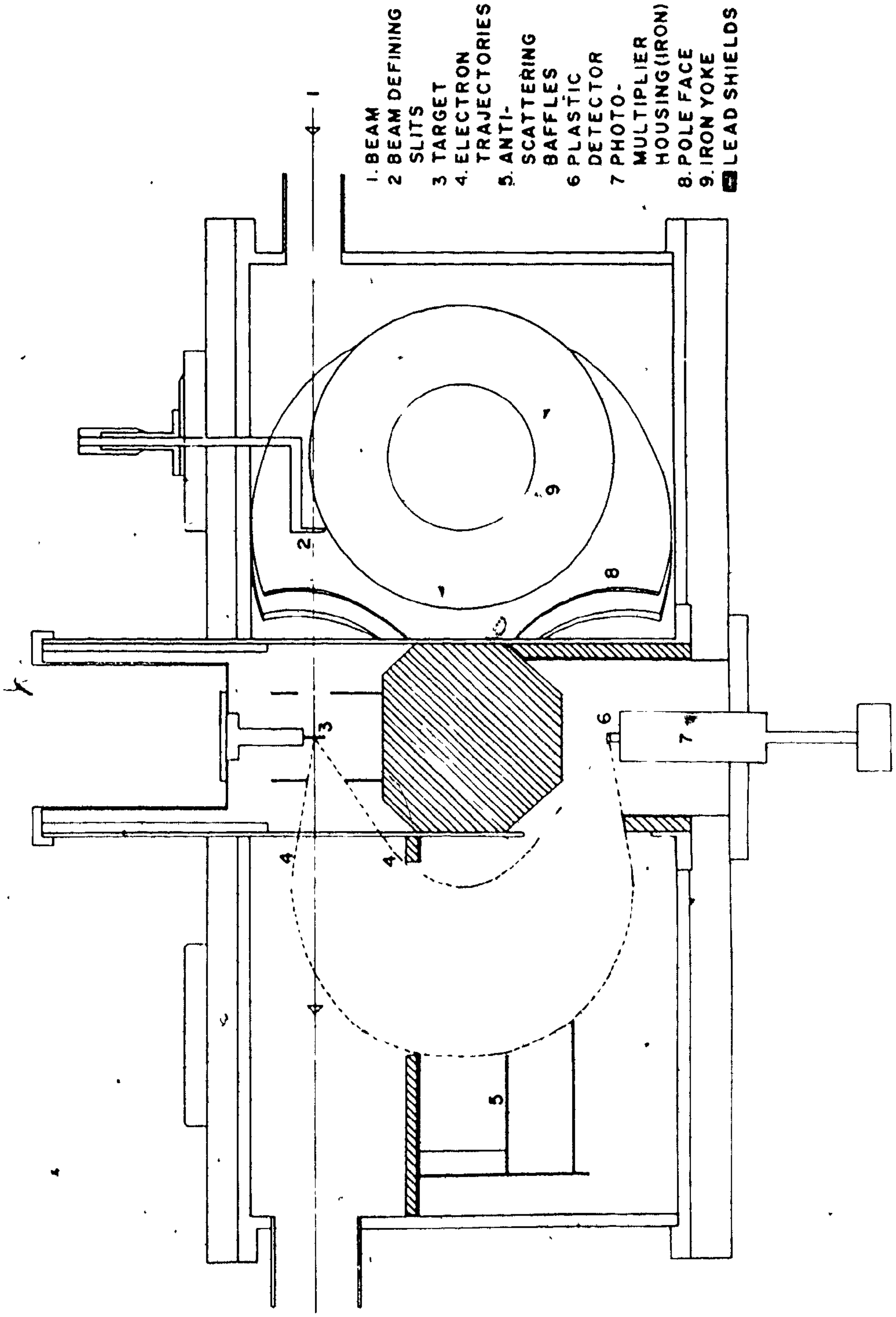

spectrometer and mounted on a photomultiplier. The electrons enter the curved surface of the cylinder through an annular ring (see Fig. 4.12). Scintillations are converted into electric pulses by the photomultiplier and the pulses amplified by a DDL amplifier before being analyzed.

The momentum resolution of a given one gap spectrometer depends on the width of the detector entrance ring typically 1.5 mm in height and the source dimensions, which for the beam measurements are defined by the size of the beam interacting with the target. The beam size was limited by a set of four tantalum jaws with an open gap of 2 x 5 mm placed upstream 24 cm from the target.

Momentum resolution tests were made using a radioactive source of ^{198}Au of dimensions 2 x 5 mm to correspond to the in-beam situation. The resolution, $\Delta p/p$, for the K conversion peak of the 411 keV transition in ^{198}Au was of the order of ∿.55% for each gap. The instrumental resolution using 6 gaps was ∿.7%, since each gap has slightly different focussing characteristics. Because the magnetic field in the spectrometer is very closely proportional to the momentum of the focussed electrons, the field readout was adjusted to read $B\rho$ directly. This was done by adjusting the readout to 2222.5 $B\rho$ for the 411 keV K conversion peak. In the beam experiment, instabilities in beam position as well as the spread in electron energies created by the finite thickness of the target increase the overall momentum resolution to 0.9 - 1.0%.

The response function of the plastic detector to monoenergetic electrons was measured at various electron energies using the beta spectrum of ^{198}Au. The response function at a given momentum consisted of Gaussian full energy peak and a tail with a roughly Wood-Saxon shape created by backscattered electrons which leave only part of their energy in the crystal (see Fig. 4.13 A, curve a). When this detector is used for a beam experiment with the magnetic field set to focus electrons of a given Bρ, the response function is complicated by the presence of a low energy background component (Fig. 4.13 A, curve b) due to unfocussed electrons or X -rays created by the interaction of the intense gamma-ray flux with the walls of the spectrometer. To avoid recording this background component, it was necessary to set a discriminator to maintain an advantageous ratio of the true electrons to the background counts. This ratio is maximized when the discrimination level is set just below the Gaussian peak. Since the position of this peak is proportional to electron energy, the discrimination level was adjusted frequently as the spectrum was scanned. For each discriminator setting, the fraction of the total response function accepted was determined in the manner described below.

The experimental response function of the detector in a beam experiment with the spectrometer focussed on monoenergetic electrons can be approximated by the function:

$$\begin{aligned} I(x) = \Big(a - bx + c\cdot\exp(-dx) \Big) + & \\ & \qquad [4 - 16] \\ g\Big(\exp[-(\tfrac{x-h}{s})^2] + f[1 + \exp(\tfrac{x^2-h^2}{s^2})]^{-1} \Big) & \end{aligned}$$

where the first bracket combines linear and exponential terms which attempt to describe the background component, and the second describes the response to monoenergetic electrons. The latter consists of a

Figure 4.13

The details of the electron data analysis:

(A) typical response spectrum of the electron detector.

(B) the efficiency curves deduced from the experimental data at 14 MeV.

(C) the relationship between the energy of the electrons and the centroid of the Gaussian peak in the detector's response function.

(D) the curve $1/\delta$ (the resolution of the spectrometer) vs. $B\rho$ for the 14 and 18 MeV experiments.

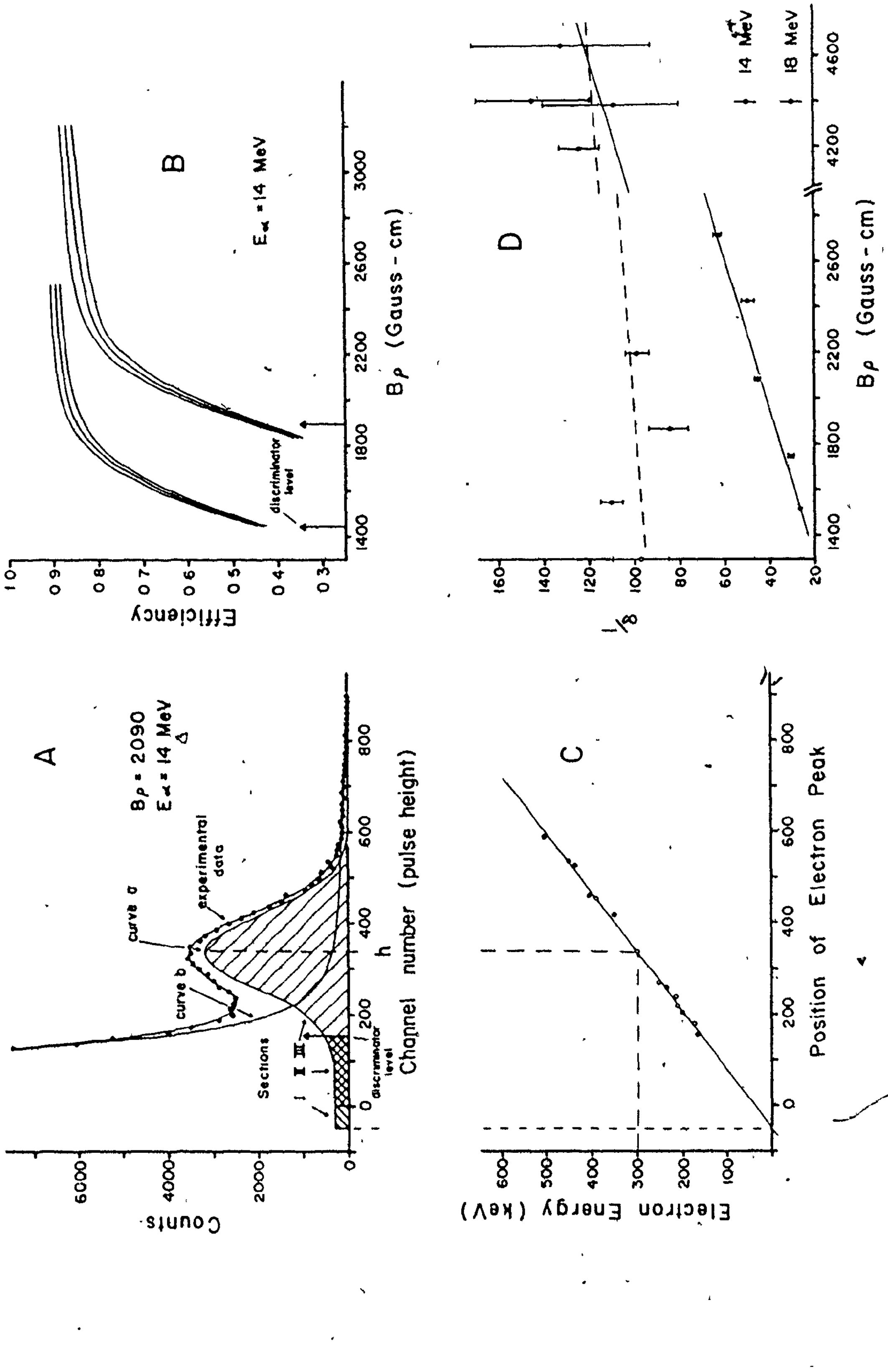
A
Bρ = 2090
Eα = 14 MeV
curve a
curve b
experimental data
Sections
I
II
III
discriminator level
Counts
6000
4000
2000
0
0
200
400
600
800
h
Channel number (pulse height)
B
Eα = 14 MeV
discriminator level
Efficiency
1.0
0.9
0.8
0.7
0.6
0.5
0.4
0.3
1400
1800
2200
2600
3000
Bρ (Gauss-cm)
C
Electron Energy (keV)
600
500
400
300
200
100
0
200
400
600
800
Position of Electron Peak
D
1/δ
160
140
120
100
80
60
40
20
14 MeV expt
18 MeV expt
1400
1800
2200
2600
4200
4600
Bρ (Gauss-cm)

Gaussian peak centered on channel h and a Wood-Saxon tail. The parameter f was determined from the response functions measured with a ^{198}Au source. The remaining parameters were obtained by a χ^2-fit to the data recorded in the beam experiment.

Since the parameter h is a linear function of the electron energy, a plot of electron energy versus the position of the Gaussian peak (see Fig. 4.13 C) may be used to establish the channel number corresponding to zero electron energy and the fraction of the Wood-Saxon tail cut off by the discriminator (see Fig. 4.13 A). The knowledge of the portion of the response function rejected by the electronics, rejected by the discriminator and passed by the discriminator (sections I,II,III respectively in Fig. 4.13 A) yields the efficiency of the system for the Bρ at which the response function was measured. Since this efficiency is a slowly varying function of electron energy except when the Gaussian is close to the discriminator level, it was sufficient to determine it at a few selected points and to interpolate for intermediate values.

For electron energies where the background component was not well separated from the Gaussian peak, a more complex procedure was required. The data was first fitted using expression [4-16] as before. Because the first term in this expression provides at best an approximation to the background component, the fit in these cases was rather poor, shifting the centroid of the Gaussian downward by several channels from the position established by visual inspection or that predicted by the linear relationship of Fig. 4.13 C from data taken at higher electron energies. Since a few channels error in the peak position has a large effect on the efficiency the centroid of the peak was assigned using a combination of factors mentioned above. Next the linear relationship of h and s versus electron energy were determined. Since these are the only energy dependent parameters of the Gaussian and Wood-Saxon response function, it was possible to calculate the efficiency of the system as a function of electron energy. The results of such efficiency calculations are shown in Fig. 4.13 B. The two curves are related to the two discriminator settings used, while the three closely spaced lines mark the uncertainty in the efficiency caused by the uncertainty in f ($f=0.12 \pm .02$).

Two electron experiments were performed in the "orange" spectrometer using the same 0.9 mg/cm^2 target. A measure of the number of (α,n) reactions occurring in the target was obtained by recording the alpha particles Rutherford scattered from the target at an angle of 52° to the beam. The charge collected in a Faraday cup at the beam dump was also recorded (see Fig. 4.5 A). The latter was found to be less reliable than the former because it was insensitive to the conditions in the target. The instrument automatically scanned a preset momentum region in discrete momentum steps (either 2 Bρ or 5 Bρ), recording the electron count in each position until a predetermined number of scattered alphas had been recorded and then moving on to a new magnetic field setting. In addition to the electron and alpha counts, the teletype print-out recorded the magnetic field setting, the time of counting at each setting and the charge collected in the Faraday cup.

Hysteresis effects in the iron portion of the magnetic circuit meant that the momentum of the electrons focussed at a given field setting was sensitive to a small degree to the recent history of the magnetic field setting. To reduce this effect to a minimum, the spectrum was always scanned with the field increasing and the magnet put through a standard demagnetization cycle whenever the field was reduced. With these precautions the field settings for focussing of electrons of given momentum were reproducible to ∿0.5%. The rough calibration of the spectrometer given by the read-out was used to relate the observed electron peaks to their associated gamma-rays. The gamma-ray energies together with the K, L and M shell binding energies were then employed for a more precise calibration.

In the 18 MeV experiment the electron spectrum was scanned from Bρ 1100 to 2500 together with selected sections from Bρ 4000 to 4700 . The interest was focussed on relatively few intense transitions associated with the high-spin states of ^{96}Tc. For these measurements, the 1% resolution achievable with all six gaps was adequate (see the spectrum of Fig. 4.14). In the 14 MeV experiment, the interest was centered on the complex spectrum of the low spin transitions which are strongly enhanced at this energy. For these transitions the 0.55% resolution achievable with one gap was barely adequate. The gap centered at 52° to the beam line was used alone and the target was placed so that the normal to the target plane was centered on the gap. The electron spectrum was scanned from Bρ 1400 to 3000 and from Bρ 4350 to 4450 . The background in this experiment was relatively high since the transmission of true electrons was reduced to one sixth while the unfocussed electrons were not reduced proportionally, (see Fig. 4.15) .

Figure 4.14

A comparison of the gamma-ray and electron spectra of ^{96}Tc measured with an 18 MeV alpha beam. Note that only certain selected regions of the electron spectrum were scanned.

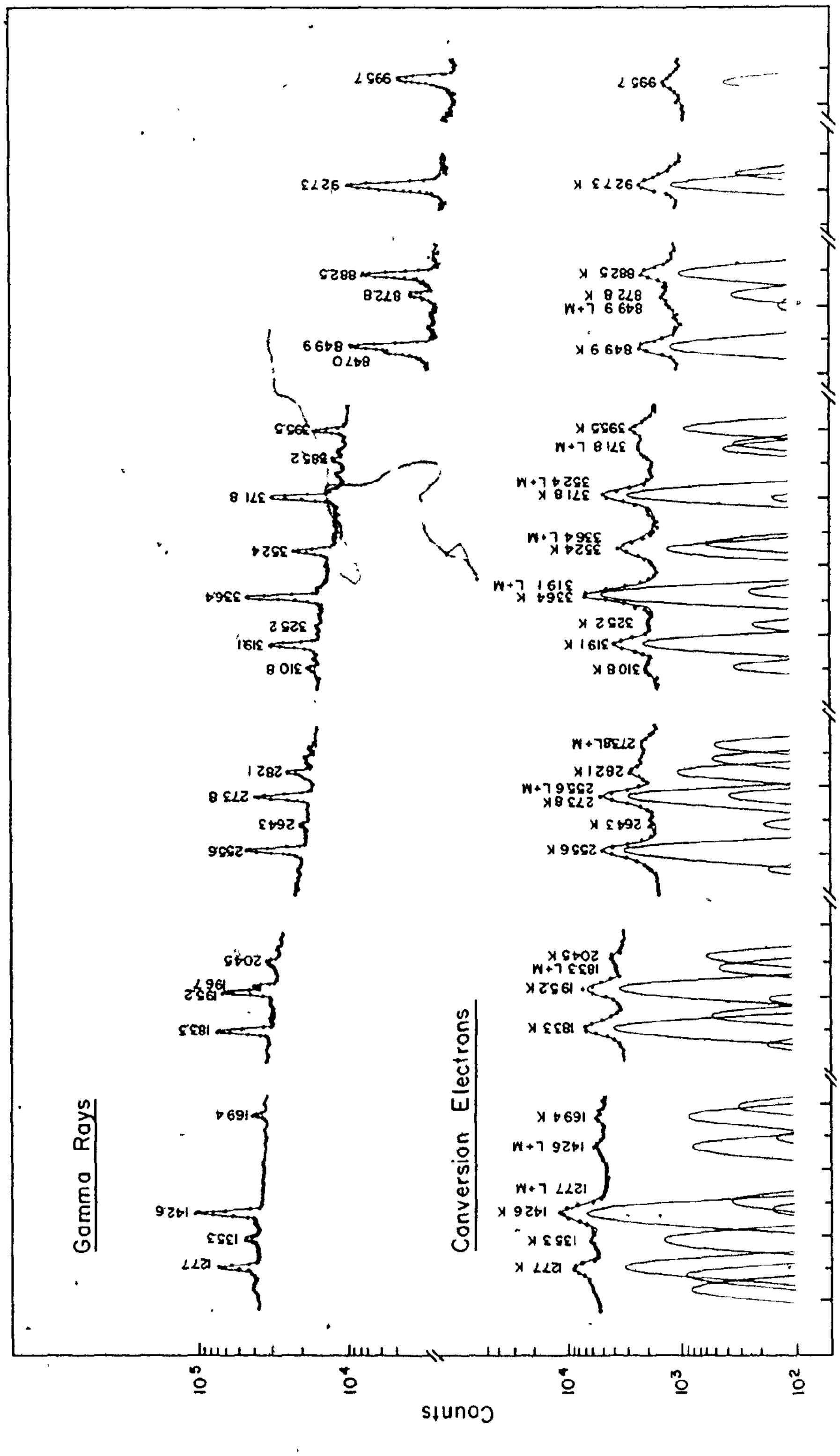
Gamma Rays
127.7
135.3
142.6
169.4
183.3
195.2
196.7
204.5
255.6
264.3
273.8
282.1
310.8
319.1
325.2
336.4
352.4
371.8
385.2
395.5
847.0
849.9
872.8
882.5
927.3
995.7
Conversion Electrons
127.7 K
135.3 K
142.6 K
127.7 L+M
142.6 L+M
169.4 K
183.3 K
195.2 K
183.3 L+M
204.5 K
255.6 K
264.3 K
273.8 K
255.6 L+M
282.1 K
273.8 L+M
310.8 K
319.1 K
325.2 K
336.4 K
319.1 L+M
352.4 K
336.4 L+M
371.8 K
352.4 L+M
371.8 L+M
395.5 K
849.9 K
849.9 L+M
872.8 K
882.5 K
927.3 K
995.7
Counts
10^5
10^4
10^4
10^3
10^2
1100
1200
1300
1400
1500
1600
1800
1900
2100
2200
2300
2400
4100
4200
4400
4600
Bρ (Gauss-cm)

Figure 4.15

A comparison of the gamma-ray and electron spectra of ^{96}Tc for selected momentum regions obtained at 14 MeV.

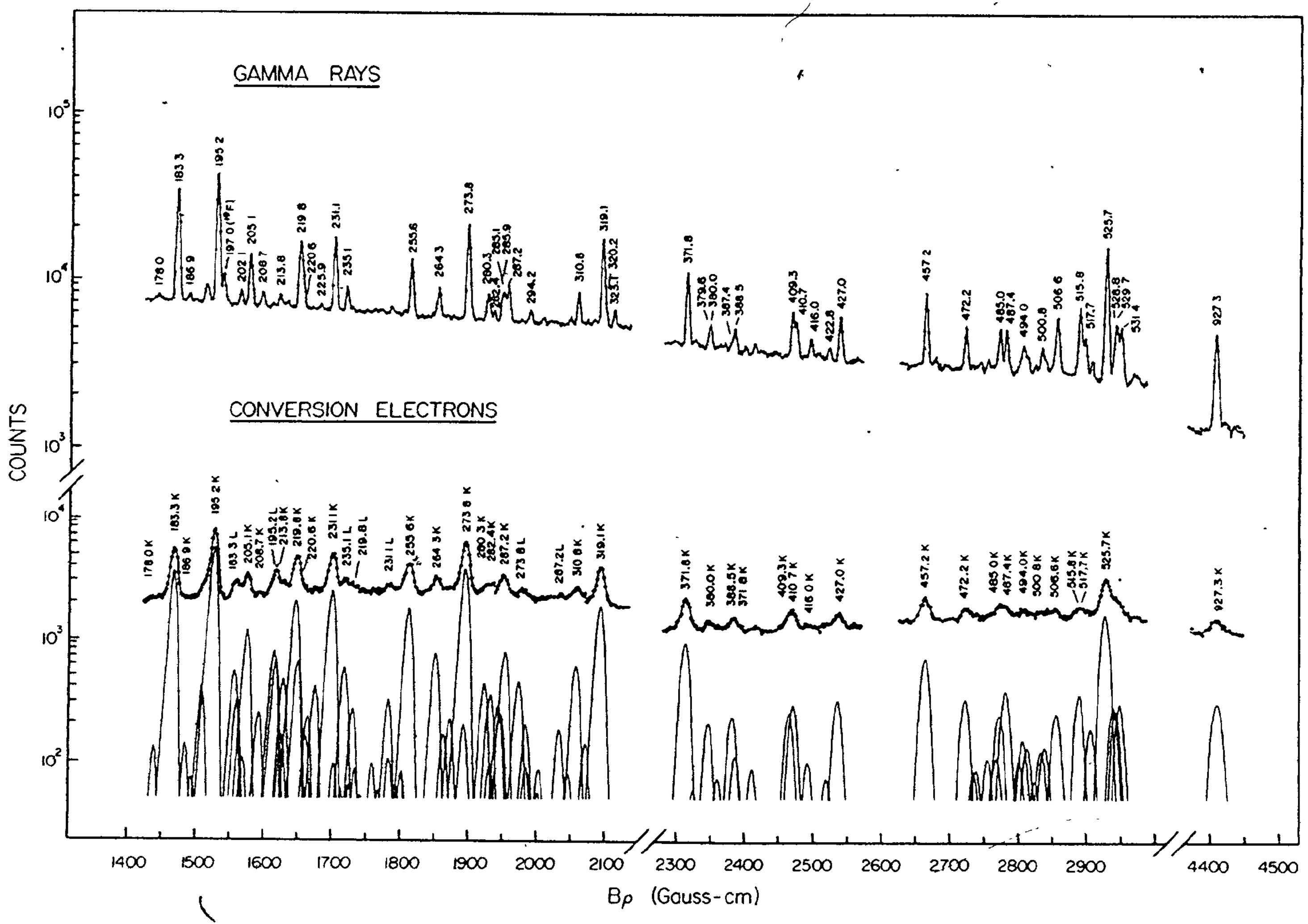
GAMMA RAYS
178.0
183.3
186.9
195.2
197.0 (19F)
202.1
205.1
208.7
213.8
219.8
220.6
225.9
231.1
235.1
255.6
264.3
273.8
280.3
282.4
283.1
285.9
287.2
294.2
310.6
319.1
320.2
325.1
371.8
379.6
380.0
387.4
388.5
409.3
410.7
416.0
422.8
427.0
457.2
472.2
485.0
487.4
494.0
500.8
506.6
515.8
517.7
525.7
528.8
529.7
531.4
927.3
CONVERSION ELECTRONS
178.0 K
183.3 K
186.9 K
195.2 K
183.3 L
205.1 K
208.7 K
195.2 L
213.8 K
219.8 K
220.6 K
231.1 K
235.1 L
219.8 L
231.1 L
255.6 K
264.3 K
273.8 K
280.3 K
282.4 K
287.2 K
273.8 L
287.2 L
310.6 K
319.1 K
371.8 K
380.0 K
388.5 K
371.8 K
409.3 K
410.7 K
416.0 K
427.0 K
457.2 K
472.2 K
485.0 K
487.4 K
494.0 K
500.8 K
506.6 K
515.8 K
517.7 K
525.7 K
927.3 K
COUNTS
10^5
10^4
10^3
10^4
10^3
10^2
1400
1500
1600
1700
1800
1900
2000
2100
2300
2400
2500
2600
2700
2800
2900
4400
4500
Bρ (Gauss-cm)

The electron data was analysed with the computer program ANABEL which provided a more sophisticated peak fitting tool than that used by earlier workers in this laboratory. A general description of ANABEL is given next. In this program the momenta of the weaker peaks in the region are fixed with respect to the stronger ones. In the first stage of analysis, the peak shape parameters were established setting narrow windows around selected strong peak and fitting the data to the function [4-2] . The peak shape was assumed to be skewed Gaussian with constant width and tailing parameters across each window. For the 18 MeV experiment with poorer resolution, the parameters changed so slowly that this assumption was valid even for wide windows. In the 14 MeV experiment with better resolution, δ was required to change smoothly across a window, using the linear relationship existing between $1/\delta$ and $B\rho$ determined from the strong peaks (see Fig. 4.13 D). After the dependence of δ on momentum had been established the data was refitted to determine the parameter ε. For practical purposes , ε was found to be independent of momentum.

With the δ and ε parameters known, the spectrum was divided into wider windows with clearly defined background regions at each end and the peak fitting analysis carried out. After the multipolarity and mixing ratio of a strong peak was determined through a combination of its angular distribution and electron intensity, K/L and K/M were estimated and used to define the intensities of each L and M peaks relative to its K peak in the fitting process. The analysis was then repeated, with both the momenta and intensities of these L and M peaks fixed with respect to the strong K peak. Whereas the earlier program, which had fixed the positions of all

Figure 4.16

The experimental K-conversion coefficients for ^{96}Tc compared with theoretical conversion coefficients for E1, M1, E2, and M2 multipoles (after Hager and Seltzer, 1968).

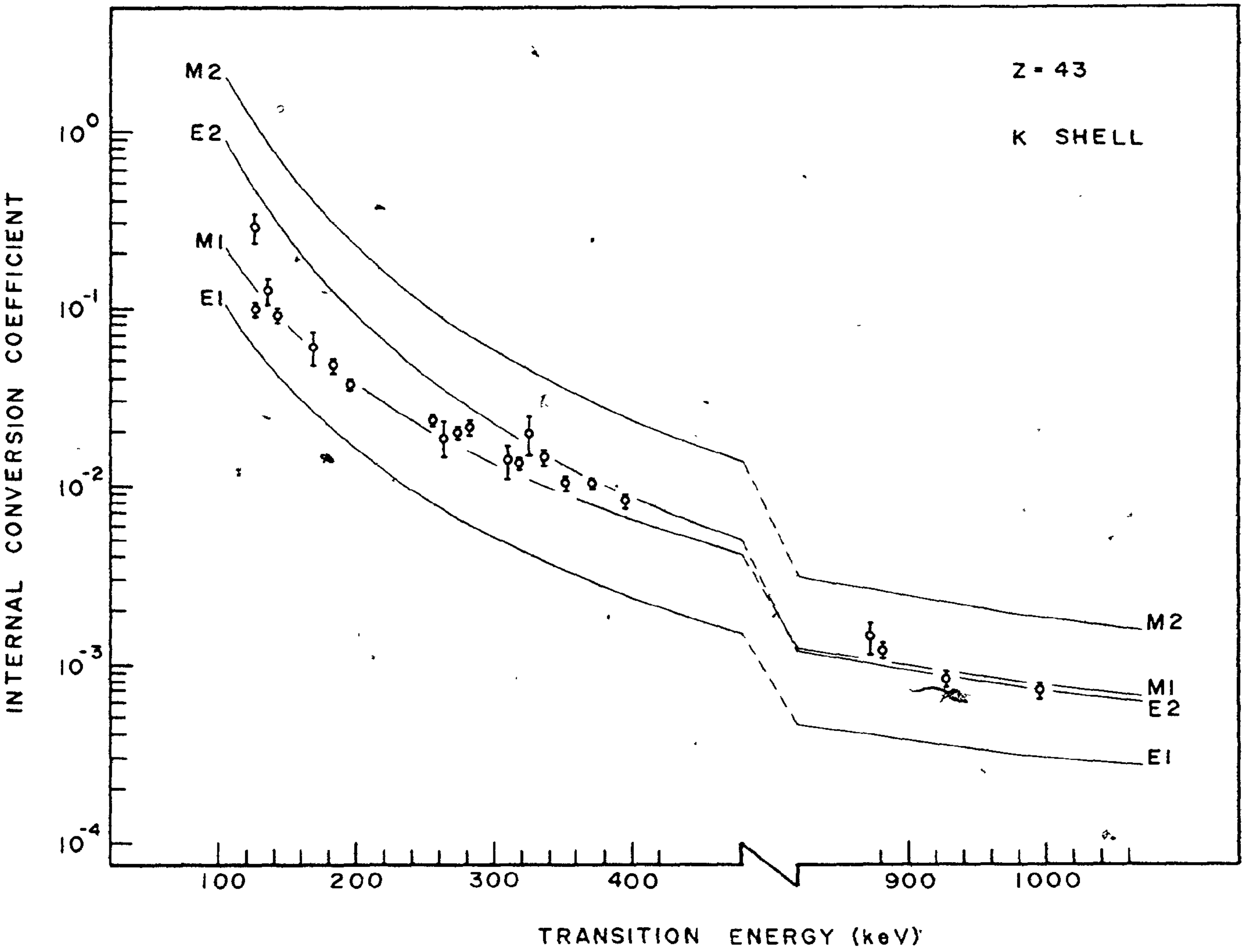
Z = 43
K SHELL
M2
E2
M1
E1
M2
M1
E2
E1
10^{0}
10^{-1}
10^{-2}
10^{-3}
10^{-4}
INTERNAL CONVERSION COEFFICIENT
100
200
300
400
900
1000
TRANSITION ENERGY (keV)

the peaks tended to fail on complex spectra, ANABEL consistently provides reduced χ^2 values near unity, even for very complex spectra.

The electron intensity e is related to the peak area A by:

$$e = \frac{A}{\varepsilon \cdot B\rho} \qquad [4\text{-}17]$$

where ε is the efficiency of the system. The effect of dividing by Bρ is to correct for the fact that the instrumental line width is proportional to Bρ .

Normalization between the photon and electron intensity scales was provided through the 927 and 995 keV transitions which angular distribution and linear polarization indicate that they are stretched E2 in character. Since the theoretical α_K versus energy curves for M1 and E2 transitions cross at ∿700 keV and are only slightly separated up to 1 MeV (see Fig. 4.16), these transitions would provide a calibration insensitive to the degree of M1/E2 mixing even if they were of M1+E2 character.

The coefficients determined for strong peaks in these experiments can be trusted to ∿10% , if one ignores systematic errors. For the six gap measurements anisotropy in the conversion electron emission coupled with the characteristics of the "orange" type spectrometer can cause the electron intensity for pure E1 or E2 transitions to be increased by ∿10% relative to those for pure M1 transitions. In the one-gap geometry errors due to anisotropy are estimated to be about half as great. These estimates were derived using the theoretical results of Hager and Seltzer (1968) .

CHAPTER 5

EXPERIMENTAL RESULTS

5.1 Introduction

A number of workers have contributed to the knowledge of low spin states in ^{96}Tc. Information concerning the ground state and the 34.4 keV isomer in ^{96}Tc was first found from decay studies. These results, which have been summarized by Medsker (1972) form a starting point for all the reaction work that has followed.

^{96}Tc has been extensively investigated by the (p,n) reaction which preferentially populates low-spin states. As a result of the work of Doukellis et al. (1974), Kern et al. (1978), and Miracle et al. (1979) a fairly rich level structure for the ^{96}Tc low-spin states up to 1200 keV has been established. Their results have in general been confirmed by the (d,2n) experiments of Madueme and Arita (1978). In addition to these, this nucleus has been studied by Emigh et al. (1979) through the (^{3}He,d) reaction and by Bini et al. (1976) using the (α,n) reaction with alphas in the 10-14 MeV energy range.

Whereas there is a general agreement among these workers on the excitation energies of the low-lying levels, there is poor agreement on to spin and parity assignments.

Doukellis et al. gave spin and parity assignments to a number of levels based on the neutron enhancement and angular distributions observed on and off resonance of the $^5/_2{}^+$ isobaric analog state in ^{97}Tc. Their results however were handicapped by heavy dependence on theoretical calculations as well as on the arbitrary normalization of the data to the spin and parity assignments assumed for the four lowest energy levels observed in ^{96}Tc.

The spin assignments attempted by Madueme and Arita were not well supported by the experimental evidence. They relied heavily on unconvincing excitation functions and electron conversion measurements and made inconsistent use of Doukellis et al's work.

Miracle et al. obtained internal conversion coefficients for a number of transitions, which led to different spin and parity assignments to those of Madueme and Arita.

The (α,n) work of Bini et al. included only excitation functions and gamma-gamma coincidence measurements with rather poor statistics. Although relatively incomplete, their work is supported by the present experiments. In summary, previous work on ^{96}Tc is neither complete nor selfconsistent.

The (α,n) study reported in this thesis gives a quite different level structure with different spin assignments to many of the previously known states. Because this reaction populates a large number of states not observed in the (p,n) or (d,2n) reactions, the present work records a large number of new transitions and many new levels. These levels are connected by intense gamma-ray cascades which have made it possible to arrive at a unique and self consistent level scheme, which does not contradict the data of earlier workers.

Complete series of experiments were performed at both 14 and 18 MeV. These experiments complemented each other, the lower and higher energies favouring the excitation of low-spin and high-spin states respectively. With the 14 MeV alpha beam, a rich structure of states of low and intermediate spin is excited, including most of those observed in the proton and deuteron work. Whereas in previous work, two separate level structures were observed, one directly connected to the ground state, and the other to the isomer, the (α,n) reaction populates a number of intermediate levels, which cascade to both the ground state and the isomer. This fact led to a good deal of new information. Morever the 14 MeV gamma-ray spectrum is almost entirely due to ^{96}Tc, since no lines from ^{95}Tc and ^{95}Mo are excited.

When the beam is raised to 18 MeV, the spectra are dominated by transitions from the high-spin states extending to 3 MeV with relatively weak transitions feeding the states excited at 14 MeV. None of these levels have been previously observed. The 18 MeV spectra are contaminated by ^{95}Tc and ^{95}Mo lines.

The results of these experiments are summarized in Tables 5.1, and 5.5 . Table 5.1 presents information concerning photon energies, intensities,classifications,angular distribution coefficients and multipole assignments for all of the transitions attributed to ^{96}Tc. Table 5.5 presents the results of the linear polarization and internal conversion coefficients measurements (both our own and those of other workers) which support the assignments made in Table 5.1 . Detailed reference to these tables will be made in subsequent sections.

5.2 Gamma-Ray Energies and Intensities

The first column of Table 5.1 presents the transition energies derived from the 14 MeV data with the experimental uncertainties shown in parenthesis. The 18 MeV measurements gave similar results, but since the data was slightly less accurate and since many of the transitions were only observed at 14 MeV, the 18 MeV data has not been used. For the fifty or so gamma-rays identified by other workers, the agreement between their measurements and those presented in this thesis is very good. Column 6 presents photon intensities measured at 18 MeV (coded d) and 14 MeV respectively. All intensities were normalized to 100 for the strong 525 keV transition.

5.3 The Excitation Functions

The excitation functions in conjunction with the neutron-gamma experiment served to separate the ^{96}Tc transitions from the impurity lines from ^{93}Nb, ^{95}Mo, ^{96}Mo and ^{95}Tc. These functions are characterized by a broad peak whose peak position exhibits strong spin dependence. They played an important role both in the construction of the decay scheme and in spin assignments.

Fig. 5.1 presents a number of characteristic excitation functions for transitions in ^{96}Tc and ^{95}Tc obtained in the first set of measurements. Quadrants 1, 2, and 3 show the characteristic downward shift in the peak of the excitation function as one looks at transitions from initial states of lower and lower spin. Functions for most of the prominent transitions of interest observed in the 18 MeV studies are shown in these three quadrants. The fourth quadrant presents a characteristic excitation function

Figure 5.1

Excitation functions for the transitions deexciting high spin states in ^{96}Tc as determined in the first set of measurements. The yields are expressed in terms of photons per micro-coulomb of charge collected. For clarity of presentation, the yields for different gamma-rays have been arbitrarily adjusted on the vertical axis.

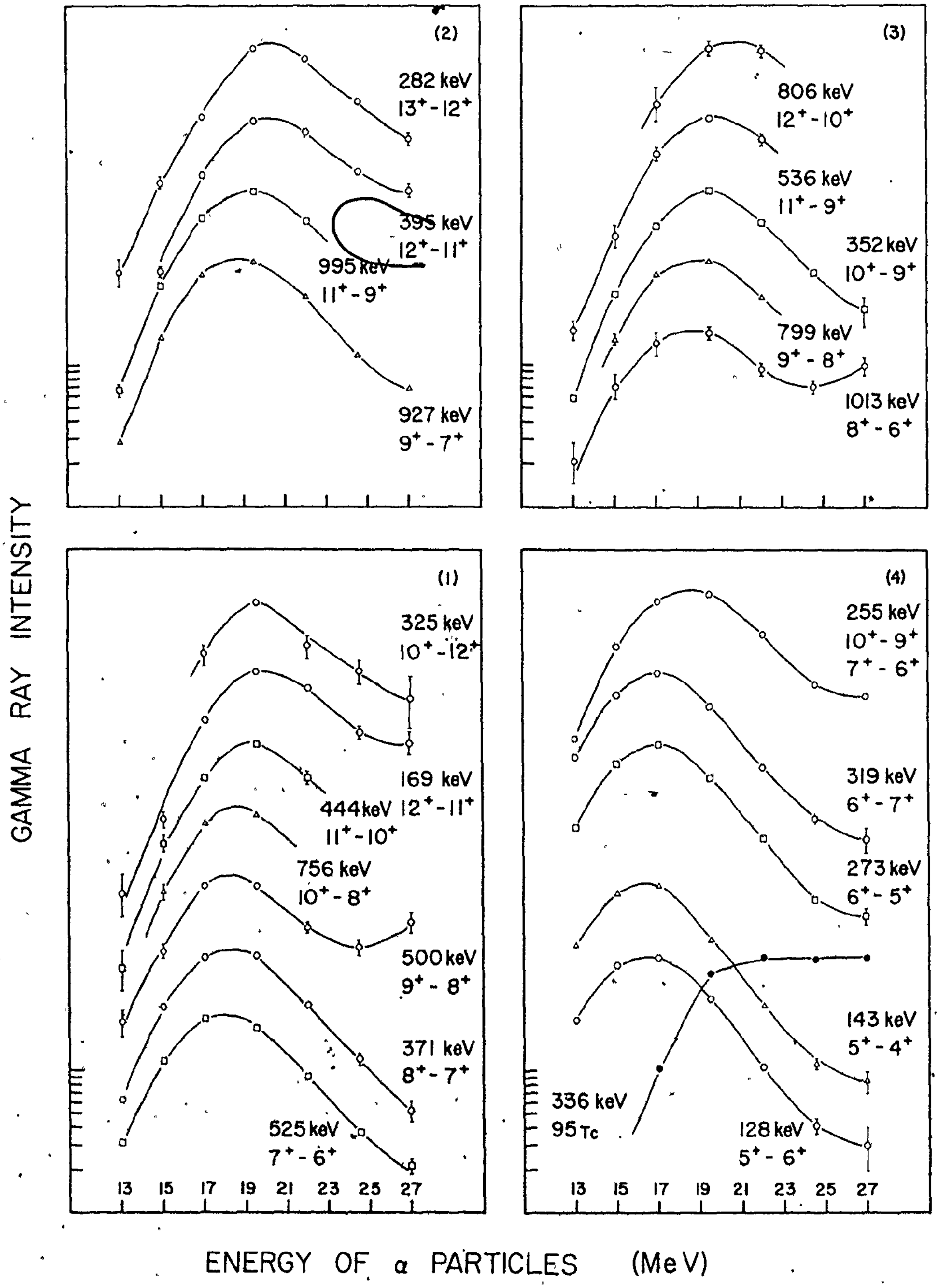
(2)
282 keV
13+-12+
395 keV
12+-11+
995 keV
11+-9+
927 keV
9+-7+
(3)
806 keV
12+-10+
536 keV
11+-9+
352 keV
10+-9+
799 keV
9+-8+
1013 keV
8+-6+
(1)
325 keV
10+-12+
169 keV
12+-11+
444keV
11+-10+
756 keV
10+-8+
500keV
9+-8+
371 keV
8+-7+
525keV
7+-6+
(4)
255 keV
10+-9+
7+-6+
319 keV
6+-7+
273 keV
6+-5+
143 keV
5+-4+
336 keV
95Tc
128 keV
5+-6+
13 15 17 19 21 23 25 27
13 15 17 19 21 23 25 27
GAMMA RAY INTENSITY
ENERGY OF α PARTICLES (MeV)

Figure 5.2

Quadrants one, two and three present excitation functions for transitions deexciting low and medium spin states in ^{96}Tc as obtained in the second set of measurements. The fourth quadrant presents the relationship between the spin of the initial state and the beam energy corresponding to maximum excitation yield for a wide range of spins. The experimental points fit rather well a smooth curve, except for states with J_i=7 or 8.

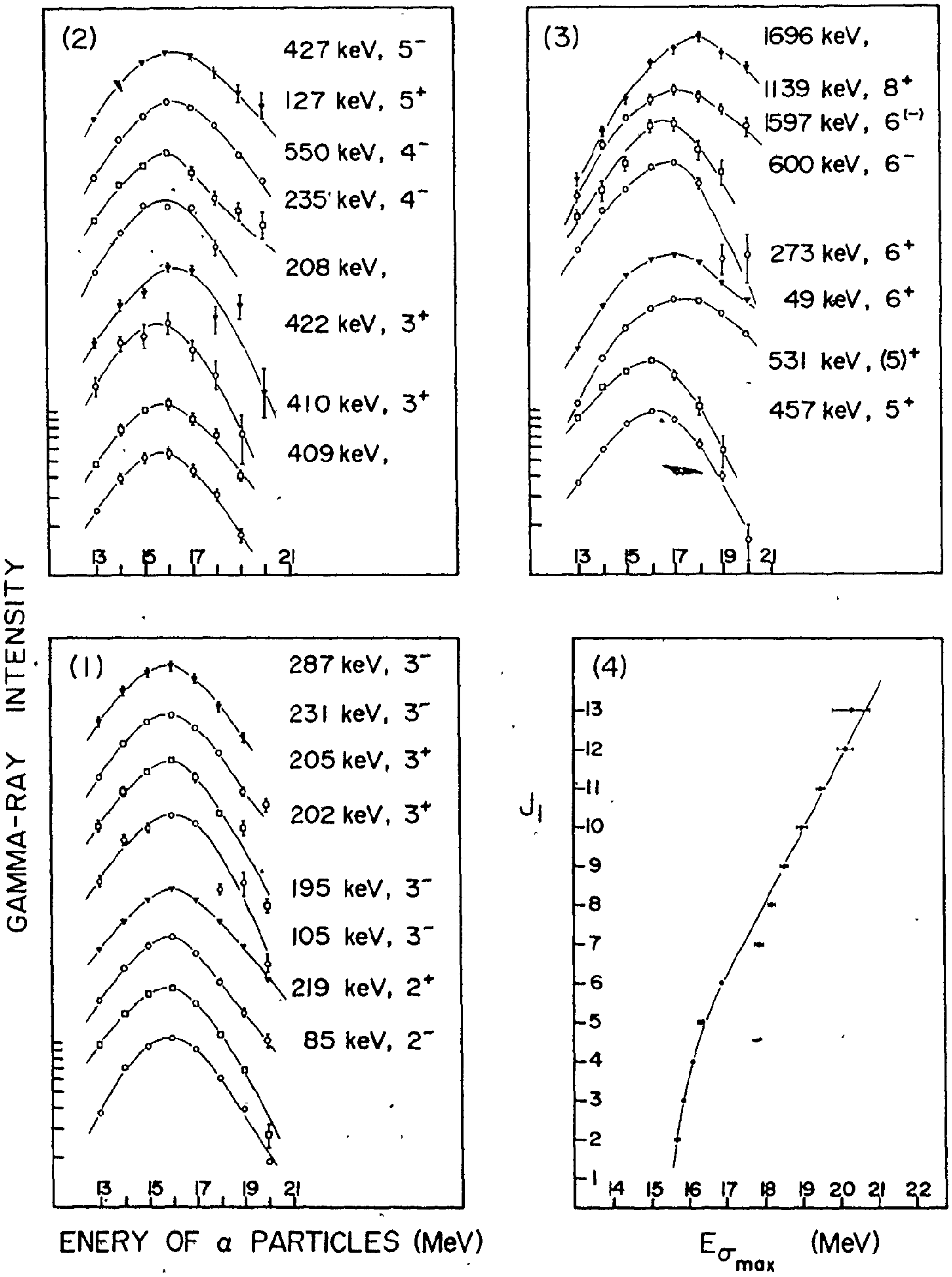
(2)
427 keV, 5⁻
127 keV, 5⁺
550 keV, 4⁻
235 keV, 4⁻
208 keV,
422 keV, 3⁺
410 keV, 3⁺
409 keV,
13 15 17 21
(3)
1696 keV,
1139 keV, 8⁺
1597 keV, 6⁽⁻⁾
600 keV, 6⁻
273 keV, 6⁺
49 keV, 6⁺
531 keV, (5)⁺
457 keV, 5⁺
13 15 17 19 21
GAMMA-RAY INTENSITY
(1)
287 keV, 3⁻
231 keV, 3⁻
205 keV, 3⁺
202 keV, 3⁺
195 keV, 3⁻
105 keV, 3⁻
219 keV, 2⁺
85 keV, 2⁻
13 15 17 19 21
ENERY OF α PARTICLES (MeV)
(4)
J₁
1 2 3 4 5 6 7 8 9 10 11 12 13
14 15 16 17 18 19 20 21 22
Eσmax (MeV)

for ^{95}Tc, functions for transitions between states of medium spin and the functions for the 255 keV doublet, which contains both a high spin and a medium spin component.

Fig. 5.2 presents the excitation functions obtained in the second sequence of measurements. Quadrants 1, 2, and 3 include a selection of excitation functions of transitions originating from low and medium spin states. The shapes of the functions for more than 200 gamma-rays in the two sequences of experiments were determined. An analysis of these functions shows that they have a full width at half maximum of 5.2 ± 1.0 MeV and that the beam energy corresponding to maximum cross-section varies smoothly and almost linearly with the spin of the initial state in the transition. Column 4 of Table 5.1 presents the beam energy corresponding to maximum cross-section for all the transitions for which excitation functions were determined. The entries in the table are averages deduced from three excitation functions recorded with different detectors.

The correlation between these energies and the spins of the initial state is displayed in Table 5.2 for all the cases where the spin of the initial state could be identified from angular distribution, internal conversion and/or polarization data. The same correlation is presented in the fourth quadrant of figure 5.2 where spin is plotted against the mean value of the excitation energy corresponding to the maximum cross-section. This curve proved very useful in identifying the spins of initial states, particularly in the low and medium spin range, and offering support for spin assignments made by other means for all spin values.

5.4 Gamma-Gamma Coincidence Measurements

Seventy-six of the coincidence spectra obtained in the manner described in 4.6.3 are presented in Fig. 5.3 to 5.8 below. These were chosen from the 14 and 18 MeV spectra recorded using a large and a small detector operating in coincidence, and possessing moderate and very good resolution respectively. The spectra chosen for presentation are sufficient to determine the decay scheme. In order to assist the reader, Table 5.3 may be used as a guide to locate the figure in which each spectrum may be found.

The data of Fig. 5.3 has already been published (Mach et al.1980). Its 13 spectra include the most important transitions in ^{96}Tc excited at 18 MeV and give evidence for the high spin structures which extend to 3 MeV. The data presented were chosen from more than 120 gates which were analysed. Each of the seven spectra on the left of Fig. 5.3 is associated with a single transition. Evidence that both the 183 and 255 keV gates include closely spaced doublets is presented at the right of Fig. 5.3 .

The sequence of figures from 5.4 to 5.8 presents 63 coincidence spectra chosen from 160 different gates in the 14 MeV experiment. The energies of the peaks and their associated errors are labelled on the figures. These coincidence spectra were recorded and analysed in 4096 channels. However, except for the very complex 49 and 85 keV gates, the spectra have been compressed into 2048 channels for the purposes of presentation. Because the Compton back-scatter peaks make it very difficult to determine the background in the 200 keV region,the background subtraction process used often introduced spurious but very characteristic positive and negative spikes in the coincidence spectra. In the interest of clarity, a number of these have been "smoothed out" in the spectra presented.

Because the coincidence experiments matched a high-resolution, low efficiency detector with a moderate resolution, high efficiency detector, it was useful to compare the spectra associated with a given gamma-ray as recorded in each of the two detectors. By gating on the high resolution detector, it was often possible to effectively separate the coincidence spectra associated with each member of a close doublet. The 515, 517 keV and the 285, 287 keV gates of Fig. 5.6 and 5.8 respectively illustrate this point. On the other hand, by gating on the high efficiency-poor resolution detector, one could maximize the intensity of the combined coincidence spectrum, as illustrated in the 515+517 keV and 285+287 keV gates of the same figures.

Fig. 5.4 and 5.5 present coincidence spectra for transitions connecting the high spin states observed first at 18 MeV and states of intermediate spin which were only strongly excited at 14 MeV. Because the 14 MeV data had better statistics and the reaction strength was distributed over many more decay chains, this data confirmed nearly all of the 18 MeV results and, in addition, led to the identification of many new levels not observed in the earlier experiments.

The 255, 273, 371 and 525 keV spectra of Fig. 5.3, taken at 18 MeV, are to be compared with those of the same energy in Fig. 5.4 . The assumption that the 255 keV includes a doublet, made on the basis of the 18 MeV results is clearly confirmed in the 14 MeV data. While the 273 keV gate at 18 MeV appeared to contain a single gamma-ray, the data of Fig. 5.4 shows clearly that a 274 keV transition is also excited at 14 MeV. The 310, 799 and 319-320 keV gates of Fig. 5.4 identify three additional close doublets. Further evidence for these doublets is presented in the 85, 231 and 550 keV spectra of Fig. 5.6 and 5.7 . Finally, the simple 720 keV spectrum of Fig. 5.4 establishes the existance of the 1041 keV state.

Fig. 5.5 presents evidence for a large number of levels which were not observed either in our 18 MeV experiment or in the (p,n) experiments of earlier workers. Most of the peaks in the spectra of Fig. 5.5 are associated with gamma-rays feeding the three states at 49.3, 177.0 and 506.0 keV. The excitation energies of these three levels and of the important 34.4 keV state with respect to the ground state were established from the singles energies, on the basis of the 49, 127, 142 and 457 keV gated spectra . The 49 keV spectrum is to be compared with the 49 keV gated spectrum taken at 18 MeV and presented in Fig. 5.3 . To aid the reader who wishes to study this evidence in detail, the partial level structure of Fig. 5.5 is presented in enlarged version in Fig. 5.5A . Similar enlargements of partial level structures occur in Fig. 5.6A and 5.7A .

In our earlier publication (Mach et al. 1980) , it was suggested that in addition to the pair of levels at 34 and 35 keV, there might be a pair at 45 keV. This question is clearly resolved by the data presented in Fig. 5.5, 5.6 and 5.7 . It will be shown that there is only one level at 45 keV but there is a new level at 36.4 to make a 34.4, 35.6, 36.4 keV triplet.

In our earlier work, it was assumed that the 85 and 86 keV doublet fed the 35 and 34 keV states respectively. Following this assumption, the 18 MeV data then established a 235-195-85 keV cascade to define a level at 549.9 keV,(see Fig. 5.6). This level was deexcited via a 323-183 keV cascade to locate levels at 227.0 and 43.8 keV respectively. The question as to whether the proposed 43.8 keV state was the same level as the 45.3 keV level defined by the 255-273 and 255-319 keV cascades could not be resolved.

The discovery of the 52.0 keV transition in the 14 MeV experiment and the strong coincidence evidence for 52-127, 52-142 and 52-264 keV cascades solidly established the energy of the previously identified 227.0 keV state as 228.8 keV (see Fig. 5.5 and 5.5A) , changed the energy of the proposed 43.8 keV level to 45.5 keV and removed the necessity for a 45 keV doublet. Support for these conclusions is provided by the 264 keV gates of Fig. 5.6 which show that the 264 keV transition is in coincidence with the 183 keV gamma-ray and that the latter deexcites the 228.8 keV level.

A reinterpretation of the 18 MeV data, confirmed by the 14 MeV results for the 323 keV gates of Fig. 5.6 leads naturally to a state at 552.0 keV and, via the 235-195 cascade, to the 121.6 keV level (see the 235 and 195 keV gates of Fig. 5.6). In this new picture, the 85.9 keV gamma-ray feeds the 35.6 keV state and the 85.1 keV transition defines a new level at 36.4 keV. Support for the 36.4 keV level is supplied by the pair of gamma-rays of energy 515.8 and 517.7 keV which feed the 36.4 and 34.4 keV levels respectively. These gamma-rays are both in coincidence with the 427 and 600 keV transitions which feed the 552.0 keV level, as is seen in the 515, 517, 515+517, 427 and 600 keV gates of Fig. 5.6 .

The remaining gates at the right of Fig.5.6 identify a number of levels feeding the 316 keV state. In the same way, the 427 keV gamma-ray locates transitions deexciting the 552.0 keV level. The 506 keV gate shows that the 506 keV radiation is really a triplet with one component feeding the 227.4 keV state, one the 121.6 keV level and one the 45.3 keV level.

Fig. 5.7 presents the rich spectrum associated with the 85 keV gate. The strongest lines feeding the 121.6 keV level are those of energy 105, 195 and 231 keV. The spectra in coincidence with the 105 and 231 keV transitions appear in Fig. 5.7 while the 195 keV gated spectrum is found in Fig. 5.6. To aid the reader, transitions feeding the 195-85 keV cascade are indicated by a dot over the peak label in the 85 keV coincidence spectrum. These transitions and the levels associated with them are shown only in symbolic form in Fig. 5.7, the complete structure built on the 316 keV state having already been presented in Fig. 5.6. These three gates, together with the reverse gates also found in Fig. 5.7 support the right hand half of the array of levels in Fig. 5.7A.

The 380, 588, 612 and 912 keV peaks are all doublets. One member of each doublet appears in the structure discussed in the last paragraph; the other fits into the pattern shown at the extreme left of Fig. 5.7A. Further evidence for the doublet character of the 588 and 612 keV peaks appears in the 285 and 287 keV gates of Fig. 5.8 .

Because transitions deexciting the states up to 45.3 keV are unobservable, the construction of the level scheme based on these states has been carried out by combining the present energy measurements and the (p,n) threshold measurements of Doukellis et al. (1974). The following table presents the energy separations of a number of the doublets seen in this and earlier works together with the final state excitations deduced from (p,n) thresholds. These separations are to be compared with the values of 0.8 and 2.0 keV for the spacing of the 35.6-36.4 and 34.4-36.4 members of the 35 keV triplet. This comparison provides strong evidence for states at 256.2 and 321.6 keV. It also confirms the location of the 121.6,316.8 and 552.0

Doublet (keV)	Separation ΔE (keV)	Final State Excitation from (p,n) (keV)	Initial State Energy Deduced from present work (keV)
85 - 86	0.81 ± 0.05	34 ± 2	121.6
219 - 220	0.82 ± 0.07	35 ± 3	256.2
280 - 282	2.00 ± 0.20		316.8
285 - 286	0.81 ± 0.10	34 ± 3	321.6
285 - 287	2.08 ± 0.08		
515 - 517	1.91 ± 0.11		552.0
205.1 ± 0.1		35 ± 5	239.5

keV states already discussed.

The coincidence data of Fig. 5.8 provides support for the array of levels based on the 256.2, 321.6 and 239.5 keV states. The 65 keV peak in the 220 keV gated spectrum provides a strong link between the 256.2 and 321.6 keV states. However, the 65 keV gate shows that the situation is somewhat more complex than that indicated in the level structure of Fig. 5.8. The weak 85, 105 and 195 keV peaks in this spectrum cannot be explained without assuming that one (most probably the 65 keV line) or more of the transitions are doublet. However, the coincidence data is too poor to justify extension of the level structure beyond that shown. Similarly, it is difficult to explain the weak 49 keV peaks in the 208 and 346 keV gates without involving additional, albeit very weak ~208 and ~346 keV transitions lying high up in the decay scheme.

From the evidence in the table, the 205 keV transition could feed any one of the triplet states. The 34.4 keV choice, with consequent location of the initial state at 239.5 keV is based on three independent lines of argument, none of which is as strong as one would like. The first involves the ascending 85-195-269 keV and the descending 346-205 keV chains which start at 36.4 keV and ends on the 34.6 keV levels. Unfortunately, although 85-269 coincidences have been observed, the decrease in detector efficiency with photon energy resulted in failure to observe 195-269 keV coincidences. Thus one stage in the loop has been based on energy alone. The second, involving the 45-577 keV ascending sequence and the 383-205 keV descending sequence, suffers from the same weakness, since no 45-577 coincidences have been observed. The third, more circuitous argument, proceeds as follows. The 205 keV transition is known to be ΔJ=±1 from its angular distribution and the excitation functions suggest that it deexcites a J=3 state. Thus the final state must be J=2 or 4, which would permit either the 34.4 or 35.6 keV choice (see Fig. 5.12). Since in this decay scheme, nearly every transition which feeds the 35.6 keV level feeds the 36.4 keV state much more strongly, the absence of a stronger 204.3 keV transition favors the 34.4 keV option.

The level structures proposed have been tested for consistency by comparing the measured coincidence probabilities with those expected from the proposed level scheme. In general, these agree within ∿30% . In a few cases, levels have been included for which the measured coincidence probability is less than the predicted one by significantly more than this 30% figure. Although these levels have not been especially indicated in the level

Figure 5.3

Coincidence spectra recorded in the 17% Ge(Li) detector for a selection of gates set-up on the 10cc Ge detector. The spectra are chosen to illustrate the quality of the data for the high-lying, high-spin states observed in the 18 MeV experiment.

Figure 5.3

Coincidence spectra recorded in the 17% Ge(Li) detector for a selection of gates set-up on the 10cc Ge detector. The spectra are chosen to illustrate the quality of the data for the high-lying, high-spin states observed in the 18 MeV experiment.

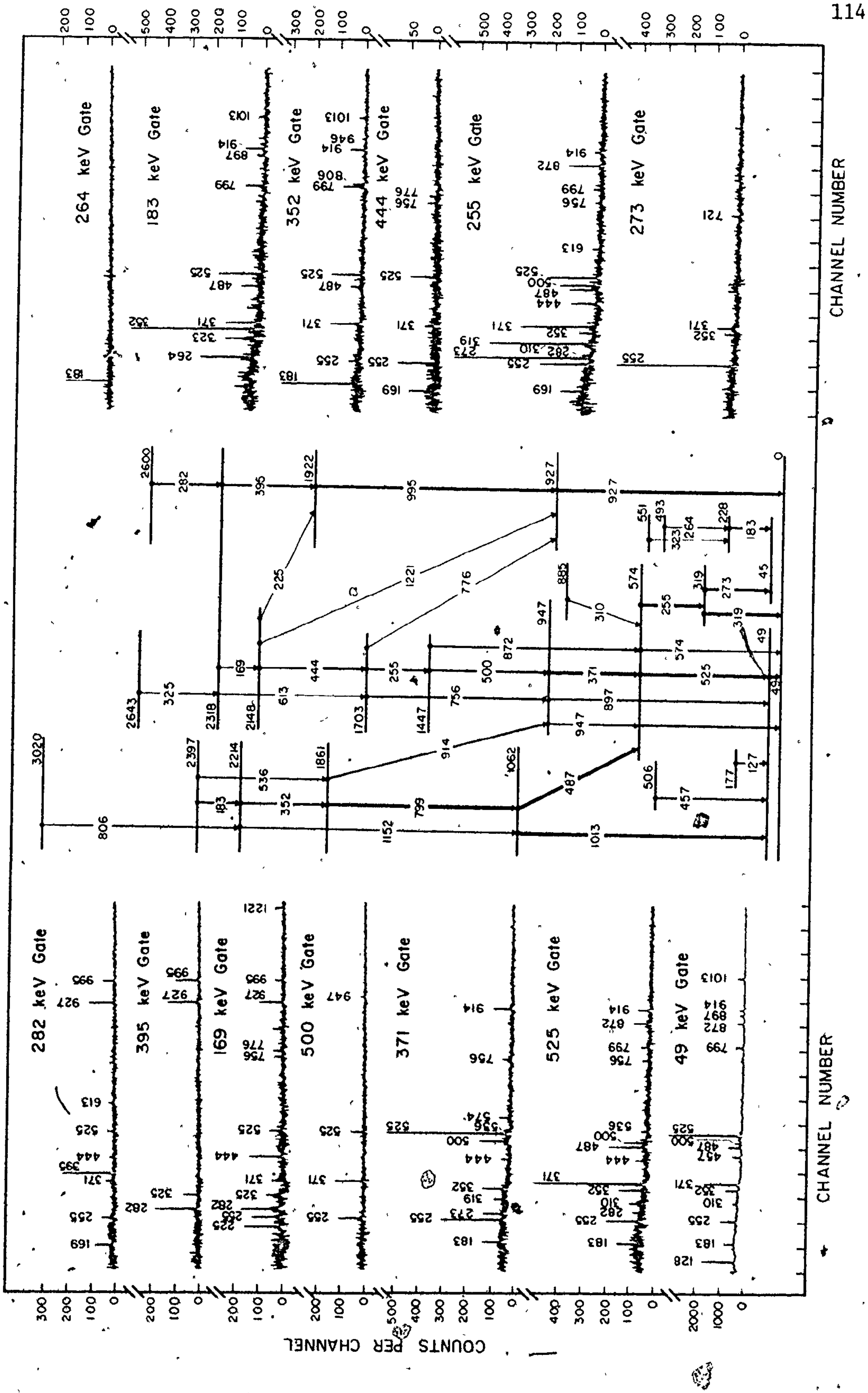
264 keV Gate
183 keV Gate
352 keV Gate
444 keV Gate
255 keV Gate
273 keV Gate
282 keV Gate
395 keV Gate
169 keV Gate
500 keV Gate
371 keV Gate
525 keV Gate
49 keV Gate
CHANNEL NUMBER
CHANNEL NUMBER
COUNTS PER CHANNEL
3020
2643
2600
2397
2318
2214
2148
1922
1861
1703
1447
1062
947
927
885
574
551
506
0

Figure 5.4

Coincidence spectra recorded at 14 MeV in the 50cc Ge(Li) detector corresponding to gates set-up on the 9cc Ge detector. The spectra are partially to illustrate the dramatic changes between the coincidence spectra at 14 and 18 MeV for medium spin states. The gates indicated by a dot are "reverse" gates ie: a gate set up on the 50cc detector to record the spectrum in the 9cc detector.

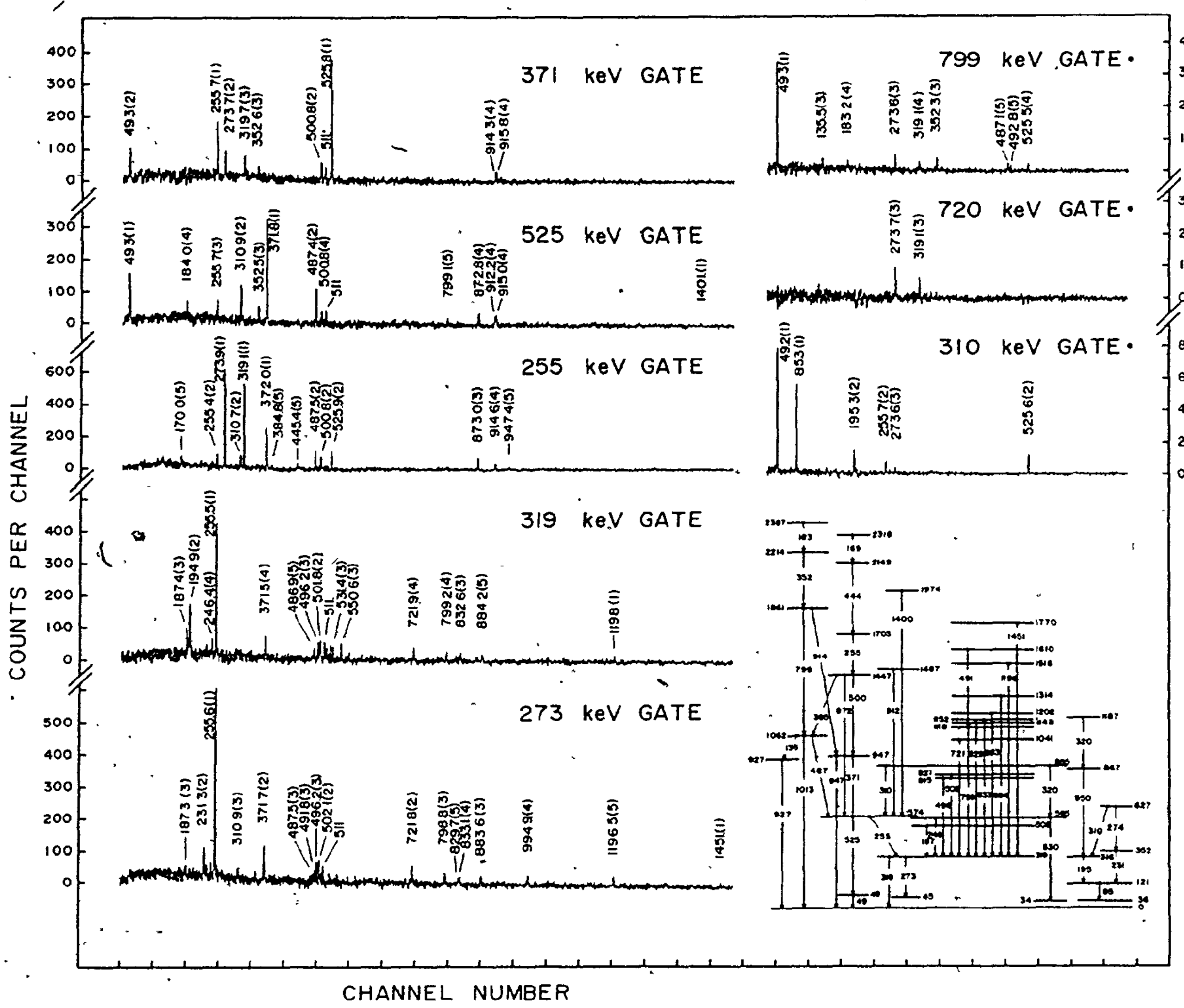
371 keV GATE
493(2)
255.7(1)
273.7(2)
319.7(3)
352.6(3)
500.8(2)
511
525.8(1)
914.3(4)
915.8(4)
525 keV GATE
493(1)
184.0(4)
255.7(3)
310.9(2)
352.5(3)
371.8(1)
487.4(2)
500.8(4)
511
799.1(5)
872.8(4)
912.2(4)
915.0(4)
1401(1)
255 keV GATE
170.0(5)
255.4(2)
273.9(1)
310.7(2)
319.1(1)
372.0(1)
384.8(5)
445.4(5)
487.5(2)
500.8(2)
525.9(2)
873.0(3)
914.6(4)
947.4(5)
319 keV GATE
187.4(3)
194.9(2)
246.4(4)
255.5(1)
371.5(4)
486.9(5)
496.2(3)
501.8(2)
511
531.4(3)
550.6(3)
721.9(4)
799.2(4)
832.6(3)
884.2(5)
1198(1)
273 keV GATE
187.3(3)
231.3(2)
255.6(1)
310.9(3)
371.7(2)
487.5(3)
491.8(3)
496.2(3)
502.1(2)
511
721.8(2)
798.8(3)
829.7(5)
833.1(4)
883.6(3)
994.9(4)
1196.5(5)
1451(1)
799 keV GATE •
493(1)
135.5(3)
183.2(4)
273.6(3)
319.1(4)
352.3(3)
487.1(5)
492.8(5)
525.5(4)
720 keV GATE •
273.7(3)
319.1(3)
310 keV GATE •
492(1)
853(1)
195.3(2)
255.7(2)
273.6(3)
525.6(2)
COUNTS PER CHANNEL
CHANNEL NUMBER
0
100
200
300
400
500
600
800

Figure 5.5

Coincidence spectra for transitions feeding the 49 and 177 keV levels in ^{96}Tc. Although all the coincidence data were recorded in 4k spectra, for ease of presentation, all except the 49 keV gated spectrum have been compressed into 2k channels. Since the 142 and 127 keV gates result in the same coincidence spectrum, the quality of the spectrum above 700 keV available for analysis was improved by combining them.

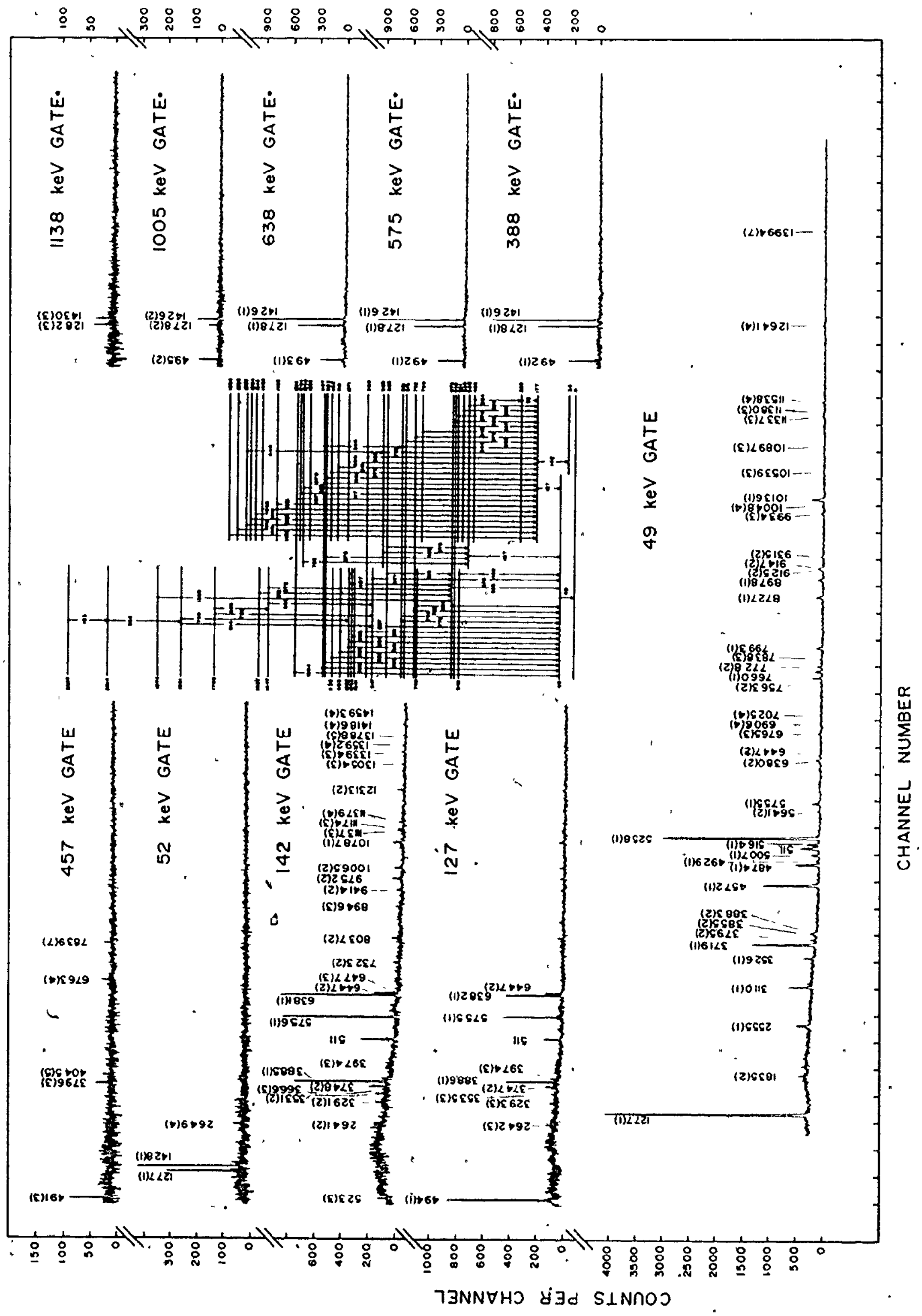
1138 keV GATE*
1005 keV GATE*
638 keV GATE*
575 keV GATE*
388 keV GATE*
457 keV GATE
52 keV GATE
142 keV GATE
127 keV GATE
49 keV GATE
127(1)
183.5(2)
255.5(1)
311.0(1)
352.6(1)
371.9(1)
379.5(2)
385.5(2)
388.3(2)
457.2(1)
487.4(1)
492.9(1)
500.7(1)
511
516.4(1)
525.8(1)
564.1(2)
575.5(1)
638.0(2)
644.7(2)
676.5(3)
690.6(4)
702.5(4)
756.3(2)
766.0(1)
772.8(2)
783.6(3)
799.5(1)
872.7(1)
897.8(1)
912.5(2)
914.7(2)
931.5(2)
993.4(3)
1004.8(4)
1013.6(1)
1053.9(3)
1089.7(3)
1264.1(4)
1399.4(7)
CHANNEL NUMBER
COUNTS PER CHANNEL

Figure 5.5A

An enlarged version of the partial decay scheme of Fig. 5.5 .

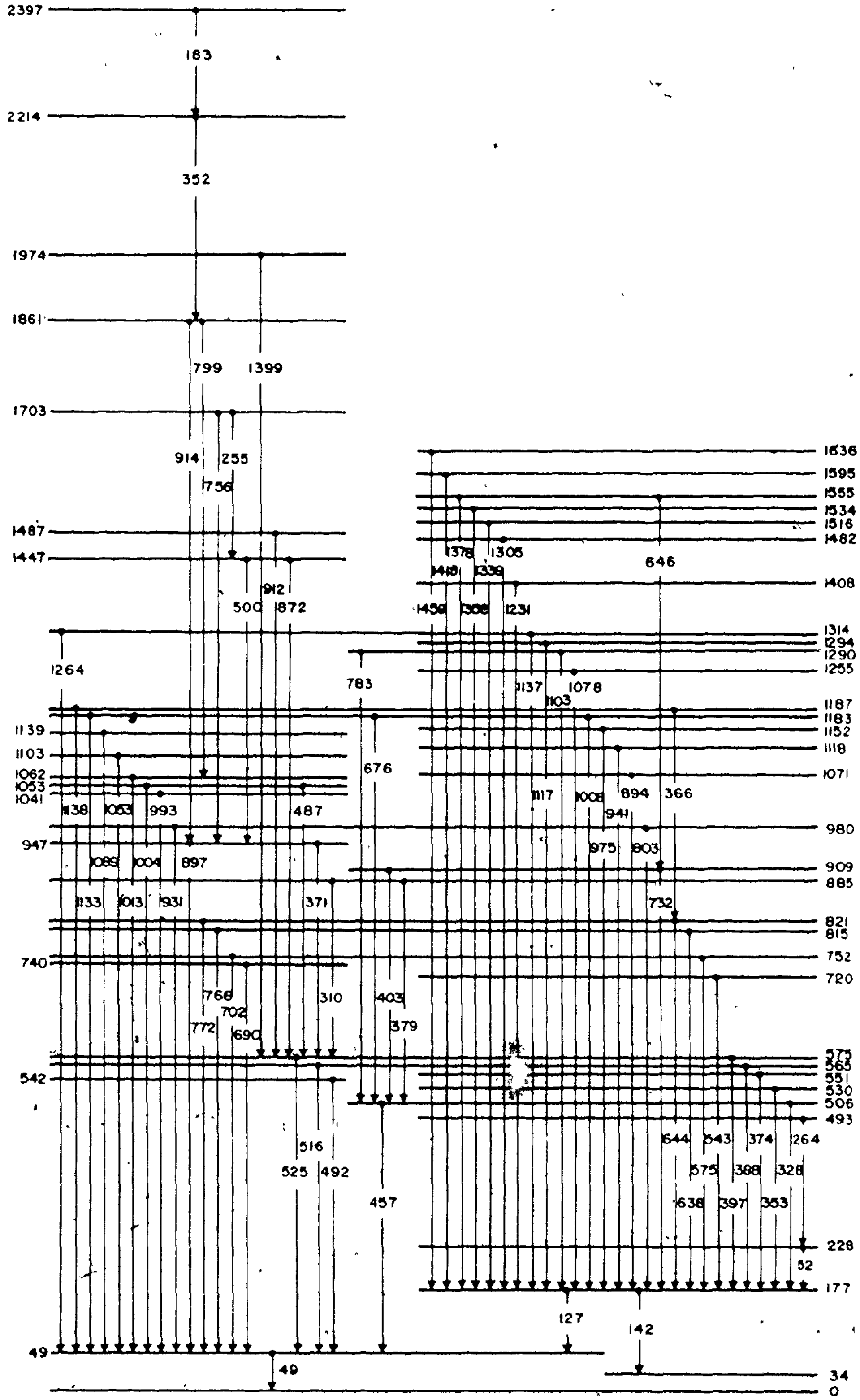
2397
183
2214
352
1974
1861
799
1399
1703
914
255
756
1487
1447
912
500
872
1264
1139
1103
1062
1053
1041
1138
1053
993
487
947
1089
1004
897
1133
1013
931
371
740
766
702
772
690
310
542
525
516
492
783
676
403
379
457
49
49
1636
1595
1555
1534
1516
1482
1378
1305
646
1418
1339
1408
1459
1368
1231
1314
1294
1290
1255
1137
1078
1103
1187
1183
1152
1118
894
366
1071
1117
1008
941
980
975
803
909
885
732
821
815
752
720
575
565
551
530
506
493
644
543
374
264
575
388
328
638
397
353
228
52
177
127
142
34
0

Figure 5.6

The coincidence spectra related to the important triplet of levels at 35 keV and to the 45 and 49 keV states. The partial decay scheme (shown in enlarged version in Fig. 5.6A) illustrates the transitions identified in these coincidence spectra. The reduced decay scheme in the upper right corner and the 323, and 264 keV gated spectra emphasize the role of the 52 keV transition (see Fig. 5.5). The two short sections of spectra just above the 427 keV gated spectrum present the 4k version of the 500 keV region in the direct and "reverse" spectra respectively.

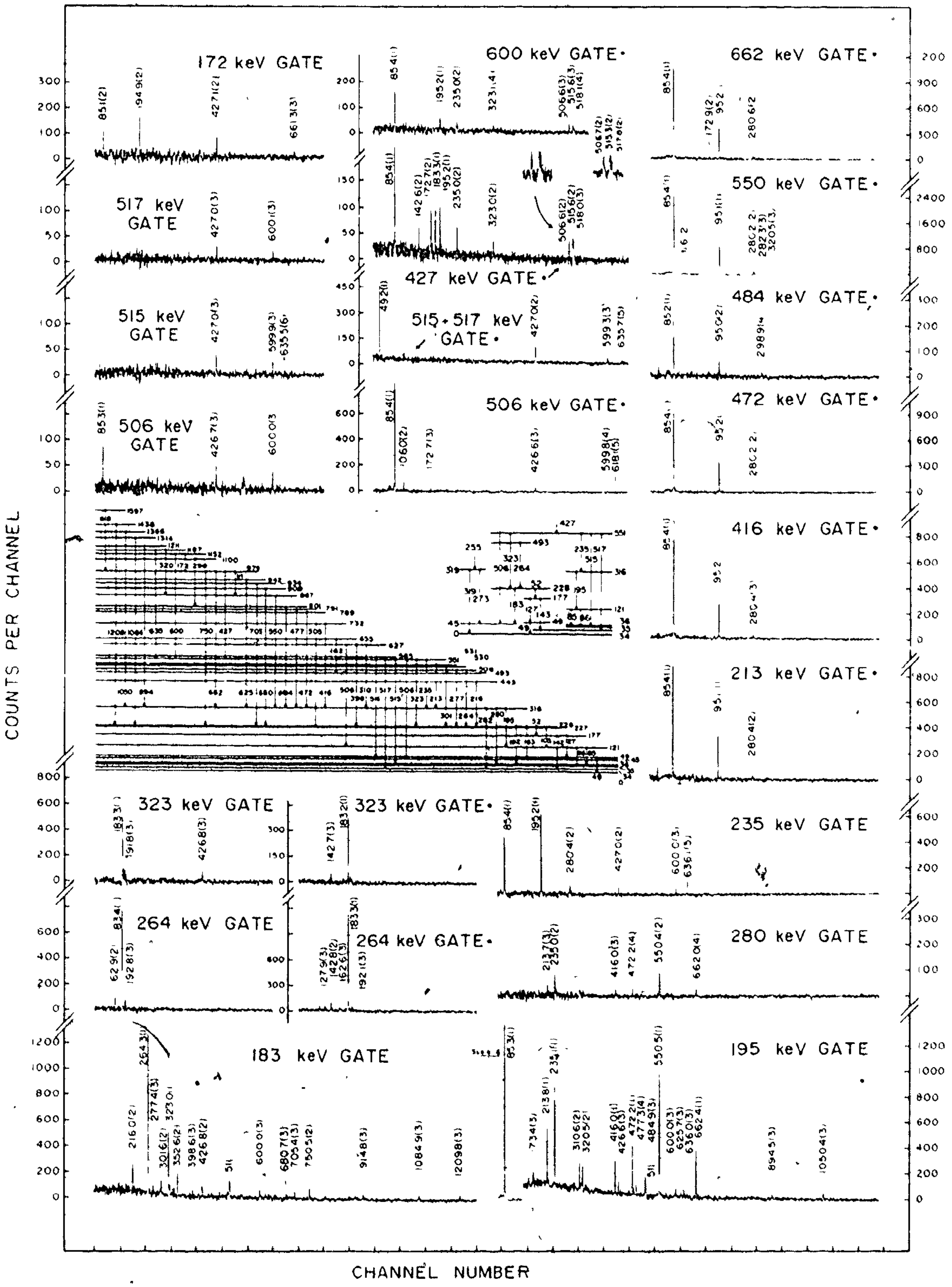
172 keV GATE
600 keV GATE•
662 keV GATE•
517 keV GATE
550 keV GATE•
427 keV GATE•
515 keV GATE
515+517 keV GATE•
484 keV GATE•
506 keV GATE
506 keV GATE•
472 keV GATE•
416 keV GATE•
213 keV GATE•
323 keV GATE
323 keV GATE•
235 keV GATE
264 keV GATE
264 keV GATE•
280 keV GATE
183 keV GATE
195 keV GATE
COUNTS PER CHANNEL
CHANNEL NUMBER

Figure 5.6A

The enlarged version of the partial decay scheme of Fig. 5.6 .

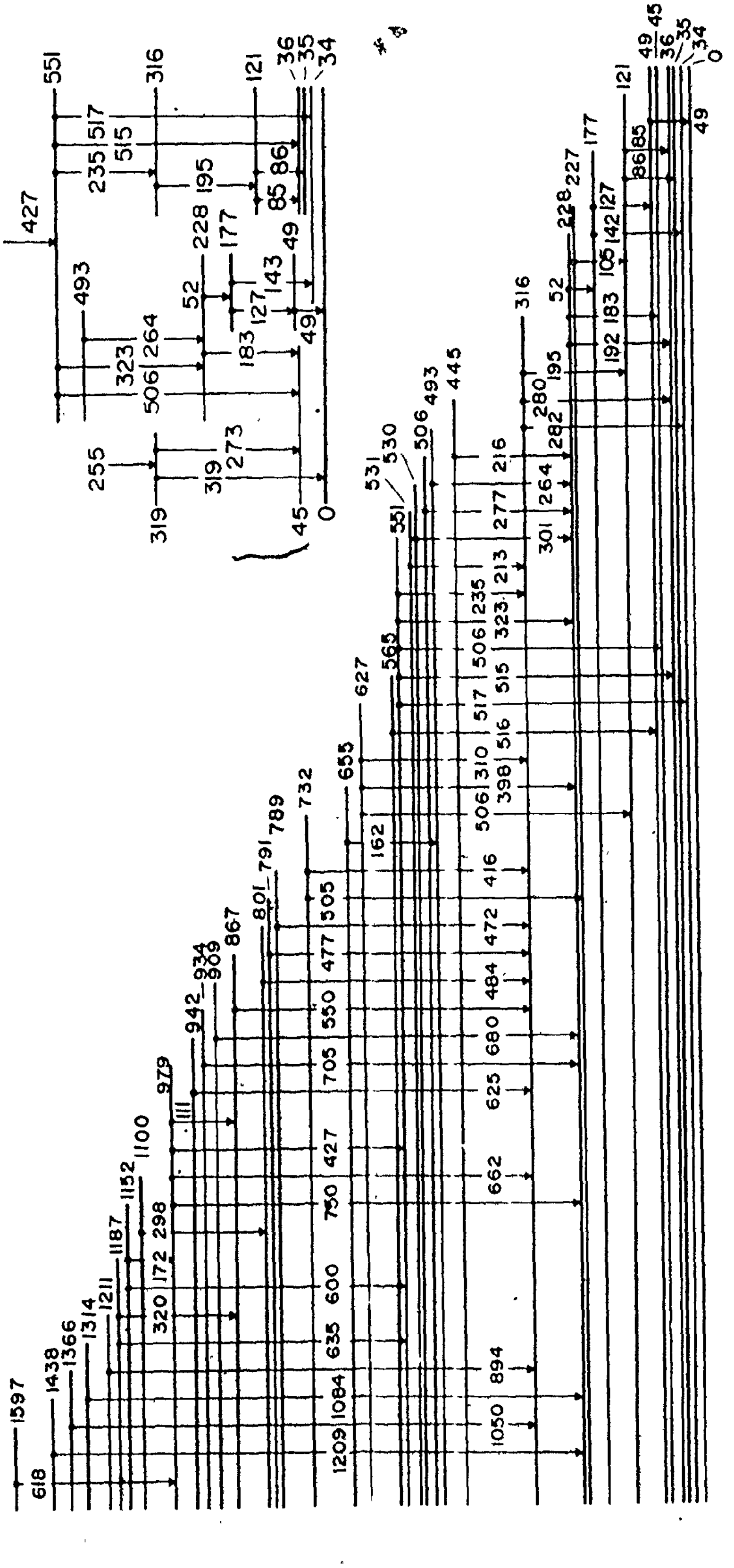

551
427
517
515
235
316
195
121
86
85
36
35
34
493
323
264
506
228
52
177
183
127
143
49
255
273
319
45
0
1597
618
1438
1366
1314
1211
1187
1152
1100
979
942
934
909
867
801
791
789
732
655
627
565
551
531
530
506
493
445
320
172
298
111
1209
1084
635
600
750
427
705
550
477
505
162
310
398
517
516
216
277
213
235
323
416
472
484
680
625
662
894
1050
280
282
264
301
195
192
183
52
228
227
105
142
127
177
121
49
45
36
35
34
0

Figure 5.7

Coincidence spectra related to the important 121 keV state. The 85 keV gated spectrum displayed is the 4k channel version. For clarity, in the 85 keV gate, the transitions feeding the 195-85 keV cascade are indicated by a dot above the peak energy. These transitions are displayed in Fig. 5.6A.

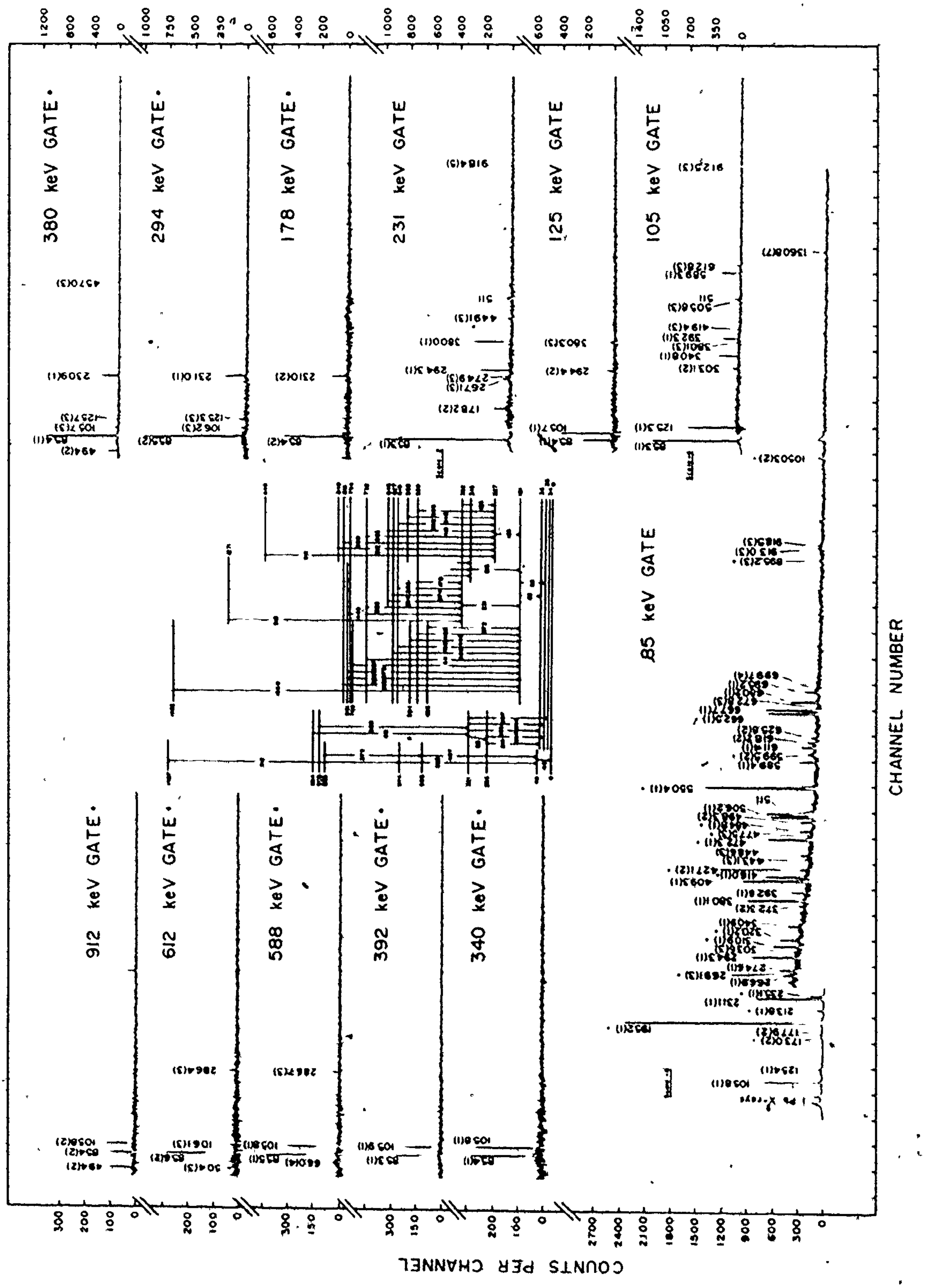
380 keV GATE
294 keV GATE
178 keV GATE
231 keV GATE
125 keV GATE
105 keV GATE
85 keV GATE
912 keV GATE
612 keV GATE
588 keV GATE
392 keV GATE
340 keV GATE
CHANNEL NUMBER
COUNTS PER CHANNEL

Figure 5.7A

An enlarged version of the partial decay scheme of Fig. 5.7 .

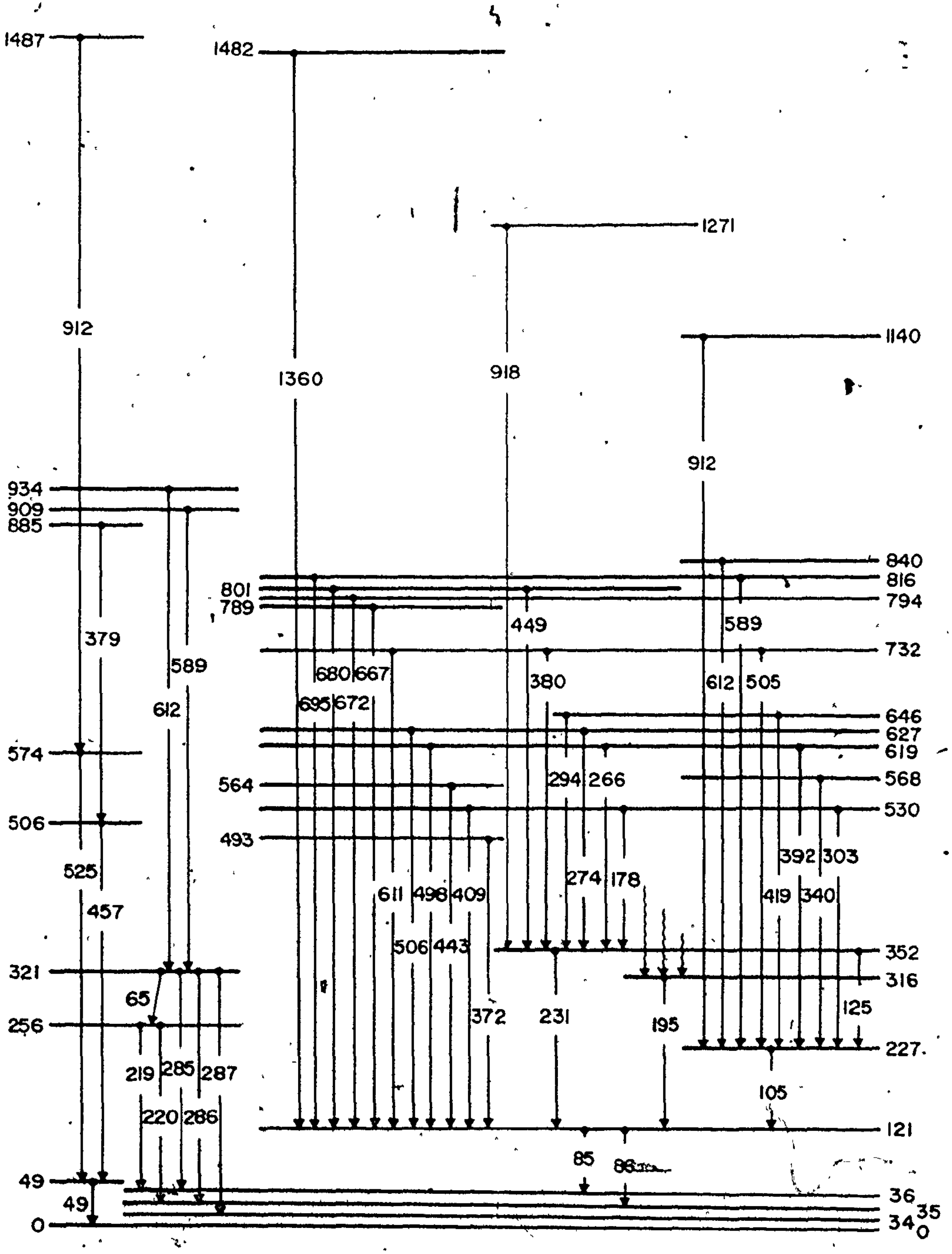
1487
1482
1271
1140
912
1360
918
912
934
909
885
840
816
801
794
789
449
589
379
589
732
680
667
380
612
695
672
612
505
646
627
619
574
568
564
294
266
506
530
493
392
303
525
274
178
457
611
498
409
419
340
506
443
352
321
316
65
372
231
195
125
256
227
219
285
287
105
220
286
121
85
86
49
49
36
35
34
0
0

Figure 5.8

Further coincidence evidence for the triplet of levels ~35 keV. The inserts in the 202 and 208 keV gated spectra are the 4k versions of the 220 and 285 keV regions respectively. The insert in the 65 keV spectrum is a portion of the reverse gating spectrum.

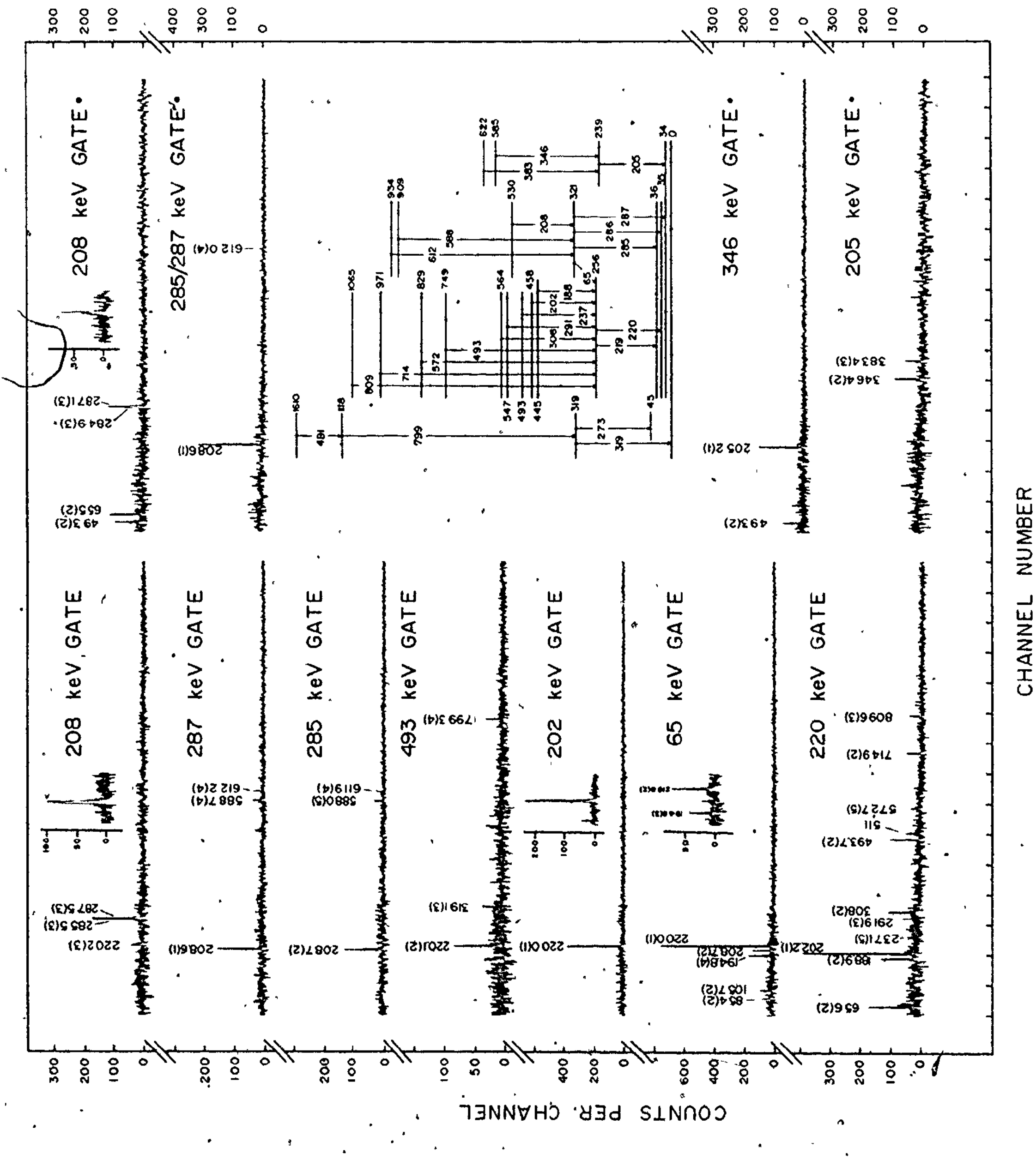
208 keV GATE
287 keV GATE
285 keV GATE
493 keV GATE
202 keV GATE
65 keV GATE
220 keV GATE
208 keV GATE•
285/287 keV GATE•
346 keV GATE•
205 keV GATE•
COUNTS PER CHANNEL
CHANNEL NUMBER
220.2(3)
285.5(3)
287.5(3)
208.6(1)
588.7(4)
612.2(4)
208.7(2)
588.0(5)
611.9(4)
220.1(2)
319.1(3)
799.3(4)
220.0(1)
65.6(2)
85.4(2)
105.7(2)
188.9(2)
194.8(4)
208.7(2)
220.0(1)
202.2(1)
237.1(5)
291.9(3)
308(2)
493.7(2)
511
572.7(5)
714.9(2)
809.6(3)
49.3(2)
65.5(2)
284.9(3)
287.1(3)
612.0(4)
205.2(1)
346.4(2)
383.4(3)

scheme, the fact of the discrepancy has been noted under footnote i in Table 5.1. Such a discrepancy probably means that this line is a doublet or that the simple $\gamma_1 - \gamma_2$ cascade assumed in locating the upper level is really a triple cascade $\gamma_1 - \gamma_x - \gamma_2$ in which γ_x has not been observed and there is branching from the intermediate levels.

The results of the coincidence experiments reported in this thesis are in excellent agreement with those observed in previous works. This is of special importance since the decay scheme in the (α,n) study is derived mainly from the coincidence data. However, the 85-85 and 183-141 keV coincidences reported by Doukellis et al. (1974) and Madueme and Arita (1977) respectively are not confirmed by this work. Also the 547-280 and 205-341 keV coincidences observed by Madueme and Arita (1977) and Kern and coworkers (1978) respectively are most probably the 550-280 and 205-346 keV coincidences reported in this thesis. The 550-280 keV coincidences were also observed by Bini et al. (1974).

These few discrepancies can be attributed to the difficulties associated with the gamma-gamma coincidence experiments using the (p,n) and (d,2n) reactions. Due to the selective character of these reactions many of the transitions placed higher in the level structure are much less intense than the low lying ones, consequently these experiments lack the statistics and precision typical of the (α,n) work.

5.5 Angular Distributions

A large number of angular distribution functions were measured at 14 and 18 MeV as described in section 4.7.1 . Each distribution was least-squares fitted to a function of the form:

$$W(\Theta) = A_0[\ 1 + A_2P_2(\cos\Theta) + A_4P_4(\cos\Theta)\ ] \qquad [5\text{-}1]$$

Columns 7 and 8 of Table 5.1 present these "experimental" A_2 and A_4 coefficients from either the 14 or 18 MeV measurements.

As described in chapter 2.3 angular distributions for a transition interconnecting levels of spin J_i and J_f may be predicted theoretically as a function of the mixing ratio $\delta=\langle J_f\|L+1\|J_i\rangle/\langle J_f\|L\|J_i\rangle$ and the population parameters of the initial state. The population distribution among the m substates for levels populated in (α,xn) reactions can be as well represented by a Gaussian of width σ. Thus a two-parameter search for a minimum in the surface $\chi^2(\sigma,\delta)$ is required to find the best fit of the experimental data to the model for a given set of J_i and J_f spins. Unfortunately, except for transitions when large positive A_2 coefficients have been determined with high statistical accuracy χ^2_{min} is found at the bottom of a narrow valley of almost constant depth. The search thus fails to identify a unique value of δ but rather a range of values (typically of the order of 10° in arctanδ), each associated with an appropriate value of σ, which yield equally acceptable values of χ^2_{min} . Theoretical and empirical methods of limiting the range of σ values have been discussed in section 2.4. The results are presented in Table 5.4, which tabulates the σ values used in deriving the theoretical angular distribution coefficients. These values range from 1.5 to 3.2 for the 18 MeV measurements and from 2.5 to 3.0 for the 14 MeV measurements. The values so obtained are in good agreement with those found from

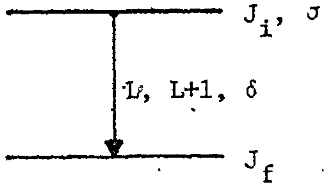

the two-parameter search for the few cases where the search led to a unique solution.

The angular distribution results for a transition connecting two energy levels limit the choice of spins for these levels in the manner discussed below. Prompt transitions are predominantly E1, M1, M1+E2 or pure E2 in character since those of higher order are strongly retarded with respect to dipole and quadrupole transitions except for special configurations of the decay scheme. Thus if the spin of the final level, J_f , is known, there are only five possible choices for the spin of the initial level, J_i ,namely: J_f-2, J_f-1, J_f , J_f+1, J_f+2. This choice of possible spin pairs can be further reduced after fitting the angular distribution functions derived from from the theoretical predictions for a given spin pair to the experimental data points. Using the minimum of χ^2 on the (σ,δ) surface as a selection criterion against different spin pairs one observes that transitions with positive A_2 and small A_4 are associated with $\Delta J=\pm 2,0$ while those with negative A_2 and small A_4 are associated with $\Delta J=\pm 1$.

Fig. 5.9 illustrates the method of analysis. The left hand panel of the upper row presents for the 927 keV gamma-ray plots of χ^2 versus a series of values of σ when δ is a free variable. These plots show that acceptable χ^2_{min} values occur in both the 14 MeV and 18 MeV data for the 7-7 and 9-7 but not for the 5-7 spin choice. For the σ values corresponding to these acceptable χ^2_{min} , the three adjacent panels present plots of χ^2 versus arctanδ for both beam energies. For the 9-7 spin sequence, there are sharp minima in χ^2 at arctanδ ∿0° in both the 14 and 18 MeV data; for the 7-7 spin sequence, there is a minimum at arctanδ ∿36° for both

Figure 5.9

Graphs to illustrate the method of data analysis in the angular distributions and linear polarization measurements. By combining the results of those two experiments unique spin and parity assignments to the states feeding the 927 and 995 keV transitions can be made. The details are discussed in the text.

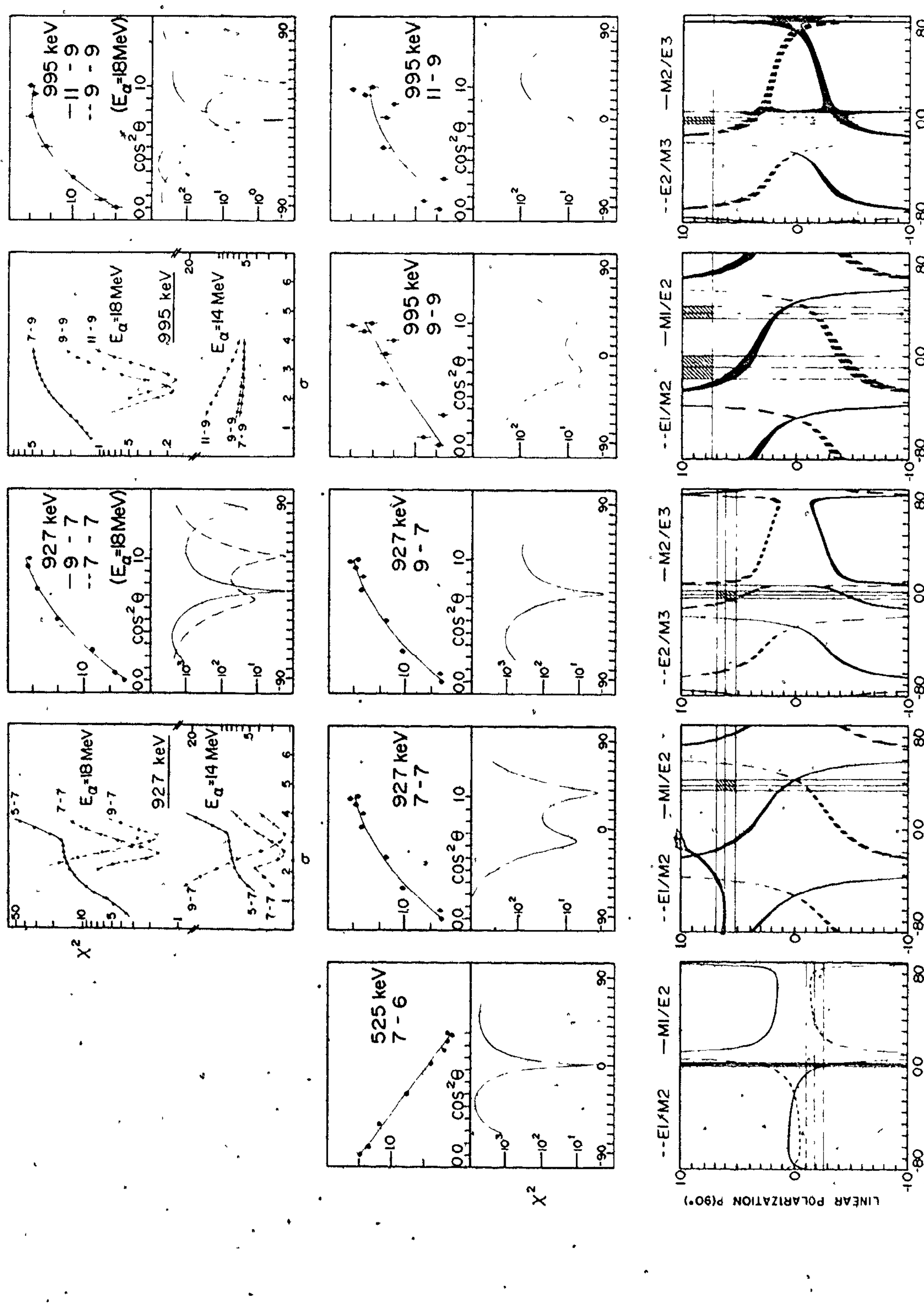
χ²
σ
927 keV
E_α=18 MeV
E_α=14 MeV
5-7
7-7
9-7
995 keV
7-9
9-9
11-9
927 keV
—9 - 7
-- 7 - 7
(E_α=18MeV)
995 keV
—11 - 9
-- 9 - 9
(E_α=18MeV)
525 keV
7 - 6
927 keV
7 - 7
927 keV
9 - 7
995 keV
9 - 9
995 keV
11 - 9
cos²θ
--E1/M2
—M1/E2
--E2/M3
—M2/E3
δ=TANβ
LINEAR POLARIZATION P(90°)

energies. Finally the quality of the fit to the experimental distributions is shown in the upper half of these three panels where the theoretical W(θ) function for the δ, σ combination giving the minimum χ^2 is presented along with the experimental values. The theoretical curves corresponding to the 7-7 and 9-7 spin sequences fit the data equally well. The polarization data presented in the lowest row of Fig. 5.9 resolves the ambiguity. This data, which will be discussed in the next section, shows that the 927 keV transition is stretched E2 in character between states of spin 9 and 7 respectively,

The four panels in the upper right hand area of Fig. 5.9 present similar data for the 995 keV transition which is also stretched E2 in nature. The 525 keV transition can only be fitted by a $\Delta J=\pm 1$ spin change.

Columns 9, 10, 11 of Table 5.1 present the A_2, A_4 and δ values corresponding to the spin sequences shown in column 3 for a large number of transitions. Those values were deduced in the manner described above for the 927 keV radiation. The experimental coefficients and those calculated from the model agree very closely. The quoted uncertainties in δ correspond to the $\chi^2_{limit} = \chi^2_{min}+1$ established by Rogers (1975). The limits have been widened in each case to allow for the uncertainty in σ. Fig. 5.10, and 5.11 show the quality of fit to the experimental data for a large number of the calculated coefficients of Table 5.1. The data in Fig. 5.10 was taken at 14 MeV, that in Fig. 5.11 at 18 MeV.

In the gamma-ray spectrum there are number of cases when two transitions form an unresolved peak. In general the character of the stronger member of the doublet dominates the angular distributions, so that

Figure 5.10

Angular distributions for 30 important gamma-rays in ^{96}Tc, as measured in the 14 MeV experiment. The 49, 85 and 86 keV distributions were obtained from 7 point measurements using a small 1cc Ge(Li) detector. The remaining distributions were measured using a 14cc Ge(Li) detector. The solid curves correspond to the "calculated coefficients" given in Table 5.1 .

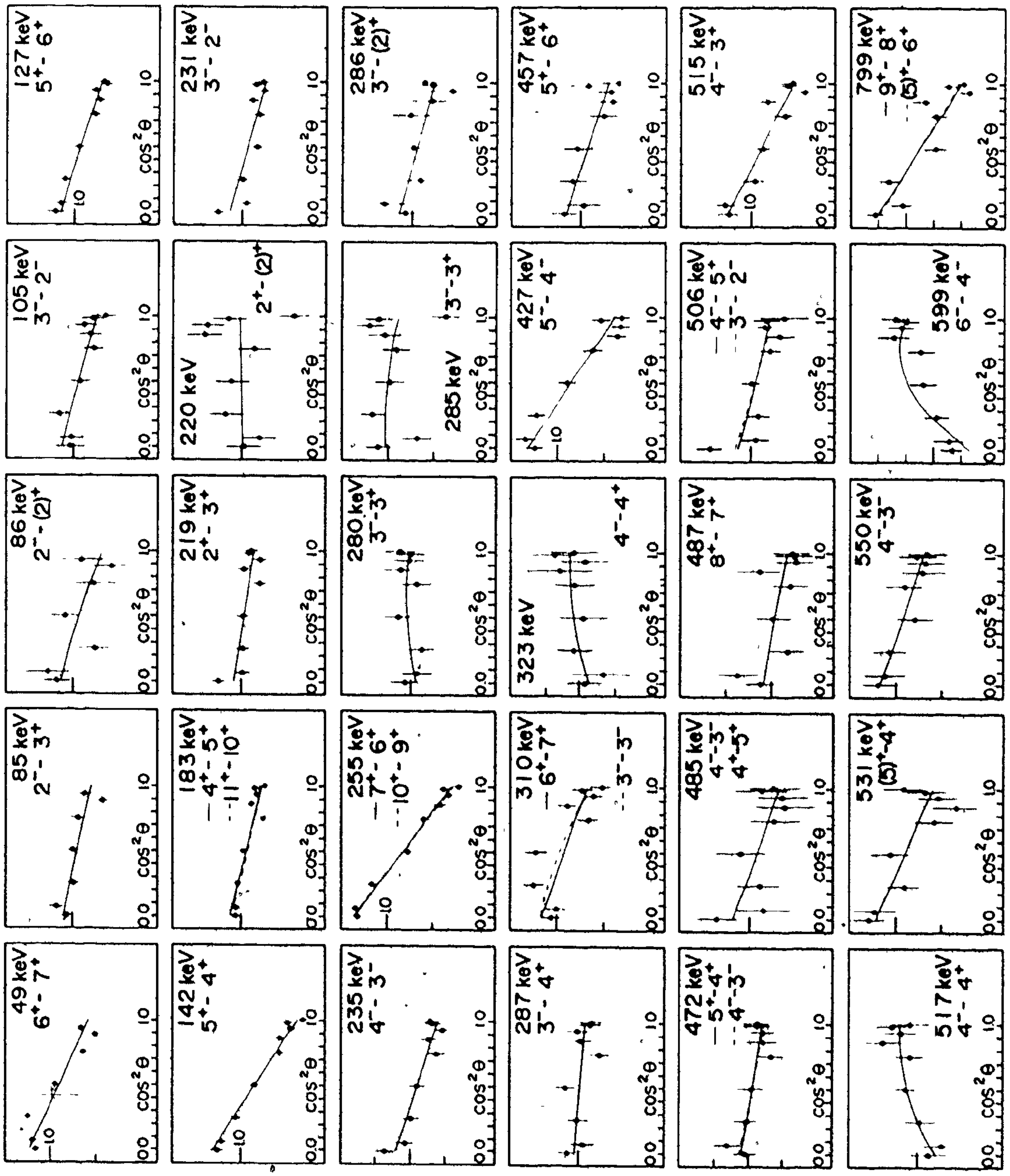
49 keV 6⁺- 7⁺
85 keV 2⁻- 3⁺
86 keV 2⁻-(2)⁺
105 keV 3⁻- 2⁻
127 keV 5⁺- 6⁺
142 keV 5⁺- 4⁺
183 keV — 4⁺- 5⁺ - - 11⁺-10⁺
219 keV 2⁺- 3⁺
220 keV 2⁺-(2)⁺
231 keV 3⁻- 2⁻
235 keV 4⁻- 3⁻
255 keV — 7⁺- 6⁺ - - 10⁺- 9⁺
280 keV 3⁻-3⁺
285 keV 3⁻-3⁺
286 keV 3⁻-(2)⁺
287 keV 3⁻- 4⁺
310 keV — 6⁺-7⁺ - - 3⁻-3⁻
323 keV 4⁻-4⁺
427 keV 5⁻- 4⁻
457 keV 5⁺- 6⁺
472 keV — 5⁺-4⁺ - - 4⁻-3⁻
485 keV 4⁻-3⁻ 4⁺-5⁺
487 keV 8⁺- 7⁺
506 keV — 4⁻- 5⁺ - - 3⁻- 2⁻
515 keV 4⁻- 3⁺
517 keV 4⁻- 4⁺
531 keV (5)⁺-4⁺
550 keV 4⁻-3⁻
599 keV 6⁻- 4⁻
799 keV — 9⁺- 8⁺ - - (5)⁺- 6⁺
cos²θ
0.0
1.0
1.0

Figure 5.11

The angular distributions for the 30 selected transitions deexciting high and medium spin states measured at 18 MeV.

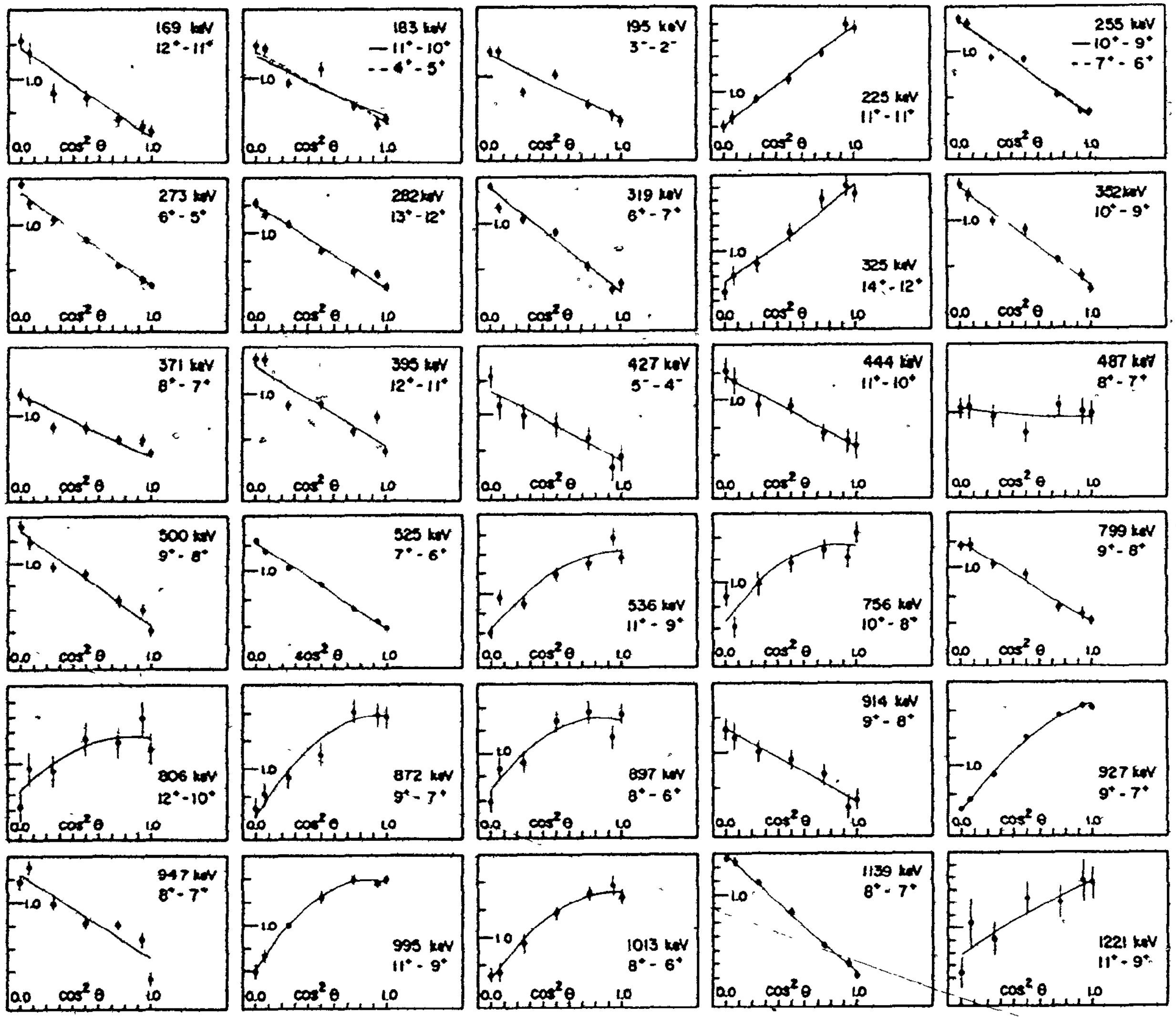
169 keV
12+ - 11+
183 keV
— 11+ - 10+
- - 4+ - 5+
195 keV
3− - 2−
225 keV
11+ - 11+
255 keV
— 10+ - 9+
- - 7+ - 6+
273 keV
6+ - 5+
282 keV
13+ - 12+
319 keV
6+ - 7+
325 keV
14+ - 12+
352 keV
10+ - 9+
371 keV
8+ - 7+
395 keV
12+ - 11+
427 keV
5− - 4−
444 keV
11+ - 10+
487 keV
8+ - 7+
500 keV
9+ - 8+
525 keV
7+ - 6+
536 keV
11+ - 9+
756 keV
10+ - 8+
799 keV
9+ - 8+
806 keV
12+ - 10+
872 keV
9+ - 7+
897 keV
8+ - 6+
914 keV
9+ - 8+
927 keV
9+ - 7+
947 keV
8+ - 7+
995 keV
11+ - 9+
1013 keV
8+ - 6+
1139 keV
8+ - 7+
1221 keV
11+ - 9+
1.0
0.0
cos² θ
1.0

little can be said about the other line. If both transitions are of equal strength and the angular distribution of the doublet looks like one for a pure and strongly anisotropic ΔJ=$\pm$1 transition, both gamma-rays must be of ΔJ=$\pm$1 character. For a number of unresolved peaks the intensities of the individual components and the total angular distributions were measured at both alpha beam energies, thus providing additional information which in many cases yields the character of both transitions of the doublet. Two specific cases, (the 183 and 255 keV doublets) will serve as an example of the type of analysis, which was conducted in each case of a double peak.

The 183 keV peak is a doublet involving the low excitation 228-45 keV and the high excitation 2397-2214 keV transition. The high excitation component is responsible for 33% and 4% of the total peak intensity at 18 and 14 MeV, respectively. Thus the angular distribution measurement at 14 MeV yields pure A_2 and A_4 coefficients characteristic of a ΔJ=$\pm$1 transition for the low excitation component. The fact that the A_2 coefficient for the composite peak at 18 MeV is larger than that for the "pure" peak at 14 MeV gives a strong indication that the high excitation component is also of ΔJ=$\pm$1 character. The 255 keV peak is also a doublet involving high and low excitation components. However, in this case, the ratio of intensities only changes from 60% to 30% so that neither the 14 MeV nor the 18 MeV angular distributions are "pure". Because the angular distributions determined at 14 and 18 MeV are identical and both characteristic of ΔJ=$\pm$1 transitions, it appears that both components must be of ΔJ=$\pm$1 character. The conclusions drawn for both the 183 and 255 keV doublets are consistent with the requirements of the level structure of

Fig. 5.12 - 5.14, based on the properties of other transitions.

The 487, 721, and 947 keV peaks in the 18 MeV spectra are contaminated to the extent of about 10% by ^{95}Mo decay lines or ^{95}Tc lines. At 14 MeV no ^{95}Tc is created. The data at different angles was collected in a time sequence which minimized the distortion of the distribution created by the build up of activity.

5.6 Linear Polarization of Gamma-Rays

It was shown in chapter 2 that the linear polarization coefficients can be expressed by combinations of the same parameters and functions as the angular distribution coefficients. In the notation of section 2.6 , the linear polarization coefficient of a gamma-ray is given by:

$$P(\ \phi=90^\circ\ ) = \pm \frac{3A_2'Q_2 - 7.5A_4'Q_4}{1 - 0.5A_2Q_2 + 0.375A_4Q_4} \qquad [5 - 2]$$

where the plus and minus signs refer to magnetic and electric multipole transitions respectively. The Q_2 and Q_4 coefficients which express the attenuation due to the finite solid angle subtended by the detectors are very close to unity under the conditions of these experiments (Khan et al., 1980) and will be treated as unity in the analysis which follows.

The A_ν' and A_ν coefficients are given by:

$$\begin{aligned} A_\nu' &= \alpha_\nu \cdot f_\nu'(J_i,J_f,\delta) \\ A_\nu &= \alpha_\nu \cdot f_\nu(J_i,J_f,\delta) \end{aligned} \qquad \nu = 2,4 \qquad [5 - 3]$$

in which α_ν are the attenuation coefficients which depend in a rather complex way on the σ values tabulated in Table 5.4 (see equations 14 and 16 of chapter 2), and, like these values, cannot be determined with high precision, either experimentally or theoretically. The functions f'_ν and f_ν are readily calculable, depending as they do on Clebsch-Gordan coefficients, spins and mixing ratios for completely aligned states.

Because the same attenuation coefficients occur in both A_ν and A'_ν the necessity for determining them can be avoided by expressing A'_ν in terms of A_ν as follows:

$$A'_\nu = H_\nu(\delta) \cdot A_\nu \qquad [5 - 4A]$$

where $\nu = 2,4$

$$H_\nu(\delta) \equiv f'_\nu(J_i,J_f,\delta) \,/\, f_\nu(J_i,J_f,\delta) \qquad [5 - 4B]$$

Since $H_\nu(\delta)$ can be calculated theoretically with precision, all that remains is to obtain values of A_ν that do not depend on knowledge of α_ν. Fortunately, for the values of δ that correspond to χ^2_{min} in the χ^2 vs. δ plot (see Fig. 5.9) the A_ν values are very close to the A_ν^{exp} values obtained by fitting the experimental distributions to a sum of Legendre polynomials in the manner described in Section 5.5. These A_ν^{exp} values are tabulated in Table 5.1. For these particular values of δ one can then write:

$$A'_\nu = A_\nu \cdot H_\nu(\delta)\Big|_{\delta=\delta_{min}} \cong (A_\nu^{exp} \pm \Delta A_\nu^{exp}) \cdot H_\nu(\delta=\delta_{min}) \qquad [5 - 5]$$

For other values of δ this equality does not hold, but the errors introduced by using A_ν^{exp} instead of A_ν will not be large for δ values reasonably close to δ_{min}. We now rewrite expression [5-2] as:

$$P(\phi=90^\circ) = \pm \frac{3A_2^{exp} H_2(\delta) - 7.5A_4^{exp} H_4(\delta)}{1 - 0.5A_2^{exp} + 0.375A_4^{exp}} \qquad [5 - 6]$$

while recognizing that the values of P predicted will not be correct except for δ values close to δ_{min} . Since we are only concerned with the polarization for values of δ allowed by the angular distribution data, this inadequacy of equation [5-6] is quite unimportant.

By means of the computer program MABEL, expression [5-6] was used to calculate P as a function of $\beta = \tan^{-1}\delta$ for each transition whose polarization was measured. The results of such calculation for the 525, 927, and 995 keV transitions are plotted in the five panels across the bottom of Fig. 5.9 . The line widths in the P vs. β curves reflect the uncertainties in P created by uncertainties in A_{ν}^{exp}. In each panel, the horizontal band defines the measured polarization and its experimental uncertainty while the vertical band defines the acceptable range of β deduced from the angular distribution measurements. The crosshatched areas which mark the intersection of these bands define the region through which all physically acceptable P curves must pass. As we have seen, it is only in this region of the P vs. β plot that the P values have physical meaning; indeed, for values of β far from these regions, equation [5-6] predicts physically impossible polarizations of greater than unity.

For the 927 keV transition, Fig. 5.9 presents the angular distribution fits for a 9-7 and 7-7 spin assignment. The 5-7 assignment cannot be fitted with any reasonable σ value. For both the 14 and 18 MeV data the 7-7 choice yields minimum χ^2 for $\tan^{-1}\delta \sim 35°$. For this spin choice, the P vs. β curves for E1/M2 and M1/E2 admixtures fail to pass through the acceptable rectangle by a wide margin. On the other hand, for a 9-7 spin choice, the acceptable β is close to zero and the P vs. β curve for the E2/M3 admixture passes through the acceptable rectangle. The 927 keV transition is thus a stretched E2 between states of spin 9 and 7.

In a similar way, one concludes that the 995 keV transition is also E2 and involves an 11-9 spin sequence, although the evidence is not quite as strong. The angular distribution fits to the 18 MeV data show clearly that $\beta=0°$ for the 11-9 and $\beta\sim35°$ for the 9-9 spin choice. Since this transition is not strongly excited at 14 MeV, the angular distribution fit at 14 MeV, is of much poorer quality than the one taken at 18 MeV experiment. Nevertheless it leads to β values consistent with the 18 MeV data. Because the polarization experiment was carried out at 14 MeV, the A_ν^{exp} values from the 14 MeV data must be used despite their poor quality. For the 9-9 case, there are apparently two acceptable regions in the P vs. β plot. However, it is clear from the 18 MeV data that the area near $\beta=-10°$ is not acceptable and, therefore, there is no acceptable solution for 9-9 choice. For the 11-9 spin sequence, the E2/M3 choice is marginally acceptable, given the large uncertainty in the polarization measurement.

For the 525 keV transition, both the 7-6 and 5-6 spin choice yield equally acceptable fits to the angular distribution and polarization data. The data shows that this transition is of stretched M1 character between states for which $\Delta J=\pm1$, but cannot distinguish between a 7-6 and 5-6 spin sequences.

Angular distribution and linear polarization coefficients were measured for a very large number of transitions, of which those discussed above form a small sample. For many of the weaker transitions, the statistical errors inherent in the determination of the angular distribution and polarization coefficients were so large as to make the results worthless. Tables 5.1 and 5.5 present the results for those transitions, for which the data analysis was meaningful.

For some of the double peaks, it was possible to draw useful conclusions for the cases when $|P|>>0$, even though one could not distinguish the transitions involved in any way. The 799 keV doublet is a case in point. This peak contains both a high excitation 1861-1062 keV and a low excitation 1118-319 keV component. The latter is responsible for 8% and 30% of the total peak intensity at 18 and 14 MeV respectively. The experimental distributions are strongly anisotropic at both beam energies, indicating that both transitions are of the $\Delta J=\pm 1$ type. The polarization data shows clearly that the stronger component is M1 in character and suggests that the weaker component is also M1.

5.7 Internal Conversion Coefficients

The results of the internal conversion measurements for alpha beams of 14 and 18 MeV are tabulated in columns 4 and 5 of Table 5.5 . For comparison, columns 6 and 7 present the coefficients obtained by Madueme and Arita (1978) and Miracle et al. (1979) respectively. In addition to the K-shell conversion coefficients measured with the "orange" beta-ray spectrometer, the table includes total conversion coefficients for a few low energy transitions deduced from coincidence probabilities and intensity balancing using the methods of section 4.6.3 .

Fig. 4.16 presents the experimental coefficients, together with the theoretical conversion coefficients for pure multipoles calculated by Hager and Seltzer (1968) and illustrates the essence of the graphical method used to classify the experimentally determined coefficients.

The experimental data from this work agrees well with that of Miracle et al. but there are sharp disagreements with the results of Madueme and Arita. In particular, our results show that the stronger component of the 183 keV doublet is M1 rather than E2, as claimed by these authors. The interpretation of the 191 keV transition as M1 follows naturally from the decay scheme of this work; Miracle et.al. , using an incorrect level structure, were forced to interpret the transition as an unlikely E1+M2 mixture.

The total conversion coefficient for the 49 keV transition was derived from the intensity balance using the intensities provided by Madueme and Arita as well as using the intensities of the present work. However, by reworking the data of Madueme and Arita one can gain the advantage, that the low excitation spectra obtained in the (d,2n) reaction were much simpler than the high excitation spectra of the present work.

The data analysis of peaks known to be close doublets was similar to that performed in the angular distributions and linear polarization experiments. The comparison of the results obtained at both beam energies was particularly helpful in the interpretation of the data involving the 183 and 255 keV lines.

5.8 Discussion of the Decay Scheme

Information concerning the energies, spins and parities of states in ^{96}Tc is summarized in columns 2 and 3 of Table 5.1 and in the figures 5.12 to 5.14. In addition to the 251 gamma-rays which have been placed conclusively in the decay scheme, there are 12 other transitions which show excitation functions characteristic of ^{96}Tc. These have been included in Table 5.1 .

The level scheme of Fig. 5.12 to 5.14 presents graphically the information of Table 5.1. In these figures, the energies, spins and parities of the levels are shown together with the approximate energies of the transitions involved. A rough indication of the intensities of the stronger transitions is given by the width of the transition arrow. A full dot above (or below) a transition indicates that it has been observed to be in coincidence with at least one transition feeding its initial (or deexciting its final) state as the case may be. A half-dot indicates that the transition was placed on the basis of energy balance or some other evidence than the coincidence relationship. In general the vertical axis of each figure reflects a linear excitation-energy scale; however, in a few regions, the high density of states made it impossible to present the data and still preserve the proper spacing between levels.

Although the decay scheme is almost entirely based on the experimental evidence reported in this thesis, it is gratifying to note that the experimental results already published by other workers, generally support and, in a few cases, supplement this work.

Gamma-gamma coincidence results formed the starting point in the construction of the decay scheme. Starting with the most intense gamma-rays, transition by transition they were put together into the scheme of coincidence relationships. Then energy and intensity balances were checked and the excitation functions were compared for the gamma-rays deexciting the same levels. Finally the decay scheme was tested against the results

Figure 5.12 to 5.14

The level structure of ^{96}Tc as revealed in the (α,n) reaction. The level energies are presented in the right hand margin, while the spin and parity assignments are given in the left hand margin. Uncertain assignments are enclosed in parenthesis. Strength of a transition is roughly indicated by the width of the transition arrow. Coincidence evidence is indicated by a dot at either one or both ends of a transition arrow.

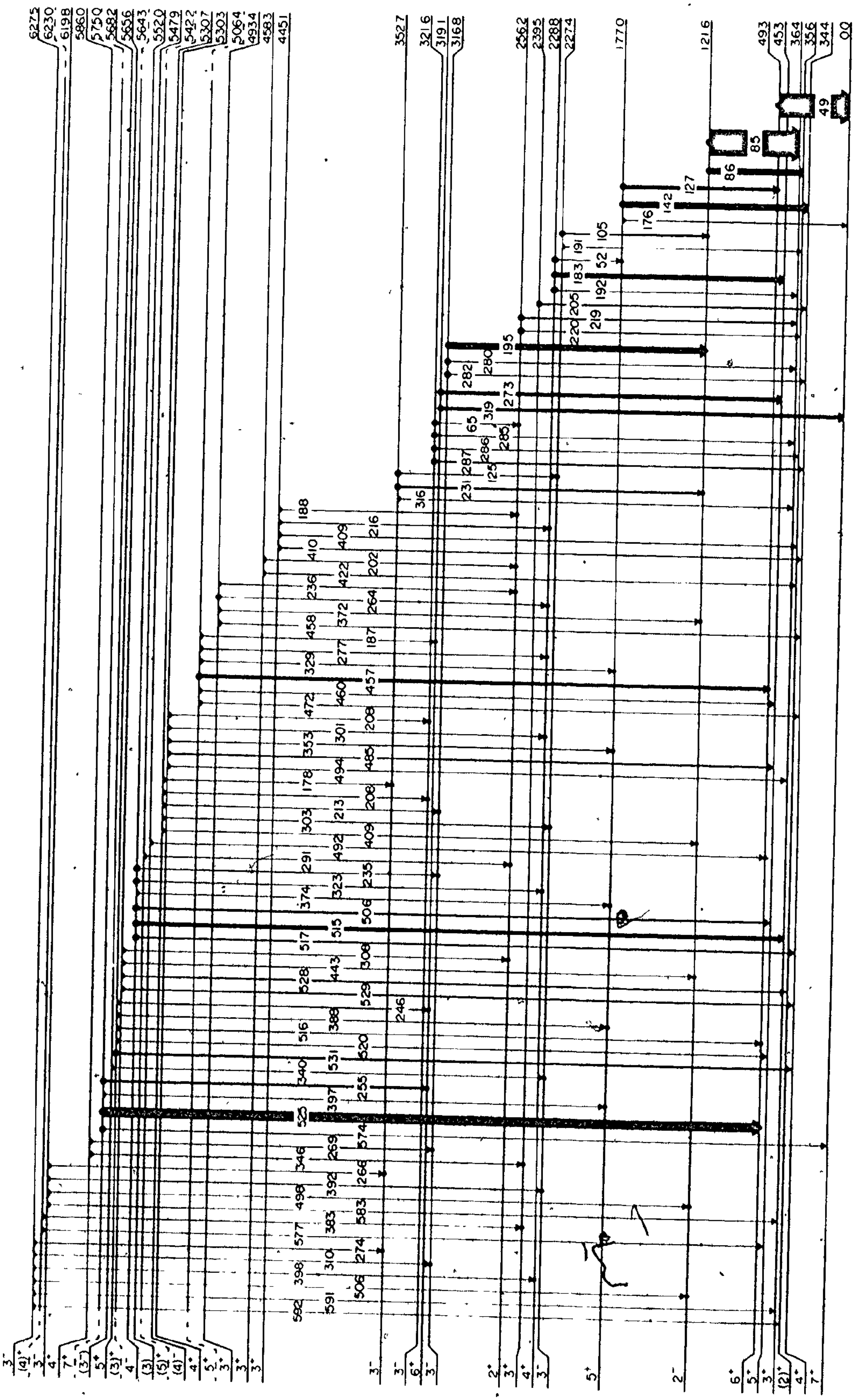
6275
6230
6198
5860
5750
5682
5656
5643
5520
5479
5422
5307
5303
5064
4934
4583
4451
3527
3216
3191
3168
2562
2395
2288
2274
1770
1216
493
453
364
356
344
00
3-
(4)+
3-
4+
7+
(3-)
5+
(3)+
4-
(3)
(5)+
(4)-
4+
5-
3+
3+
3+
3-
3-
6+
3-
2+
3+
4+
3-
5+
2-
6+
5+
3+
(2)+
4+
7+
49
85
86
127
142
176
105
191
52
183
192
205
219
220
195
280
282
273
319
65
286
285
287
125
231
316
188
216
409
410
202
422
236
264
372
458
187
277
329
457
460
472
208
301
353
485
494
178
208
213
303
409
492
291
235
323
374
506
515
517
308
443
528
529
246
388
516
520
531
340
255
397
525
374
269
346
266
392
498
583
383
577
274
310
398
506
591
582

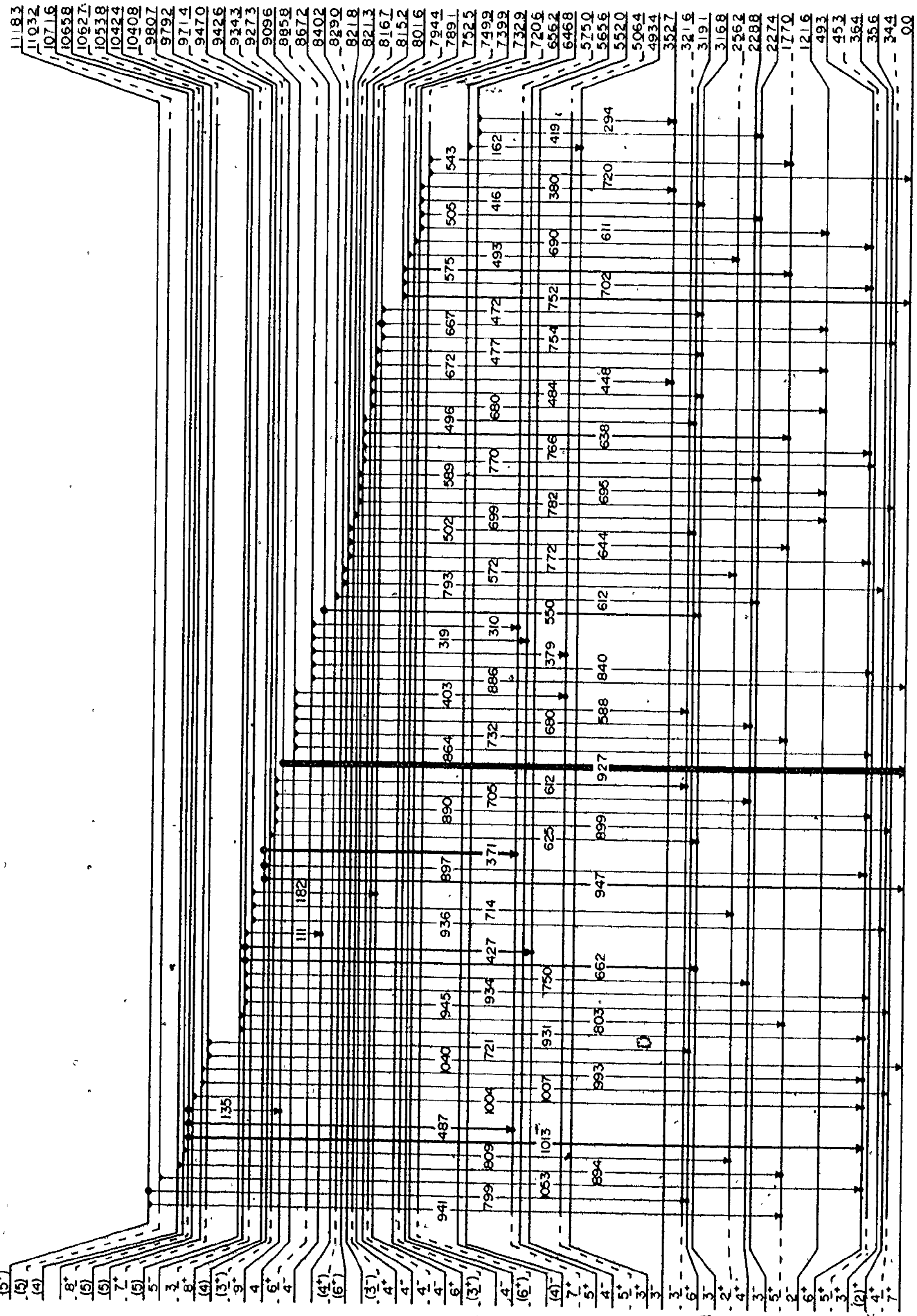
11183
11032
10716
10658
10627
10538
10424
10408
9807
9792
9714
9470
9426
9243
9273
9096
8858
8672
8402
8290
8218
8213
8167
8152
8016
7944
7891
7525
7499
7399
7329
7206
6562
6468
5750
5656
5520
5064
4934
3527
3216
3191
3168
2562
2288
2274
1770
1216
493
453
364
356
344
0.0
294
162
419
543
720
380
416
505
611
690
493
575
702
752
472
667
754
477
672
448
484
680
496
638
766
770
589
695
782
699
502
644
772
572
793
612
550
310
319
379
840
886
403
588
680
732
864
927
612
705
890
899
625
371
897
947
182
714
936
111
427
662
750
934
945
803
931
721
1040
993
1007
1004
135
487
1013
809
894
1053
799
941
(5+)
(5)
(4)
8+
(5)
(5)
7+
(5)
5-
3
8+
(4)
(3+)
9+
4
6+
4-
(4+)
(6+)
(3-)
4+
4-
4-
4-
6+
(3+)
4-
(6+)
(4)
7+
5+
4-
5+
3+
3-
3-
6+
3-
2+
4+
3-
5+
2-
6+
5+
3-
(2)+
4+
7+

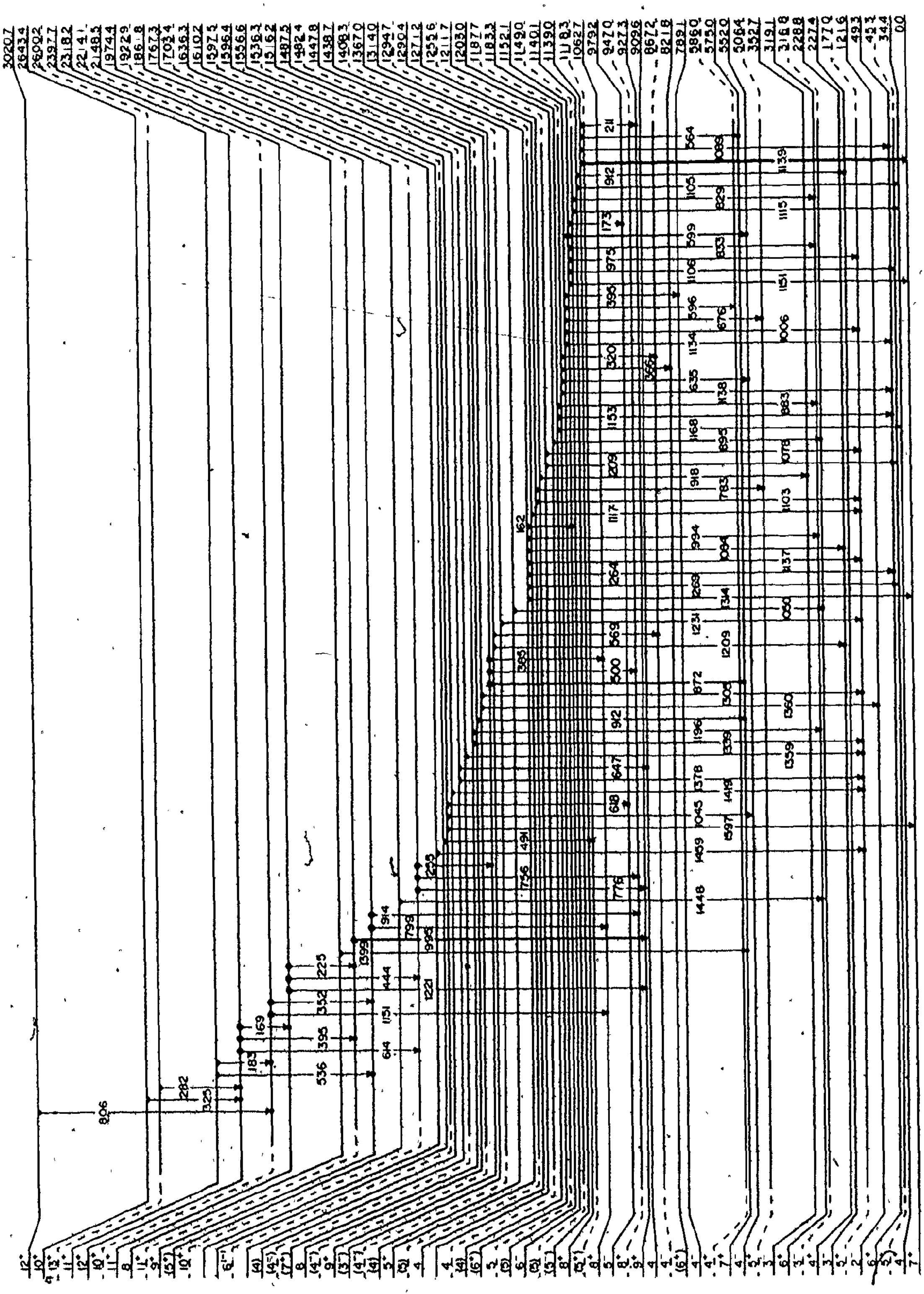
3020.7
2643.4
2609.2
2397.7
2318.2
2214.1
2148.5
1974.4
1922.9
1861.8
1767.3
1703.4
1636.3
1619.2
1597.5
1596.4
1556.6
1536.3
1516.2
1487.5
1482.4
1447.8
1438.7
1408.3
1367.0
1314.0
1294.7
1290.4
1271.2
1255.6
1211.7
1203.0
1187.7
1183.3
1152.1
1149.0
1140.1
1139.0
1118.3
1062.7
979.2
947.0
927.3
909.6
867.2
821.8
789.1
586.0
575.0
552.0
506.4
352.7
319.1
316.8
228.8
227.4
177.2
121.6
49.3
45.3
34.4
0.0
12+
10+
13+
11+
12+
10+
11+
8
11+
9+
(5+)
10+
6(+)
(4)
(4+)
(7+)
8
(4+)
9+
(3+)
(4+)
(4)
5+
5+
(5)
4
4
(4)
(6+)
5
(5)
6
(6)
(5)
8+
(5+)
6+
5
8+
9+
4
4
(6+)
4
4+
7+
4
5+
3
6+
3+
4+
3
5+
2
6+
(5)
4
7+
806
282
325
183
169
395
536
614
352
225
1151
444
1399
914
798
998
1221
1448
776
756
491
1459
1597
648
1045
1419
647
1378
1339
1359
912
1196
1305
1360
385
500
872
569
1209
1231
1050
264
1314
1268
1137
162
1117
994
1094
209
918
783
1103
1153
1168
695
1078
320
635
1138
883
558
395
1134
596
676
1006
975
1106
599
833
1151
173
912
1105
829
1115
211
564
680
1139

obtained by previous workers. Once the low-lying levels at 34.4, 35.6, 36.4, 45.3 and 49.3 keV had been established, it became possible to build the entire decay structure. With the exception of the 34.4 keV and 49.3 keV levels quoted above and a few other states, most of the 105 energy levels discussed in this thesis are reported here for the first time.

The excitation functions, angular distributions, and the linear polarization and internal convesion coefficients provided the primary source of information concerning spins and parities. In addition the data of previous workers were carefully examined. In particular, the results of Doukellis et al. (1974) on the on and off-resonance of the $5/2^+$ isobaric analog state in ^{97}Tc were reinterpreted in the light of new evidence obtained from the present investigation. The data of Doukellis et al. were useful since they provided clues to the character of the low spin states, which can be populated in the ^{96}Mo(p,n)^{96}Tc reaction. In particular, the states of spin 2 and 3 of both parities are strongly populated in the on and off-resonance spectra. The levels of spin 0 or 1 of both parities are very strong in the off-resonance spectra, while the levels of spin J>4 are very weakly populated in both the on and off-resonance cases.

Some of the tentative parity assignments will be based on the observation that most of the transitions of Table 5.1 are of M1 in character. Thus, if a level of unknown parity is feeding only positive parity levels it is highly probable that it also possesses positive parity. This expectation is supported by the fact that in general the positive and negative parity states arise from quite different configurations and and that transitions between them are ℓ-forbidden.

The 7^+ Ground State and the 4^+ State at 34.4 keV.

The ground state of ^{96}Tc decays by electron capture to ^{96}Mo with a 4.28 day half-life (Medsker, 1972). The 34.4 keV state which has a lifetime of 51.5 min., decays to the ground state of ^{96}Tc via an M3 transition (98%) and to ^{96}Mo by electron capture (2%). The spins and parities of these two levels are well established as 7^+ and 4^+, respectively, from these decay studies and these assignments will be accepted as a starting point for the construction of the decay scheme. There is no evidence from the internal conversion data of Ageev et al. (1970), decay studies, or the present in-beam work for levels between the ground state and the 34.4 keV level.

The 35.6 keV level, $J^\pi=(2)^+$.

The results of section 5.4 require a triplet of levels at ∿35 keV. From the decay studies it is known that the 34.4 keV member of the triplet is 4^+ in character. Conclusions concerning J^π for the 35.6 and 36.4 members of the triplet must be arrived at by a process of deduction involving several levels and transitions. The 36.4 keV state is discussed first.

The E1, $\Delta J=0$ character of the 517 keV line leads to a unique 4^- assignment to the 552.0 keV state. The M1, $\Delta J=\pm 1$ nature of the 235 keV transition which deexcites this level limits the spin of the 316.8 keV state to 3^- or 5^-. Since this state is strongly populated in the (p,n) reaction, the 5^- choice must be rejected. Finally, the E1, $\Delta J=0$ character of the 280 keV transition connecting the 316.8 and 36.4 states defines J^π for the latter as 3^+. This conclusion is supported by the E1,

$\Delta J=\pm 1$ nature of the 515 keV gamma-ray connecting the 552.0 keV and 36.4 keV states.

The data available for determining the spin of the 35.6 keV level is somewhat contradictory. One can proceed by defining first the spin of the 121.6 keV state which feeds both the 35.6 and 36.4 keV levels. The M1, $\Delta J=\pm 1$ character of the 195 keV transition connecting the 3^- 316.8 keV state to the 121.6 keV level restricts the spin of the latter to 2^- or 4^-. The E1, $\Delta J=\pm 1$ character of the 85 keV transition connecting the 121.6 keV state to the 3^+ 36.4 keV state yields the same result. However, the maximum of the excitation function of the 85 keV transition cannot be reconciled with the 4^- choice and we conclude that the 121.6 keV state has a 2^- character. The angular distribution data of Fig. 5.10 for the weak 86 keV member of the 85-86 keV doublet is best fitted with $\Delta J=\pm 1$ spin sequences and the internal conversion data of Miracle et al. suggests that it is probably E1. If one takes this data at face value, the 35.6 keV level must be 1^+ or 3^+ in character. However, this assignment is inconsistent with the properties of transitions deexciting the 321.6 and 256.2 keV levels.

Alternatively, one can reach the 35.6 keV state via the 321.6 or 256.2 keV states. The former is deexcited by a 285-286-287 keV triplet feeding all three states ∿35 keV. The E1, $\Delta J=\pm 1$ character of the 287 keV transition defines the 321.6 keV state as 3^- or 5^-. The latter choice is ruled out by the strong presence of this state in the (p,n) spectra. The E1, $\Delta J=\pm 1$ nature of the 286 keV line now leads to a 2^+ or 4^+ choice for the 35.6 keV level.

The 256.2 keV state is deexcited by a 219-220 keV doublet. The 219 keV member is M1, ΔJ=±1 while the latter is M1 (or E1), ΔJ=0 in character. The 219 keV transition allows a 2^+ or 4^+ assignment for the 256.2 keV level, but the latter choice is ruled out by the strength of this state in the (p,n) spectra. The nature of the 220 keV transition now leads to a $2^{(+)}$ assignment for the 35.6 keV level.

Thus the weight of the evidence is in favour of the 2^+ choice for the 35.6 keV state. However, none of it is beyond reproach since in every case it has been necessary to use angular distribution results for the weaker member of a close doublet. While the detector resolution was better in the 85-86 case than in the 219-220 or 285-286-287 cases, the quality of the 86 keV data suffered from normalization problems and from all the problems inherent in angular distribution measurements for photon enegies below 100 keV. Some further support for the choice of 2^+ is provided by the work of Doukellis et al. (1974) on the neutron enhancement and angular distributions observed on and off-resonance for the $5/2^+$ isobaric analog state in ^{97}Tc. The data of these workers has been reworked, using the level structure of Fig. 5.12 .

The method used by Doukellis et al. involves the comparison of the experimental cross-sections observed on and off-resonance to the cross-sections predicted by the simplified Hauser-Feshbach model. A variety of spin sequences are tested untill a selfconsistent set is found. The results of this method depend strongly on the transmission coefficients used, the approximations applied to the model, and the detail knowledge of the decay scheme, since the normalization of the experimental to the theoretical values is based on the spin assignments assumed for the lowest energy levels. The following two comments are based on an attempt to rework Doukellis et al. data. In the first place, his data cannot be reconciled with the 4^- spin assignment to the 121.6 keV level, once the new level at 35.6 keV is included into the calculations regardless of whether the spin of this new level is 1^+, 2^+ or 3^+. In the second place, once the 2^- spin assignment to the 121.6 keV level is secured, only the 2^+ or 3^+ spin choice is possible for the 35.6 keV state on the basis of on-resonance data, while the off-resonance data gives strong preference to the 2^+ choice. Thus, we adopt $J^\pi=2^+$ for the 35.6 keV state.

The 36.4 keV level, $J^\pi=3^+$, see discussion for the 35.6 keV level.

The 45.3 keV level, $J^\pi=5^+$.

The M1 and $\Delta J=\pm1$ character of the 273 and 319 keV transitions connecting the 319.1 and 45.3 keV levels, and the 319.1 and the 7^+ ground state, respectively, coupled with the E1, $\Delta J=\pm1$ character of the 506 keV line connecting the 4^- 552.0 keV state to the 45.3 keV level are sufficient to uniquely define the spins and parities for the 319.1 and 45.3 keV levels as 6^+ and 5^+ respectively.

The 49.3 keV level, $J^\pi=6^+$.

The M1, $\Delta J=\pm1$ character of the 49, 127 and 143 keV lines involving the 7^+ ground state, the 4^+ level at 34.4 keV and the 49.3 and 177.0 keV levels uniquely define the spins and parities to the 177.0 and 49.3 keV levels as 5^+ and 6^+ respectively.

The 121.6 keV level, $J^\pi=2^-$, see discussion for the 35.6 keV level.

The 177.0 keV level, $J^\pi=5^+$, see discussion for the 49.3 keV level.

It should be noted that the (^{3}He,d) data obtained by Emigh et al.

(1979) and confirmed by the (^{3}He,d) measurements of this laboratory shows strong peaks corresponding to levels near 121.6 and 177.0 keV. Emigh's analysis suggests that both of these peaks behave as ℓ=1 transfers with an ℓ=4 admixture. The particle work can be reconciled with the 2^- assignment to the 121.6 keV state providing the weak ℓ=4 component is really ℓ=3 or 5. However, one cannot reconcile the particle work with the 5^+ assignment to the 177.0 keV state since the dominant ℓ=1 component requires negative parity. It is likely therefore that there are two states near 177 keV, with J^π values of 1^- (or 4^-) and 5^+ respectively, and that only the higher spin state is excited in the (p,n), (d,2n) or (α,n) reactions. No 1^- state has been identified in these experiments.

The 227.4 keV level, $J^\pi=3^-$.

The M1, $\Delta J=\pm 1$ character of the 105 keV transition limits the spin of this level to the $J^\pi=1^-$ or 3^- choice. The 1^- choice seems to be inconsistent with the pattern of intensities observed by Doukellis et al. for this level in the on and off-resonance spectra.

The 228.8 keV level, $J^\pi=4^+$.

The E1, $\Delta J=0$ character of the 323 keV transition feeding this state from the 552.0 keV 4^- level and the M1, $\Delta J=\pm 1$ character of the 183 keV transition leading to the 5^+ level at 45.3 keV uniquely defines $J^\pi=4^+$ for this level.

The 239.5 keV level, $J^\pi=3^+$.

The excitation functions and the M1, $\Delta J=\pm 1$ character of the 205 keV line, assign spin and parity 3^+ to this level.

The 256.2 keV level, $J^\pi=2^+$, see discussion for the 35.6 keV level.

The 316.8 keV level, $J^{\pi}=3^{-}$, see discussion for the 35.6 keV level.

The 319.1 keV level, $J^{\pi}=6^{+}$, see discussion for the 45.3 keV level.

The 321.6 keV level, $J^{\pi}=3^{-}$, see discussion for the 35.6 keV level.

The 352.7 keV level, $J^{\pi}=3^{-}$.

The M1, $\Delta J=\pm 1$ character of the 231 keV line together with the results of the excitation functions for the 125 and 231 keV transitions, uniquely define $J^{\pi}=3^{-}$ to this level. The 316.3 keV line deexciting this level was not observed in the coincidences and was placed in the decay scheme on the basis of energy balance.* The spectra show 314 and 316 keV transitions in ^{96}Mo originating in a common level. However, the 316/314 intensity ratio is a function of the alpha beam energy, proving conclusively that there is also a 316 keV transition in ^{96}Tc, with an excitation function consistent with an origin in the 352.7 keV state.

The 445.1 keV level, $J^{\pi}=3^{+}$.

The M1, $\Delta J=\pm 1$ character of the 188 and 410 keV transitions decaying to levels of spin 2^{+} and 4^{+} respectively uniquely define $J^{\pi}=3^{+}$ for the 445 keV level. One should note that neither the angular distribution nor the internal conversion results of Table 5.1 for the 216 keV transition support this spin assignment. However, because the 216 keV transition was not clearly resolved from a cluster of close-lying lines, we are not prepared to give those results much weight.

The 458.3 keV level, $J^{\pi}=3^{+}$.

The M1, $\Delta J=\pm 1$ character of the 202 keV transition coupled with the results of its excitation function assign $J^{\pi}=3^{+}$ to this level.

The 493.4 keV level, $J^{\pi}=3^{+}$.

Due to the M1, $\Delta J=\pm 1$ character of the 264 keV line and the $\Delta J=\pm 1$

character of the 236 keV transition connecting this level to levels of spin 4^+ and 2^+ respectively, the spin and parity of this level is uniquely defined as 3^+.

The 506.4 keV level, $J^\pi=5^+$.

The M1, $\Delta J=\pm 1$ character of the 457 keV transition feeding the level of spin 6^+ and the fact that this level was weakly populated in the (p,n) reaction leads to a unique J^π assignment of 5^+ to this state. The excitation functions for the weak 460 keV transition does not support this spin assignment. However, since there is some evidence that the 460 keV peak is a doublet, its excitation function is not to be trusted. The position of this line in the decay scheme is based on the energy balance only.

The 530.3 keV level, $J^\pi=4^+$.

Based on the energy balance, closely spaced levels are proposed at 530.3 and 530.7 keV. Due to the M1, $\Delta J=\pm 1$ character of the 485 and 494 keV transitions decaying from the 530.3 keV level to 5^+ and 3^+ states respectively, a J^π value of 4^+ seems to be uniquely defined for this level. The assignment for the 530.7 keV state is less reliable. The 208 and 213 keV lines are both M1, $\Delta J=\pm 1$ in character, which coupled to the excitation function results for the 213 keV line gives spin and parity of $J^\pi=4^-$ to the 530.7 keV level. There remains a difficulty with the 208 keV transition, since its energy fits a $530.3 \rightarrow 321.6$ assignment better than the $530.7 \rightarrow 321.6$ assignment assumed above. It may well be an unresolved doublet deexciting both levels.

The 530.7 keV level, $J^\pi=(4)^-$, see discussion for the 530.3 keV level.

The 542.2 keV level, $J^{\pi}=(5)^{+}$.

The M1, $\Delta J=\pm 1$ character of the 492 keV line indicates spin $J^{\pi}=5^{+}$ or 7^{+} for this level. Since the 492 keV transition is stronger in the 14 MeV spectrum than in the one at 18 MeV the latter choice is unlikely (see section 2.2, which explains how the ratio of intensities in the 18 and 14 MeV spectra is related to the spin of the initial level).

The 547.9 keV level, $J^{\pi}=(3)$.

Due to the $\Delta J=\pm 1$ character of the 291.7 keV transition the spin of this level can be 1 or 3. However, the large anisotropy observed for the angular distribution of this line rules out the first choice.

The 552.0 keV level, $J^{\pi}=4^{-}$, see discussion for the 35.6 keV level.

The excitation function results for the 374 keV transition contradict the spin assignment of this level. Since this line is the weakest of all the lines deexciting the 552.0 keV level and is also the only one not confirmed in coincidence with the 427 keV transition feeding this level, it may well be that it belongs elsewhere in the decay scheme.

The 564.3 keV level, $J^{\pi}=(3)^{+}$.

The internal conversion data identifies the 529, 528 and 308 keV transitions as predominantly M1 in character. Since these transitions feed levels with $J^{\pi}=4^{+}$, 2^{+} and 2^{+} respectively, J^{π} for the 564.3 keV state must be 3^{+}. The angular distribution data for the four transitions deexciting this state are not inconsistent with this choice, although for the 528 and 308 keV transitions the fit would be better if the 564.3 keV state had spin 2 or 4. Moreover the excitation function of the 308 keV line suggests that it is being fed from a level of spin 6 rather than 3.

For these reasons, we regard the 3^+ assignment as tentative.

The 565.6 keV level, $J^\pi=5^+$.

The transitions deexciting this level feed five states ranging in spin from 4^+ to 6^+. The M1, $\Delta J=\pm1$ character of the 246 and 531 keV transitions to states with $J^\pi=6^+$ and 4^+ respectively, lead to a unique 5^+ assignment for this level.

The 568.2 keV level, $J^\pi=(3^-)$.

This level was seen in both the (p,n) and (d,2n) reactions and is identified in the present work by a single gamma-ray of energy 340 keV. The spin of this level is based on the excitation function of this transition while the parity assignment rests on the results of Emigh et al. (1979) who found the level to be populated by an $\ell=1$ transfer.

The 575.0 keV level, $J^\pi=7^+$.

The assignment to this level can be made by using a loop which ascends from the 7^+ ground state through the 927.3 keV state to the 1062.7 keV level and then descends via the 575.0 keV state to the 6^+ 49.3 keV level. The E2, $\Delta J=-2$ character of the 927 keV transition leads to a 9^+ assignment for the 927.3 keV level. The M1, $\Delta J=\pm1$ character of the 135, 487 and 525 keV transitions then leads to unique assignments of 8^+ and 7^+ for the 1062.7 and 575.0 keV states respectively.

The 586.0 keV level, $J^\pi=4^+$.

The $\Delta J=\pm1$ character of the 346 keV transition feeding the 3^+ 239.5 keV state restricts the spin of this level to 2 or 4. The particle work of Doukellis et al.(1974) identified a 4^+ level at 590 keV. Since there are no other levels in this energy region, we have identified the 586 keV state with their 590 keV level and accepted their J^π assignment. The only other transition from this level observed in this work is the 269 keV gamma-ray, placed in the decay scheme on the basis of energy balance and coincidences with the 85 keV transition.

The 619.8 keV level, $J^{\pi}=3^{-}$.

This level feeds states with $J^{\pi}=3^{+}$, 2^{-}, 3^{-} and 3^{-}. The M1, $\Delta J=\pm 1$ character of the 498 keV transition to the 2^{-} state would permit either a 1^{-} or 3^{-} assignment. However, the large anisotropy in the observed angular distribution pattern would not permit the 1^{-} choice. The angular distributions of other transitions, although of poor quality, are consistent with this spin choice.

The 623.0 keV level, $J^{\pi}=(4)^{+}$.

The M1/E2 and $\Delta J=\pm 1$ character of the 383 keV line together with the Doukellis et al.(1974) observation that the spin of this level is J>2, yields $J^{\pi}=(4)^{+}$ as the most probable choice.

The 627.5 keV level, $J^{\pi}=3^{-}$.

This level is deexcited by six weak transitions to states with J^{π} values of 2^{+}, 3^{+}, 2^{-}, 4^{+}, 3^{-} and 3^{-} respectively. The $\Delta J=\pm 1$ character of the 398 keV line feeding the 4^{+} state and the M1, $\Delta J=\pm 1$ character of the 506 keV transition feeding the 2^{-} state lead to the 3^{-} assignment given above. It should be noted that the 506 keV transition is the weaker member of an unresolved doublet, whose combined K-shell internal conversion coefficient is midway between the theoretical E1 and M1 values. Since the stronger component is known to be E1 from the level scheme, the weaker one must be M1 and leads to a negative parity for the 627.5 keV level. The angular distributions of the other four transitions are of poor quality but consistent with the 3^{-} assignment.

The 646.8 keV level, $J^{\pi}=(4)^{-}$.

This state is based on the presence of 294 and 419 keV transitions feeding levels with $J^{\pi}=3^{-}$. The M1, $\Delta J=\pm 1$ character of the 294 keV line restricts J^{π} for the 646.8 keV level to 2^{-} or 4^{-}. However, the large anisotropy of the angular distribution observed for this gamma-ray and its small intensity in the (p,n) spectrum favour the 4^{-} choice. The excitation function of the 419 keV line suggests that it deexcites a state of spin greater than 4. On the available evidence it was not possible to decide if this transition should be placed somewhere else in the decay scheme or whether it is a member of a doublet whose second component deexcites a high spin state.

The 656.2 keV level, $1 \leq J \leq 5$.

This level is defined by only one transition for which no information is available. Most probably this line is dipole in character.

The 720.6 keV level, $J^{\pi}=(6^{+})$.

This level is defined by transitions of energy 543 and 720 keV leading to states of $J^{\pi}=5^{+}$ and 7^{+} respectively, with coincidence evidence for the former line. The 720 keV transition is known to be M1 from the polarization data, has a $\Delta J=\pm 1$ character, and is in coincidence with no other transition. The 543 keV line is of $\Delta J=\pm 1$ character and unknown multipolarity. On the evidence, the 720.6 keV level must have $J^{\pi}=6^{+}$. However, since the 720 keV assignment to the decay scheme was based on energy balance alone, we regard the J^{π} assignment as tentative.

The 732.9 keV level, $J^{\pi}=4^{-}$.

This level is deexcited by four relatively weak transitions to states of $J^{\pi}=2^{-}$, 3^{-}, 3^{-} and 3^{-} respectively. The M1, $\Delta J=\pm 1$ character of the 416 keV transition feeding a 3^{-} state leads to a 2^{-} or 4^{-} spin assignment. However, the excitation function for this transition suggests that it originates in a state of spin 4 rather than 2. The fact that this level escaped detection in all the (p,n) and (d,2n) experiments except the very sensitive work of Kern et al.(1978), also suggests that the 4^{-} assignment is to be preferred.

The 739.9 keV level, $3<J<9$.

This level is based on one piece of coincidence information involving a very weak line and nothing can be said about its nature.

The 749.9 keV level, $J^{\pi}=(3^{+})$.

The evidence for this level is based on one piece of coincidence information, involving the 493 keV transition, which feeds the 2^{+} 256.2 keV state. Unfortunately, this transition is part of a close doublet which could not be resolved in either the gamma-ray or electron spectra. The data suggests that it is an M1, $\Delta J=\pm 1$ transition, but the evidence is not very conclusive. This level was weakly observed in the (p,n) and (d,2n) reactions, therefore the $J^{\pi}=3^{+}$ assignment is highly probable.

The 752.5 keV level, $J^{\pi}=6^{+}$.

This level feeds states of $J^{\pi}=7^{+}$; 6^{+} and 5^{+} respectively. The M1, $\Delta J=\pm 1$ character of the 752 and 575 keV transitions lead to a unique J^{π} of 6^{+} for this state. The excitation functions for these two transitions are identical in shape. Although, these functions would favour a spin 4 rather than a spin 6 assignment, the peaks involved are so difficult to analyse that the functions have little predictive value.

The 789.1 keV level, $J^{\pi}=4^{-}$.

This level is deexcited by transitions to states of spin 4^{+}, 2^{-} and 3^{-}. The M1, $\Delta J=\pm 1$ character of the 472 keV transition to the 3^{-} state and the $\Delta J=\pm 2,0$ character of the 667 keV line to the 2^{-} level limit J^{π} to 2^{-} or 4^{-}. The 2^{-} assignment to the 789.1 keV state would not allow transitions to the positive parity levels. Moreover, the absence of this state in the (p,n) work supports the 4^{-} assignment.

The 794.4 keV level, $J^{\pi}=4^{-}$.

This level feeds states of 2^{-} and 3^{-}. The excitation function and the $\Delta J=\pm 1$ character of the 477 keV transition feeding the 3^{-} level indicate a J=4 assignment. The existence of a $4\rightarrow 2^{-}$ transition defines the parity as negative.

The 801.6 keV level, $J^{\pi}=4^{-}$.

This level feeds states of $J^{\pi}=2^{-}$, 3^{-} and 3^{-}. The $\Delta J=\pm 1$ character of the 448 and 484 keV transitions to the 3^{-} levels restrict J to 2 or 4. The strong component of the 680 keV doublet which feeds the 2^{-} level has an excitation function characteristic of an origin in a J=4 state, and also defines the parity as negative since a $4^{+}\rightarrow 2^{-}$ transition would not be observed.

The 815.2 keV level, $J^{\pi}=4^{+}$.

This level feeds states of $J^{\pi}=5^{+}$, 6^{+}, 5^{+} and 6^{+}. The $\Delta J=\pm 1$ character of the 638 keV line to the upper 5^{+} state and the E2 character of the 496 keV transition to the upper 6^{+} state uniquely defines J^{π} for the 815.2 keV level as 4^{+}.

The 816.7 keV level, $J^{\pi}=(3^{-})$.

This state feeds levels of $J^{\pi}=4^{+}$, 2^{-} and 3^{-}. The $\Delta J=\pm 2,0$ character of the 589 keV transition feeding the 3^- state and the $\Delta J=\pm1$ character of the 782 keV transition to the 4^+ level limit J to 3 or 5. The presence of a 695 keV transition feeding the 2^- state excludes the J=5 choice. The 816.7 keV level was also observed in the (p,n) reaction by Kern et al. (1978) who suggested that it is of negative parity.

The 821.3 keV level, $1 \leq J \leq 5$.

The evidence for this level is based on one piece of coincidence information involving a very weak line and nothing can be said about its nature.

The 821.8 keV level, $J^\pi=(6^+)$.

This level feeds states of $J^\pi=6^+$, 5^+ and 6^+. The $\Delta J=\pm1$ character of the 644 keV line feeding the 5^+ level indicates that J=4 or 6. The angular distribution of the 772 keV transition feeding the lower 6^+ state suggests a $\Delta J=\pm2,0$ transition. Thus we make a tentative 6^+ assignment.

The 829.0 keV level, $J^\pi=(4^+)$.

This level feeds states of $J^\pi=3^+$ and 2^+. The $\Delta J=\pm2,0$ character of the 572 keV transition to the 2^+ level and the possible $\Delta J=\pm1$ character of the 793 keV transition to the 3^+ state limits J to 2 or 4. The large anisotropy for the 572 keV angular distribution rules out the first choice. The presence of a 4 to 2^+ transition requires that [illegible]e state has positive parity.

The 840.2 keV level, $0<J<6$.

This state is defined by only one transition for which no information is available. Most probably this line is dipole in character.

The 867.2 keV level, $J^{\pi}=4^{-}$.

This level is located in the decay scheme on the basis of two pieces of coincidence data. However, the excitation function and the $\Delta J=\pm1$ character of the 550 keV transition to the 3^{-} state identifies spin as 4. Emigh et al. (1979) observed a level at 873±3 keV populated by an $\ell=1$ particle transfer in the (^{3}He,d) reaction. Its parity must therefore be negative.

The 885.8 keV level, $J^{\pi}=6^{+}$.

The evidence for this level is based on transitions to states with $J^{\pi}=7^{+}$, 5^{+}, 5^{+}, 5^{+} and 7^{+}. Due to the M1, $\Delta J=\pm1$ character of the 310 keV line feeding the upper 7^{+} state and the $\Delta J=\pm1$ character of the 379 keV transition feeding the middle 5^{+} state the spin and the parity are uniquely determined. The $\Delta J=\pm1$ character of the 886 keV transition to the 7^{+} state also fits this assignment. Although the $\Delta J=0$ character of the weak 840 keV transition to the lower 5^{+} state does not agree with this assignment, its angular distribution is of poor quality.

The 909.6 keV level, J=4.

Due to the $\Delta J=\pm1$ character of the 403 and 588 keV transitions feeding levels of spin 5^{+} and 3^{-}, spin 4 is uniquely determined for the 909.6 keV level.

The 927.3 keV level, $J^{\pi}=9^{+}$, see discussion for the 575.0 keV level.

The 934.3 keV level, $J^{\pi}=(3^{+})$.

This level feeds states of $J^{\pi}=4^{+}$, 5^{+}, 4^{+} and 3^{-}. The 899 keV transition to the lower 4^{+} state is $\Delta J=\pm1$ in character and leads to J=3 or 5. The presence of transitions to both the 5^{+} and 3^{-} states eliminates all but the 5^- and 3^+ options. The positive parity choice is made on the basis of the particle work of Emigh et al. (1979) who observed a level at 933$\pm$5 keV populated by an ℓ=2 transfer.

The 942.6 keV level, J=(4).

Both the location and spin of this level must be regarded as tentative since the assignment is based on evidence from one $\Delta J=\pm1$ transition to a 3^- level. The large anisotropy in the angular distribution for this 625 keV transition favours a J=4 assignment. Because the calculated and "theoretical" c_{ij} coefficients for this line are rather different, it may be that the transition has been incorrectly located in the level scheme.

The 947.0 keV level, $J^\pi=8^+$.

This level is deexcited by strong transitions to states of $J^\pi=7^+$, 6^+ and 7^+ and fed from three high lying states. The M1, $\Delta J=\pm1$ character of the 371 keV transition to the 7^+ 575.0 keV level identifies J^π as 6^+ or 8^+. The peak in the excitation function of 18.2 MeV for transitions from this state strongly imply the 8^+ choice, since the appropriate value for a 6^+ state, based on 13 transitions would be 16.7 MeV.

Alternatively, one can arrive at the same conclusion by starting from the 9^+ state at 927.3 keV (see discussion of the 575.0 keV level), proceeding upward to the 1922.9 keV state whose 11^+ character is defined by the E2, $\Delta J=-2$ character of the strong 995 keV transition, thence proceeding to the 2148.5 keV state whose 11^+ character is defined by the results of the excitation function, the dipole $\Delta J=0$ character of the 225 keV radiation and the M1, $\Delta J=\pm1$ character of the 169 and 395 keV transitions. (Unfortunately, the region of the electron spectrum which could have uniquely established the M1 character of the 225 keV transition was not scanned). From the 2148.5 keV 11^+ state, one then proceeds downward via a triple cascade of $\Delta J=\pm 1$ transitions of energy 444, 255 and 500 keV respectively to the 947.0 keV state. The minimum spin possible for this state is thus 8 with the J=6 value being ruled out. The established M1 character of two members of the triple cascade now lead automatically to J^π values of 9^+ and 10^+ for the 1447.8 and 1703.4 keV states.

The 971.4 keV level, J=3.

This level is deexcited by weak transitions to states of $J^\pi=2^+$, 2^+ and 4^-. The $\Delta J=\pm 1$ character of the 714 keV transition to the upper 2^+ state leads to a J=3 assignment. The J=1 choice is inconsistent with the observed transition to the 4^- level. The parity of the 971.4 keV state is unknown.

The 979.2 keV level, $J^\pi=5^-$.

This level is deexcited by six relatively weak transitions to states of $J^\pi=4^+$, 5^+, 4^+, 3^-, 4^- and 4^-. The M1, $\Delta J=\pm 1$ character of the medium strength 427 keV transition feeding the lower 4^- state, coupled with the excitation function results for this transition leads to a unique 5^- assignment to this level.

The 980.7 keV level, J=(5).

This level is identified by two transitions to levels with $J^\pi=6^+$ and 5^+ respectively. The $\Delta J=\pm 1$ character of the 931 keV transition to the 6^+ state and the fact that this gamma-ray is excited more strongly in the 14 MeV than in the 18 MeV experiment favours the J=5 choice. The parity of this level is unknown.

The 1040.8 keV level, $J^\pi=7^+$.

This level is deexcited by two moderately intense transitions to levels with $J^\pi=7^+$ and 6^+. The M1 character of the $\Delta J=\pm1$ 721 keV transition to the 6^+ level, and the M1/E2 nature of the $\Delta J=0,\pm2$ ground state transition uniquely define J^π as 7^+ for this level.

The 1042.4 keV level, $J^\pi=5$.

This level is based on two transitions feeding states of 4^+ and 6^+ respectively. The $\Delta J=\pm1$ character of the 1007 and 993 keV transitions to these states lead to a unique spin assignment of 5. The parity is unknown.

The 1053.8 keV level, $J^\pi=(5)$.

This level is based on single piece of coincidence evidence which shows that the 1004 keV transition feeds the 6^+ state at 49.3 keV. The $\Delta J=\pm1$ character of this fairly weak transition indicates a 5 or 7 spin assignment. The 5 choice is favoured because the transition is more strongly excited in the 14 MeV than in the 18 MeV experiment.

The 1062.7 keV level, $J^\pi=8^+$, see discussion for the 575.0 keV level.

The 1065.8 keV level, $0\leqslant J<5$.

This level is based on coincidence data for the weak 809 keV transition which feeds the 256.2 keV 2^+ state.

The 1071.6 keV level, $J^\pi=(4)$.

This level is based on coincidence data for the weak 894 keV transition which feeds the 177.0 keV 5^+ state. The transition appears to be of $\Delta J=\pm1$ character and is more strongly excited at 14 than at 18 MeV. A J=4 assignment to this level is therefore favoured.

The 1103.2 keV level, $J^{\pi}=(5)$.

This level is based on coincidence data for the weak 1071 keV transition which feeds the 49.3 keV 6^+ state. The probable $\Delta J=\pm1$ character of this gamma-ray which is more strongly excited at 14 MeV than at 18 MeV suggests a J=5 assignment.

The 1118.3 keV level, $J^{\pi}=(5^+)$.

This level is based on coincidence data for two transitions which feed states of $J^{\pi}=5^+$ and 6^+ respectively. The level is also fed from a state of unknown character at 1610.2 keV. The 799 keV transition which feeds the 6^+ state is part of an unresolved doublet. At 14 MeV, roughly 33% of the total intensity is associated with this transition, a fraction that drops to less than 10% at 18 MeV. Since the composite angular distributions are identical and characteristic of $\Delta J=\pm1$, at both energies, it is concluded that both components are $\Delta J=\pm1$ in character. One would expect the spin of the 1118.3 keV state to be 5 or 7 with the lower value favoured. The 941 keV transition feeding the 5^+ state must also be part of an unresolved doublet since the measured coincidence probability for 941-143 keV is more than 30% smaller than expected from the singles intensity. Thus little significance can be attached to the $\Delta J=\pm1$ angular distribution character of this transition. We conclude that the spin of the 1118.3 keV level is probably 5. Its parity is positive, if one accepts the weak evidence for the M1 character of the 799 keV line.

The 1139.0 keV level, $J^{\pi}=8^+$.

This state is based on transitions feeding levels of $J^{\pi}=7^+$, 6^+, 7^+ and 9^+. The strong transition to the 7^+ ground state is $\Delta J=\pm1$ and M1/E2, and that to the 6^+ state is $\Delta J=0,\pm2$ in character. These facts and the existence of a transition to the 9^+ state uniquely define $J^\pi=8^+$.

The 1140.1 keV level, $J^\pi=(5^-)$.

This level is based on coincidence data involving a member of the 912 keV doublet and the energy fit of the 1105 keV gamma-ray, transitions feeding states of 3^- and 4^+ respectively. Both transitions are components of unresolved doublets in the angular distribution measurements. The excitation function for the 1105 keV line favours spin J=5, and consequently negative parity is required for this level.

The 1149.0 keV level, $J^\pi=(5)$.

This state is based on coincidence data involving an 829 keV transition to a 6^+ level and the energy fit of the 1115 keV radiation to the 34.4 keV 4^+ state. The angular distributions are poor but the spin is probably 5, due to the $\Delta J=\pm1$ appearance of the 1115 keV line.

The 1152.1 keV level, $J^\pi=6^-$.

There are six transitions deexciting this level, feeding states with $J^\pi=7^+$, 5^+, 5^+, 6^+, 4^- and 5^- respectively. The M1 character of the $\Delta J=\pm1$ transition to the 5^- state, the E2 nature of the $\Delta J=0,\pm2$ transition to the 4^- state and the $\Delta J=\pm1$ character of the transitions to the 7^+, 5^+ and 5^+ states uniquely define J^π for this level.

The 1183.3 keV level, $J^\pi=(5)$.

There are five transitions deexciting this level and leading to states with $J^\pi=6^+$, 5^+, 5^+, 4^+ and 4^- respectively. The excitation function results and the $\Delta J=\pm1$ character of the relatively strong 1134 keV transition to the 6^+ state indicate a spin 5 assignment. However, the $\Delta J=\pm1$ character of the 676 keV transition to the upper 5^+ and the $\Delta J=0,\pm2$ nature of the 596 keV transition to the lower 4^+ state contradict this assignment.

It may well be that there are two levels very close to this energy.

The 1187.7 keV level, $J^\pi=5$.

This level is based on four transitions feeding states of $J^\pi=6^+$, 4^-, (6^+) and 4^- respectively. The $\Delta J=\pm 1$ character of the 1138 and 635 keV transitions feeding the lower 6^+ and 4^- states define J as 5.

The 1203.0 keV level, $J^\pi=(6^+)$.

The existence of this level is based on two pieces of coincidence evidence and the energy fit of a third gamma-ray. The state feeds levels with $J^\pi=4^+$, 6^+ and 6^+ respectively. While the positive anisotropy of the moderately intense 1153 keV transition feeding the lower 6^+ state suggests an assignment of 4 or 6, the negative anisotropy of the weak 883 keV transition suggests an assignment of 5 or 7. The angular distribution for the 1168 keV transition to the 4^+ state is unknown. However, the excitation function for this line favours the J=6 choice. In the face of this contradictory evidence we favour the 6^+ assignment based on the strongest line.

The 1211.7 keV level, $J^\pi=(2,4)$

The existence of this state depends on the presence of 895-195 keV coincidences involving the 3^- 316.8 keV state. The $\Delta J=\pm 1$ character of the 895 keV transitions limits the spin assignment to 2 or 4; the upper value being slightly preferred because of the strong anisotropy of the 895 keV angular distribution.

The 1255.6 keV level, $J^\pi=4$.

The existence of this level depends on 1078-142 keV coincidences involving the 5^+ 177.0 keV intermediate state and the energy fit of the 1209 keV gamma-ray which is the stronger member of a close doublet.

The excitation function of the 1078 keV transition and the ΔJ=±1 character of the 1209 keV line assign spin 4 to the 1255.6 keV level.

The 1271.2 keV level, 0<J<6.

The existence of this level rests on the presence of 918-231 keV coincidences. Its spin and parity are unknown.

The 1290.4 keV level, $J^{\pi}=4$.

The excitation function results and the ΔJ=±1 character of the 1113 keV line feeding the 5^+ state at 177.0 keV uniquely assign spin 4 to this level. The parity of this level is unknown.

The 1294.7 keV level, $J^{\pi}=(5)$.

The existence of this level rests on the presence of 1117-142 keV coincidences involving the 5^+ 177.0 keV intermediate state. The 1117 keV transition is probably a doublet, of which at least 70% belongs at this location in the level structure. The positive anisotropy of this doublet suggests ΔJ=0,±2 . The spin is probably 5 although the values of 3 and 7 are possible.

The 1314.0 keV level, $J^{\pi}=5^+$.

This level is based on seven transitions, leading to states of spin 7^+, 5^+, 6^+, 5^+, 4^+, 6^+ and 6^- respectively. The ΔJ=±1 character of the transitions of energy 1084 and 1264 to 6^+ and 4^+ states and the existence of the ground state transition uniquely define J^{π} as 5^+.

The 1367.0 keV level, $J^{\pi}=(4)$.

The existence of this state is based on 1050-195 keV coincidences involving the 3^- 316.8 keV intermediate state. The ΔJ=±1 character of the 1050 keV keV transition suggests that J=2 or 4. The strong anisotropy of the angular distribution strongly favours the J=4 choice.

The 1408.3 keV level, $J^{\pi}=(4^{-})$.

This level is based on the presence of 1231-142 keV coincidences involving the 5^{+} 177.0 keV intermediate state. Emigh et al. (1979) observed a level at 1402$\pm$6 keV, populated by an $\ell=1$ particle transfer. This level therefore has $J^{\pi}=1^{-}$ to 4^{-}. If the 1408.3 keV level observed here is the same level, it must have $J^{\pi}=4^{-}$.

The 1438.7 keV level, $J^{\pi}=(3^{-})$.

This level is based on coincidence data for the 1209 and 569 keV transitions which feed states of $J^{\pi}=4^{+}$ and 4^{-} respectively. The $\Delta J=\pm1$ character of these transitions limit J to 3 or 5. However, the low value for the maximum of the excitation function for the composite 1209 keV peak suggests the J=3 spin choice, while the M1/E2 character of the 569 keV transition identifies the parity as negative. Since the 1209 keV line is a doublet and the 569 keV may be one, the assignment must be regarded as tentative.

The 1447.8 keV level, $J^{\pi}=9^{+}$, see discussion for the 947.0 keV level.

The 1482.4 keV level, $J^{\pi}=(4^{-})$.

This level is based on the weak transitions of energy 1360 and 1305 keV feeding the 2^{-} 121.6 keV and 5^{+} 177.0 keV states respectively. Its spin and parity is thus limited to the 3^{+} or 4^{-} choice. Emigh et al. observed a negative parity state at 1460$\pm$10 keV populated by an $\ell=1$ particle transfer. If one can assume we are dealing with the same level, its J^{π} value must be 4^{-}.

The 1487.5 keV level, $J^{\pi}=8$.

This level is based on the presence of strong 912-525 keV coincidences involving the 7^{+} 575.0 keV intermediate state. Although the 912 keV transition is the strongest component of a doublet, its ΔJ=±1 character limits the spin of the initial state to 6 or 8. The excitation function is consistent only with the J=8 choice. The parity is unknown.

The 1516.2 keV level, $J^{\pi}=(7^{+})$.

This level is based on coincidence data involving the 1339 and 1196 keV transitions which feed the 5^{+} 177.0 keV and 6^{+} 319.1 keV levels respectively. The ΔJ=±1 character of the strong 1196 keV transition limits J to 5 or 7. The very strong anisotropy of the pattern suggests the higher spin value. With this choice, the parity must be positive.

The 1536.3 keV level, $J^{\pi}=(4^{-})$.

This state is based solely on evidence for 1359-142 keV coincidences involving the 5^{+} 177.0 keV intermediate state. Emigh et al. identified a level at 1540±15 keV populated by an ℓ=1 particle transfer. If we identify the 1536.3 keV level with this state, it must be 4^{-} in character.

The 1556.6 keV level, $J^{\pi}=(4,6)$.

This state is based on coincidence evidence for transitions leading to the 5^{+} 177.0 keV and 4 909.6 keV levels respectively. Both transitions are weak. However, the ΔJ=0,±2 appearance of the transition to the 4 state suggests a J=4 or 6 assignment. The experimental data were fitted to the J=4 choice.

The 1596.4 keV level.

The identification of this level rests on 1419-142 keV coincidences involving the 5^{+} 177.0 keV intermediate state. A level at 1595±10 keV populated by an ℓ=1 or 2 particle transfer was identified by Emigh et al.. Even if this level is the same as the one observed in the present work, the data does not permit a unique J^{π} assignment. However, it limits the

J^{π} choice to 4^-, 3^+, 4^+ and 5^+.

The 1597.5 keV level, $J^{\pi}=6^{(-)}$.

The evidence for this level includes one piece of coincidence information involving the 618 keV transition to the 5^- 979.2 keV state and two transitions to the 4^- 552.0 keV level and to the 7^+ ground state. These two transitions were placed in the decay scheme on the basis of energy balance alone. Since the 1597.5 keV transition falls in a region of low peak density in the spectrum, its energy fit and its J=6 type excitation functions are meaningful. On the other hand, since the 1045 keV gamma-ray is in a very dense region of the spectrum, its energy fit may well be accidental and are given little weight to either its J=8 type excitation function or its $\Delta J=0,\pm 2$ character.

The 1610.2 keV level, $2<J<8$.

This level is based solely on 491-799 keV coincidences involving the 1118.3 keV 5^+ intermediate state. Nothing can be said about its spin or parity.

The 1636.3 keV level, $2<J<8$.

This level is based solely on weak 1459-142 keV coincidences involving the 177.0 keV 5^+ state. Nothing can be said about its spin or parity.

The 1703.4 keV level, $J^{\pi}=10^+$, see discussion for the 947.0 keV level.

The 1767.3 keV level, $J^{\pi}=(4^+,5^+)$.

This level is based on weak 1448-273 keV coincidences involving the 319.1 keV 6^+ intermediate state. Emigh et al. identified a level at 1772±9 keV populated by an $\ell=1$ or 2 particle transfer, its spin might be 1^- to 4^- or 1^+ to 5^+. If their state is the same as the 1767.3 keV state identified here, J^π must be 4^+ or 5^+. The experimental data were fitted to the $J^\pi=5^+$ choice.

The 1861.8 keV level, $J^\pi=9^+$.

This level is based on strong transitions to the 8^+ states at 947.0 and 1062.7 keV. The $\Delta J=\pm 1$ character of the 914 and 799 keV transitions involved and the M1 nature of the latter establish J^π as 7^+ or 9^+. The excitation functions make the higher spin choice mandatory.

The 1922.9 keV level, $J^\pi=11^+$, see discussion for the 947.0 keV level.

The 1974.4 keV level, $J^\pi=8$.

Evidence for this level rests on strong 1399-525 keV coincidences involving the 575.0 7^+ intermediate state. The angular distribution of the 1399 keV transition suggests a $\Delta J=\pm 1$ character while its excitation function supports a spin 8 rather than a spin 6 assignment.

The 2148.5 keV level, $J^\pi=11^+$, see discussion for the 947.0 keV level.

The 2214.1 keV level, $J^\pi=10^+$.

This level is based on two pieces of coincidence evidence involving a weak transition to the 1062.7 keV 8^+ state and a strong one to the 9^+ 1861.8 keV state. The M1, $\Delta J=\pm 1$ character of the strong 352.2 keV transition, together with its excitation function uniquely defines J^π as 10^+ for this state.

The 2318.2 keV level, $J^\pi=12^+$.

This level is firmly based on transitions to the 10^+ 1703.4 keV, the 11^+ 1922.9 keV and the 11^+ 2148.5 keV states. The M1, $\Delta J=\pm 1$ character of the 169 and 395 keV transitions and their excitation functions uniquely determine J^π as 12^+ for this level.

The 2397.7 keV level, $J^{\pi}=11^{+}$.

This level is firmly based on two transitions to states of $J^{\pi}=9^{+}$ and 10^{+} respectively. The $\Delta J=0,\pm2$ character of the 536 keV transition and the M1, $\Delta J=\pm1$ character of the 183 keV line as well as their excitation functions lead to a unique 11^{+} assignment.

The 2600.2 keV level, $J^{\pi}=13^{+}$.

This level is based on strong 282-614, 282-395 and 282-169 keV coincidences involving the 2318.2 keV 12^{+} intermediate state. The M1, $\Delta J=\pm1$ character of the 282 keV transition and its excitation function lead to a unique 13^{+} assignment to this level. The fact that there is also a second and weak 282 component in the composite 282 keV peak has no influence on this conclusion.

The 2643.4 keV level, $J^{\pi}=10^{+}$.

This level is based on moderately weak 325-395 and 325-169 keV coincidences involving the 12^{+} 2318.2 keV intermediate state. The E2, $\Delta J=0,\pm2$ character of the 325 keV transition and its excitation function requires that it originates in a 10^{+} state. It should be noted that in an earlier report from this laboratory (Mach et al.,1980) made before confidence in the use of excitation functions to determine spins, had been established, this state was tentatively assigned $J^{\pi}=14^{+}$.

The 3020.7 keV level, $J^{\pi}=12^{+}$.

This level is based on the presence of 806-352 keV coincidences involving the 10^{+} 2214.1 keV intermediate state. The $\Delta J=0,\pm2$ character of the 806 keV transition and its excitation function assign spin 12 to this level. Since a $\Delta J=-2$ transition must almost certainly be E2, we arrive at $J^{\pi}=12^{+}$ for the 3020.7 keV level.

Table 5.1

Energies, intensities, angular distribution coefficients and multipolarities of the gamma-ray transitions in ^{96}Tc.

Table 5.1

Photon energy (keV)	Classification (keV)	J^π Assignment	Energy for σ_{max} (MeV)	Multipolarity	Photon Intensities a)	Experimental Coefficients $A_2 \times 100$	Experimental Coefficients $A_4 \times 100$	Calculated Coefficients b) $A_2 \times 100$	Calculated Coefficients b) $A_4 \times 100$	$\delta \times 100$
45.3(1) c)	45.3→ 0.0	$5^+ - 7^+$			d) < 1.8					
49.3(1)	49.3→ 0.0	$6^+ - 7^+$	17.4(2)	M1	d) 68					
					102	- 9.0(5)	- 2.4(7)	- 9.3(5)	0.0	-3(4)
52.0(1) e)	228.8→ 177.0	$4^+ - 5^+$		M1	2.5 e)					
65.5(1) e)	321.6→ 256.2	$3^- - 2^+$		E1	3.3 e)					
85.1(1)	121.6→ 36.4	$2^- - 3^+$	15.7(1) f)	E1	d) 69					
					267	- 2.8(6)	- .6(9)	- 2.7(2)	0.0	18(-7 to 65)
85.9(1)	121.6→ 35.6	$2^- -(2)^+$	15.7(1) f)	E1	d) 14					
					56	- 4(2)	.7(26)	- 3.6(8)	-.2(1)	-41(-∞ to -20)
105.8(1)	227.4→ 121.6	$3^- - 2^-$	15.8(2)	M1	d) 6.6					
					18.2	- 2.8(14)	-.6(15)	- 3.0(5)	.1(1)	0(18)
111.6(2)	979.2→ 867.2	$5^- - 4^-$			.44					
125.3(1)	352.7→ 227.4	$3^- - 3^-$	16.0(2)	M1/E2	d) 1.9					
					1.9	- 5(4)	7(5)	-.9(3)	-.9(4)	-45(± ∞)
127.7(1)	177.0→ 49.3	$5^+ - 6^+$	16.5(2)	M1	d) 17.0					
					37.9	- 4.7(8)	0.0(9)	- 4.4(4)	0.	- 5(5)
135.3(2)	1062.7→ 927.3	$8^+ - 9^+$	18.2(2)	M1	d) 4.5	-15(4)	5(4)	-13.9(2)	0.	- 2(6)
					3.1	-15(4)	4(5)	-12.5(10)	0.	- 2(7)
142.6(1)	177.0→ 34.4	$5^+ - 4^+$	16.4(2)	M1	d) 33.7	- 7.4(6)	1.6(7)	- 6.5(6)	.1(1)	10(5)
					80.2	- 7.6(6)	0.0(6)	- 7.6(7)	.1(1)	5(5)
162.3(4)	1314.0→1152.1	$5^+ - 6^-$	15.5(5) f)		.8 e)					
162.8(3)	656.2→ 493.4	$- 3^+$	15.5(5) f)		.3 e)					
169.6(1)	2318.2→2148.5	$12^+ - 11^+$	19.6(3)	M1	d) 5.2	-18(2)	5(2)	-17(1)	0.	4(3)
					.86	-21(11)	3(13)	-19(1)	0.	2(14)
173.0(1)	1152.1→ 979.2	$6^- - 5^-$	16.8(4)	M1	2.4	-14(5)	-4(6)	-16.5(10)	0.	2(14)

Table 5.1 (continued)

Photon energy (keV)	Classification (keV)	J^π Assignment	Energy for σ_{max} (MeV)	Multipolarity	Photon Intensities[a)]	Experimental Coefficients[b)] $A_2 \times 100$	Experimental Coefficients $A_4 \times 100$	Calculated Coefficients $A_2 \times 100$	Calculated Coefficients $A_4 \times 100$	$\delta \times 100$
176.8(3)	177.0→ 0.0	$5^+ - 7^+$	16.3(2)[f)]		d) .6					
					.4	24(19)	21(23)	25(8)	3(1)	-140(-∞ to +24)
178.0(1)	530.7→ 352.7	$(4)^- - 3^-$	16.3(2)[f)]	M1	1.4	2(9)	- 2(10)	1.2(2)	.3(1)	20(-42 to +∞)
182.6(2)[e)]	971.4→ 789.1	$3 - 4^-$			3.0[e)]					
183.3(1)	228.8→ 45.3	$4^+ - 5^+$	16.5(3)[f)]	M1	d) 18	- 7.3(7)[f)]	.8(8)	- 6.8(5)	0.	-2(4)
					63	- 2.5(4)[f)]	.0(5)	- 2.5(5)	0.	-4(5)
183.5(1)[e)]	2397.7→2214.1	$11^+ - 10^+$	16.5(3)[f)]	M1	d) 8.7[e)]	- 7.3(7)[f)]	.8(8)	- 7.3(9)	.3(1)	11(2)
					2.6[e)]	- 2.5(4)[f)]	.0(5)	- 3.2(2)	.4	12(2)
187.0(1)	506.4→ 319.1	$5^+ - 6^+$	15.8(4)	M1	1.6	- 2(5)	- 6(6)	- 4.4(4)	0.	0.(18)
188.9(1)	445.1→ 256.2	$3^+ - 2^+$		M1/E2	.5	-24(22)	-10(27)	-15(11)	- 4(2)	0.(± ∞)
191.8(3)[g)]	227.4→ 35.6	$3^- -(2)^+$	15.7(3)[f)]		2.5					
192.2(3)[g)]	228.8→ 36.4	$4^+ - 3^+$	15.7(3)[f)]	M1	5.0					
195.2(1)	316.8→ 121.6	$3^- - 2^-$	16.0(1)	M1	d) 25.7	- 6.4(6)	.3(8)	- 6.4(1)	.1(1)	10(7)
					83.7	- 2.1(3)	- .2(4)	- 2.2(3)	.2(1)	11(11)
202.1(1)	458.3→ 256.2	$3^+ - 2^+$	15.9(2)	M1	4.1	- 4(2)	3(3)	- 3(1)	0.	-7(40)
205.1(1)	239.5→ 34.4	$3^+ - 4^+$	15.8(2)	M1	17.5	- 2.3(9)	1(1)	- 1.6(4)	0.	2(15)
208.7(1)	530.7→ 321.6	$(4)^- - 3^-$	16.0(2)	M1	4.0	- 5(3)	3(4)	- 3.1(5)	0.	7(20)
	530.3→ 321.6	$4^+ - 3^-$								
211.5(3)	1139.0→ 927.3	$8^+ - 9^+$			1.	-17(14)	-13(16)	-24.4(8)	0.	6(24)
213.8(1)	530.7→ 316.8	$(4)^- - 3^-$	16.0(2)	M1/E2	d) 0.8					
					3.6	-3(3)	-4(4)	-4.9(7)	.1(1)	9(-21 to +28)
216.1(1)	445.1→ 228.8	$3^+ - 4^+$		(E2)	1.5	6(10)	-1(12)	5.3(7)	0.	-17(±∞)
219.8(1)	256.2→ 36.4	$2^+ - 3^+$	15.6(2)[f)]	M1	d) 4.8					
					25.5	-2.8(7)	1.3(8)	-2.2(4)	0.	22(27)
220.6(2)	256.2→ 35.6	$2^+ -(2)^+$	15.6(2)[f)]	M1	d) 2.5					

Table 5.1 (continued)

Photon energy (keV)	Classification (keV)	J^{π} Assignment	Energy for σ_{max} (MeV)	Multipolarity	Photon Intensities[a]	Experimental Coefficients $A_2 \times 100$	Experimental Coefficients $A_4 \times 100$	Calculated Coefficients[b] $A_2 \times 100$	Calculated Coefficients[b] $A_4 \times 100$	$\delta \times 100$
					7.9	1.9(18)	-3.5(22)	.2(1)	.1(1)	-40(-∞ to +40)
225.8(2)	2148.5→1922.9	$11^{+} - 11^{+}$	19.6(2)		d) 3.8	39(3)	2(3)	39(1)	0.	-2(-20 to +43)
					1.	42(13)	- 5(15)	41(1)	- 3(1)	36(-52 to +90)
231.1(1)	352.7→ 121.6	$3^{-} - 2^{-}$	15.8(1)	M1	d) 8.4					
					32.1	- 3.5(7)	1.5(8)	- 3.0(5)	0.	5(11)
233.1(1)	552.0→ 316.8	$4^{-} - 3^{-}$	16.2(2)	M1	d) 2.6	-11(4)	4(5)	- 9.3(4)	.1(1)	7(11)
					7.9	-10(2)	3(2)	- 8.3(5)	0.	- 5(13)
236.8(3)	493.4→ 256.2	$3^{+} - 2^{+}$			.94	-13(13)	12(17)	- 7.0(5)	0.	11(±∞)
246.3(2)	565.6→ 319.1	$5^{+} - 6^{+}$		M1	.84	-22(15)	21(18)	-10.5(8)	0.	4(±∞)
253.5(2)			18.5(3)	M1	1.2	22(13)	14(15)			
255.6(1)	575.0→ 319.1	$7^{+} - 6^{+}$	18.8(2)[f]	M1	d) 18.7[e]	-14.0(7)[f]	.5(9)	-14.0(6)	0.	5(4)
					17.1[e]	-14.2(7)[f]	.5(8)	-14.6(6)	0.	5(4)
	1703.4→1447.8	$10^{+} - 9^{+}$	18.8(2)[f]	M1	d) 12.6[e]	-14.0(7)[f]	.5(9)	-14.3(7)	.1	5(19)
					6.0[e]	-14.2(7)[f]	.5(8)	-14.7(7)	.1	5(4)
264.3(1)	493.4→ 228.8	$3^{+} - 4^{+}$	15.6(2)	M1	d) 2.4	- 9(5)	1(6)	- 8.7(2)	0.	5(19)
					10.0	.7(15)	- 1.5(19)	.1(1)	0.	-14(27)
266.9(2)	619.8→ 352.7	$3^{-} - 3^{-}$			.7	24(18)	-30(21)	8(3)	3(3)	-40(±∞)
269.1(2)	585.0→ 316.8	$4^{+} - 3^{-}$			.9	-27(13)	-10(16)	-25(7)	.6(6)	-32(-∞ to +21)
273.8(1)	319.1→ 45.3	$6^{+} - 5^{+}$	16.8(1)	M1	d) 29.7	-14.2(6)	1(1)	-14.4(4)	0.	4(3)
					55.0	-11.6(5)	- .6(5)	-12.3(9)	0.	5(3)
274.6(1)[e]	627.5→ 352.7	$3^{-} - 3^{-}$			1.3[e]					
277.4(2)[e]	506.4→ 228.8	$5^{-} - 4^{+}$			.5	-41(26)	52(36)	-17(10)	0.	4(±∞)
280.3(1)	316.8→ 36.4	$3^{-} - 3^{+}$	16.1(2)	E1	d) 2.3	8(3)	23(3)	13.7(7)	- .1(1)	- 9(-23 to +140)
					11.3	.4(15)	.6(19)	1.0(3)	.7(4)	-36(37)
282.0(1)	2600.2→2318.2	$13^{+} - 12^{+}$	20.3(5)	M1	d) 10.4	-20(1)	2(2)	-19.4(5)	0.	2(3)

Table 5.1 (continued)

Photon energy (keV)	Classification (keV)	J^π Assignment	Energy for δ_{max} (MeV)	Multipolarity	Photon Intensities[a]	Experimental Coefficients $A_2 \times 100$	Experimental Coefficients $A_4 \times 100$	Calculated Coefficients[b] $A_2 \times 100$	Calculated Coefficients[b] $A_4 \times 100$	$\delta \times 100$
					1.2	-11(6)[f]	- 3(8)	-11.9(6)	0.	7(9)
282.3(3)[e]	316.8 → 34.4	$3^- - 4^+$			1.6[e]	-11(6)[f]	- 3(8)	-11(2)	.3(3)	90(-20 to +∞)
285.1(2)	321.6 → 36.4	$3^- - 3^+$	15.8(2)	E1	7.6	- .6(22)	- 3(3)	- 1.4(4)	- .9(3)	-70(-∞ to -5)
285.9(2)	321.6 → 35.6	$3^- -(2)^+$	15.8(2)	E1	7.4	- 3(2)	- .3(30)	- 3.0(5)	0.	- 4(30)
287.2(1)	321.6 → 34.4	$3^- - 4^+$	15.9(2)	E1	15.2	- 1.3(11)	- .3(13)	- 1.3(3)	0.	2(17)
291.7(3)	547.9 → 256.2	$(3) - 2^+$			.7	-26(16)	10(21)	-15(7)	.8(8)	-30(±∞)
294.2(1)	646.8 → 352.7	$(4)^- - 3^-$	16.0(5)	M1	3.9	-11(6)	9(8)	- 7.1(7)	0.	- 4(-∞ to +40)
301.6(2)[h]	530.5 → 228.8	$4^+ - 4^+$			1.3[e]	76(12)	-27(14)	25(15)	- 1.0(5)	40(70)
303.3(1)[e]	530.7 → 227.4	$(4)^- - 3^-$			1.0	- 6(15)	-25(18)	-18.5(12)	.4(4)	-20(±∞)
308.1(2)	564.3 → 256.2	$(3)^+ - 2^+$	17.3(2)	M1	2.0	18(11)	- 7(13)	- 2.0(5)	0.	11(45)
310.8(1)[e]	627.5 → 316.8	$3^- - 3^-$	16.7(2)[f]		d) .6[e]	- 9(3)[f]	- 2(4)	- 9.6(4)	- 1.5(4)	-90(-∞ to -50)
					2.0[e]	- 4.4(15)[f]	- 5(2)	- 5.4(14)	- 1.7(8)	-72(-∞ to -50)
310.9(1)[e]	885.8 → 575.0	$6^+ - 7^+$	16.7(2)[f]	M1	d) 4.4[e]	- 9(3)[f]	- 2(4)	-10.0(5)	0.	- 2(7)
					10.2[e]	- 4.4(15)[f]	- 5(2)	- 7.0(6)	0.	- 5(6)
316.3(3)	352.7 → 36.4	$3^- - 3^+$			1.3[i]					
319.1(1)	319.1 → 0.0	$6^+ - 7^+$	16.8(1)	M1	d) 28.6	-14(1)	0(1)	-13.6(2)	0.	2(4)
					45.8	-13.2(5)	1.9(6)	-12.4(2)	0.	2(4)
319.9(3)[e]	885.8 → 565.6	$6^+ - 5^+$			3.4[e]					
320.4(1)[e]	1187.7 → 867.2	$5 - 4^-$			2.0[e]					
323.1(1)	552.0 → 228.8	$4^- - 4^+$	16.1(2)	E1	d) 1.5	20(9)	- 9(10)	18.4(12)	- 4.6(12)	120(-50 to +230)
					5.3	3(4)	0(5)	3.8(3)	- 1.1(9)	- 27(-1 to +∞)
325.2(2)	2643.4 → 2318.2	$10^+ - 12^+$	19.5(4)	E2	d) 2.4	57(7)	- 7(7)	50.8(6)	6.0(6)	- 30(-173 to -12)
					.6	58(29)	0(30)	53.8(2)	7.0(7)	- 32(-∞ to +20)
329.1(2)	506.4 → 177.0	$5^+ - 5^+$			.9	20(14)	8(19)	19(4)	.3(3)	5(-120 to +300)
340.9(2)	568.2 → 227.4	$(3^-) - 3^-$	15.9(2)		1.7	6(12)	-16(16)	4(4)	- 4(2)	140(±∞)

Table 5.1 (continued)

Photon Energy (keV)	Classification (keV)	J^π Assignment	Energy for σ_{max} (MeV)	Multipolarity	Photon Intensities a)	Experimental Coefficients $A_2 \times 100$	Experimental Coefficients $A_4 \times 100$	Calculated Coefficients b) $A_2 \times 100$	Calculated Coefficients b) $A_4 \times 100$	$\delta \times 100$
346.5(2)	586.0→ 239.5	$4^+ - 3^+$			2.2	-16(9)	0(12)	-16.2(8)	0.	0(-∞ to +21)
352.2(1)	2214.1→1861.8	$10^+ - 9^+$	19.5(2)	M1	d) 21.1	-14(1)	0(1)	-14.3(7)	0.	5(1)
					8.4	-14(2)	1(3)	-13.5(5)	0.	5(4)
353.2(1)e)	530.3→ 177.0	$4^+ - 5^+$			.54e)					
366.6(3)	1187.7→ 821.8	$5\ -(6^+)$		M1	.51	35(31)	-21(33)	20(5)	1.2(4)	-57(±∞)
371.8(1)	947.0→ 575.0	$8^+ - 7^+$	18.3(2)	M1	d) 44.3	- 5.4(7)	1(1)	- 5(1)	.2(1)	11(2)
					32.2	- 6.8(7)	.3(8)	- 6.3(4)	.2(1)	11(2)
372.3(2)e)	493.4→ 121.6	$3^+ - 2^-$			.52e)					
374.7(1)	552.0→ 177.0	$4^- - 5^+$	18.5(2)		2.3	- 9(12)	4(14)	- 7.1(4)	0.	7(±∞)
379.6(2)	885.8→ 506.4	$6^+ - 5^+$	16.2(2)f)	M1	2.1	-17(13)	45(15)	- 8.0(6)	.6(2)	24(-4 to +∞)
380.0(1)	732.9→ 352.7	$4^- - 3^-$	16.2(2)f)	M1	6.6	1(5)	-12(5)	- 5.0(5)	.1(1)	0(36)
383.5(2)	623.0→ 239.5	$(4)^+ - 3^+$		M1/E2	1.5	-14(10)	-18(11)	-24.4(7)	.6(6)	-73(-∞ to +12)
385.2(2)	1447.8→1062.7	$9^+ - 8^+$		M1	d) 2.1e)	- 2(4)	- 2(4)	- 3.4(4)	.3(1)	12(5)
					2.1e)	-12(7)	-11(8)	-17.4(9)	0.	4(9)
388.5(1)	565.6→ 177.0	$5^+ - 5^+$		M1	7.0	1(5)	- 7(6)	.5(2)	- 3(1)	-60(-173 to -20)
392.5(1)	619.8→ 227.4	$3^- - 3^-$			1.8	12(14)	6(17)	10(4)	.2(2)	18(±∞)
395.3(2)	2318.2→1922.9	$12^+ - 11^+$	20.3(3)	M1	d) 16.8	-12(1)	3(1)	-11.6(6)	.1	7(1)
					3.0	-16(11)f)	4(13)	-13.1(7)	.1(1)	5(16)
395.5(5)e)	1183.3→ 789.1	$(5) - 4^-$			1.5e)	-16(11)f)	4(13)	-14(2)	0.	5(-∞ to +40)
397.6(3)	575.0→ 177.0	$7^+ - 5^+$			d) 0.9	52(20)	- 3(21)	47.3(8)	3(1)	23(-15 to +∞)
					0.9	46(22)	-58(25)	19.7(3)	-13(3)	-12(-65 to +65)
398.6(2)e)	627.5→ 228.8	$3^- - 4^+$			.6	-47(30)	48(40)	-16(8)	.3(3)	18(±∞)
403.5(5)e)	909.6→ 506.4	$4\ - 5^+$			1.3	- 6(15)	0(18)	- 6.7(7)	0.	4(±∞)
409.3(1)e)	530.7→ 121.6	$(4)^- - 2^-$	15.9(2)f)	M1	8.6e)	- 4(2)f)	- 1(3)	- .7(40)	-12(6)	-140(-270 to -25)
409.3(3)	445.1→ 35.6	$3^+ -(2)^+$	15.9(2)f)	M1	6.9	- 4(2)f)	- 1(3)	- 4.9(2)	.1(1)	4(17)

Table 5.1 (continued)

Photon energy (keV)	Classification (keV)	J^{π} Assignment	Energy for σ_{max} (MeV)	Multipolarity	Photon Intensities a)	Experimental Coefficients A_2 x 100	Experimental Coefficients A_4 x 100	Calculated Coefficients b) A_2 x 100	Calculated Coefficients b) A_4 x 100	δ x 100
410.7(1)	445.1→ 34.4	$3^+ - 4^+$	15.8(1)	M1	11.8	- 4(3)	1.5(38)	- 3.0(3)	0.	7(-46 to +∞)
416.0(1)	732.9→ 316.8	$4^- - 3^-$	16.0(2)	M1	6.1	- 5(3)	4(4)	- 3.9(7)	.2(2)	7(21)
418.2(5)			17.9(2)		2.1	-31(6)	0(7)			
419.3(2)	646.8→ 227.4	$(4)^- - 3^-$	19.5(2)		.80	-64(15)	38(20)	-35(15)	6(5)	-80(-∞ to 0)
422.8(2)	458.3→ 35.6	$3^+ -(2)^+$	15.6(3)	M1	4.0	-16(5)	1(6)	-13(3)	.7(7)	-70(-471 to +14)
427.0(1)	979.2→ 552.0	$5^- - 4^-$	16.3(1)	M1	d) 6.2	-14(3)	1(4)	-14.1(6)	0.	3(11)
					16.6	-13(1)	- 2(2)	-13.6(1)	0.	- 5(12)
443.1(3)	564.3→ 121.6	$(3)^+ - 2^-$	16.2(3)		.53	1(16)	-23(20)	- 9(1)	.2(2)	0(±∞)
444.9(2)	2148.5→1703.4	$11^+ - 10^+$	19.4(3)		d) 7.4	-17(3)	1(4)	-17.2(8)	0.	4(4)
					2.4	-36(7)	9(9)	-31(1)	0.	- 5(9)
448.7(2)	801.4→ 352.7	$4^- - 3^-$			2.2	-12(10)	- 7(13)	-15.2(7)	.2(2)	-40(-∞ to +40)
457.2(1)	506.4→ 49.3	$5^+ - 6^+$	16.3(2)	M1	d) 12.2	- 7(2)	8(2)	- 2.6(6)	0.	- 9(6)
					36.5	- 3.7(16)	- .4(19)	- 3.9(7)	0.	- 2(7)
458.4(7) h)	493.4→ 34.4	$3^+ - 4^+$			< 2.0					
460.8(3) h)	506.4→ 45.3	$5^+ - 5^+$	17.4(5)		1.4					
472.2(1)	506.4→ 34.4	$5^+ - 4^+$	16.2(2) f)	M1	d) 5.2	-22(6)	23(7)	-11.5(3)	0.	5(13)
					9.7	- 5(3) f)	2(3)	- 4.6(5)	.1(1)	7(11)
	789.1→ 316.8	$4^- - 3^-$	16.2(2) f)	M1	7.3	- 5(3) f)	2(3)	- 5.0(5)	.1(1)	7(18)
477.6(2)	794.3→ 316.8	$4^- - 3^-$	16.5(4)		1.8	-14(6)	-2(8)	-14.5(5)	.2(2)	0(-∞ to +15)
484.8(1) e)	801.6→ 316.8	$4^- - 3^-$	16.0(1) f)	(M1)	2.0 e)	- 5(3) f)	- 1(3)	- 3.9(7)	.1(1)	9(18)
485.0(1)	530.3→ 45.3	$4^+ - 5^+$	16.0(1) f)	M1	15	- 5(3) f)	- 1(3)	- 4.1(5)	0.	4(21)
487.4(1)	1062.7→ 575.0	$8^+ - 7^+$		M1	d) 20 h)	- 1(1)	2(2)	- .9(1)	.4(1)	14(2)
					16.1	- 5(3)	2(3)	- 4.8(12)	.3(1)	12(5)
491.9(4) e)	1610.2→1118.3	$-(5^+)$	16.2(4)		.9 e)	-39(9) f)	37(11)			
492.9(2) e)	542.2→ 49.3	$(5)^+ - 6^+$	16.2(2) f)	M1	2.2 e)	-39(9) f)	37(11)	-21.2(4)	2(2)	21(±∞)

Table 5.1 (continued)

Photon energy (keV)	Classification (keV)	J^{π} Assignment	Energy for σ_{max} (MeV)	Multipolarity	Photon Intensities[a]	Experimental Coefficients		Calculated Coefficients[b]		
						$A_2 \times 100$	$A_4 \times 100$	$A_2 \times 100$	$A_4 \times 100$	$\delta \times 100$
493.7(1)[e]	749.9→ 256.2	$(3)^+ - 2^+$	16.2(2)[f]	M1	2.8[e]	- 8(3)[f]	- 2(3)	- 9.3(5)	.4(4)	0(-210 to +15)
494.0(2)	530.3→ 36.4	$4^+ - 3^+$	16.2(2)[f]	M1	6.0	- 8(3)[f]	- 2(3)	- 9.3(3)	0.	-12(26)
496.1(2)[e]	815.2→ 319.1	$4^+ - 6^+$	16.5(4)	E2	5.0	4(5)	- 8(5)	.6(7)	- 1.4(7)	18(69)
498.4(1)	619.8→ 121.6	$3^- - 2^-$		M1/E2	2.3	-30(9)	- 3(10)	-21(10)	.6(6)	-70(-300 to +14)
500.8(1)	1447.8→ 947.0	$9^+ - 8^+$	18.2(2)	M1	d) 12	-27(2)	1(3)	-27.0(7)	0.	- 4(3)
					8.6	-25(3)	2(4)	-25.0(9)	0.	- 1(5)
502.3(3)	821.8→ 319.1	$(6^+) - 6^+$			4.1	- 8(6)	4(8)	- 3.5(11)	- 5.0(14)	-75(-188 to -42)
505.8(3)[e]	732.9→ 227.1	$4^- - 3^-$			.4[e]					
506.1(1)[e]	627.5→ 121.6	$3^- - 2^-$	16.3(3)[f]	(M1)	d) 1.4[e]	-14(4)[f]	1(5)	-13.9(5)	0.	0(12)
					7.1[e]	- 5(1)[f]	1.4(15)	- 4.0(5)	.1(1)	9(-20 to +18)
506.6(1)[e]	552.0→ 45.3	$4^- - 5^+$	16.3(3)[f]	E1	d) 7.0	-14(4)[f]	1(5)	-13.7(5)	0.	7(11)
					18.5	- 5(1)[f]	1.4(15)	- 3.4(3)	0.	0(12)
515.8(1)	552.0→ 36.4	$4^- - 3^+$	16.3(3)	E1	d) 11.	-12(4)	1(5)	-11.7(3)	0.	4(11)
					30.	- 6.7(11)	.7(12)	- 6.0(5)	.1(1)	2(10)
516.4(1)[e]	565.6→ 49.3	$5^+ - 6^+$			d) 2.8[e]					
					7.4[e]					
517.7(2)	552.0→ 34.4	$4^- - 4^+$	16.2(2)	E1	d) 6.8	17(3)	- 9(3)	11.2(2)	- .6(4)	-26(-41 to -3)
					15.0	4.4(18)	- 1.3(18)	4.5(5)	- 1.5(5)	-25(27)
520.3(3)	565.6→ 45.3	$5^+ - 5^+$		M1/E2	4.9	-11(5)	1(6)	- 6.7(5)	- 5.1(5)	-80(-∞ to -48)
525.7(1)	575.0→ 49.3	$7^+ - 6^+$	17.9(1)	M1	d) 100.	-21.1(7)	1(1)	-20.4(7)	0.	0(2)
					100.	-19.5(4)	.2(5)	-19.9(8)	0.	2(2)
528.8(3)	564.3→ 35.6	$(3)^+ - (2)^+$	15.8(2)[f]	M1	12.5	10(3)	- 7(4)	6.5(10)	.7(3)	36(+11 to +∞)
529.7(2)	564.3→ 34.4	$(3)^+ - 4^+$	15.8(2)[f]	M1	14.8	-18(3)	2(4)	-13(5)	.3(3)	21(+11 to +∞)
531.4(1)	565.6→ 34.4	$5^+ - 4^+$	16.0(1)	M1	21.5	-10(3)	4(4)	- 8.0(7)	.1(1)	0(14)
536.0(2)	2397.7→1861.8	$11^+ - 9^+$	19.8(4)		d) 6.7[h]	27(3)	- 5(4)	31(2)	- 8.8(3)	- 2(5)

Table 5.1 (continued)

Photon energy (keV)	Classification (keV)	J^π Assignment	Energy for σ_{max} (MeV)	Multipolarity	Photon Intensities	Experimental Coefficients		Calculated Coefficients[b)]		
						A_2 x 100	A_4 x 100	A_2 x 100	A_4 x 100	δ x 100
					2.0	7(6)	11(8)	24.5(6)	-14(2)	- 7(11)
543.5(2)	720.6→ 177.0	$(6^+)- 5^+$	16.8(6)[f)]		1.4	-72(13)	29(17)	-60(5)	10(5)	-173(-372 to -14)
544.8(2)			16.8(6)[f)]		5.4	18(5)	- 6(6)			
550.4(1)	867.2→ 316.8	$4^- - 3^-$	16.0(1)		d) 6	-17(4)	- 2(5)	-16.7(4)	0.	0(17)
					19.9	- 7(3)	1(4)	- 6.0(5)	.1(1)	- 4(19)
557.6(6)			16.0(2)		6.4	- 2(4)	10(6)			
560.4(1)			16.3(5)		12.3	-12(2)	- 1(3)			
564.1(2)[e)]	1139.0→ 575.0	$8^+ - 7^+$			1.7[e)]	9(12)	- 2(14)	6.9(4)	.7(1)	24(20)
569.6(4)	1438.7→ 867.2	$(3^-)- 4^-$		M1/E2	4[h)]	-28(3)[h)]	7(4)	-15(8)	.3(3)	22(-4 to +∞)
572.3(4)	829.0→ 256.2	$(4^+)- 2^+$			2.0[h)]	16(8)	- 2(10)	18(4)	- 5(7)	-18(-50 to +∞)
574.8(2)	575.0→ 0.0	$7^+ - 7^+$	18.0(3)		d) 10.5	31(5)	- 2(9)	30.0(1)	- 6(2)	70(-23 to +87)
					8.	12(9)	14(12)	20.1(5)	- 1.9(4)	-31(-67 to +154)
575.5(1)	752.5→ 177.0	$6^+ - 5^+$	16.5(4)	M1	d) 7.2[e)]					
					16.0	- 7(3)	2(3)	- 6.2(8)	.1(1)	9(7)
577.0(5)	623.0→ 45.3	$(4)^+- 5^+$			3.3	24(6)	-15(7)	13(4)	.4(1)	-36(-∞ to -9)
583.4(4)	619.8→ 36.4	$3^- - 3^+$			1.3	-34(15)	68(22)	- .3(14)	- .6(6)	-40(±∞)
588.5(3)	909.6→ 321.6	$4 - 3^-$	15.3(3)[f)]		6.2	-16(4)	.8(5)	-16.2(7)	.3(3)	-20(-373 to +5)
589.3(1)	816.7→ 227.4	$(3^-)- 3^-$	15.3(3)[f)]		3.8	7(5)	3(7)	7(1)	- .3(3)	0(±∞)
591.4(6)	627.5→ 36.4	$3^- - 3^+$	15.3(4)[f)]		4.0	-19(6)	20(8)	- 5(2)	-1.4(5)	-57(±∞)
592.3(3)	627.5→ 35.6	$3^- -(2)^+$	15.3(4)[f)]		4.0	7(6)	-23(7)	- 4.8(4)	.1(1)	7(-∞ to +78)
596.4(6)	1183.3→ 586.0	$(5) - 4^+$			2.9	8(7)	-17(9)	0.	.3(1)	16(14)
599.9(2)	1152.1→ 552.0	$6^- - 4^-$	16.9(2)	E2	15.8	12(3)	.3(42)	18(3)	- 9(4)	- 9(12)
611.4(1)	732.9→ 121.6	$4^- - 2^-$			3.6	- 3(6)	-19(8)	-22(10)	-14(8)	-80(-248 to -16)
612.1(3)	934.3→ 321.6	$(3^+)- 3^-$			1.3	- 4(17)	85(25)	17(12)	- .2(2)	22(±∞)
612.8(3)	840.2→ 227.4	$- 3^-$			.6					

Table 6.1 (continued)

Photon energy (keV)	Classification (keV)	J^π Assignment	Energy for σ_{max} (MeV)	Multipolarity	Photon Intensities a)	Experimental Coefficients b) $A_2 \times 100$	Experimental Coefficients $A_4 \times 100$	Calculated Coefficients b) $A_2 \times 100$	Calculated Coefficients $A_4 \times 100$	$\delta \times 100$
614.0(3)	2318.2→1703.4	$12^+ - 10^+$			d) 4.3	34(3)	-11(4)	33.1(4)	- 8(2)	0(7)
					1.7	36(14)	1(16)	40(1)	- 4.4(9)	7(-14 to +49)
618.3(2)	1597.5→ 979.2	$6^{(-)} - 5^-$			5.6					
625.8(2)	942.6→ 316.8	$(4) - 3^-$			4.0 j)	-12(6)	9(7)	- 8.8(10)	.2(2)	0(-∞ to +30)
635.9(2)	1187.7→ 552.0	$5 - 4^-$			5.2	- 4(4)	- 1(5)	- 4.6(5)	.1(1)	7(18)
638.0(1) e)	815.2→ 177.0	$4^+ - 5^+$			d) 7.0	-19(3)	3(3)	-17.3(3)	0.	12(11)
					14.3	- 9(2)	- 2(2)	- 9.4(4)	0.	5(-5 to +53)
644.7(1)	821.8→ 177.0	$(6^+) - 5^+$			d) 1.4 e)					
					5.6	-12(6)	11(8)	- 6.8(6)	.1(1)	8(14)
647.7(2)	1556.6→ 909.6	$(4) - 4$			1.4 j)	59(14)	-36(15)	24(14)	- 1.6(12)	42(-72 to +300)
662.5(1)	979.2→ 316.8	$5^- - 3^-$			d) 3.7 e)	18(8)	- 1(10)	23(2)	- 6(3)	- 4(29)
					12.7	- 5.7(24)	2(3)	- 5(2)	-15(5)	-30(9)
667.7(1)	789.1→ 121.6	$4^- - 2^-$			d) 7.9	18(4)	5(6)	23(2)	- 5(3)	0(24)
					11.2	3.3(27)	- .1(34)	9(4)	-10(7)	-20(25)
672.8(3) e)	794.3→ 121.6	$4^- - 2^-$			.34 e)					
676.5(3)	1183.3→ 506.4	$(5) - 5^+$			3.6	- 7(5)	- 6(7)	- 7.8(14)	- 4.7(10)	-100(-∞ to -49)
680.3(1) e)	801.6→ 121.6	$4^- - 2^-$	16.2(2) f)		7.0 e)	- 2(4) f)	6(5)	8(4)	-10(6)	-22(15)
680.7(2) e)	909.6→ 228.8	$4 - 4^+$	16.2(2) f)		1.4 e)	- 2(4) f)	6(5)	2.0(7)	- 1.3(8)	-45(-173 to +∞)
690.6(4) e)	739.9→ 49.3	$- 6^+$			1.2 e)					
695.2(1) e)	816.7→ 121.6	$(3^-) - 2^-$			3.7 e)					
699.7(3) e)	821.3→ 121.6	$- 2^-$			1.3 e)					
702.5(4) e)	752.5→ 49.3	$6^+ - 6^+$			1.2 e)					
705.4(2) e)	934.3→ 228.8	$(3^+) - 4^+$			2.0 e)					
714.9(2)	971.4→ 256.2	$3 - 2^+$			2.7	-32(8)	18(10)	-17(7)	.8(8)	-18(-∞ to +11)
719.5(3)			16.2(3)		6.0					

Table 5.1 (continued)

Photon energy (keV)	Classification (keV)	J^π Assignment	Energy for σ_{max} (MeV)	Multipolarity	Photon Intensities[a]	Experimental Coefficients		Calculated Coefficients[b]		
						$A_2 \times 100$	$A_4 \times 100$	$A_2 \times 100$	$A_4 \times 100$	$\delta \times 100$
720.9(5)	720.6→ 0.0	$(6^+)-7^+$		M1	5.0	-15(4)	.2(52)	-14.7(4)	0.	5(12)
721.9(2)	1040.8→ 319.1	$7^+ - 6^+$			d) 4.0[e]	-21(5)	1(6)	-20.5(7)	0.	0(18)
					5.6	-15(4)	.8(5)	-11.5(9)	.1	7(7)
732.3(3)[e]	909.6→ 177.0	$4 - 5^+$			1.2[e]					
750.5(2)[e]	979.2→ 228.8	$5^- - 4^+$			3.1	-24(7)	11(9)	-20(1)	1(1)	- 9(-∞ to +12)
752.6(1)	752.5→ 0.0	$6^+ - 7^+$	16.3(4)	M1	d) 5.2	-29(7)	5(8)	-26.9(5)	.1(1)	14(22)
					14.8	- 4.5(25)	- 1(3)	- 5.2(3)	0.	- 5(7)
754.7(6)	789.1→ 34.4	$4^- - 4^+$			1.3	67(20)	-61(20)	23(13)	- 2(2)	49(±∞)
756.3(1)	1703.4→ 947.0	$10^+ - 8^+$	18.5(2)		d) 9.6	22(4)	- 3(4)	27.7(7)	-10(1)	- 5(7)
					4.0	20(6)	13(7)	34(1)	- 7.5(10)	3(11)
766.0(1)[e]	815.2→ 49.3	$4^+ - 6^+$			d) 4.2[e]					
					6.0	1(4)	2(5)	2.4(3)	- .8(12)	14(18)
770.0(4)	815.2→ 45.3	$4^+ - 5^+$			2.5	20(10)	-20(11)	10(1)	.2(2)	-57(∓∞ to +36)
772.7(2)	821.8→ 49.3	$(6^+)-6^+$			5.3	4(4)	- 5(5)	3.0(5)	- 4.5(5)	-60(15)
776.7(5)	1703.4→ 927.3	$10^+ - 9^+$			d) 10.3[e]	-48(11)	31(14)	-35(1)	.2(1)	- 9(19)
					3.5[e]	-46(7)	11(8)	-41(1)	.3(1)	-11(11)
782.0(5)	816.7→ 34.4	$(3^-)-4^+$			1.3	-15(18)	-20(22)	-16(8)	.2(2)	40(±∞)
783.8(2)	1290.4→ 506.4	$4 - 5^+$			2.6	- 5(9)	- 1(11)	- 5.0(5)	0.	- 2(±∞)
793.0(3)	829.0→ 36.4	$(4^+)-3^+$			3.7	- .2(67)	- 3(8)	- 1.1(3)	.2(2)	14(-41 to +83)
799.1(3)[e]	1118.3→ 319.1	$(5^+)-6^+$	18.9(2)[f]	(M1)	d) 1.7[e]	-18(2)[f]	0(2)	-19.5(5)	0.	11(9)
					4 [e]	-19(3)[f]	0(3)	-19.2(4)	.2(2)	18(-4 to +60)
799.3(1)	1861.8→1062.7	$9^+ - 8^+$	18.9(2)[f]	M1	d) 20.7	-18(2)[f]	0(2)	-20(1)	0.	2(2)
					8.0	-19(3)[f]	0(3)	-19(1)	0.	2(5)
803.7(2)[e]	980.7→ 177.0	$(5^+)-5^+$			3.0					
806.6(3)	3020.7→2214.1	$12^+ - 10^+$	20.8(4)		d) 4.3[e]	31(9)	-15(10)	28.1(7)	-11(1)	- 5(13)

Table 5.1 (continued)

Photon energy (keV)	Classification (keV)	J^π Assignment	Energy for σ_{max} (MeV)	Multipolarity	Photon Intensities[a]	Experimental Coefficients $A_2 \times 100$	Experimental Coefficients $A_4 \times 100$	Calculated Coefficients[b] $A_2 \times 100$	Calculated Coefficients[b] $A_4 \times 100$	$\delta \times 100$
809.6(1)[e]	1065.8→ 256.2	$- 2^+$			2.1[j]					
829.7(4)	1149.0→ 319.1	$(5) - 6^+$			4.0	4(6)	9(8)	7.9(11)	1.6(16)	-19(-∞ to -5)
833.0(3)	1152.1→ 319.1	$6^- - 6^+$			4.1	31(7)	-12(8)	27(2)	- 5(3)	60(-42 to +133)
840.7(3)	885.8→ 45.3	$6^+ - 5^+$			4.3	4(6)	3(8)	5.2(7)	.6(2)	24(16)
864.5(5)	909.6→ 45.3	$4 - 5^+$			2.4	-27(11)	- 4(14)	-23(7)	.3(3)	20(-11 to +∞)
872.8(1)	1447.8→ 575.0	$9^+ - 7^+$	17.7(3)	E2	d) 19.7	25(3)	- 4(4)	27.7(7)	- 9(1)	- 4(10)
					13.7	16(3)	4(3)	26.7(7)	-11.5(11)	- 5(5)
883.7(3)	1203.0→ 319.1	$(6^+) - 6^+$			3.2	-25(16)	-12(60)	-21(3)	-10(3)	-200(-∞ to -42)
886.0(5)	885.8→ 0.0	$6^+ - 7^+$			2.3	-26(13)	-20(15)	-36.2(4)	.4(1)	27(-5 to +∞)
890.0(3)	934.3→ 45.3	$(3^+) - 5^+$			4.0	4(9)	17(11)	9(4)	.1(4)	-40(-∞ to +24)
894.6(3)[e]	1071.6→ 177.0	$(4) - 5^+$			1.2[e]	-42(11)[f]	44(14)	-19(3)	.3(3)	36(-16 to +∞)
895.0(3)	1211.7→ 316.8	$(4) - 3^-$			2.1	-42(11)[f]	44(14)	-19(4)	1(1)	-18(-∞ to +18)
897.9(2)	947.0→ 49.3	$8^+ - 6^+$	18.1(2)		d) 9.7	26(4)	-13(5)	24(2)	-10(1)	- 7(7)
					8.5	21(5)	2(6)	27.6(8)	-10(1)	- 4(10)
899.6(4)	934.3→ 34.4	$(3^+) - 4^+$			2.2	-28(16)	49(22)	- 6.3(7)	.4(4)	0(±∞)
912.5(2)[e]	1487.5→ 575.0	$8 - 7^+$	17.8(5)[f]		4.3[e]	-24(5)[f]	- 2(6)	-25.8(8)	0.	0(9)
912.8(2)[e]	1140.1→ 227.4	$(5^-) - 3^-$	17.8(5)[f]		2.0[e]	-24(5)[f]	- 2(6)	- 8(2)	-20(4)	-121(-321 to -40)
914.7(2)	1861.8→ 947.0	$9^+ - 8^+$	19.0(3)		d) 21.2	-13(3)	- 2(3)	-14.2(7)	0.	5(5)
					11.5	-10(3)	- 3(4)	-11.8(6)	.1	2(5)
918.5(3)	1271.2→ 352.7	$- 3^-$			2.1[e]					
927.3(1)	927.3→ 0	$9^+ - 7^+$	18.9(3)	E2	d) 122	28.0(6)	- 5(1)	28.4(4)	- 6(2)	0(2)
					64.5	25.7(9)	- 6(1)	25.7(9)	- 6(2)	- 2(4)
931.5(2)	980.7→ 49.3	$(5^+) - 6^+$			2.8	-23(9)	2(12)	-23.0(2)	.4(4)	18(-9 to +∞)
934.4(6)	979.2→ 45.3	$5^- - 5^+$			1.2	30(26)	-57(29)	3(2)	- 9(3)	205(±∞)
936.2(6)	971.4→ 35.6	$3 - (2)^+$			2.3					

Table 5.1 (continued)

Photon energy (keV)	Classification (keV)	J^π Assignment	Energy for Q_{max} (MeV)	Multipolarity	Photon Intensities[a]	Experimental Coefficients A_2 x 100	Experimental Coefficients A_4 x 100	Calculated Coefficients[b] A_2 x 100	Calculated Coefficients[b] A_4 x 100	δ x 100
941.2(3)	1118.3 → 177.0	$(5^+)-5^+$			5.0[j]	-35(6)	3(8)	-18(8)	- 9(2)	-20(-∞ to -100)
945.4(4)	979.2 → 34.4	$5^- / 4^+$			3.7	-19(8)	-27(10)	-30(2)	1(1)	-30(-236 to +9)
947.1(3)	947.0 → 0.0	$8^+ - 7^+$			d) 17[e]	-23(2)	- 2(3)	-23.9(9)	0.	- 2(5)
					15.4	-25(3)	5(4)	-22.3(13)	0.	0(7)
975.2(2)	1152.1 → 177.0	$6^- - 5^+$			d) 1.7[e]					
					1.9	- 7(18)	- 4(22)	- 8.8(8)	.1	7(-40 to +75)
993.4(3)[e]	1042.4 → 49.3	$(5) - 6^+$			3.6	-54(9)	23(12)	-38(10)	2.4(20)	100(+7 to +370)
994.8(3)[e]	1314.0 → 319.1	$5^+ - 6^+$			5.4	-44(6)	- 2(8)	-37(9)	1(1)	36(-11 to +∞)
995.7(2)	1922.9 → 927.3	$11^+ - 9^+$	19.5(2)	E2	d) 49	30(2)	-12(3)	30(5)	-12(6)	- 4(3)
					16	23(2)	2(3)	31.6(16)	- 9.5(5)	- 2(5)
1004.7(5)	1053.8 → 49.3	$(5) - 6^+$			2.2	-22(7)	6(9)	-19.9(10)	1.6(16)	18(-14 to +∞)
1006.5(2)	1183.3 → 177.0	$(5) - 5^+$			2.6					
1007.4(4)	1042.4 → 34.4	$(5) - 4^+$			6.0	- 9(6)	18(8)	- .8(8)	.3(1)	18(30)
1013.6(2)	1062.7 → 49.3	$8^+ - 6^+$	18.5(2)	E2	d) 27.2	24(2)	- 8(3)	23(1)	- 6(3)	- 5(9)
					24.8	26(2)	- 9(3)	26(4)	- 9(6)	0(7)
1040.7(2)	1040.8 → 0.0	$7^+ - 7^-$	17.2(3)	M1/E2	9.2	14(4)	7(5)	+19.1(4)	- 2.1(5)	-32(15)
1045.5(3)	1597.5 → 552.0	$6^{(-)} - 4^-$	18.0(2)		3.0	27(13)	7(15)	33(2)	- 2(3)	11(-21 to +∞)
1050.2(2)[e]	1367.0 → 316.8	$(4) - 3^-$			3.2	-24(11)	17(15)	-16.2(7)	1.3(13)	- 2(-∞ to +25)
1053.9(2)[e]	1103.2 → 49.3	$(5) - 6^+$			1.4[e]	- 2(20)	- 8(25)	- 6.1(5)	0.	0(±∞)
1078.7(1)	1255.6 → 177.0	$4 - 5^+$			d) 2.0[e]					
					4.2					
1084.9(3)[e]	1314.0 → 228.8	$5^+ - 4^+$	16.5(5)		2.2[j]	-13(9)	-19(11)	-10.3(5)	0.	0(-∞ to +23)
1089.7(2)[e]	1139.0 → 49.3	$8^+ - 6^+$	18.0(3)		1.1[e]	22(6)	- 7(7)	25(1)	-11(1)	- 7(-42 to +53)
1105.8(8)	1140.1 → 34.4	$(5^-) - 4^+$	16.4(2)		3.0	-17(4)[f]	5(5)	-16(2)	.1(1)	-11(22)
1106.8(1)	1152.1 → 45.3	$6^- - 5^+$	17.3(3)		9.1	-17(4)[f]	5(5)	-15.1(3)	0.	3(11)

Table 5.1 (continued)

Photon energy (keV)	Classification (keV)	J^π Assignment	Energy for δ_{max} (MeV)	Multipolarity	Photon Intensities a)	Experimental Coefficients $A_2 \times 100$	Experimental Coefficients $A_4 \times 100$	Calculated Coefficients $A_2 \times 100$	Calculated Coefficients $A_4 \times 100$	$\delta \times 100$
1113.3(2)	1290.4→ 177.0	$4 - 5^+$	15.7(5)		2.0	-35(10)	26(13)	-20(4)	.3(3)	40(-14 to $+\infty$)
1115.0(5)	1149.0→ 34.4	$(5) - 4^+$			6.4	- 3(9)	18(11)	- 5.5(7)	.6(1)	24(+5 to $+\infty$)
1117.6(3) e)	1294.7→ 177.0	$(5) - 5^+$			2.2 j)	55(14)	-61(14)	19(6)	- 5(3)	95(-80 to $+\infty$)
1134.0(1)	1183.3→ 49.3	$(5) - 6^+$	16.3(2)		4.0	-18(10)	16(13)	-10.9(5)	0.	0(-58 to $+\infty$)
1137.9(5) e)	1314.0→ 177.0	$5^+ - 5^+$			1.6 e)	-42(5) f)	8(6)	-34(6)	1(1)	60(+14 to +205)
1138.0(3) e)	1187.7→ 49.3	$5 - 6^+$			2.5 e)	[illegible]	8(6)	-33(6)	1.0(7)	36(-14 to +180)
1139.0(2)	1139.0→ 0.0	$8^+ - 7^+$	18.0(2)	M1 k)	d) 28.0	[illegible]	- 2(3)	-59.0(2)	1.4(2)	-29(7)
					28.0	-58(3)	- 1(4)	-59.1(6)	1.4(2)	-27(8)
1151.7(4)	2214.1→1062.7	$10^+ - 8^+$	16.6(2) f)		d) 2.7					
					1.0	-32(9) f)	14(12)	- 2.8(15)	-28.6(6)	-36(-64 to -20)
	1152.0→ 0.0	$6^- - 7^+$	16.6(2) f)		2.2	-32(9) f)	14(12)	-25.0(5)	.1(1)	20(28)
1153.4(3)	1203.0→ 49.3	$(6^+) - 6^+$			5.0 j)	17(6)	- 6(8)	14(3)	- 2(3)	-36(21)
1168.5(1)	1203.0→ 34.4	$(6^+) - 4^+$	17.6(2)		1.6					
1196.8(3)	1516.2→ 319.1	$(7^+) - 6^+$			4.4	-31(11)	2(14)	-30(1)	0	- 6(18)
1200.5(1)			16.1(2)		16.0					
1209.8(3)	1438.7→ 228.8	$(3^-) - 4^+$	15.4(3) f)		2.3	-28(7) f)	-12(8)	-21(13)	.3(2)	41(+8 to $+\infty$)
	1255.6→ 45.3	$4 - 5^+$	15.4(3) f)		3.8	-28(7) f)	-12(8)	-25(9)	4(2)	42(-7 to $+\infty$)
1221.4(3)	2148.5→ 927.3	$11^+ - 9^+$	19.2(3)		d) 6.0	48(12)	-13(12)	41(1)	- 2.9(7)	7(14)
					1.5					
1231.3(2)	1408.3→ 177.0	$(4^-) - 5^+$			d) 1.1 e)					
					2.7	- 9(21)	-24(25)	-18(3)	.3(3)	18($\pm\infty$)
1232.3(1)			15.8(2)		7.3	-23(9)	8(12)			
1264.9(1) e)	1314.0→ 49.3	$5^+ - 6^+$	16.5(4)		4.8 j)	-41(9)	22(11)	-29(1)	1(1)	20(-2 to $+\infty$)
1269.1(4)	1314.0→ 45.3	$5^+ - 5^+$			4.1	17(13)	- 6(15)	17(3)	- 6(4)	58(-471 to $+\infty$)
1305.4(3)	1482.4→ 177.0	$(4^-) - 5^+$			2.0	-78(16) h)	96(24)	-30(13)	1.5(15)	40($\pm\infty$)

Table 5.1 (continued)

Photon energy (keV)	Classification (keV)	J^π Assignment	Energy for δ_{max} (MeV)	Multipolarity	Photon Intensities$^{a)}$	Experimental Coefficients		Calculated Coefficients$^{b)}$		
						$A_2 \times 100$	$A_4 \times 100$	$A_2 \times 100$	$A_4 \times 100$	$\delta \times 100$
1314.1	1314.0→ 0.0	$5^+ - 7^+$	16.4(4)		7.8	- .2(76)	5(9)	4.0(7)	- 1(2)	0(-∞ to +58)
1339.4(3)$^{e)}$	1516.2→ 177.0	$(7^+) - 5^+$			2.6$^{e)}$					
1359.2(4)$^{e)}$	1536.2→ 177.0	$(4^-) - 5^+$			2.3$^{e)}$					
1360.8(5)$^{e)}$	1482.4→ 121.6	$(4^-) - 2^-$			1.0$^{e)}$					
1378.8(5)$^{e)}$	1556.6→ 177.0	$(4) - 5^+$			.6$^{e)\ c}$					
1399.4(6)$^{e)}$	1974.4→ 575.0	$8 - 7^+$	18.1(3)		4.4	- 2(13)	-16(16)	- 9.9(10)	.1(1)	10(22)
1419.4(2)	1596.4→ 177.0	$- 5^+$			1.7$^{e)}$					
1448.2(2)	1767.3→ 319.1	$(5^+) - 6^+$			2.0$^{e)}$					
1459.3(5)	1636.3→ 177.0	$- 5^+$			1.4$^{e)}$					
1548.6(2)			16.0(3)		2.8					
1569.2(2)			18.0(4)		1.4					
1597.4(1)	1597.5→ 0.0	$6^{(-)} - 7^+$	16.5(2)		4.3					
1696.6(1)			18.0(2)		6.5					
1711.7(2)			17.0(6)		3.2					

a) Gamma-ray intensities measured at each alpha beam energy are normalized to the value 100 for the 525 keV transition.

b) The range of A_2 and A_4 values permitted by the uncertainty in σ are indicated in parenthesis.

c) The argument for this assignment is given in the text.

d) The results to the left of this marker were obtained from an experiment at 18 MeV.

e) Part of an incompletely resolved doublet; the measurement derived from a γ-γ coincidence experiment.

f) A composite result for the doublet.

g) The energies are not precisely determined; there could be an unresolved triplet present.

h) Transition mixed with an impurity line.

i) Intensity deduced from the decay data of the 314 and 316 keV transitions in ^{96}Mo.

j) The singles intensity is higher (by at least 30%) than the one deduced from γ-γ coincidence experiment. This suggests that the line may be a doublet

k) This multipolarity assignment is based on the strong δ mixing ratio consistent only with M1/E2 type of transition.

Table 5.2

The energy of the maximum in the excitation function for states in ^{96}Tc.

Table 5.2

Initial Level			
J^{π}	Excitation Energy (keV)	Energies of Deexciting Transitions (keV)	Energy for σ_{max} (MeV)
2^{-} a)	121.6	85.1+85.9	15.7(1)
2^{+}	256.2	219.8+220.6	15.6(2)
3^{-}	227.4	105.8	15.8(2)
3^{-}	316.8	195.2	16.0(1)
		280.3	16.1(2)
3^{-}	321.6	285.1+285.9	15.8(1)
		287.2	15.9(2)
3^{-} a)	352.7	125.3	16.0(2)
		231.1	15.8(1)
3^{+}	445.1	410.7	15.8(1)
3^{+} a)	458.3	202.1	15.9(2)
		422.8	15.6(3)
3^{+}	493.4	264.3	15.6(2)
4^{-}	552.0	235.1	16.2(2)
		323.1	16.1(1)
		506.6	16.3(3)
		515.8	16.3(3)
		517.7	16.2(2)
$(4)^{-}$	646.8	294.2	16.0(5)
4^{+}	815.2	496.1	16.5(4)
4^{-} a)	867.2	550.4	16.0(1)
5^{+}	177.0	127.7	16.5(2)
		142.6	16.4(2)
5^{+}	506.4	187.0	16.8(4)
		457.2	16.3(2)
5^{-} a)	979.2	427.0	16.3(1)
(5) a)	1183.3	1134.0	16.3(2)
5^{+}	1314.0	1084.9	16.5(3)
		1264.9	16.5(4)
		1314.1	16.4(4)
6^{+}	49.3	49.3	17.4(2)
6^{+}	319.1	273.8	16.8(1)
		319.1	16.8(1)
6^{+}	752.5	575.5	16.5(4)
		752.6	16.3(4)
6^{-}	1152.1	599.9	16.9(2)
		1106.8	17.3(3)
7^{+}	575.0	525.7	17.9(1)
		574.8	18.0(3)
7^{+}	1040.8	1040.7	17.2(3)
8^{+}	947.0	371.8	18.3(2)
		897.9	18.1(2)
8^{+}	1062.7	135.3	18.2(2)
		1013.6	18.5(2)
8^{+}	1139.0	1089.7	18.0(3)
		1139.0	18.0(2)
9^{+}	927.3	927.3	18.9(3)
9^{+}	1447.8	500.8	18.2(2)
		872.8	17.7(3)
9^{+} a)	1861.8	799.3	18.9(2)
		914.7	19.0(3)
10^{+}	1703.4	756.3	18.5(2)
10^{+} a)	2214.1	352.2	19.5(2)
11^{+}	1922.9	995.7	19.5(2)
11^{+} a)	2148.5	225.8	19.6(2)
		444.9	19.4(3)
		1221.4	19.2(3)
11^{+} a)	2397.7	536.0	19.8(4)
12^{+} a)	2318.2	169.6	19.6(3)
		395.3	20.3(3)
12^{+} a)	3020.7	806.6	20.8(4)
13^{+} a)	2600.2	282.0	20.3(5)

a) This spin assignment was made using the excitation function results as a corroborative evidence.

Table 5.3

Tabulation of the energies of the gates associated with the coincidence spectra displayed in Fig. 5.3 to 5.8 inclusive.

Table 5.3

Energies of the Coincidence Gates					
Fig. 5.3 E_α=18MeV (keV)	Fig. 5.4 E_α=14MeV (keV)	Fig. 5.5 E_α=14MeV (keV)	Fig. 5.6 E_α=14MeV (keV)	Fig. 5.7 E_α=14MeV (keV)	Fig. 5.8 E_α=14MeV (keV)
49		49			
		52			
					65
				85	
				105	
				125	
		127			
		142			
169					
			172		
				178	
183			183		
			195		
					202
					205
					208 a)
			213		
					220
				231	
			235		
255	255				
264			264 a)		
273	273				
			280		
282					
					285 b)
					287
				294	
	310				
	319				
			323 a)		
				340	

Energies of the Coincidence Gates					
Fig. 5.3 E_α=18MeV (keV)	Fig. 5.4 E_α=14MeV (keV)	Fig. 5.5 E_α=14MeV (keV)	Fig. 5.6 E_α=14MeV (keV)	Fig. 5.7 E_α=14MeV (keV)	Fig. 5.8 E_α=14MeV (keV)
					346
352					
371	371				
				380	
		388			
				392	
395					
			416		
			427		
444					
		457			
			472		
			484		
					493
500					
			506 a)		
			515 b)		
			517		
525	525				
			550		
		575			
				588	
			600		
				612	
		638			
			662		
	720				
	799				
				912	
		1005			
		1138			

a) The coincidence gate for this line and the reverse one are present in the figure.

b) The individual gates for these lines and their common reverse one are present in the figure.

Table 5.4

Theoretical Estimates of the σ parameter associated with ^{96}Tc states of various spins.

Table 5.4

Theoretical Estimates of σ Parameter

J_i	σ Parameter at 14 MeV	σ Parameter at 18 MeV
1	2.8(17)	1.1(3)
2	2.6(14)	1.5(4)
3	2.8(14)	1.9(4)
4	2.8(12)	2.1(4)
5	2.8(10)	2.3(4)
6	2.5(5)	2.4(3)
7	2.4(2)	2.5(2)
8	2.5(2)	2.6(2)
9	2.6(2)	2.7(2)
10	2.7(3)	2.8(2)
11	2.8(3)	3.0(3)
12	2.9(4)	3.1(4)
13	3.0(4)	3.1(4)
14	3.0(5)	3.2(4)

Table 5.5

Linear polarization coefficients, internal conversion coefficients, and multipole assignments to transitions in ^{96}Tc.

Table 5.5

Gamma-ray Energy (keV)	Linear Polarization P(ϕ=90°)	Linear Polarization Multipolarity	Internal Conversion Coefficients E_α=14 MeV α_K x 100	Internal Conversion Coefficients E_α=18 MeV α_K x 100	Internal Conversion Coefficients Madueme et al α_K x 100	Internal Conversion Coefficients Miracle et al α_K x 100	Final Multipole Assignment
49.3				200(30)[a]	390(60)[a]		M1
52.0			200(40)[a]				M1
65.5			48(10)[a]				E1
85.1[b]						17.9(14)	E1
105.8	-.36(14)	M1			11.8(10)	20(2)	M1
125.3				30(6)			M1/E2
127.7	-.10(3)	M1		11(1)			M1
135.3	-.38(23)	M1		13(2)			M1
142.6	-.06(1)	M1		9(1)		9.1(12)	M1
169.6	-.15(10)	M1		6(1)			M1
173.0	-.64(9)	M1					M1
178.0			7.0(17)				M1
183.3[b]	-.02(2)	M1	4.1(3)	4.5(5)	9.6(15)	7.8(8)	M1
187.0			5(1)				M1
188.9			9(4)				M1/E2
191.8[b]			4.1(9)			4.5(9)	M1
195.2	-.01(5)	?	4.0(3)	4.0(4)	10.4(26)	5.1(5)	M1
202.1			4.2(5)		8.5(17)	6.4(14)	M1
205.1			3.4(3)			4.3(6)	M1
208.7[b]			2.9(5)				M1
213.8			8(2)				M1/E2
216.1			14(5)				(E2)
219.8[b]			3.6(4)		5.4(8)	3.8(4)	M1
231.1	-.02(2)	(M1)	3.0(3)		3.7(7)	3.5(3)	M1
235.1	-.06(7)	M1	2.8(3)				M1
246.3			2.2(12)				M1
253.5	.34(11)		2.1(4)				M1
255.6[b]	-.19(6)	M1	2.5(3)	2.3(2)			M1
264.3[b]			2.4(4)	1.9(5)	3.0(4)		M1
273.8	-.12(2)	M1	2.1(2)	2.0(2)			M1
280.3			.9(1)				E1

Table 5.5 (continued)

Gamma-ray Energy (keV)	Linear Polarization		Internal Conversion Coefficients				Final Multipole Assignment
	$P(\phi=90^\circ)$	Multipolarity	E_α=14 MeV α_K x 100	E_α=18 MeV α_K x 100	Madueme et al α_K x 100	Miracle et al α_K x 100	
282.0b)			1.7(5)	2.2(4)	2.5(3)		M1
285.1b)			.8(2)				E1
287.2			.9(2)				E1
294.2			1.5(2)		1.3(2)	1.8(2)	M1
308.1			1.1(4)				M1
310.9b)	-.13(7)	M1	1.5(2)	1.4(3)			M1
319.1	-.09(6)	M1	1.1(1)	1.37(4)			M1
323.1			0.1(2)				E1
325.2				2.0(5)			E2
352.2				1.0(1)			M1
366.6			1.2(4)				M1
371.8	-.22(6)	M1	.80(8)	1.0(1)			M1
380.0b)			7.8(2)				M1
383.5			1.1(4)				M1/E2
385.2			.5(3)				M1
388.5b)			.6(2)	1.3(3)			M1
395.3b)			.7(2)	.8(1)			M1
409.3b)			.48(6)		.70(18)	.69(8)	M1
410.7			.65(7)				M1
416.0			.45(6)				M1
422.8	-.19(27)	(M1)	.48(9)		.84(15)	.58(11)	M1
427.0	-.17(7)	M1	.49(5)				M1
457.2	-.05(7)	(M1)	.70(7)		.63(9)		M1
472.2b)	-.08(8)	M1	.47(4)				M1
485.0b)			.37(4)				M1
487.4	-.22(8)	M1	.55(6)				M1
492.9b)			.7(1)				M1
494.0b)	-.19(20)	M1	.37(5)				M1
496.1			.6(1)				M1/E2
498.4			.7(2)				M1/E2
500.8	.11(20)	(E1)	.35(5)				M1

Table 5.5 (continued)

Gamma-ray Energy (keV)	Linear Polarization		Internal Conversion Coefficients				Final Multipole Assignment
	$P(\phi=90^{\circ})$	Multipolarity	$E_{\alpha}=14$ MeV $\alpha_K \times 100$	$E_{\alpha}=18$ MeV $\alpha_K \times 100$	Madueme et al $\alpha_K \times 100$	Miracle et al $\alpha_K \times 100$	
506.6[b)]	.12(10)	E1	.24(3)				E1(+M1)
515.8	.05(9)	E1	.20(4)				E1
517.7	-.11(12)	E1	.23(6)				E1
520.3			.7(2)				M1/E2
525.7	-.18(9)	M1	.32(3)				M1
528.8			.45(12)				M1
529.7			.35(9)				M1
531.4	-.07(12)	M1	.27(4)				M1
569.6	-.53(44)	M1/E2					M1/E2
575.5	-.33(15)	M1					M1
599.9	.41(15)	E2					E2
720.9	-.96(34)	M1					M1
752.6	-.28(17)	M1					M1
799.3[b)]	-.27(21)	M1					M1
872.8	.28(20)	E2		.15(3)[c)]			E2
927.3	.61(9)	E2	.08(1)	.08(1)[c)]			E2
995.7	1.10(36)	E2		.07(1)[c)]			E2
1013.6	.25(23)	E2					E2
1040.7	.56(43)	M1/E2					M1/E2

a) α_T coefficient measured from the balance of intensity or γ-γ coincidence probabilities.

b) This line is a known close-doublet.

c) This line is used to normalize the experimental data and theoretical curves for the internal conversion coefficients.

CHAPTER 6

THE PROPERTIES OF ^{96}TC AND THE NUCLEAR MODELS

6.1 Introduction

The decay scheme presented in figures 5.12 - 5.14 shows no obvious systematic pattern which can be easily compared with the predictions of the models discussed in Chapter 3. This is clearly a consequence of the complexity of the intrinsic nucleon configuration in ^{96}Tc. Thus the explanation of the experimental results for this nucleus must be sought through an extension of the proposed theoretical models for the adjacent nuclei, which possess much simpler intrinsic structure. The following section 6.2 discusses the structure of such nuclei. Attempts will then be made in section 6.3 to explain some selected features of the ^{96}Tc decay scheme.

6.2 Nuclear Properties in the 90 - 100 Mass Region

6.2.1 General Description of the Region

A survey of nuclear properties in the mass region 90 - 100 reveals clearly that ^{96}Tc is within the transitional region located between the spherical and deformed nuclei. The nucleus of ^{88}Sr (see Fig. 6.1) exhibits spherical shape and its excitation spectrum is of vibrational character. On the other side of the region the Ru, Rh, Pd and Ag nuclei can be explained in the framework of collective models based on a permanent nuclear deformation. In particular,

Figure 6.1

A symplified chart of the nuclides for the mass region 90 - 100.

protons																				
$_{47}\text{Ag}$								99	100	101	102	103	104	105	106	107	108	109	110	111
$_{46}\text{Pd}$								98	99	100	101	102	103	104	105	106	107	108	109	110
$_{45}\text{Rh}$						95	96	97	98	99	100	101	102	103	104	105	106	107	108	109
$_{44}\text{Ru}$					93	94	95	96	97	98	99	100	101	102	103	104	105	106	107	108
$_{43}\text{Tc}$					92	93	94	95	96	97	98	99	100	101	102	103	104	105	106	107
$_{42}\text{Mo}$		88	89	90	91	92	93	94	95	96	97	98	99	100	101	102	103	104	105	106
$_{41}\text{Nb}$	86	87	88	89	90	91	92	93	94	95	96	97	98	99	100	101	102	103	104	105
$_{40}\text{Zr}$	85	86	87	88	89	90	91	92	93	94	95	96	97	98	99	100	101	102		
$_{39}\text{Y}$	84	85	86	87	88	89	90	91	92	93	94	95	96	97	98	99				
$_{38}\text{Sr}$	83	84	85	86	87	88	89	90	91	92	93	94	95	96	97					
$_{37}\text{Rb}$	82	83	84	85	86	87	88	89	90	91	92	93	94	95	96	97				
$_{36}\text{Kr}$	81	82	83	84	85	86	87	88	89	90	91	92	93	94	95					
	45	46	47	48	49	50	51	52	53	54	55	56	57	58	59	60	61	62	63	64

neutrons

$^{104-112}$Ru are described by a soft triaxial rotor (Sümmerer et al., 1980), while the $^{103-104}$Ag isotopes are well fitted by the Nilsson model (Ludziejewski et al., 1980). Furthermore, the character of the Mo and Zr spectra undergoes a transition from pure vibrational to pure rotational as the neutron number is increased above $n_n = 50$ (see Fig. 6.2 A and B). Thus starting from ^{88}Sr, nuclei slowly acquire deformed shape with increasing proton or neutron number. A similar situation is observed when nucleons are gradually removed from the ^{88}Sr core.

This transitional region is characterized by strong configuration mixing. Such mixing indicates the existence of strong residual interactions which undercut the applicability of the shell model. $^{88}_{38}\mathrm{Sr}_{50}$ and $^{90}_{40}\mathrm{Zr}_{50}$ are no exception. These nuclei are often considered to be "doubly magic" which means that they are characterized by the closure of both a neutron and a proton shell, (i.e. $n_n = 50$ and $n_p = 38$ or 40). However the experimental evidence indicates that neither of those nuclei are truly doubly magic. In ^{90}Zr, the valence protons are divided with equal strength between the ($2p_{1/2}$) and ($1g_{9/2}$) shells, whereas the shell model predicts a filled ($2p_{1/2}$) shell with no strength in the ($1g_{9/2}$) orbital (see Fig. 6.3). ^{88}Sr is a better "magic" nucleus since the $p_{3/2}$ shell is nearly filled with small occupancy of the ($2p_{1/2}$) and ($1g_{9/2}$) orbitals (Alford et al., 1977). A similar lack of complete closure occurs in nuclei with neutron number $n_n = 38$ or 40.

Another measure of a "magic" even-even nucleus is the separation between the ground state and the first excited 2^+ state.

Figure 6.2

The systematics of the level structures of the even-even Zr(A) and Mo(B) nuclei (from Federman and Pittel, 1979). The A_γ coefficients of the proton wave function for the ground state of the even-even Mo isotopes are defined by the equation 6-1. Graph C presents the A_γ coefficients plotted as a function of neutron number (from Cheung et al., 1975).

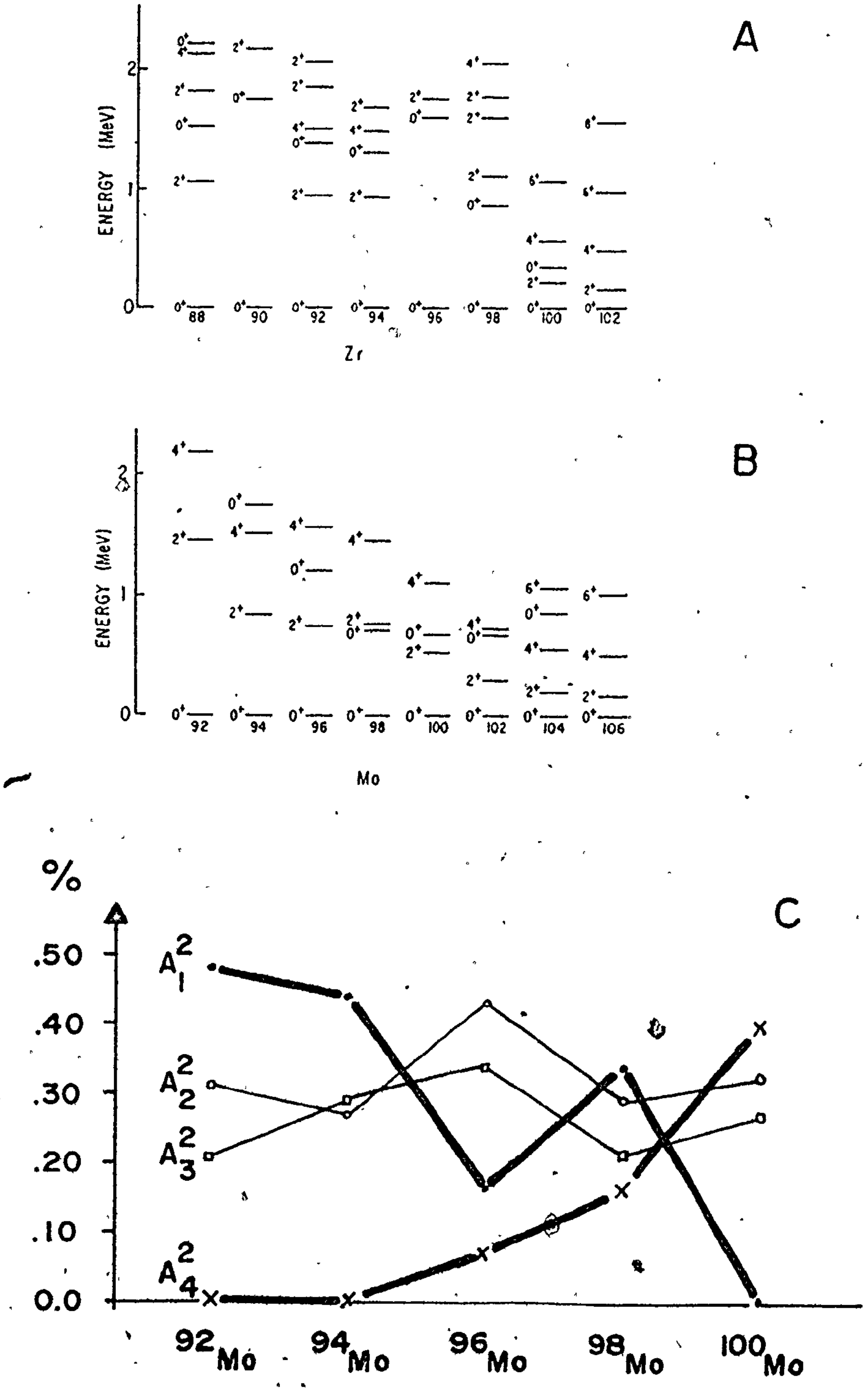
A
ENERGY (MeV)
0
1
2
88
90
92
94
96
98
100
102
Zr
B
ENERGY (MeV)
0
1
2
92
94
96
98
100
102
104
106
Mo
C
%
.50
.40
.30
.20
.10
0.0
A_1^2
A_2^2
A_3^2
A_4^2
^{92}Mo
^{94}Mo
^{96}Mo
^{98}Mo
^{100}Mo

Figure 6.3

Ordering of the shell model orbitals for ^{96}Tc as deduced from the experimental data of the mass region 90 - 100.

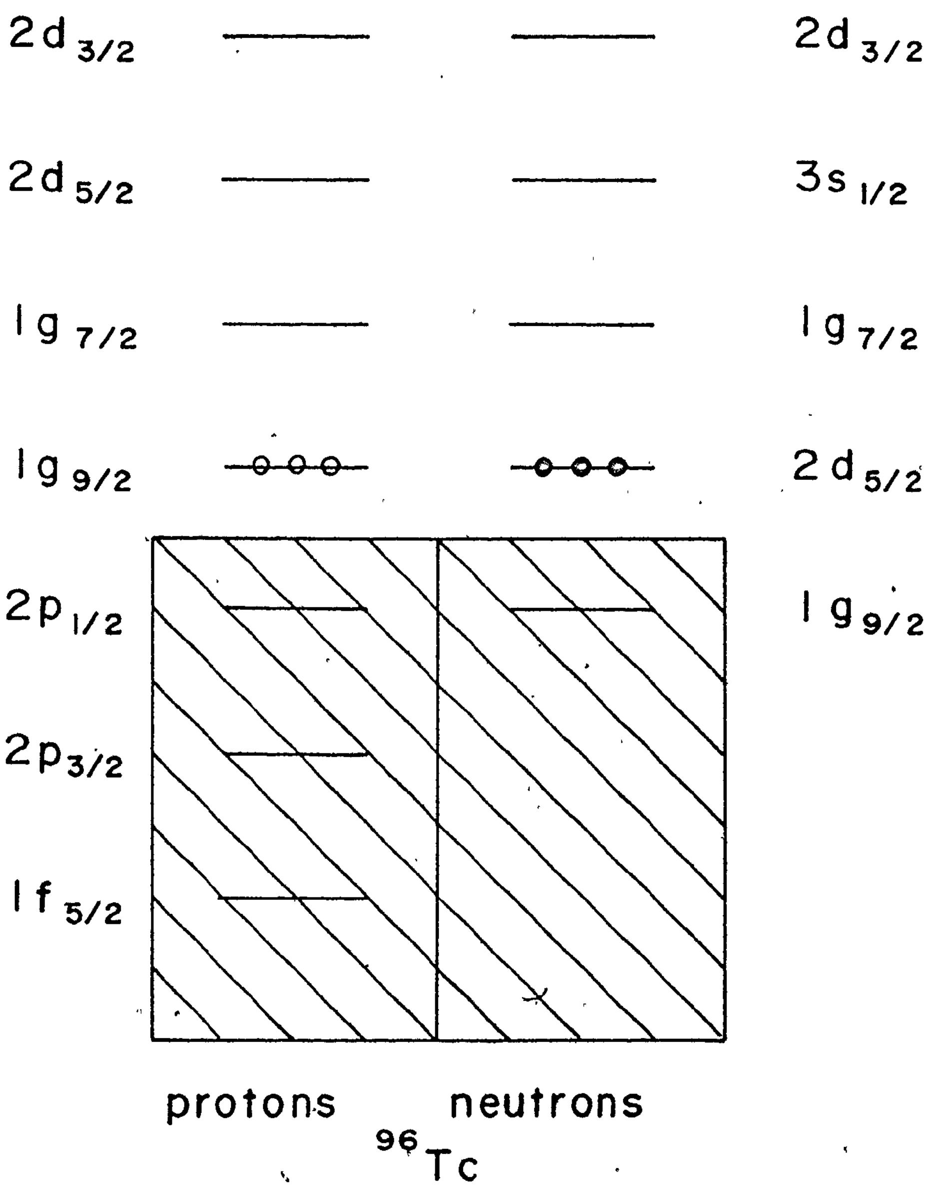

2d 3/2
2d 5/2
1g 7/2
1g 9/2
2p 1/2
2p 3/2
1f 5/2
2d 3/2
3s 1/2
1g 7/2
2d 5/2
1g 9/2
protons
neutrons
96Tc

This separation is very large for a "doubly magic" nucleus and decreases dramatically with the addition or removal of nucleons. Using this measure, ^{90}Zr is a better "magic" nucleus than is ^{88}Sr (see Fig. 6.4). In contrast to the evidence discussed above, the nucleons in the partially filled shells of ^{90}Zr are more tightly bound than those of ^{88}Sr.

Whereas among light nuclei, the order of filling of vacant orbitals is not greatly affected by the number of nucleons present in a partially filled shell, this is no longer so in the mass 100 region where the ordering of shell model states fluctuates as one crosses the region. Thus, the interaction between nucleons in adjacent orbitals determines the level structure of these nuclei.

6.2.2. The Even-even Nuclei

The even-even Sr, Zr and Mo nuclei in the 50 neutron region display typical vibrational spectra characterized by a 0^+ ground state, a 2^+ first excited state at $\sim$ 800 keV and a 0^+, 2^+, 4^+ multiplet of levels $\sim$ 1600 keV. According to the vibrational model, the low-lying states are attributed to one and two-phonon vibrational oscillations (see Fig. 6.2 A and B). With increasing neutron number the two-phonon triplet separates indicating the growing strength of some competing interaction. Furthermore, the lowering of the excitation energy of the first 2^+ state indicates a gradual softening of the nuclear core and a transition toward shape deformation.

The most dramatic effect is the rapid lowering of the first excited 0^+ state as a function of increasing neutron number (see Fig.

Figure 6.4

"Contour plot of the experimental energy of the lowest 2^+ state given in keV as a function of N and Z. Stable isotopes are indicated by solid block squares. Note "hills" and "valleys" associated with Z=40", (from Sheline et al., 1972).

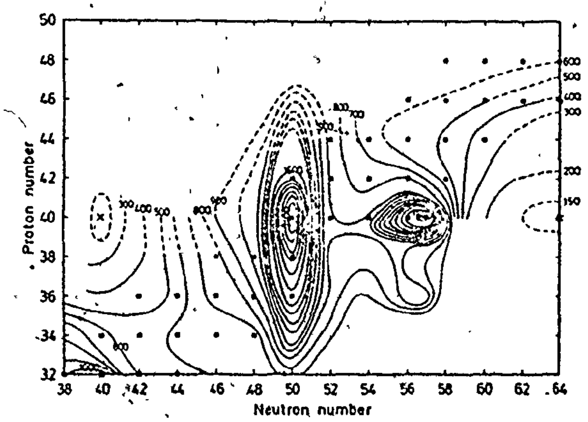
Proton number
50
48
46
44
42
40
38
36
34
32
Neutron number
38
40
42
44
46
48
50
52
54
56
58
60
62
64
300
400
500
800
900
1600
800
700
900
600
500
400
300
200
150
600
1000

6.2 A and B). This "0^+ effect" is also observed in other transitional regions. In the mass region 100, it has been interpreted as evidence for shape isomerism, since a highly deformed secondary minimum is associated with such 0^+ states (Khan et al., 1978).

Federman and Pittel (1979) have attempted to explain this phenomenon through the isovector neutron-proton interaction between the $(1g_{7/2})_\nu$ and the $(1g_{9/2})_\pi$ "partner" orbitals. In their approach the excited 0^+ state must contain a substantial admixture of the $(1g_{9/2})$ proton orbital to account for the strong neutron-proton interaction.

Reiner (1957) investigated the $0^+ \rightarrow 0^+$ transitions over an extended mass region and tried to explain the results through the uplifting of a pair of identical nucleons from the $(2p_{1/2})^2_\pi$ to $(1g_{9/2})^2_\pi$ orbitals. In particular ^{90}Zr would be characterized by the $(2p_{1/2})^2 \rightarrow (1g_{9/2})^2$ proton-pair excitation while the ^{88}Zr would be characterized by the $(2p_{1/2})^{-2} \rightarrow (1f_{5/2})^{-2}$ hole-pair excitation.

Reiner's mechanism is possible provided that the $(1f_{5/2})^2_\pi$ proton pair rather than the $(2p_{1/2})^2$ is involved. The $(f_{5/2})^2_\pi$ shell is not only energetically accessible but also the $(1f_{5/2})^2 \rightarrow (1g_{9/2})^2$ transition can proceed by an $\ell=1$ transfer per nucleon rather than by the $\ell=3$ transfer per nucleon Reiner's model would require. Support for this idea is discussed below.

The ground state proton configuration for the even-even Mo isotopes can be written as (after Cheung et al., 1975):

$$\psi_{\pi}^{g.s.}(\mathrm{Mo}) = A_1(1g_{9/2})^2_{J=0} + A_2(2p_{1/2})^{-2}_0(1g_{9/2})^4_0 + A_3(2p_{3/2})^{-2}_0(1g_{9/2})^4_0$$
$$+ A_4(1f_{5/2})^{-2}_0(1g_{9/2})^4_0 \qquad [6 - 1]$$

From the analysis of data presented in Fig. 6.2 C, one observes that the rapid decrease in A_1 and the rapid rise in A_4 are closely correlated with the lowering of the 0^+ excited state. A_2 and A_4 are essentially constant over the region of interest. If Federman's model is used, the lowering of the 0^+ state is related to the decrease in amplitude of the $(1g_{9/2})^2_0$ component in the configuration.

This easy removal of particle pairs from the already filled shells indicates a softening of the "shell structure" and consequently a departure from a central potential picture. Furthermore the $(1f_{5/2})$ shell occupancy must be a critical factor in the fast growing deformmation. Summing up the above observations, one may conclude that: the uplifting of the $(1f_{5/2})$ proton pair (and perhaps neutron pairs to the $(1g_{7/2})$ orbitals) is the microscopic mechanism responsible for the nuclear deformation (or shape isomerism). However, this provides the microscopic and macroscopic description of the phenomenon, without giving any explanation. The explanation perhaps is provided by the n-p interaction as indicated by Federman and Pittel (1979).

A satisfactory interpretation of the 0^+ state behaviour cannot be provided at present; a fact which has significant consequences for the applicability of the theoretical models. The rapid lowering of nuclear states is not yet completely understood, partially because we do not know how to deal with "core excitations". For example, the current theories oversimplify this process by assuming that there is no mixing between neutron and proton core excitations, despite the fact that such mixing does occur. Since the treatment of odd-A or odd-odd nuclei depends on coupling the motion of the odd proton or odd neutron to the core, an improper treatment of the latter is propagated into the calculations for those more complex nuclei.

From the experimental data for odd-A nuclei, one can often determine the order in which single particle orbitals are filled. However, since the coupling of the particle to the core leads to a multiplet of levels, which tend to mix with the single particle states it is very difficult to predict the ordering and separation of the single particle orbitals with any confidence. Also the spacing and ordering of the nuclear shells vary rapidly as a function of proton and neutron number. These effects further invalidate the shell model approach which uses experimentally determined model parameters from adjacent even-even or odd-A nuclei to calculate the level schemes of other nuclei.

6.2.3 The Odd Tc Isotopes

Since the valence protons constitute the most active nucleons in this mass region it is pertinent for ^{96}Tc to examine the structures of the odd-A Tc isotopes. Fig. 6.5 presents the low-lying levels of these nuclei as a function of neutron number.

The lowering of the $5/2^+$ and $7/2^+$ states (Fig. 6.5 A) with increasing neutron number is strikingly similar to the "0^+ effect" discussed above. This behaviour is paralleled by the lowering of the

Figure 6.5

"The measured positive (A) and negative (B) parity levels in odd Tc isotopes. Levels of presumable equal character are connected. For the negative parity states the $1/2^-$ isomeric level is used to define the basic line. The relative positions of the $9/2^+$ ground states are also indicated", (from Krämer and Huber, 1974).

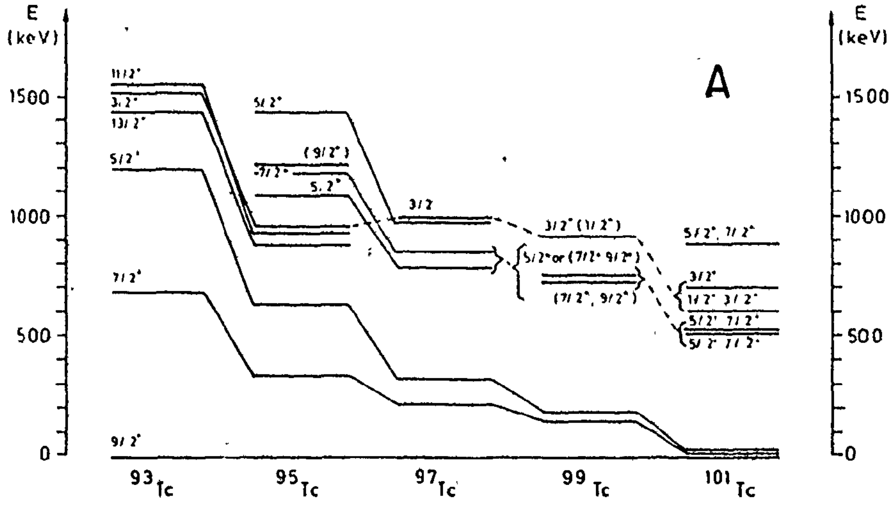
E (keV)
1500
1000
500
0
A
11/2+
3/2+
13/2+
5/2+
7/2+
9/2+
5/2+
(9/2+)
7/2+
5/2+
3/2
3/2+ (1/2+)
5/2+ or (7/2+ 9/2+)
(7/2+, 9/2+)
5/2+, 7/2+
3/2+
1/2+ 3/2+
5/2+ 7/2+
5/2+ 7/2+
93Tc
95Tc
97Tc
99Tc
101Tc

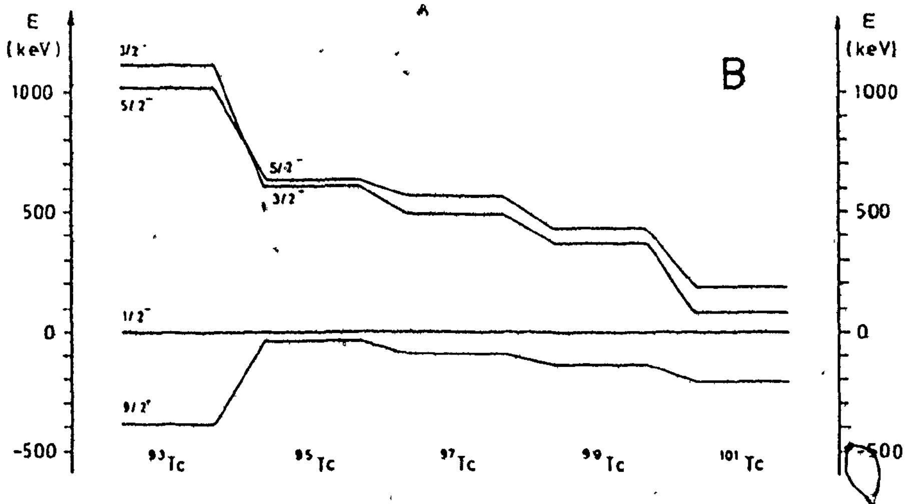
E (keV)
1000
500
0
-500
B
3/2−
5/2−
5/2−
3/2−
1/2−
9/2+
93Tc
95Tc
97Tc
99Tc
101Tc

unoccupied $d_{5/2}$ and $d_{3/2}$ proton states. This lowering can be deduced from the particle transfer data of Cheung et al. (1975). This correlation goes even further since the first excited $5/2^+$ state is collective in nature for ^{93}Tc, while it can be populated by an $\ell=2$ proton transfer for ^{97}Tc. Thus the lowering of the $5/2^+$ state is proportional to the amplitude of the $d_{5/2}$ proton shell present in the wave function for this level.

Although the separation of the $f_{5/2}$, $p_{3/2}$ and $p_{1/2}$ shells from the $g_{9/2}$ shell decreases as a function of the neutron number, the changes are not as dramatic as those for the even-even Mo nuclei. Fig. 6.5 B also presents the excitation levels of the negative parity states in Technetium. The decrease in excitation of these states with increasing mass can be associated with an increase in the amplitude of the $f_{5/2}$-component in the wave functions of those states. Furthermore, Riley et al. (1971) have noted the rapid increase in fragmentation of the proton states with increasing neutron number.

^{95}Tc is the only odd-Tc isotope, which has been investigated carefully in (α,2n), (p,n) and proton transfer reactions. Thus the low-lying, low-spin states and the pattern of the high-spin states in this nucleus are well known. Fig. 6.6 presents the experimental results of Mashall et al. (1978) obtained through the ^{93}Nb(α,2n)^{95}Tc reaction. One observes negative and positive parity bands involving sequences of intense stretched E2 transitions. Although these bands do not display any regular pattern, they must be collective in nature.

Figure 6.6

"The level structure of ^{95}Tc as deduced from the (α,2n) reaction data", (from Marshall et al., 1978).

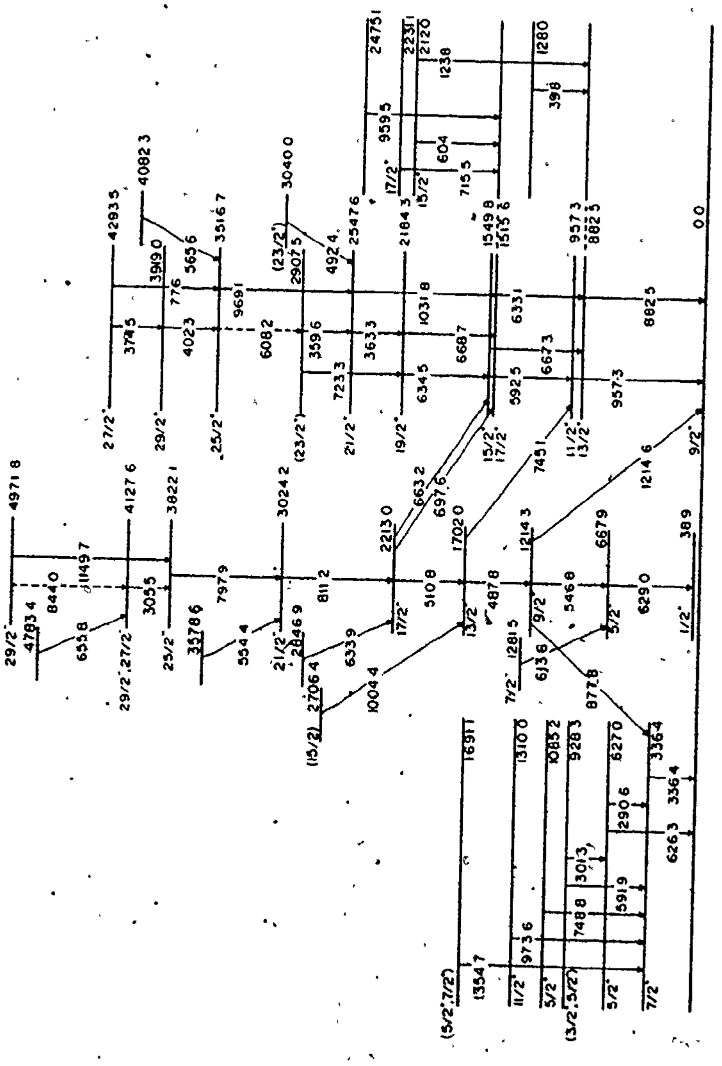
4971.8
29/2
4783.4
844.0
1149.7
655.8
4127.6
305.5
29/2,27/2
3822.1
25/2
3578.6
797.9
554.4
3024.2
21/2
2846.9
811.2
2706.4
(15/2)
633.9
1004.4
2213.0
17/2
663.2
697.6
510.8
1702.0
13/2
487.8
745.1
1214.3
9/2
1281.5
7/2
613.6
546.8
667.9
5/2
877.8
629.0
389
1/2
1214.6
4293.5
27/2
374.5
4082.3
3919.0
29/2
776
402.3
565.6
3516.7
25/2
969.1
608.2
3040.0
(23/2)
2907.5
(23/2)
359.6
723.3
492.4
2547.6
21/2
363.3
2184.3
19/2
1031.8
634.5
1549.8
1515.6
15/2
17/2
668.7
592.5
633.1
957.3
882.5
11/2
13/2
667.3
882.5
957.3
9/2
0.0
2475.1
17/2
959.5
2231.1
15/2
2120
604
715.5
1238
1280
398
1691.1
(5/2,7/2)
1354.7
1310.0
11/2
973.6
1085.2
5/2
748.8
928.3
(3/2,5/2)
301.3
591.9
627.0
5/2
290.6
336.4
7/2
336.4
626.3

The positive parity band is based on the $9/2^+$ state and on the configuration of protons from the $(1g_{9/2})$ shell. All the present theoretical models applied to this nucleus accepted the simple shell model prediction that this configuration consists of 3 protons. However based on the observed proton-pair vacancies in the $p_{1/2}$ and $p_{3/2}$ orbitals in ^{94}Mo (Cheung et al., 1975) it seems more likely that this configuration should include 5 protons rather than three. Furthermore, whereas the high spin states of positive parity must be obtained by the coupling of those protons, the neutron-pair excitations will also contribute to the structure of levels above 1 MeV.

The negative parity band starts with the $1/2^-$ state. However it is not based on a pure $(2p_{1/2})^{-1}(1g_{9/2})^4$ proton configuration as assumed in all the theoretical calculations done so far, but must include a $(1f_{5/2})^{-1}(1g_{9/2})^4$ component as well. This can be deduced from Fig. 6.6 where the reduced transition probabilities for a number of transitions connecting the high spin states of negative and positive parity indicate that a more ℓ-favourable proton configuration is involved. The $(1f_{5/2})$ shell which is accessible at ∿ 600 keV becomes the obvious choice. The work of Cheung et al. on ^{97}Tc also suggests the participation of the $f_{5/2}$ shell.

So far the theoretical models have failed to consider either the 5 proton configuration in the $g_{9/2}$ shell as responsible for the high spin positive parity based, or the $f_{5/2}$ proton hole in relation to the negative parity structure. Also no mixing of the proton and neutron "core" excitations have been included. Consequently, the models cannot explain either the pattern of the experimental levels, or the number of levels involved in the decay scheme of odd-Tc isotopes.

6.3 The Properties of the ^{96}Tc Level Scheme

This section includes a discussion of selective features of the ^{96}Tc decay scheme. The inability to discuss the complete level structure is a consequence of the complexity of the odd-odd nuclear system.

Fig. 6.7 A presents the low-lying sextet of levels ranging in spin from 2^+ to 7^+, which has been found experimentally and attributed to the ground state configuration. According to the shell model the coupling of an odd neutron in the $d_{5/2}$ shell to an odd proton in the $g_{9/2}$ shell indeed results in a sextet of positive parity levels ranging in spin from 2 to 7. However one should also note the presence of a low-lying $d_{5/2}$ proton and $g_{7/2}$ neutron shells. Thus the extension of the proton and neutron active spaces to include these shells results in additional multiplets of levels of spin between 2^+ and 8^+. Since these levels may mix, the observed, low-lying sextet of levels may as well contain admixture of configurations including terms other than those arising from the coupling of the $g_{9/2}$ proton and $d_{5/2}$ neutron.

Fig. 6.7 presents some attempts to estimate the low-lying sextet using the shell model. In the estimates of Madueme and Arita (1978) presented in Fig. 6.7 B the Pandya relation was used. This relation correlates the multiplet energies of one odd-odd nucleus to the multiplet energies of the next odd-odd isotope. In the present case the levels in ^{96}Tc were predicted on the basis of the ^{94}Tc experimental results. In the estimates of Fig. 6.7 C the shell model calcula-

Figure 6.7

The low-lying energy levels in ^{96}Tc:

1) the experimental results of this thesis (A);
2) the theoretical estimates of Madueme and Arita (1978) using Pandya relation (B) and shell model (C);
3) the simplified shell model calculations of Emigh et al. (1979) are plotted in (D).

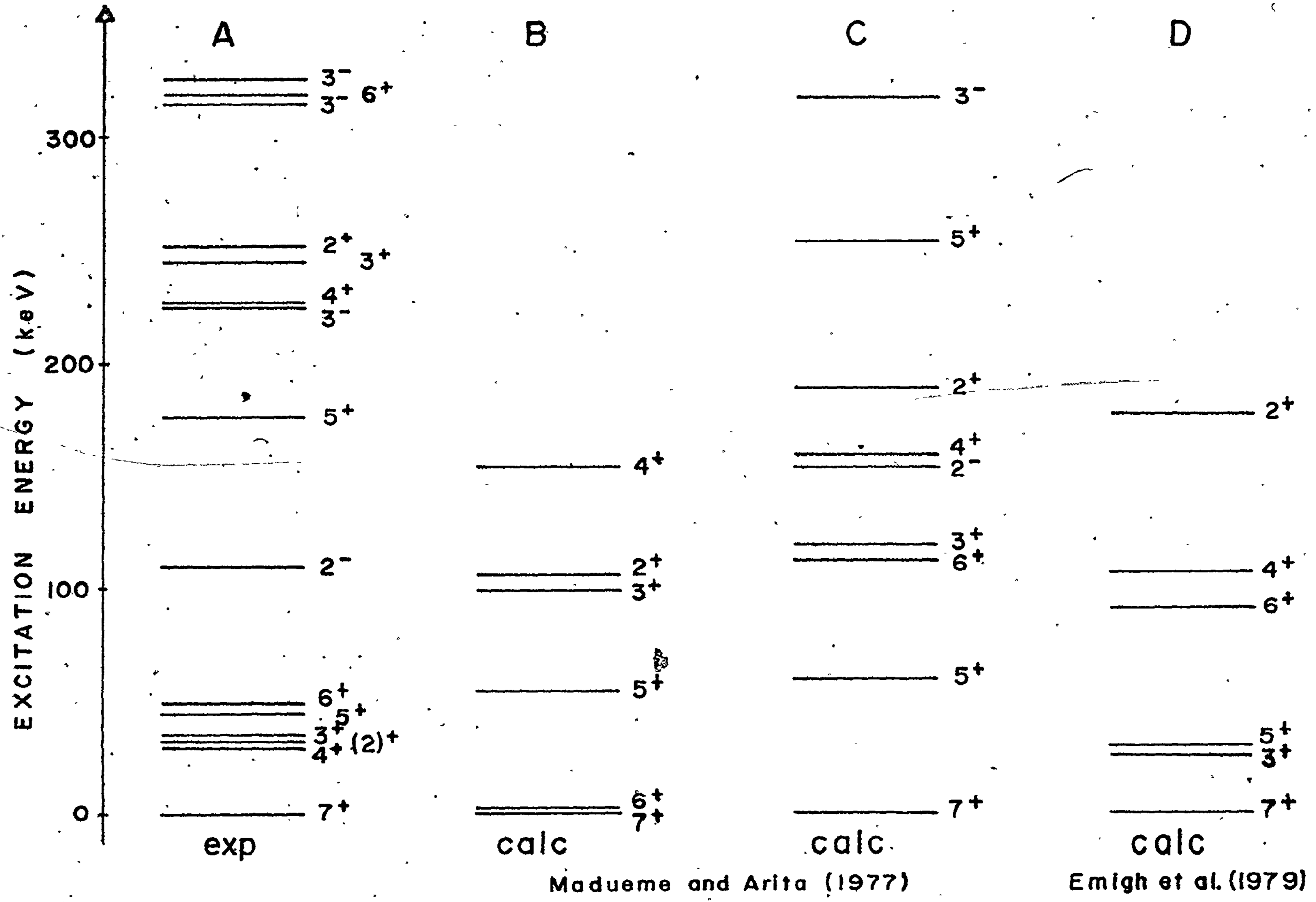
A
B
C
D
EXCITATION ENERGY (keV)
300
200
100
0
3⁻
3⁻ 6⁺
3⁻
2⁺
3⁺
4⁺
3⁻
5⁺
2⁻
6⁺
5⁺
3⁺ (2)⁺
4⁺
7⁺
4⁺
2⁺
3⁺
5⁺
6⁺
7⁺
3⁻
5⁺
2⁺
4⁺
2⁻
3⁺
6⁺
5⁺
7⁺
2⁺
4⁺
6⁺
5⁺
3⁺
7⁺
exp
calc
calc
calc
Madueme and Arita (1977)
Emigh et al. (1979)

tions were performed by assuming ^{88}Sr as an inert core and considering the residual interactions for protons residing in the $p_{1/2}$ and $g_{9/2}$ shells and neutrons in the $d_{5/2}$ shell. The necessary strength of the nucleon-nucleon interactions were taken from the adjacent nuclei, in particular from ^{92}Zr. The shell model calculations of Emigh et al. (1979) presented in Fig. 6.7 D were based on a much simpler shell model. The residual two body matrix elements were deduced from the experimental spectrum of ^{98}Tc, despite the fact that the decay scheme of ^{98}Tc has not been yet thoroughly investigated. It is evident that none of the models have much predictive power.

Fig. 6.8 presents a comparison of the low-lying levels in a series of odd-odd Tc and Nb isotopes (the Niobium isotopes differ from their Technetium counterparts only in having two less protons in the $g_{9/2}$ shells). The sextet of low-lying levels of spin between 2^+ and 7^+ is of prime interest. Whereas the structures of ^{92}Nb and ^{94}Tc show a few, well separated levels, those of the remaining nuclei (except ^{96}Nb) reveal an increasingly dense group of states whose energy falls as the neutron number increases.

The level structures of ^{94}Tc and ^{98}Tc (or ^{92}Nb and ^{96}Nb) should be similar according to the shell model since we are comparing a nucleus with a single neutron in the $d_{5/2}$ shell with one which has a single neutron vacancy in the same shell. If one looks at the excitation of the first 2^+ states in ^{90}Zr and ^{96}Zr (see Fig. 6.2), it appears that the $d_{5/2}$ shell is well separated from other shells. On the other hand, evidence from ^{92}Mo and ^{98}Mo in the same figure, shows

Figure 6.8

A comparison of the experimentally determined low-lying energy levels in ^{94,96,98}Tc and ^{92,94,96}Nb odd-odd isotopes.

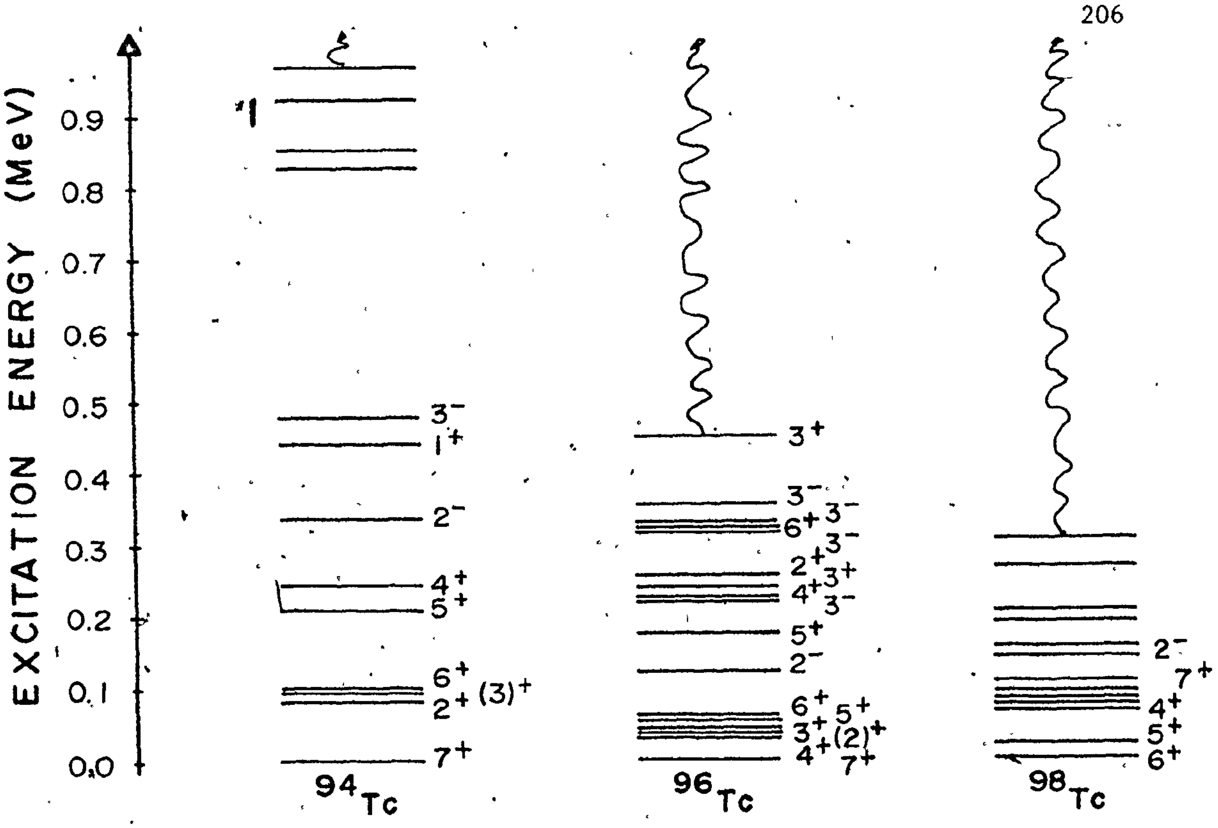
EXCITATION ENERGY (MeV)
0.9
0.8
0.7
0.6
0.5
0.4
0.3
0.2
0.1
0.0
3⁻
1⁺
2⁻
4⁺
5⁺
6⁺
2⁺ (3)⁺
7⁺
94Tc
3⁺
3⁻
6⁺ 3⁻
2⁺ 3⁻
4⁺ 3⁺
3⁻
5⁺
2⁻
6⁺ 5⁺
3⁺ (2)⁺
4⁺ 7⁺
96Tc
2⁻
7⁺
4⁺
5⁺
6⁺
98Tc

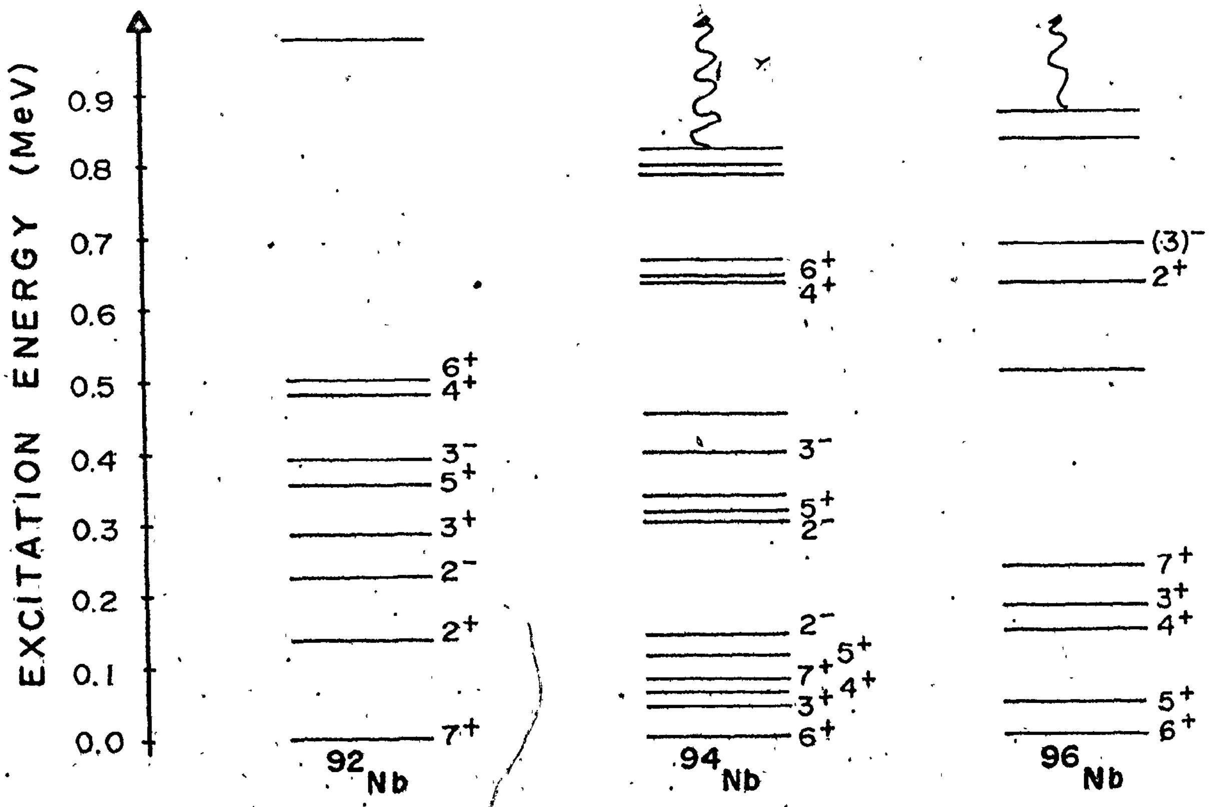
EXCITATION ENERGY (MeV)
0.9
0.8
0.7
0.6
0.5
0.4
0.3
0.2
0.1
0.0
6⁺
4⁺
3⁻
5⁺
3⁺
2⁻
2⁺
7⁺
92Nb
6⁺
4⁺
3⁻
5⁺
2⁻
2⁻
7⁺ 5⁺
3⁺ 4⁺
6⁺
94Nb
(3)⁻
2⁺
7⁺
3⁺
4⁺
5⁺
6⁺
96Nb

that the $d_{5/2}$ shell is mixed with others so that there is no distinct closure at $n_n = 56$ for these nuclei. Consequently, the shell model picture is qualitatively correct for ^{94}Tc, ^{92}Nb and ^{96}Nb but fails for ^{98}Tc. In fact, the presence of strong fragmentation of single particle levels and configuration mixing in ^{98}Tc indicates that the sextet of levels in ^{96}Tc also cannot be a pure $d_{5/2} - g_{9/2}$ configuration. Because of this fragmentation the current models cannot even predict the correct number of states to be expected below 1 MeV.

A selection of negative parity states of ^{96}Tc is presented in Fig. 6.9. The presence of the low-lying $1/2^-$ level in ^{95}Tc populated by an ℓ=1 proton transfer indicates a $(2p_{1/2})^{-1}$ configuration. Thus by coupling of the $d_{5/2}$ neutron to this $p_{1/2}$ proton-hole one expects to observe in ^{96}Tc a low-lying doublet of levels of spin 2^- and 3^- respectively. However, as it is evident in this mass region, the particle holes in the $p_{3/2}$ and $f_{5/2}$ orbitals are highly possible and already contribute to the low-lying energy levels in the even-even and even-odd nuclei. Thus one has to consider additional 1^-, 2^-, 3^-, 4^- and 0^-, 1^-, 2^-, 3^-, 4^-, 5^- multiplets formed by a coupling of an $d_{5/2}$ neutron to those proton-holes. Furthermore, these states may mix.

The observed 2^- level at 121.6 keV is connected to the 3^+ and 2^+ levels of the ∿ 35 keV triplet by a doublet of E1 transitions. The 2^- level has a mean lifetime of $37.0^{+0.6}_{-0.3}$ nanosec (McDaniel and Snyder, 1974) which is too fast to be a pure $p_{1/2} \rightarrow g_{9/2}$ transition, since an ℓ- change of 3 is highly forbidden. Clearly the wave function of the

Figure 6.9

A selection of the low-lying negative parity levels in ^{96}Tc.

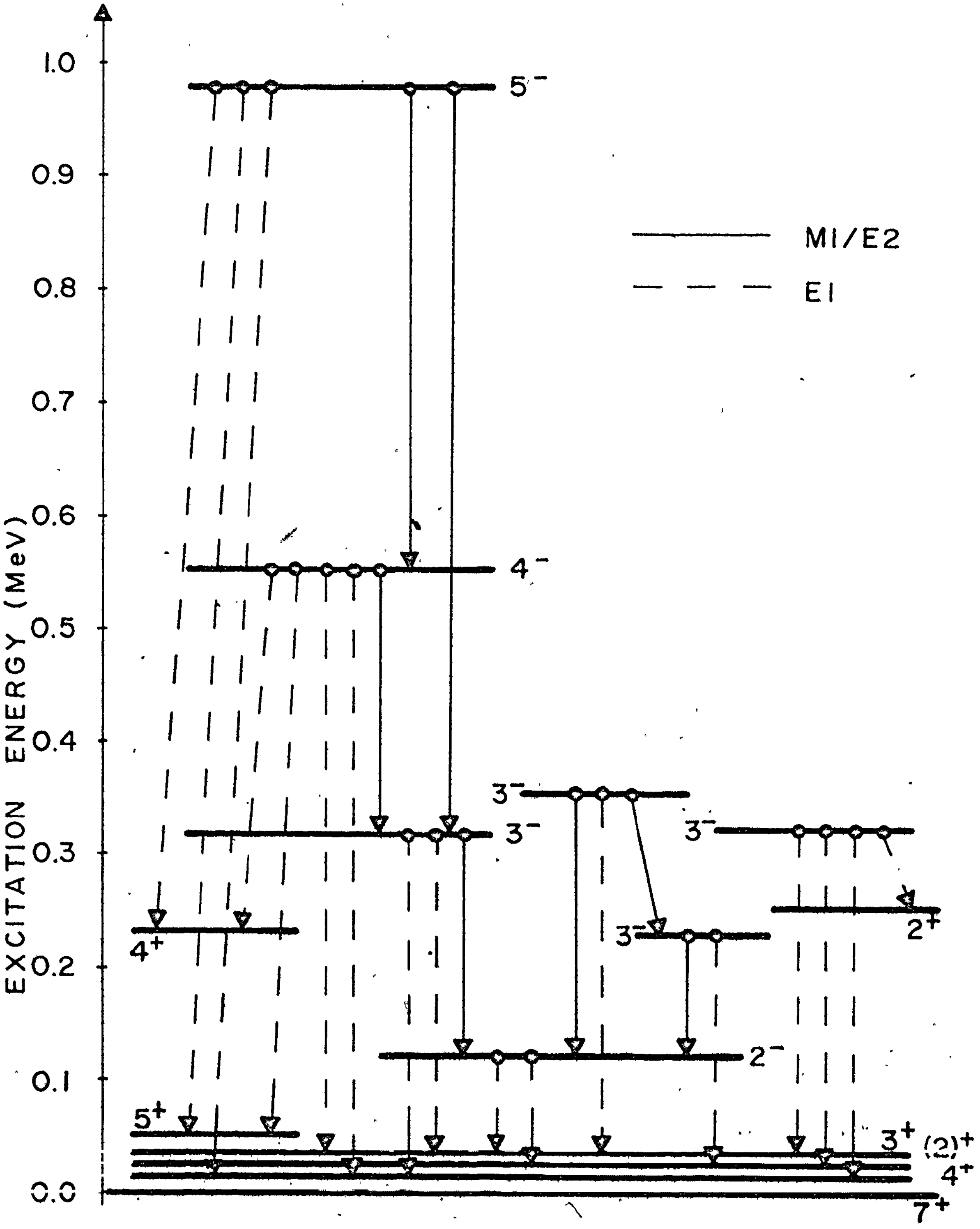
EXCITATION ENERGY (MeV)
1.0
0.9
0.8
0.7
0.6
0.5
0.4
0.3
0.2
0.1
0.0
MI/E2
EI
5⁻
4⁻
3⁻
3⁻
3⁻
3⁻
3⁻
4⁺
2⁺
5⁺
2⁻
3⁺
(2)⁺
4⁺
7⁺

2^- state includes components such as the $(1f_{5/2})_\pi^{-1}$ or the wave functions of the 2^+ and 3^+ states include components such as the $(d_{5/2})_\pi^1$; all such admixtures will speed up the transition since they introduce ℓ changes of one. Emigh et al. (1979) reports in their $(^3He,d)$ work that the angular distribution for the 121 keV peak is best fitted by an $\ell = 1 + 4$ mixture. It would appear that an $\ell = 1 + 3$ fitting would also have been satisfactory. This fit would be consistent with a mixed $(1p_{1/2})^{-1}$ and $(1f_{5/2})^{-1}$ wave function.

The presence of a small $(1f_{5/2})^{-1}$ admixture in the negative parity states is required to explain the transitions between the low-lying negative and positive parity states. In particular the 3^- 321.6 keV, 4^- 552.0 keV and 5^- 979.2 keV levels have E1 transitions linking them to the positive parity levels characterized by a predominant $g_{9/2}$ component.

One should note a contrast between the positive parity "band" which is populated up to spin 13 (see Fig. 6.10) and the negative parity "band" which terminates at spin 6 (see Fig. 6.9). The explanation probably lies in the fact that the 7^+ ground state is the "band head" for the positive parity sequence which forms the Yrast levels, while the "band head" for the negative parity sequence is a 2^- state. The difference of 5 units of angular momentum means that for states of the same spin, the negative parity number lies much higher than its positive counterpart and its strength is drained to the positive parity sequence.

Figure 6.10

A sequence of the high-lying, high-spin states in ^{96}Tc (from Mach et al., 1980).

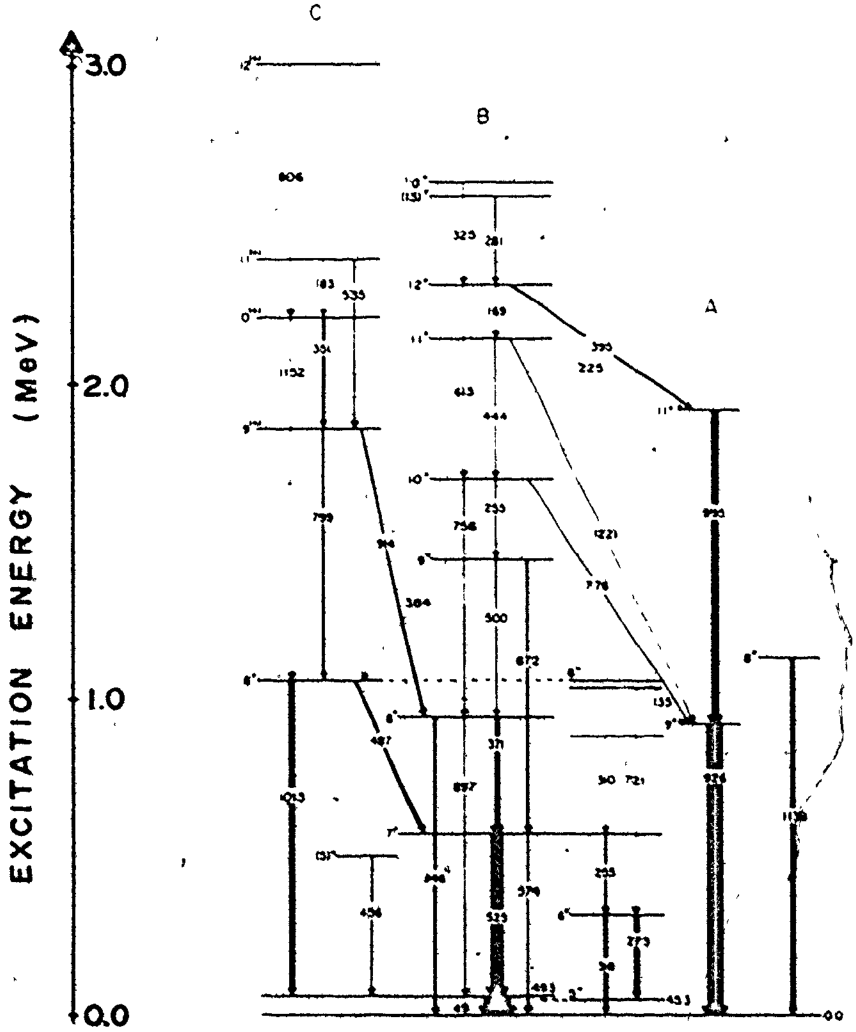
EXCITATION ENERGY (MeV)
3.0
2.0
1.0
0.0
C
B
A
806
325
281
183
535
12⁺
169
390
225
1152
11⁺
613
444
799
10⁺
255
756
(122)
990
300
384
776
872
135
371
487
897
310
721
1013
255
456
579
525
273
926
1139
453
0.0

The positive parity high-lying, high-spin states are discussed next. The vibrational character of the positive parity levels in ^{95}Tc and ^{94}Mo indicates that one can expect the high-lying positive parity levels in ^{96}Tc also to be vibrational. However the situation in ^{96}Tc will be much more complex. By coupling one or two phonons to the sextet of the low-lying positive parity levels of spins between 2^+ and 7^+ one obtains a number of multiplets. Furthermore, these states may mix with one another and with single particle configurations, to generate an unmanageably complex structure. However, the one and two "stretched" phonon coupling to the 7^+ ground state gives Yrast levels, which are expected to be intensely populated. Indeed the levels connected by the 927 and 995 keV stretched E2 transitions appear to be good candidates for these two states (see Fig. 6.10). One might have expected a state of spin 13^+ at about 3 MeV representing the three phonon coupling to the 7^+ ground state. This level is not populated because such a level would not be in the Yrast band. Instead, the observed 13^+ state decays by an M1 transition to a 12^+ level.

The 10^+ state at 2643.4 feeds the 12^+ level at 2318.2 keV, while the energetically favoured transitions to the lower 9^+ levels are not observed. This suggests that the nature of this state is different from the rest of the "band".

The low-lying sextet of levels indicates a soft n-p coupling while the vibrational character of the 927 and 1922 keV levels indicates a "hard" core. Thus, it seems that the valence nucleons are loosely attached to the core, which itself remains tightly bound despite the strong configuration mixing present in the decay structure.

The available models cannot provide an adequate description of ^{96}Tc. However, the possible extension of the IBFA model to the odd-odd nuclei or new models based on the Federman and Pittel (1979) approach may provide a substantial improvement in the theoretical estimates for ^{96}Tc.

CHAPTER 7

CONCLUSIONS AND THE DIRECTION OF THE FUTURE STUDIES

The work enclosed in this thesis clearly shows that it is feasible to determine with high confidence the decay structure of such complex nuclei as odd-odd ^{96}Tc using the presently available tools of gamma-ray spectroscopy. Since the ground state spins of the odd-odd nuclei in this mass region are generally rather large, the (p,n) reactions have not been successful in probing the low-lying levels. These are more accessible through the (α,n) reaction which populates states with a wide range of spin values including states up to spin 13. It appears from recent experiments performed in this laboratory that Lithium induced reactions are more successful than (α,n) in populating high spin states. These reactions populate selectively states of high spin and therefore create spectra which are considerably simpler than those produced by the (α,n) reaction.

Whereas the experimental techniques are able to provide a verifiable level scheme for ^{96}Tc, the theoretical models are clearly inadequate to explain the observed structure. Future models must contain a substantially new microscopic understanding of the nature of nuclear forces to be successful, since minor extensions of the existing approaches are doomed to fail. Although the IBFA model and the model of Federman and Pittel (1979) contain promising ingredients the "Grand Unified Model" is not in sight. Since the properties of the high-spin states of nuclei in this mass region will be a crucial component in the testing of the future model, it is important that these be determined with high confidence.

This thesis provides new techniques to determine the spins of high spin states. The ratio of intensities method described in the thesis becomes even more powerful when combined with coincidence techniques. In the recent Lithium experiments, the ratio of the intensities of a peak in the coincidence projection at one beam energy to that at another was found to be excellent indicator of the spin of the initial state involved. Further work to establish the applicability of this method is needed.

In the light of new evidence from the (α,n) work, ^{96}Tc should be reinvestigated using the (p,n) reaction. High quality proton transfer reaction data to complement the gamma-ray work would also be useful.

In summar, this mass region still poses challenging experimental and theoretical questions.

REFERENCES

AGEEV, V.A., GAVRILYUK, V.I., KUPRYASHKIN, V.T., LATYSHEV, G.D., LYUTYI, I.N., MAIDANYUK, V.K., MAKOVETSKII, Y.V. and FEOKTISTOV, A.I. Bull. Acad. Sci. USSR, Phys. Ser. 33 (1970) p. 1180.

ALFORD, W.P., ANDERSON, R.E., BATAY-CSORBA, P.A., LIND, D.A., WIEMAN, H.H. and ZAFIRATOS, C.D. Nucl. Phys. A293 (1977) p. 83.

ARIMA, A. and IACHELLO, F. Phys. Rev. C, 14 (1976) p. 761.

BINI, M., BIZETTI SONA, A.M., BIZZETTI, P.G., BLASI, P., OLMI, A. and TACCETTI, N. Nvovo Cimento A35, (1976) p. 69.

BOHR, A. and MOTTELSON, B.R. K. Dan. Vidensk. Selsk. Mat. Fys. Medd. 27, No. 16 (1953).

CASTEN, R.F. and SMITH, G.J. Phys. Rev. Lett., 43 (1979) p. 337.

CHEUNG, H.C., KITCHING, J., LEE, J.K.P. and MARK, S.K. J. Phys. G, 1 (1975) p. 737.

COOK, B.W. Ph.D. thesis (1972), McMaster University

DOUKELLIS, G., McKENNA, C., FINLAY, R., RAPAPORT, J. and KIM, H.J. Nucl. Phys. A229 (1974) p. 47.

EJIRI, H., SHIBATA, T., SHIMIZU, A. and YAGI, K. J. Phys. Soc. Jpn. 33 (1972) p. 1515.

EMIGH, R.A., KRAUSHAAR, J.J. and SHASTRY, S. Nucl. Phys. A320 (1979) p. 335.

FAGG, L.W. and HANNA, S.S. Rev. Mod. Phys. 31 (1959) p. 711.

FEDERMAN, P. and PITTEL, S. Phys. Rev. C, 20 (1979) p. 820.

GALLAGHER, C.J. and MOSZKOWSKI, S.A. Phys. Rev. 111 (1958) p. 1282.

GEIGER, J.S. (1965) AECL Report CRGP-1214.

GOVE, N.B. and WAPSTRA, A.H. Nucl. Data A11, 2 & 3 (1972).

GRAHAM, R.L., GEIGER, J.S. and JOHNS, M.W. Can. J. Phys. 50 (1972) p. 513.

HAGER, R.S. and SELTZER, E.C. Nucl. Data A4, 1 & 2 (1968).

HAMILTON, W.D. The Electromagnetic Interaction in Nuclear Spectroscopy. North-Holland Publ. Comp. (1975).

HUIZENGA, J.R. and IGO, G. Argonne National Laboratory report ANL-6373 (1961).

JÄGARE, S. Nucl. Phys. A95 (1967) p. 481.

KAUP, U., GELBERG, A. and von BRENTANO, P. Phys. Rev. C, 22 (1980) p. 1738.

KERN, B.D., GABBARD, F., KRUZEK, R.G., McPHERSON, M.R., SEKHAVAN, K.K. and SNYDER, F.D. Phys. Rev. C, 18 (1978) p. 1938.

KHAN, T.A., LAUPPE, W.D., SISTEMICH, K., LAWIN, H. and SELIC. Z. Phys. A284 (1978) p. 313.

KHAN, T.A. MILCHBERG, H., SINGHAL, N.C. and JOHNS, M.W. Nucl. Instrum. Meth. 169 (1980) p. 527.

KHOO, T.L. Ph.D. thesis (1972) McMaster University.

KOFOED-HANSEN, O., LINDHARD, J., NIELSEN, O.B. Mat. Fys. Medd. Dan. Vid. Selsk. 25, No. 16 (1950).

KRÄMER, K. and HUBER, B. Z. Physik 267 (1974) p. 117.

LEDERER, C:M. and SHIRLEY, V.S. Tables of Isotopes, 7th Edition, A. Wiley - Interscience Publication (1978).

LUDZIEJEWSKI, J., KALSHOVEN, A.W.B., HESSELINK, W.H.A., RRON, J., VAN POELGEEST, A. and VERHEUL, A. Nucl. Phys. A344 (1980) p. 266, also ibid p. 283.

MACH, H.A., JOHNS, M.W. and THOMPSON, J.V. Can. J. Phys. 58 (1980) p. 174.

MACPHAIL, M. Ph.D. Thesis, McMaster University, 1973.

MADUEME, G.CH. and ARITA, K. Nucl. Phys. A297 (1978) p. 347.

MARSHALL, K.A., THOMPSON, J.V., COOK, W.B. and JOHNS, M.W. Can. J. Phys. 56 (1978) p. 117.

MATSUO, T., MATUSZEK, J.M., DUDEY, N.D. and SUGIHARA, T.T. Phys. Rev. C 139 (1965) p. 886.

MAYER, M.G. and JENSEN, J.H.D. Elementary Theory of Nuclear Shell Structure, Wiley, New York (1955).

McDANIEL, F.D. and SNYDER, F.D. Phys. Rev. C, 10 (1974) p. 1124.

MEDSKER, L.R. Nucl. Data, B8, 6 (1972).

MILLER, J.M. Proceedings of the International Conference on Nuclear Physics, Munich, 1973, Vol. 2, p. 598, North-Holland Publishing Company (1973).

MIRACLE, D.E. and KERN, B.D. Nucl. Phys., A320 (1979) p. 353.

MOLDAUER, P.A. Argonne National Laboratory report ANL-6323 (1961).

NILSSON, S.G. K. Dan. Vidensk. Selsk. Mat. Fys. Medd. 29 (1955).

NORDHEIM, L. Phys. Rev. 78 (1950) p. 294.

PRESTON, M.A. Physics of the Nucleus, Addison-Wesley Publishing Company Inc. (1963).

REINER, A.S. Physica 23 (1957) p. 338, also: Nucl. Phys. 27 (1961) p. 115.

RILEY, P.J., HORTON, J.L., HOLLAS, C.L., ZAIDI, S.A.A., JONES, C.M. and FORD, J.L.C. Phys. Rev. C, 4 (1971) p. 1864.

ROGERS, D.W.O. Nucl. Instrum. Methods 127 (1975) p. 253.

SCHOLTON, O. Ph.D. thesis (1980) Groningen University, Holland.

SHELINE, R.K., RAGNARSSON, I. and NILSSON, S.G. Phys. Lett. 41B (1972) p. 115.

SHIBATA, T., ITAHASHI, T. and WAKATSUKI, T. Nucl. Phys. A237 (1975) p. 382.

SMITH, H.J. Ph.D. thesis (1977) McMaster University.

SÜMMERER, K., KAFFRELL, N., STENDER, E., TRAUTMANN, N., BRODEN, K., SKARNEMARK, G., BJÖRNSTAD, T. and HALDORSEN, I. Nucl. Phys. A339 (1980) p. 74.

WEISSKOPF, V.F. Phys. Rev. 83 (1951) p. 173.

YAMAZAKI, T. Nucl. Data A3, 1 (1967).